# Interaction-free measurements with electrons and optical field enhancement at nanotips

Sebastian Thomas

München 2015

# Interaction-free measurements with electrons and optical field enhancement at nanotips

**Sebastian Thomas**

Dissertation
an der Fakultät für Physik
der Ludwig–Maximilians–Universität
München

vorgelegt von
Sebastian Thomas
aus Kassel

München, den 30.10.2015

Erstgutachter: Prof. Dr. Peter Hommelhoff
Zweitgutachter: Prof. Dr. Matthias Kling

Datum der mündlichen Prüfung: 4. April 2016

# Zusammenfassung

Sogenannte wechselwirkungsfreie Messungen sind ein aus der Quantenmechanik bekanntes Interferenzphänomen, mit dessen Hilfe die Anwesenheit eines Objekts detektiert werden kann, ohne das Objekt in irgendeiner Weise zu stören. Der erste Teil dieser Arbeit befasst sich mit wechselwirkungsfreien Messungen mit Elektronen. Integriert in ein Mikroskop könnte diese Technik es ermöglichen, die bei Elektronenmikropskopie auftretenden Strahlenschäden erheblich zu reduzieren.

Es werden verschiedene Ansätze zur Realisierung von wechselwirkungsfreien Messungen mit Elektronen und die dabei auftretenden Schwierigkeiten besprochen. Hauptthema hierbei ist der benötigte Elektronen-Strahlteiler. Wir stellen einen möglichen Ansatz vor, der auf der Kontrolle und dem Einschluss eines Elektronenstrahls durch Mikrowellenfelder beruht. Mit diesem Strahlteiler ist es gelungen, einen langsamen Elektronstrahl mit kinetischer Energie von ungefähr 1 eV in zwei Strahlen zu spalten. Wir diskutieren in einem vereinfachten quantenmechanischen Modell, welche Eigenschaften ein solcher Strahlteiler aufweisen muss, um Elektronenwellen ohne Störung zu teilen und wechselwirkungsfreie Messungen zu ermöglichen. Außerdem beschäftigen wir uns mit der Anwendung von interaktionsfreien Messungen in der Bildgebung, insbesondere mit der Frage, inwiefern sie die Messung und Unterscheidung von Graustufen erlauben. Es stellt sich heraus, dass die Messung von Graustufen im typischen Interferenzaufbau einer wechselwirkungsfreien Messung zwar möglich ist, aber der dabei entstehende Schaden am Messobjekt nur in speziellen Fällen geringer ist als in einer herkömmlichen Transmissionsmessung. Wir untersuchen auch den Einfluss von Phasenverschiebungen. Bei Messobjekten, die Graustufen aufweisen und Phasenverschiebungen verursachen, können wechselwirkungsfreie Messungen für Objekte mit hoher Transparenz weniger Schaden verursachen als konventionelle Transmissionsmessungen und Messungen mit einem Mach-Zehnder-Interferometer.

Ein weiteres Thema dieser Arbeit ist die optische Feldverstärkung an Nanospitzen. Wir untersuchen in numerischen Simulationen über einen großen Parameterbereich, wie die Höhe der Feldverstärkung von der Geometrie und dem Material der Spitze abhängt. Dabei stellen wir fest, dass neben dem Krümmungsradius der Spitze auch der Öffnungswinkel einen überraschend großen Einfluss auf die Feldverstärkung hat, welchen wir durch ein vereinfachtes Modell qualitativ erklären können. Anwendung findet die optische Feldverstärkung in der Photoemission von Elektronen aus scharfen Metallspitzen. Hierzu zeigen wir Experimente in verschiedenen Regimes der Photoemission: einerseits Multiphotonenemission mit einem Erbium-Faserlaser und andererseits Photoemission im Starkfeldregime mit einem Titan-Saphir-Oszillator. Letztere Messungen erlauben es, mit Hilfe einer neuen, auf Elektronen-Rückstreuung beruhenden Methode die optische Feldverstärkung in unmittelbarer Nähe der Spitzenoberfläche zu ermitteln. Die so erhaltenen Ergebnisse stimmen gut mit den Simulationen überein.

# Abstract

Using an interference phenomenon well known from quantum mechanics and often called an "interaction-free measurement", it is possible to detect an object's presence without disturbing the object in any way. The first part of this thesis is about realizing an interaction-free measurement with electrons. If this technique can be integrated into an electron microscope, it could enable a significant reduction of radiation damage during imaging.

We discuss different approaches towards the realization of an interaction-free measurement with electrons and the challenges that arise there. One necessary component and the main topic of our discussion is an electron beam splitter. We present a possible approach to realize such a beam splitter based on the control and guiding of an electron beam with microwave fields. Using this beam splitter, we were able to split a slow electron beam with a kinetic energy of approximately 1 eV into two beams. In a simplified quantum-mechanical model, we discuss what properties such a beam splitter must have in order to split electron waves without disturbing them and to allow interaction-free measurements. Additionally, we discuss the application of interaction-free measurements to imaging, in particular the question of measuring and distinguishing gray values. It turns out that the measurement of gray values in the typical interference setup of an interaction-free measurement is possible, but it is only in special cases that the resulting damage to the sample is smaller than in a regular transmission measurement. We also investigate the effect of phase shifts. For samples with both phase shifts and gray levels, interaction-free measurements cause less damage than conventional transmission measurements and Mach-Zehnder interferometers if the samples are highly transparent.

Another topic of this thesis is optical field enhancement at nanotips. In numerical simulations over a large range of parameters, we investigate how the strength of the field enhancement depends on the geometry and the material of the nanotip. Our results show that, next to the radius of curvature, the tip's opening angle also has a surprisingly strong effect on the enhancement, which we can explain qualitatively in a simplified model. An application of optical field enhancement is the photoemission of electrons from sharp metal tips. We show experiments for two different types of photoemission: on the one hand, multiphoton photoemission with an erbium fiber laser, and on the other hand, strong-field photoemission with a titanium-sapphire oscillator. Using a new method based on electron rescattering, the latter measurements make it possible to determine the strength of the enhanced near-field in close vicinity to the surface of the tip. The results are in good agreement with our simulations.

# Contents

*Contents*

# Introduction and overview

As indicated by the title, this thesis can be broadly divided into two topics: interaction-free measurements with electrons and optical field enhancement at nanotips.

The first part of the thesis discusses the proposal of performing an interaction-free measurement with electrons (Elitzur and Vaidman, 1993; Kwiat et al., 1995; Putnam and Yanik, 2009). If this quantum-physics-based scheme can be carried out with electrons and integrated into an imaging system, it may open up a new field of "quantum electron microscopy" with significantly reduced radiation damage as compared to existing electron microscopes. The thesis includes an introduction to interaction-free measurements and their history, a study of their performance in the imaging of gray levels, and a discussion of the necessary components for an electron-based realization. In particular, an electron beam splitter based on a Paul trap is presented.

The second part of the thesis is about the phenomenon of optical near-field enhancement at nanotips (Martin and Girard, 1997; Martin et al., 2001; Hartschuh, 2008), particularly in relation to photoemission of electrons from laser-illuminated nanotips (Hommelhoff et al., 2006a,b; Ropers et al., 2007; Barwick et al., 2007). The strength of the field enhancement depends on the features of the nanotip, in particular, on its radius of curvature, overall geometry, and material. The variation of the enhancement as a function of these parameters is discussed based on numerical simulations, and the results are compared to strong-field photoemission experiments at gold and tungsten tips (Bormann et al., 2010; Schenk et al., 2010; Krüger et al., 2011).

As laser-illuminated nanotips are a promising electron source for a future realization of an interaction-free measurement, there is a connection between the two parts of the thesis. However, they are essentially independent of each other and can be read separately by a reader only interested in one of the topics.

The form of this thesis is cumulative, also called "publication-based", so large parts of it (chapters 3 to 8) consist of material that was previously published in scientific journals. This material is presented here in a consistent layout different from the publications where it first appeared and there are minor differences in language (e.g., consistent use of American English in this thesis, use of author-year citation style, or changes to punctuation by the copy editors of the journals). The content, however, is identical to their previously published versions. The bibliographies of both the new material and the previously published parts of the thesis have been combined into one large bibliography at the end.

All the previously published articles in this thesis are the results of collaborations with coworkers and scientists at other institutions. Credit for them is shared among the authors. As far as the quantum electron microscopy part is concerned (chapters 1, 3, and 4), I worked on the simulations of interaction-free measurements with semitransparent

samples and of the beam splitter's quantum properties, as well as on the requirements and challenges for realizing an interaction-free measurement with electrons. In the optical field enhancement part (chapters 2, 5, 6, 7, and 8), I worked on the photoemission experiments with the erbium fiber laser and the titanium sapphire oscillator, as well as on the FDTD simulations and further discussions of optical field enhancement at nanotips.

## Outline

The thesis is organized as follows:

- **Chapter 1** gives an introduction to interaction-free measurements in general and a proposal for realizing them with electrons with the ultimate goal of building a "quantum electron microscope". Interaction-free measurements of semitransparent samples are discussed, and Paul traps for electrons are introduced as a means of realizing a beam splitter for electrons. The topics of this chapter are discussed further in the articles reproduced in chapters 3 and 4.

- **Chapter 2** gives a brief overview of optical field enhancement at nanotips and photoemission of electrons from such tips. It summarizes results from the articles reproduced in chapters 5 to 8, where the topics are discussed in more detail.

- **Chapter 3**, originally published in Physical Review A (Thomas et al., 2014), discusses the performance of interaction-free measurements in the determination of gray levels and phase shifts of a sample. The results are based on numerical simulations.

- **Chapter 4**, originally published in Physical Review Letters (Hammer et al., 2015), presents the design of an electron beam splitter based on a microwave chip trap for electrons. Experimental results demonstrate the splitting of a ~1 eV electron beam into two beams.

- **Chapter 5**, originally published in Optics Express (Thomas et al., 2012), discusses the compression of laser pulses of an erbium fiber laser to a pulse duration of ~23 fs using a highly nonlinear fiber. The laser system is applied in a multiphoton photoemission experiment with a tungsten nanotip.

- **Chapter 6**, originally published in Nano Letters (Thomas et al., 2013), shows results from a measurement of the field enhancement factor of gold and tungsten nanotips based on strong-field effects in the photoemission of electrons. The results are compared to Maxwell simulations.

- **Chapter 7**, originally published in Journal of Physics B: Atomic, Molecular and Optical Physics (Krüger et al., 2014), is a follow-up article to the one reproduced in chapter 6, and gives more details on the background of strong-field photoemission and on the experimental analysis of the field enhancement measurements.

- **Chapter 8**, originally published in New Journal of Physics (Thomas et al., 2015), gives results of a large series of numerical simulations on optical field enhancement at nanotips. The results highlight the importance of the tips' opening angle.

# List of publications

## Publications that are included in this thesis

- **Generating few-cycle pulses for nanoscale photoemission easily with an erbium-doped fiber laser**
  Sebastian Thomas, Ronald Holzwarth, and Peter Hommelhoff
  Optics Express **20**, 13663 (2012)
  Reproduced in chapter 5.

- **Probing of optical near-fields by electron rescattering on the 1 nm scale**
  Sebastian Thomas[†], Michael Krüger[†], Michael Förster, Markus Schenk, and Peter Hommelhoff
  Nano Letters **13**, 4790 (2013)
  Reproduced in chapter 6.

- **Self-probing of metal nanotips by rescattered electrons reveals the nano-optical near-field**
  Michael Krüger, Sebastian Thomas, Michael Förster, and Peter Hommelhoff
  Journal of Physics B: Atomic, Molecular and Optical Physics **47**, 124022 (2014)
  Reproduced in chapter 7.

- **Semitransparency in interaction-free measurements**
  Sebastian Thomas, Christoph Kohstall, Pieter Kruit, and Peter Hommelhoff
  Physical Review A **90**, 053840 (2014)
  Reproduced in chapter 3.

- **Large optical field enhancement for nanotips with large opening angles**
  Sebastian Thomas[†], Georg Wachter[†], Christoph Lemell, Joachim Burgdörfer, and Peter Hommelhoff
  New Journal of Physics **17**, 063010 (2015)
  Reproduced in chapter 8.

- **Microwave chip-based beam splitter for low-energy guided electrons**
  Jakob Hammer, Sebastian Thomas, Philipp Weber, and Peter Hommelhoff
  Physical Review Letters **114**, 254801 (2015)
  Reproduced in chapter 4.

---

[†]     Both authors contributed equally to this work.

## Other publications

- **Interaction-free measurements with electrons**
  Sebastian Thomas and Peter Hommelhoff
  Conference on Coherence and Quantum Optics **M6.28**, Optical Society of America (2013)

- **Ultrashort laser oscillator pulses meet nano-structures: from attosecond physics at metal tips to dielectric laser accelerators**
  Sebastian Thomas, Michael Krüger, John Breuer, Michael Förster, and Peter Hommelhoff
  Journal of Physics: Conference Series **467**, 012004 (2013)

- **From above-threshold photoemission to attosecond physics at a nanometric tungsten tip**
  Michael Krüger, Markus Schenk, John Breuer, Michael Förster, Jakob Hammer, Johannes Hoffrogge, Sebastian Thomas, and Peter Hommelhoff
  Chapter in Progress in Ultrafast Intense Laser Science Vol. **IX**, 213, published by Kaoru Yamanouchi and Katsumi Midorikawa, Springer, Heidelberg (2013)

- **Can a quantum electron microscope achieve low-damage biological imaging?**
  Sebastian Thomas, Jakob Hammer, Philipp Weber und Peter Hommelhoff
  Proceedings of the Ninth International Conference on Charged Particle Optics, submitted to Microscopy and Microanalysis (2014)

# 1 Quantum electron microscopy

Transmission electron microscopes (TEM) allow the imaging and characterization of objects and materials on the nanoscale and are an important tool with many applications both in science and in industry (Reimer and Kohl, 2008; Williams and Carter, 2009; Spence, 2013). After the introduction of aberration correction to compensate the various aberrations of electron lenses (Haider et al., 1998; Urban, 2008), they have now reached a resolution significantly smaller than 100 pm, which is limited by magnetic field noise from thermally driven currents (Haider et al., 2010; Uhlemann et al., 2013). As this resolving power is sufficient even for the imaging of individual atoms, a further improvement of spatial resolution is only one of many goals for the future development of electron microscopes (Zhu and Dürr, 2015).

In some cases and especially in biological applications, the imaging of a given sample in an electron microscope is impossible not because of insufficient resolution but because of the radiation damage the sample incurs from the electron beam (Egerton et al., 2004; Spence, 2013). Thus, whether a sample can be imaged in an electron microscope depends on how much radiation damage it can sustain. In fact, this is not a new development in electron microscopy but was already discussed in the context of pioneering experiments (Ruska, 1934; Marton, 1934) only two years after the first demonstration that electron microscopy is possible (Knoll and Ruska, 1932). But while many technical challenges can be solved with the development of better instruments, the influence of sample damage is a more fundamental problem: the formation of an image is only possible because there is an interaction between the probing electrons and the sample, but this interaction also gives rise to sample damage.

The first part of this thesis discusses the application of a quantum effect called an "interaction-free measurement" (IFM) to the problem of radiation damage in electron microscopy (Putnam and Yanik, 2009). The basic idea of this effect is that, due to the wave-particle duality in quantum mechanics, one can detect the possibility of an interaction with only a low probability that the interaction actually occurs. Applied to electron microscopy, this may allow the formation of an image with significantly reduced radiation damage.

In this chapter, we will first discuss the process of interaction-free measurements and related phenomena in a historical context. We will then focus on applications in imaging and the problem of measuring gray values and phase shifts in an interaction-free measurement. Finally, we will turn to electron microscopy and the question of how to realize an IFM experiment with electrons, especially using a linear Paul trap (Hoffrogge et al., 2011).

This work was done as part of an international collaboration trying to demonstrate the underlying science of a device that enables imaging with electrons using interaction-

free measurements (Kruit et al., 2015; QEM, 2015). Such a device could be called a "quantum electron microscope" (QEM), which is the name of both the collaboration and this chapter.

## 1.1 Interaction-free measurements

While we aim at using electrons as probe particles in interaction-free measurements, they were originally discussed (and first realized experimentally) with photons as probe particles. In this section, we will follow the historical development and only come back to the case of electrons later. Note that the basic mechanism of IFMs is independent of the type of probe particle and works equally well with photons and electrons. Only the realization of a suitable setup may be very different depending on the used probe particle.

### 1.1.1 Mach-Zehnder interferometer

Interaction-free measurements were first discussed by Elitzur and Vaidman (1993) in the context of a Mach-Zehnder interferometer[†]. For an interaction-free measurement, the interferometer should be set up in such a way that the beam is fully transmitted to one of its exits while the other exit remains dark, as shown in Fig. 1 (a). We now assume that there is a point along one of the paths that may or may not be blocked by an opaque object as in Fig. 1 (b). If the path is blocked, the beam is no longer fully transmitted to one exit but the intensity is split between the two. This is the only case when light can enter detector 2 in Fig. 1. Therefore, a signal at this detector reveals the presence of the opaque object in the path.

It is well known that Mach-Zehnder interferometers allow the detection of opaque objects (or phase shifts) in one of the beam paths. The crucial insight by Elitzur and Vaidman was to realize that such a measurement has interesting and rather unintuitive consequences if only a single photon is coupled into the interferometer. The opaque object is then treated as a macroscopic absorber or scatterer, which causes a quantum measurement of whether the photon is in the upper or the lower path. In this case, the behavior of the Mach-Zehnder interferometer does not change fundamentally, but the beam intensities discussed above now represent probabilities of detecting the single photon.

If the object is absent, the photon is always detected by detector 1. If the object is present, there is a 50 % chance that the photon is absorbed or scattered by the object and a 25 % chance for each of the two detectors to detect the photon. The presence of the object can then be discovered if the photon is detected by detector 2. If this happens, an interaction-free measurement has occurred because a detection of the photon at detector 2 implies that it cannot have interacted (i.e., exchanged energy) with the object:

---

[†]    There are some earlier discussions of similar effects in the literature (Renninger, 1960; Dicke, 1981) but they were mostly concerned with the behavior of the probe particle's wave function in an IFM-like setup and with interpretational issues, not with applying the effect to detect something.
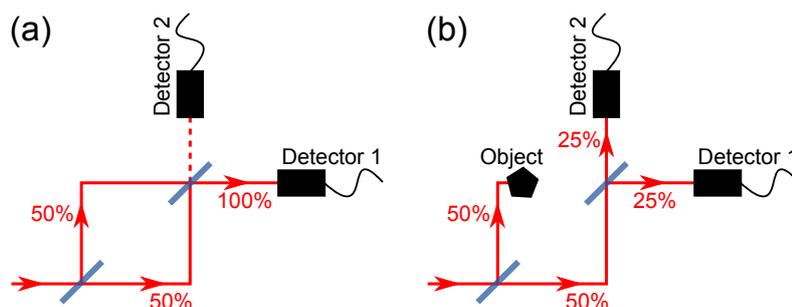
Figure 1: Illustration of a Mach-Zehnder interferometer with two 50/50 beam splitters (in blue). (a) By choosing the right path length difference between the upper and lower path, the interferometer can be set up in such a way that 100 % of the beam intensity is directed to detector 1. (b) If the upper path is blocked by an opaque object, half of the beam intensity is lost while the other half is split equally between the two detectors. Any event at detector 2 thus implies the existence of the object in one of the paths (assuming that this is the only way the setup can change). If the experiment is carried out with a single photon and this photon is detected in detector 2, the result can be considered an interaction-free measurement because information about the presence of the object was gained even though the photon was not absorbed by the object.

the result of the quantum measurement must have been that the photon was in the lower beam path.

To emphasize the unintuitive consequences of such a measurement in a more dramatic way, Elitzur and Vaidman present a thought experiment that has been adopted in much of the literature on the subject. They imagine the object as an ultra-sensitive, fully opaque bomb that explodes if it absorbs a single photon. Intuitively, one would think that it is impossible to detect such a bomb with photons because any photon hitting the bomb would cause it to explode. However, as shown above, by putting the bomb into a Mach-Zehnder interferometer there is a non-zero probability to detect it without an explosion. For the case of 50/50 beam splitters, the probability of a successful detection is 1/3 and the explosion probability is 2/3[†].

The success probability of the interaction-free measurement can be increased up to a value of 1/2 by changing the reflectivity of the interferometer's beam splitters. Based on an argument from the many-worlds interpretation of quantum mechanics (DeWitt et al., 1973), Elitzur and Vaidman originally hypothesized that this value can never be exceeded by an interaction-free measurement. Fortunately, the argument turned out to be incorrect (Vaidman, 2001): it is possible to achieve a success probability arbitrarily close to 1 with a more elaborate setup.

---

[†]   To explain where these probabilities come from: If the photon is detected at detector 1, the measurement needs to be repeated because this outcome does not distinguish between the presence and the absence of the bomb. Therefore, if the bomb is present, the experiment will eventually terminate either with a detection by detector 2 (probability 1/3) or with an explosion (probability 2/3). If there is no bomb in the interferometer, all photons will be detected at detector 1, making the presence of the bomb exponentially less likely with each additional photon. The experiment can then be terminated when a large number of photons has been detected.

## 1.1.2 Interaction-free measurements with high success probability

Only two years after interaction-free measurements had been first suggested by Elitzur and Vaidman (1993), their predictions were confirmed experimentally with a single-photon source coupled into a Mach-Zehnder interferometer (Kwiat et al., 1995). In the same article, Kwiat et al. went further and also suggested a theoretical way of improving the success probability of an IFM. Their idea is ultimately based on the quantum Zeno effect, which describes that a quantum state can be frozen by repeatedly measuring whether it has changed. Originally formulated as a paradox in the context of radioactive decay (Misra and Sudarshan, 1977), the effect was first demonstrated in an atomic physics experiment using an ion trap[†] (Itano et al., 1990).

Consider a system initially prepared in state $|a\rangle$ that evolves into state $|b\rangle$ over time. Let $p_b(t)$ be the probability of finding the system in $|b\rangle$ at time $t$. This is usually a nonlinear function in time. Assume that $p_b(t)$ is approximately quadratic for small $t \leq \tau$ (which is true for Rabi oscillations, for example), so $p_b(\tau) \approx \alpha\tau^2$ for some constant $\alpha$. Now consider the case where we disturb the natural evolution of the state by dividing the interval $\tau$ into $n$ smaller steps and performing a measurement at each time step $\tau/n$, which results in a periodic projection of the state either onto $|a\rangle$ or onto $|b\rangle$. Choosing $\tau$ small enough so that $p_b(\tau) \ll 1$, the probability of finding the particle in $|b\rangle$ is approximately $\alpha\tau^2/n^2$ every time the state is measured. In this case, the overall probability of finding the particle in $|b\rangle$ after $n$ such measurements is $p_b'(\tau) \approx n\alpha\tau^2/n^2 = \alpha\tau^2/n$, which is smaller than $p_b(\tau) \approx \alpha\tau^2$. In particular, $p_b'(\tau) \to 0$ for $n \to \infty$, so any change of the quantum state would become impossible under continuous observation.

The quantum Zeno effect as just presented can be applied as an interaction-free measurement in the following manner: One needs to construct a setup where the probe particle represents the evolving quantum system and the presence of an object causes periodic measurements of the probe particle's state. In this case, detecting that the state did not evolve after some time implies that periodic measurements must have prevented it from doing so, which represents a successful interaction-free measurement of the object's presence. Kwiat et al. (1995) describe two different interferometric setups that fulfill these criteria: a chain of Mach-Zehnder interferometers and a system of two coupled cavities. We will discuss the coupled cavities as an example of an interaction-free measurement using the quantum Zeno effect.

Figure 2 shows a sketch of two coupled cavities separated by a highly reflective beam splitter. We assume that a single-photon wavepacket starts out in the left cavity, which we will call the "reference state" $|R\rangle$. The photon then hits the beam splitter in the center of the cavities and part of its amplitude is split into the right cavity, which we will call the "sample state" $|S\rangle$ because a sample object may or may not be present there. If the right cavity is empty, the two wavepackets in $|R\rangle$ and $|S\rangle$ will periodically be reflected between the outer cavity mirrors and the central beam splitter, where amplitude is transferred between the two states. The lengths of the two cavities have to be matched so that

---

[†]    Note that there is some debate on whether the experiments carried out in atomic physics truly represent the original quantum Zeno paradox (Itano, 2009). The same is true for experiments on interaction-free measurements (Whitaker, 1998).
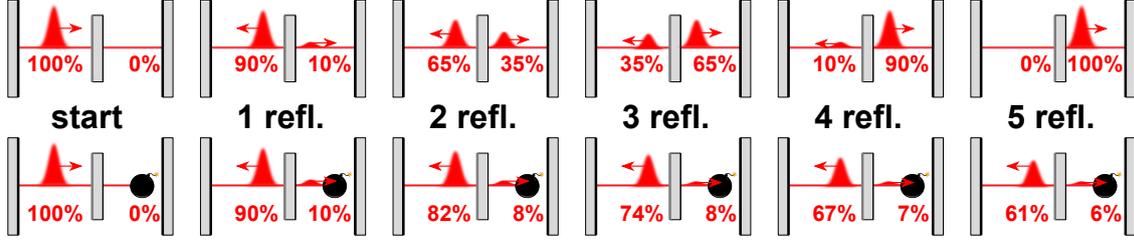
Figure 2: Example of an interaction-free measurement with a success probability of ∼0.61, using the ultra-sensitive bomb from the last section as a sample object. Two cavities are coupled via a beam splitter with reflectivity $\rho \approx 0.905$. After $N = 5$ round trips and reflections, a photon starting in the left cavity is fully transferred to the right cavity. The transfer is nonlinear because the amplitudes in the two cavities add up coherently at the beam splitter. If the second cavity is blocked by the bomb, this coherent build-up can no longer occur and the transfer of amplitude is slowed. An interaction-free detection of the bomb is carried out by measuring whether the photon is in the left or in the right cavity after $N = 5$ round trips. There is a ∼0.61 probability of detecting the bomb without making it explode.

the wavepackets overlap and interfere coherently at the beam splitter. If $\rho$ denotes the reflectivity of the beam splitter and the two quantum states representing the cavities are $|R\rangle = \left( \begin{smallmatrix} 1 \\ 0 \end{smallmatrix} \right)$ and $|S\rangle = \left( \begin{smallmatrix} 0 \\ 1 \end{smallmatrix} \right)$, the beam splitter's effect on the amplitudes of the system is given by the matrix

$$B = \begin{pmatrix} \sqrt{\rho} & -\sqrt{1-\rho} \\ \sqrt{1-\rho} & \sqrt{\rho} \end{pmatrix} = \begin{pmatrix} \cos\theta & -\sin\theta \\ \sin\theta & \cos\theta \end{pmatrix}, \tag{1}$$

which describes a rotation[†] by the angle $\theta$. Therefore, the amplitude is fully transferred from $|R\rangle$ to $|S\rangle$ after $N = \pi/(2\arccos\sqrt{\rho})$ round trips and reflections at the beam splitter (assuming that $\rho$ is chosen so that $N$ is an integer – otherwise $N$ must be rounded and the amplitude in $|R\rangle$ will not be exactly 0). An example of this is shown in the upper row of Fig. 2.

The behavior of the system is different if an opaque object is present in the right cavity. Any part of the amplitude that comes into contact with the object will no longer be coherent with the amplitude in the left cavity. This can be described by a quantum measurement with the result that the photon either remains in the left cavity or interacts with the object and is absorbed. The measurement occurs during each round trip, so there is no coherent build-up of amplitude in the right cavity (see the lower row of Fig. 2). The probability for the photon to remain in $|R\rangle$ after the first reflection is $\cos^2(\pi/(2N))$. After $N$ such reflections the probability is therefore

$$P_R = \cos^{2N}\left(\frac{\pi}{2N}\right), \tag{2}$$

which goes to 1 for $N \to \infty$ (i.e., reflectivity $\rho \to 1$).

---

[†]    More generally, $B$ could be any unitary matrix and thus introduce additional phase shifts (Zeilinger, 1981). We are using a rotation matrix here to simplify the discussion.

An interaction-free measurement can then be realized by letting the two-cavity setup run for $N$ reflections and coupling out the photon afterwards to measure whether it is in the reference or in the sample cavity. This measurement can have three results:

1. If the photon is detected in the reference cavity, there must be an object blocking the sample cavity. This is a successful interaction-free measurement because the object's presence was detected but it did not absorb the photon.

2. If the photon is detected in the sample cavity, there is no object blocking it.

3. If the photon is lost, it must have been absorbed by the object and the interaction-free measurement was unsuccessful.

In the limit $N \rightarrow \infty$, the probability of losing the photon goes to 0 while the probability of a successful interaction-free measurement goes to 1. Therefore, interaction-free measurements with arbitrarily high success probability can be carried out in the two-cavity setup.

This scheme is completely analogous to the quantum Zeno effect as discussed in the beginning of this section. The only difference here is that the coupling between the two cavities happens periodically, while the coupling between the two states in the quantum Zeno effect is continuous. However, there are other IFM proposals where the evolution of the probe particle is continuous (Putnam and Yanik, 2009). Whether the coupling is continuous or periodic does not affect the result. This is because the measurements that are ultimately responsible for freezing the state of the system are themselves periodic, not continuous.

An interferometric experiment that realizes an IFM with high success probability was carried out using polarizing beam splitters and a slow rotation of polarization during each round trip (Kwiat et al., 1999). The experiment used attenuation of a pulsed laser at a highly reflective beam splitter both to create single-photon pulses and to couple them into the IFM interferometer. The photons then made up to $N = 15$ round trips through the interferometer and were coupled out for measurement using two Pockels cells. The experiment achieved success probabilities of ~2/3 to 3/4 (depending on whether one includes the efficiency of the single-photon detector in the analysis), surpassing the theoretical limit of IFMs in a Mach-Zehnder interferometer. Crucially, Kwiat et al. realized that losses in any part of the IFM setup reduce the success probability even if the photon is lost without being absorbed by the sample object. This is because more photons have to be sent in on average to compensate for the lost photons, and all photons that enter the setup have some chance of being absorbed by the sample object, while a successful IFM only occurs if a photon completes $N$ round trips. So all possible ways the photon can be lost before the completion of $N$ round trips contribute to the probability of the photon being absorbed, but do not contribute to the success probability. To achieve a success probability close to 1, it is therefore necessary to minimize *all* losses of the IFM setup (Kwiat et al., 1999).

Finally, we would like to note that the IFM setups described so far work in the same way for classical electromagnetic waves as for single photons. In the classical case, the

interaction with the sample object can simply be described by absorption or scattering of the electromagnetic wave and it is unnecessary to consider quantum measurements. The detection of the object is then no longer interaction-free but only leads to a reduced amount of scattered or absorbed intensity as compared to a conventional detection of the object (i.e., trying to transmit a beam through it).

The interaction-free character of the measurement only occurs in the single- or few-particle case, and even there always with a probability less than 1. Partly for this reason, there is some controversy surrounding the name "interaction-free measurement" (Vaidman, 2001). Examples of alternative names found in the literature are "quantum interrogation" (Kwiat et al., 1999; Kent and Wallace, 2001), "absorption-free measurement" (Mitchison and Massar, 2001), or "quantum Zeno tomography" (Facchi et al., 2002). Nonetheless, "interaction-free measurement" seems to be the most widespread name of the effect and we will continue to use it in this thesis.

## 1.1.3 Applications and further developments

In this section, we will discuss some applications of interaction-free measurements as well as further developments in the field and in related topics. Unfortunately, we are not aware of any recent reviews on interaction-free measurements, but there are two older overview articles (Kwiat, 1998; Vaidman, 2003).

Any application of an IFM based on the quantum Zeno effect is ultimately composed of two parts. The first part is a coupler between two quantum states $|R\rangle$ and $|S\rangle$ like the two cavities discussed in the last section. The second part is the interaction of the state $|S\rangle$ with a sample that is relevant for applications. In a regular interaction-free measurement, the sample is just a fully opaque object in the path of $|S\rangle$. There are, however, many other applications, some of which may involve additional complications.

The natural application of interaction-free measurements is the imaging of sensitive samples where the act of imaging may have adverse consequences like a destruction of the sample. Elitzur's and Vaidman's thought experiment with the ultra-sensitive bomb would be an extreme example of this. Our ultimate aim is to apply IFMs to reduce radiation damage in electron microscopy (Putnam and Yanik, 2009), which will be discussed in detail later. Other possible areas of application are X-ray imaging (Vaidman, 1996), the imaging of photosensitive objects (Inoue and Björk, 2000), or the detection of the quantum state of individual particles (Volz et al., 2011). The last case, however, is conceptually different because the sample object does not just cause a measurement of the probe particle's state but must also be treated quantum mechanically (Karlsson et al., 1998; White et al., 1999; Pötting et al., 2000). This may also be relevant for quantum electron microscopy in the future, especially if atomic resolution is considered, but we will not discuss it in this thesis.

Imaging in an IFM setup can be accomplished by inserting a focusing lens system into the path of $|S\rangle$ (without disturbing the coherence between $|R\rangle$ and $|S\rangle$) and then raster scanning a sample in the path. Experiments on interaction-free imaging were carried out in a Mach-Zehnder interferometer by White et al. (1998). The authors noted that the interpretation of the interaction-free image can be complicated by the presence of

semitransparent or phase-shifting parts of the sample. We will discuss this point in the next section.

Another realization of interaction-free imaging achieved exposure-free imaging of a photographic film by using a different IFM concept not based on the quantum Zeno effect (Inoue and Björk, 2000). Instead, an interaction-free measurement is achieved via a resonant high-finesse cavity that is highly transparent to light of a certain frequency, but becomes highly reflective when an object is inserted into the cavity (Paul and Pavičić, 1996; Pavičić, 1996; Tsegaye et al., 1998). This kind of IFM setup has also been used for the detection of the quantum state of single atoms (Volz et al., 2011). While the resonant-cavity setup seems superficially similar to the two-cavity IFM discussed in the last section, it is actually a different scheme because it relies on the narrow resonance of a cavity (e.g., a Fabry-Pérot resonator). Therefore, it needs narrow-band laser pulses whose spatial width is larger than the width of the cavity. This makes the duration of the experiment less well-defined than in the quantum Zeno scheme (Kwiat et al., 1999), where arbitrarily short laser pulses can be used.

Another application of IFMs goes further than just putting an imaging system into the sample state $|S\rangle$, and instead replaces it with a quantum computer (Nielsen and Chuang, 2010) that is triggered by the probe particle. The quantum computer is set up to execute an algorithm with a yes-or-no answer. Depending on the result of the algorithm, the probe particle's amplitude is either returned to the coupler or set to 0 (equivalent to the presence or absence of the sample in a regular IFM). The setup is then run for $N$ round trips like a regular IFM. This scheme is called a "counterfactual computation" because the result of the computation can be obtained even though the quantum computer did not run (Mitchison and Jozsa, 2001; Hosten et al., 2006).

A nested version of two interaction-free measurements also leads to an interesting application. Here, the sample in the IFM is replaced by a second IFM setup, which again includes multiple round trips. This allows the execution of a "counterfactual communication" scheme where information can be transferred between two parties without exchanging any particles (Salih et al., 2013).

All-optical switching is another application of an IFM setup. Here, the sample is replaced by a nonlinear crystal that can convert the incoming photon via difference frequency generation if an additional pump beam is present. The presence or absence of the pump beam can switch the state of the probe photon (McCusker et al., 2013).

Very recently, interaction-free measurements with high success probability were also carried out using an on-chip realization of an IFM interferometer with infrared light in waveguides (Ma et al., 2014) and using an unstable Bose-Einstein condensate whose decay is inhibited by the presence of a laser beam (Peise et al., 2015).

### 1.1.4 Interaction-free imaging of semitransparency and phase shifts

While interaction-free measurements can, in principle, detect the presence or absence of a fully opaque object with arbitrarily low probability of losing the probe particle, imaging usually requires more than that. A sample may consist of parts that vary widely in transparency $\alpha$ (defined as the probability of transmitting a probe particle),

not only of black or white parts. Additionally, the presence of the sample may induce phase shifts $\phi$ that also vary widely in different parts. We have discussed the effects of semitransparency and phase shifts on IFMs in an article that is included in chapter 3 of this thesis (Thomas et al., 2014). Here we give a short overview of the topic with a summary of the results from chapter 3. We show an application of these results to electron microscopy in the next section.

Previous work on semitransparency in IFMs shows that the success probability is reduced when the presence or absence of a semitransparent sample is to be detected instead of an opaque sample, which can be compensated by increasing the number of round trips $N$, so arbitrarily high success probabilities remain possible (Kwiat, 1998; Jang, 1999; Facchi et al., 2002; García-Escartín and Chamorro-Posada, 2005; Azuma, 2006). In a series of papers, Massar, Mitchison, and Pironio generalized the concept of interaction-free measurements and showed that any quantum mechanical scheme trying to distinguish two transparencies $\alpha_1 < \alpha_2$ with a given error probability results in a minimum number of lost particles which can only be 0 if $\alpha_2 = 1$ (Mitchison and Massar, 2001; Massar et al., 2001; Mitchison et al., 2002). The formula for the minimum number can be found in Eq. 26 on page 50.

We have investigated semitransparency and phase shifts in interaction-free measurements using numerical simulations. The simulations assume that a probe particles starts out in the reference state, then completes $N$ round trips in the IFM setup (encountering the sample $N$ times), and is finally detected in either $|R\rangle$ or $|S\rangle$. The result of such a simulation are the probabilities of detecting the particle in the reference state ($P_R$), detecting it in the sample state ($P_S$), or losing it due to the presence of the sample ($P_L$). Figure 3 shows these probabilities for either a semitransparent sample or a sample that induces phase shifts. The three probabilities vary as a function of $\alpha$ and $\phi$. For this reason, the interpretation of an IFM of a semitransparent sample is more complicated than the interpretation of a black-or-white IFM, where the presence or absence of the
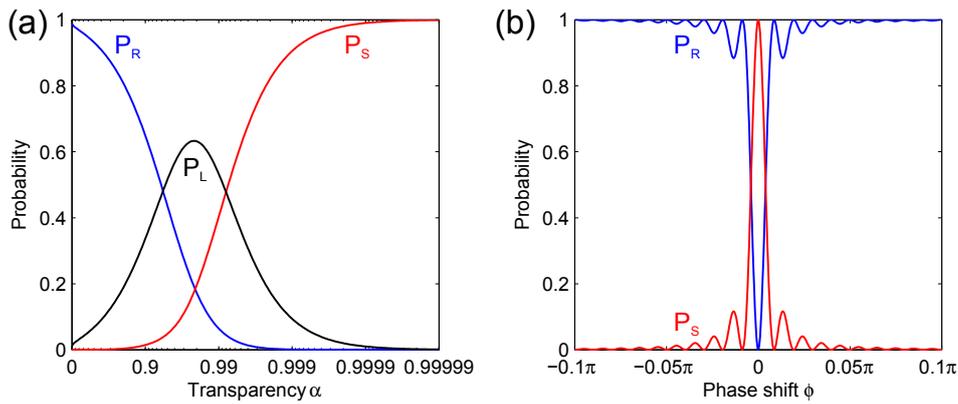


Figure 3: Results of an interaction-free measurement with $N = 200$ round trips and a sample that is either semitransparent with transparency $\alpha$ (a) or induces phase shifts $\phi$ (b). Shown here are the probabilities to detect the particle in the reference state, to detect it in the sample state, or to lose it ($P_R$, $P_S$, $P_L$).

sample can be distinguished with certainty by detecting whether the particle is in $|R\rangle$ or $|S\rangle$. In the semitransparent case, an IFM using only a single particle is not sufficient to determine the transparency.

While Fig. 3 only depicts the case $N = 200$, our simulations show the same qualitative behavior for any $N \gg 1$. The result for semitransparent samples can be roughly divided into three transparency regions. Samples with low transparency are similar to fully opaque samples: there is a high probability that the probe particle remains in the reference state due to the quantum Zeno effect, while the loss probability is low. Conversely, the effect of samples with high transparency on the probe particle is similar to the absence of a sample: the probability of detecting the probe particle in $|S\rangle$ is high, with only a low probability of losing it. In between these two cases, there is an intermediate region where the probe particle can be detected in either $|R\rangle$ or $|S\rangle$ with similar probability, while the loss probability is high. An increase of the number of round trips shifts the position of this intermediate region to higher transparencies.

The effect of a phase-shifting sample in an IFM is easy to describe. Only for a small region of phase shifts $|\phi| \approx 0$, there is a chance to detect the probe particle in $|S\rangle$. For larger phase shifts, the sample always remains in $|R\rangle$. The width of the high-$P_S$ region around 0 decreases for larger $N$. A phase-shifting sample is therefore similar to a fully opaque sample in an IFM. The reason for this similarity is that a phase shift causes the amplitudes in the reference and sample state to decohere, and thus prevents the nonlinear coherent build-up of amplitude in $|S\rangle$ just like the periodic measurements of the quantum Zeno effect.

As the result of an interaction-free measurement of a semitransparent sample is probabilistic, measuring the transparency is possible by sending in multiple particles and comparing the numbers of particles detected in the three states with the probabilities obtained from simulations. In most cases, such a measurement will also result in lost particles and, thus, not be interaction-free. To assess whether interaction-free measurements of transparency are useful, it is necessary to compare their performance to conventional measurements (i.e., sending probe particles through a sample and counting how many make it). This calculation is carried out in chapter 3. To quickly summarize the results: Interaction-free measurements mainly outperform conventional measurements if two semitransparent samples with a high contrast are to be distinguished, similar to the black-or-white IFM. Another interesting case for IFMs only occurs if it is not possible to count the exact number of probe particles (for example, because they are absorbed by the sample). In this case, IFMs also outperform classical measurements if the particle source is Poissonian and the transparency to be detected is larger than ~0.5. Finally, the extremely sensitive dependence of the probability curves on the sample's phase shift for large $N$ (see Fig. 3 (b)) also makes IFMs promising for the detection of small phase shifts.

Another area where IFM-like techniques may outperform conventional measurements, which is not discussed in our article, is when an image made up of many pixels is considered instead of the measurement of a single transparency. One example are quantum schemes based on splitting a probe particle's amplitude between many pixels and later recombining it, which is more challenging to realize experimentally than a regular IFM (Massar et al., 2001; Kent and Wallace, 2001). Another example is based

on a regular IFM but is only possible if the different transparencies of a sample are known not to be uniformly distributed. Depending on the distribution of $\alpha$ in the sample, conventional measurements can be outperformed by scanning the image and carrying out IFMs pixel by pixel, which leads to a reduced overall loss for samples that are mostly made up of dark parts with only a few lighter spots (Facchi et al., 2002).

After this rather abstract discussion of transparencies and phase shifts, we now explicitly calculate the result of an interaction-free measurement for an example of a real sample in electron microscopy.

### 1.1.5 Interaction-free thickness measurements

We have so far discussed the effects of semitransparency and phase shifts in interaction-free measurements in isolation. In any real sample, both effects will be present, so they must be considered in combination to simulate a real measurement. For any material under investigation in an interaction-free measurement, both the transparency $\alpha$ and the phase shift $\phi$ vary as a function of the thickness $d$ of the sample. We will now consider an example from electron microscopy.

Electrons moving through a sample can be lost due to both elastic and inelastic scattering events. These are usually given in the literature by an elastic mean free path $\Lambda_e$ and an inelastic mean free path $\Lambda_i$. The transparency of a sample with thickness $d$ and both elastic and inelastic scattering is then $\alpha(d) = \exp(-d/\Lambda_e)\exp(-d/\Lambda_i)$. One can also define a total mean free path $\Lambda$ that combines both scattering probabilities, which yields

$$\Lambda = \frac{\Lambda_i \Lambda_e}{\Lambda_i + \Lambda_e} \qquad \text{and} \qquad \alpha(d) = e^{-\frac{d}{\Lambda}}. \tag{3}$$

The phase shift is a result of the mean inner potential of a sample as electron waves propagating through a sample will be shifted with respect to a reference wave propagating through vacuum. The phase shift $\phi$ as a function of thickness $d$ can be obtained from an approximate formula for relativistic electrons (Reimer and Kohl, 2008, ch. 3):

$$\phi(d) = \frac{2\pi U}{\lambda E_{kin}} \frac{E_{kin} + mc^2}{E_{kin} + 2mc^2} d. \tag{4}$$

Here, $E_{kin}$, $m$, and $\lambda$ are the electron's kinetic energy, rest mass, and de Broglie wavelength, respectively. $U$ denotes the sample's mean inner potential and $c$ is the speed of light in vacuum.

As an example material, we discuss an IFM with an amorphous carbon sample using 100 keV electrons as probe particles. The mean free paths for such electrons in amorphous carbon are $\Lambda_e = 168$ nm and $\Lambda_i = 46$ nm (Angert et al., 1996), so $\Lambda = 36$ nm. The mean inner potential of amorphous carbon is $U = 11$ eV (Schowalter et al., 2005). Figure 4 (a) shows the transparency and phase shift of amorphous carbon as a function of sample thickness. From these, we can calculate the resulting detection and loss probabilities of an interaction-free measurement as a function of sample thickness and the number of round trips $N$. In Fig. 4 (b), these probabilities are shown for the examples $N = 2$ and

$N = 20$. We see that the sample state $|S\rangle$ is only relevant for thin samples with high transparency. For thicker samples, electrons are either lost or detected in $|R\rangle$. These two probabilities oscillate weakly with thickness due to the linearly increasing phase shift. Eventually, the probabilities converge to the success probability of a black-or-white IFM ($P_R = 1 - P_L = \cos^{2N}(\pi/2N)$) as the phase shift no longer matters for almost fully opaque samples.

To compare the performance of interaction-free measurements and classical transmission measurements, we consider a measurement of the sample thickness $d$

1. either by sending electrons through the sample and counting how many are transmitted

2. or by performing the IFM multiple times and counting how many electrons are detected in $|R\rangle$ and $|S\rangle$ and how many are lost.

In the first case, the thickness can be found by comparing the measurement results to the transmission probability $\alpha(d)$ from Fig. 4 (a). In the second case, the results must be compared to the $P(d)$ curves from Fig. 4 (b). As these curves are not monotonous, an interaction-free measurement can only distinguish thicknesses between any two local extrema of $P(d)$.

We assume that we carry out such a thickness measurement using an electron source with Poissonian statistics, similar to the analysis described in section 3.6. The aim of the measurement is to find out a sample's thickness within an uncertainty interval $\Delta d = 1\,\text{nm}$ and with an error probability of 5 %. Given a number of measurement signals $S_i(d)$ and a loss probability $P_L$ during each run of the measurement, the expected number $n_{\text{loss}}$ of lost particles is

$$n_{\text{loss}}(d) \approx \frac{3.92^2 P_L(d)}{\sum_i \frac{(S_i'(d)\Delta d)^2}{S_i(d)}}, \tag{5}$$

based on the normal approximation of the Poisson distribution. This formula shows that the expected number of lost particles increases with the loss probability and with the value of the signal $S_i(d)$, while it decreases with the uncertainty intervals $\Delta d$ and with the slope of the signal $S_i'(d)$. The number $3.92^2$ is due to the requirement of 5 % error probability.

We now assume that we cannot detect lost particles. (Note that this is not necessarily true in electron microscopy. However, allowing the detection of lost particles does not qualitatively change the results.) In this case, the signal of the classical measurement is simply $S(d) = \alpha(d)$ with the loss probability $P_L(d) = 1 - \alpha(d)$. For the interaction-free measurements, the two signals $P_R(d)$ and $P_S(d)$ as well as the loss probability $P_L(d)$ can be obtained from the IFM calculations shown in Fig. 4 (b). Calculating the results of Eq. 5 for a classical transmission measurement and for IFMs with different $N$, we obtain Fig. 4 (c).

We first note that the number of lost electrons $n_{\text{loss}}$ for the various IFMs contains many narrow spikes. These are due to the local extrema of the signals. As discussed before, interaction-free measurements can only measure the transparency between any
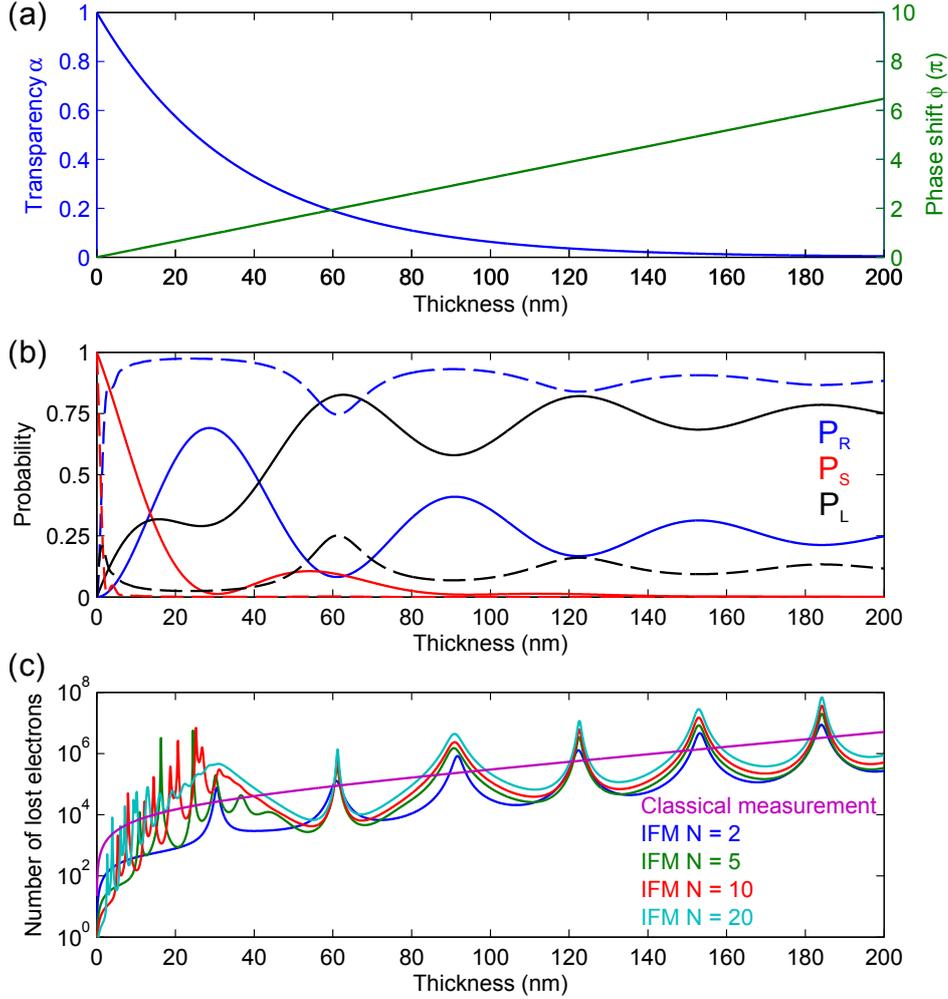
Figure 4: (a) Transparency and phase shift of amorphous carbon as a function of sample thickness for 100 keV electrons. (b) Probability to detect the electron in the reference state (blue), sample state (red), or to lose the electron (black) at the end of an interaction-free measurement. Shown here are results for a number of round trips $N = 2$ (solid lines) and $N = 20$ (dashed lines). (c) Expected number of lost electrons in a thickness measurement using either a classical transmission measurement or an IFM based on Eq. 5. The measurement has an uncertainty interval of 1 nm and an error probability of 5 %.

two of these spikes because the signals are not monotonous. For thick samples with $d \gtrsim 50$ nm, $n_{loss}$ increases exponentially for both classical measurements and IFMs at the same rate. (This behavior also holds for larger $d$ than 200 nm.) In between any two extrema, IFMs outperform classical measurements by approximately an order of magnitude, with a number of round trips $N = 2$, i.e., a Mach-Zehnder interferometer, giving the best performance.

Regions where IFMs with a larger number of round trips perform better than a Mach-Zehnder interferometer exist only at high transparency. For thin samples with $d \lesssim 10$ nm, IFMs with $N = 5$ to 20 may outperform both classical measurements and the

Mach-Zehnder interferometer within small thickness regions. IFMs with a large number of round trips are therefore only interesting for thickness measurements of samples with high transparency.

## 1.2 Interaction-free measurements with electrons

Our goal is to realize an interaction-free measurement with electrons instead of photons as probe particles, as a first step towards the construction of a quantum electron microscope (QEM). In this section, we first discuss the basic challenges of such an experiment, especially the topic of designing a suitable beam splitter. We then give a short introduction to the trapping or guiding of charged particles in Paul traps, and explain how they can be applied to construct a beam splitter. Finally, we discuss an experimental realization of such a beam splitter, and how it could be improved to achieve an IFM with electrons.

### 1.2.1 The electron beam splitter in an interaction-free measurement

An interaction-free measurement is an interferometric setup, in which a probe particle is periodically split and recombined while performing multiple round trips. To realize such an experiment with electrons, several components are required:

- a coherent electron source,

- a cycling scheme that allows multiple round trips,

- a way to couple the electron into and out of the setup,

- and a beam splitter for splitting and recombining the electrons' amplitude.

All these components present significant technical challenges. Here, we will only quickly discuss the first three, and then focus on the electron beam splitter.

Field emitter tips are sharp metal tips with radii of a curvature in the 5 nm to 100 nm range which emit an electron current if a negative voltage is applied (Gomer, 1961). Such tips are commonly used in electron holography experiments due to their excellent spatial coherence properties (Lichte and Lehmann, 2008). They may serve as electron sources in an IFM experiment. For better control of the timing of the experiment and for an operation in the single- or few-particle regime, electron emission from field emitter tips may also be triggered by ultrashort laser pulses instead of a static voltage, which largely preserves the tip's coherence properties (Ehberger et al., 2015). Laser-triggered electron emission from nanotips is discussed further in chapter 2.

There are several options for the cycling scheme, which result in completely different experimental setups. One option is to use a magnetic field to guide the electrons on circular trajectories (Putnam and Yanik, 2009). Another option would be to construct a system similar to the two-cavity IFM from section 1.1.2 and use electrostatic mirrors to reflect the electrons (see Fig. 14 on page 41). Either a lens system or a charged particle

trap may be used to ensure the stability of the cavity. Using electrostatic mirrors also offers a relatively straightforward way to couple the electrons into or out of the setup: switching the mirror voltages off for a time and then on again.

A large technical challenge in the realization of a QEM is the development of a suitable beam splitter. While there is a vibrant field of electron interferometry and holography (Missiroli et al., 1981; Hasselbach, 2010), most experiments in this field use the electron biprism as a beam splitter (see Fig. 5). Invented 60 years ago by Möllenstedt and Düker (1955), this device allows a transverse splitting of electron wavefronts, which enables the use of holographic techniques in electron microscopy (Tonomura, 1999). The electron biprism is, however, a different kind of beam splitter than the ones that are used in various IFM proposals and realizations.

Both IFMs and many other experiments in quantum optics require a beam splitter with two input and two output ports that realizes a unitary transformation of amplitudes between these ports (Zeilinger, 1981; Schleich, 2005, ch. 13). The widely used beam splitters in light optics are amplitude splitters that fulfill this requirement. An example are half-silvered mirrors: The inputs from both sides are split into a transmitted and a reflected part, so both outputs consist of a reflected part from one input and a transmitted part from another input. The transformation of amplitudes from the input at both sides into the output at both sides is described by a unitary $2 \times 2$ matrix if the splitter is lossless. It is crucial for an IFM that the output amplitudes in the two ports depend on the input amplitudes in both ports before the splitting. This allows the nonlinear coherent build-up of amplitude in the sample state, as discussed in section 1.1.2.

In contrast to the amplitude beam splitters used in light optics, the electron biprism is a wavefront beam splitter. How the amplitude is split into the two sides of the biprism wire depends on the shape of the electron beam's wavefront. Such a beam splitter does not allow a slow build-up of amplitude during multiple round trips, which is necessary for realizing an IFM. For this reason, we are studying alternative concepts of electron beam splitters.

Another method to split electron beams is based on diffraction at a lattice. Depending on the properties of the lattice, an incoming electron beam is split into many output
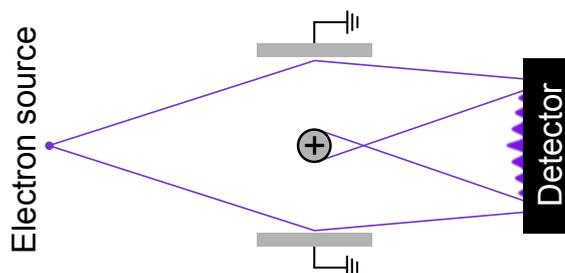


Figure 5: Sketch of an electron biprism, which typically serves as a beam splitter in electron holography. Electrons are emitted into a cone that spreads away from their source (for example, a field emitter tip). A positively charged wire splits the electron wavefront into two parts and bends the electron beam, causing the two parts of the wavefront to overlap. Interference fringes can then be detected behind the biprism.
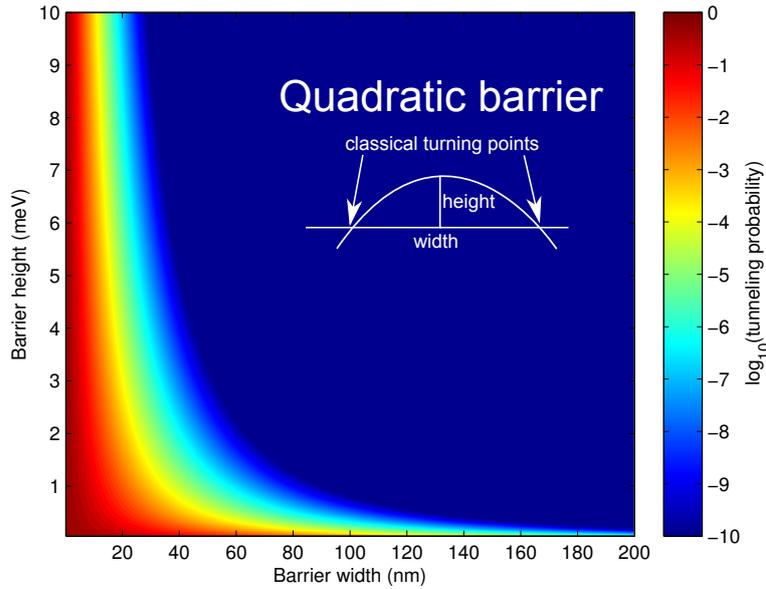
Figure 6: Tunneling probability of an electron through a potential barrier as a function of both height and width of the barrier. Calculated with the WKB approximation assuming a quadratic potential defined by its height and width as shown in the sketch.

beams. By choosing a lattice where most of the amplitude is split into two beams, an approximately unitary coupling between two states can be realized, which makes interaction-free measurements possible. Diffraction-based interferometry experiments with electrons have been carried out in the past using three single crystals in a configuration similar to a Mach-Zehnder interferometer (Marton, 1952; Marton et al., 1953, 1954). Another series of experiments used a lattice made up of standing waves of a laser beam to diffract electrons due to the Kapitza-Dirac effect (Freimund et al., 2001; Freimund and Batelaan, 2002; Batelaan, 2007).

Another possibility for an electron beam splitter would be to use an electrostatic potential as a tunnel barrier, analogous to a half-silvered mirror in light optics. As the tunneling probability of an electron through a barrier decreases exponentially with increasing barrier height and width, the properties of the barrier are technically challenging to realize. The results of a WKB calculation (Schleich, 2005) are shown in Fig. 6. Even if the electron's kinetic energy and the electrostatic potential can be controlled on the meV scale, the width of the barrier must not be larger than ~10 nm to achieve a non-negligible tunneling probability.

The first proposal of an interaction-free measurement with electrons uses a tunnel barrier as a beam splitter (Putnam and Yanik, 2009). In this case, however, the potential of the barrier is not electrostatic. Instead, the IFM setup and the tunnel barrier are realized using linear Paul traps for electrons. Paul traps use alternating electric fields to create a force on average that can confine charged particles (Paul, 1990). By coupling an electron into an eigenstate of the trap, it may be possible to control the electron's

energy well enough to allow tunneling over larger distances. In the next section, we will introduce Paul traps and explain how they can be used to construct an electron beam splitter and, ultimately, an IFM setup.

## 1.2.2 Paul traps for electrons

As a well-known method for the trapping and guiding of ions, Paul traps have applications in a wide range of fields including mass spectrometry, precision laser spectroscopy, and quantum information processing. This section gives a short introduction to the working and properties of Paul traps. A more detailed overview can be found in many textbooks and review articles (Paul, 1990; Ghosh, 1995; Leibfried et al., 2003; Major et al., 2005) or, for the case of trapping electrons, in the PhD theses of Hoffrogge (2012) and Hammer (2014).

Paul traps use electric fields to confine charged particles in a certain region of space. As electric potentials $\Phi(\mathbf{r})$ obey the Laplace equation $\nabla^2 \Phi(\mathbf{r}) = 0$ in the absence of charges, there cannot be local maxima or minima of the potential in free space. Only saddle points are possible. Thus, any configuration of static electric fields in free space $\mathbf{E}(\mathbf{r}) = \nabla \Phi(\mathbf{r})$ is divergence-free and cannot confine charged particles in a stable equilibrium around a point. (Intuitively, the field lines of an electric field cannot all converge towards a point in free space.) Paul traps overcome this problem by using an oscillating electric field with a saddle point potential, which is unstable during any instant of time but can provide a stably confining force on average if the oscillation is fast enough (but not too fast).

In a Paul trap, charged particles are trapped in an electric quadrupole potential

$$\Phi(\mathbf{r}, t) = (V_{\mathrm{DC}} + V \cos(\Omega t)) \frac{\alpha x^2 + \beta y^2 + \gamma z^2}{2} \tag{6}$$

consisting of a static potential with amplitude $V_{\mathrm{DC}}$ and an oscillating potential with amplitude $V$ and drive frequency $\Omega$. The Laplace equation implies that $\alpha + \beta + \gamma = 0$, which can be fulfilled in different ways. For our applications in electron beam splitters and QEM, we are interested in an electron guide that only traps an electron in two dimensions while allowing it to propagate freely in the third. We choose $y$ as the axis along which the electron is free, and set $\beta = 0$ and $\alpha = -\gamma = 1/R_0^2$ where $R_0$ denotes the minimum distance from the trap center to the electrodes that generate the potential (which have to have a hyperbolic shape to generate a perfect quadrupole). This configuration is called a "linear Paul trap". We obtain the potential

$$\Phi(\mathbf{r}, t) = (V_{\mathrm{DC}} + V \cos(\Omega t)) \frac{x^2 - z^2}{2R_0^2}, \tag{7}$$

which has a line of saddle points at $x = z = 0$ along $\mathbf{r} = (0, y, 0)^\top$. Such a potential and the resulting electric field are plotted in Fig. 7. For a static voltage, a charged particle would be harmonically trapped in one direction but repelled in the other direction. By applying an oscillating voltage, however, the trapping and repelling directions are
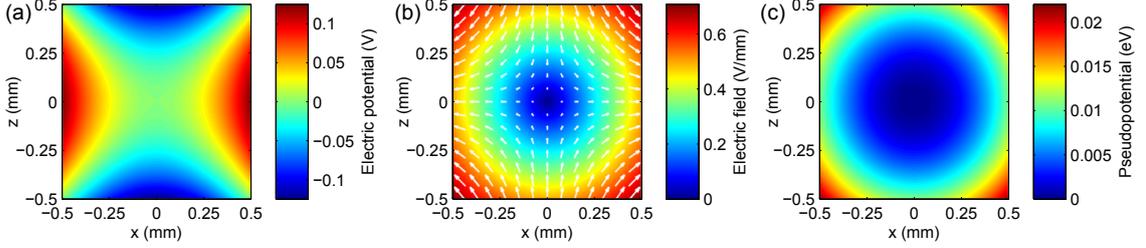
Figure 7: Electric quadrupole potential $\Phi(x, z)$ at $t = 0$ (a), the resulting electric field (b), and the resulting pseudopotential $\Psi(x, z)$ (c). The parameters here are $V = 1\,\text{V}$, $V_{\text{DC}} = 0$, $R_0 = 1\,\text{mm}$, and $\Omega = 2\pi \cdot 1\,\text{GHz}$. The particle is an electron and the resulting stability parameter is $q \approx 0.35$.

periodically reversed. One might intuitively expect the resulting force to average out to zero over time but this is not true because the strength of the electric field is not constant in the $x$-$z$ plane. A small average force called the "ponderomotive force" remains and can confine a charged particle, provided that the frequency and amplitude of the applied voltage are in the right range. In this way, we obtain a linear Paul trap that can guide charged particles along the $y$ axis.

The stability conditions of the trap can be found by analyzing the classical equations of motion of a charged particle in the trapping potential. The resulting differential equations are the so-called Matthieu equations

$$\ddot{x} + \frac{Q}{MR_0^2}(V_{\text{DC}} + V\cos(\Omega t))x = 0$$
$$\ddot{z} - \frac{Q}{MR_0^2}(V_{\text{DC}} + V\cos(\Omega t))z = 0 \tag{8}$$

with $Q$ and $M$ as the particle's charge and mass. These equations have stable solutions, where the particle oscillates in the $x$-$z$ plane with limited amplitude, and unstable solutions, where the particle's amplitude grows without bounds. Whether a particular set of parameters $V_{\text{DC}}$, $V$, $\Omega$, and $R_0$ leads to a stable solution depends on the two numbers

$$a = \frac{4QV_{\text{DC}}}{M\Omega^2 R_0^2} \quad \text{and} \quad q = \frac{2QV}{M\Omega^2 R_0^2}. \tag{9}$$

From an analysis of the Matthieu equations, one finds that several regions of stability exist in the $a$-$q$ plane (Paul, 1990). Here, we are only interested in one of these regions. If we apply only the oscillating potential without an additional static voltage, we obtain $a = V_{\text{DC}} = 0$. In this case, the linear Paul trap is stable for $0 < q \lesssim 0.9$. For this reason, $q$ is called the "stability parameter" of the trap.

If $q \ll 1$ and $a = 0$, the resulting trajectory of the particle can be given by the so-called secular approximation (Major et al., 2005)

$$x(t) = x_0\left(1 - \frac{q}{2}\cos(\Omega t)\right)\cos\left(\frac{q}{2\sqrt{2}}\Omega t\right) \tag{10}$$

assuming an initial position $x_0$ and initial velocity $v_0 = 0$ of the particle. The trajectory in $z$ direction has the same form, while the particle moves freely in $y$ direction. Note that
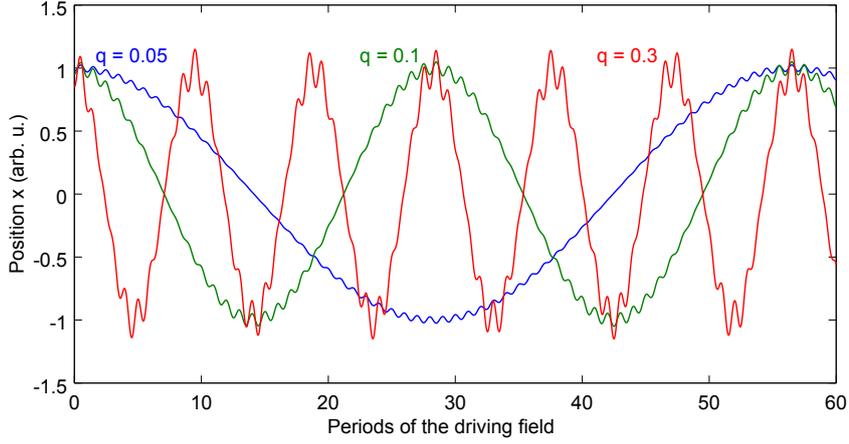
Figure 8: Position $x(t)$ of a charged particle in a linear Paul trap for three different stability parameters $q = 0.05$, 0.1, and 0.3 according to Eq. 10. Both the frequency of the macromotion and the amplitude of the micromotion increase for larger $q$.

the approximation is not valid for $q \gtrsim 0.4$. Examples of such trajectories are shown in Fig. 8. The dynamics of the stably confined particle are governed by a slow macromotion at the frequency $\omega = q\Omega/(2\sqrt{2})$, called "secular frequency" or "trapping frequency", and a faster micromotion with reduced amplitude at sidebands $\Omega \pm \omega$ of the drive frequency[†].

If we ignore the micromotion as a small perturbation, the particle dynamics are the same as those of a particle in a harmonic oscillator. We can use the so-called adiabatic approximation to describe this harmonic oscillator by introducing a pseudopotential $\Psi(\mathbf{r})$, which for $V_{DC} = 0$ is

$$\Psi(\mathbf{r}) = \frac{Q^2}{4M\Omega^2}|\nabla\Phi(\mathbf{r}, t{=}0)|^2 = \frac{Q^2 V^2}{4M\Omega^2 R_0^4}(x^2 + z^2). \tag{11}$$

The motion of a particle in the pseudopotential given by $\ddot{\mathbf{r}} = -\nabla\Psi(\mathbf{r})/M$ is a harmonic oscillation that follows the macromotion of the same particle in the Paul trap. It is a good approximation whenever the micromotion can be neglected. From the value of the pseudopotential at the electrodes (i.e., at $x^2 + z^2 = R_0^2$), we can define the pseudopotential depth

$$U = \frac{Q^2 V^2}{4M\Omega^2 R_0^2} = \frac{qQV}{8}, \tag{12}$$

which is a measure of the overall strength of the confinement in the guide.

Let us briefly consider the quantum behavior of a particle in a linear Paul trap. Using the pseudopotential approximation, the transverse eigenstates of a charged particle in the trap are simply the well-known eigenfunctions of a two-dimensional harmonic oscillator. A charged particle with a large initial displacement from the center of the

---

[†]    The sidebands arise from Eq. 10 because $\cos(a)\cos(b) = (\cos(a+b) + \cos(a-b))/2$.

trap can be described by a coherent state, whose evolution is similar to the classical trajectory.

The quantum behavior of the time-dependent quadrupole potential is more difficult to model, but the result is similar to eigenstates and coherent states in a harmonic oscillator with an additional modulation at the drive frequency, which results in a periodic expansion and recompression of the wavefunction (Leibfried et al., 2003; Hammer, 2014). Just like in the classical calculation, the adiabatic approximation is justified if this breathing of the wavefunction can be neglected, and we will use the approximation in the rest of this thesis.

So far, we assumed that the electric field of the trap is a perfect quadrupole. As the required hyperbolic electrodes are difficult to manufacture, most experiments use other types of electrode geometries, resulting in potentials that are only approximately quadrupolar. For small displacements from the trap center, the higher-order components of the potential can usually be neglected and the results described so far remain valid. However, the trap parameters must be scaled by geometry factors $u$ and $\eta$ that depend on the details of the trap geometry:

$$q' = \eta \frac{2QV}{M\Omega^2 R_0^2}, \qquad \omega' = \frac{q'\Omega}{2\sqrt{2}}, \qquad U' = u \frac{Q^2 V^2}{4M\Omega^2 R_0^2}. \tag{13}$$

Of particular importance are planar traps with all electrodes placed on a flat substrate. The fabrication of such traps can make use of techniques from semiconductor microfabrication like photolithography, which allows the realization of complex trapping and guiding structures on a chip (Chiaverini et al., 2005; Seidelin et al., 2006). For a planar guide, the largest possible scaling factors that can be achieved are (Wesenberg, 2008)

$$u_{\max} = \frac{5\sqrt{5} - 11}{2\pi^2} \approx 0.0091 \quad \text{and} \quad \eta_{\max} = \frac{1}{\pi} \approx 0.318. \tag{14}$$

The trade-off for the easier fabrication of a planar guide is thus a reduced trap depth by at least two orders of magnitude. Intuitively, this is because the electric potential is weaker further away from the electrodes, so the planar guiding mode is asymmetrical with stronger confinement closer to the chip surface.

We use such a planar guide with three grounded and two AC electrodes to guide electrons over a chip substrate (Hoffrogge et al., 2011). Due to the large charge-to-mass ratio of electrons the oscillating voltage is driven at microwave frequency, which is significantly higher than the radio frequencies usually used in ion traps. Typical parameters of the guide are $\Omega = 2\pi \cdot 1\,\text{GHz}$, $V = 30\,\text{V}$, and $R_0 = 0.5\,\text{mm}$ with geometry factors $\eta = 0.31$ and $u = 0.0079$, leading to trap parameters $q = 0.3$, $\omega = 2\pi \cdot 0.11\,\text{GHz}$, and $U = 0.03\,\text{eV}$. With this trap depth $U$, the guide is able to confine and steer slow electrons with kinetic energy on the order of several electron volts.

In the next section, we will discuss how to use such an electron guide to construct a beam splitter and to implement an interaction-free measurement.

## 1.2.3 Interaction-free measurements based on Paul traps

The first proposal for using interaction-free measurements in electron microscopy was made by Putnam and Yanik (2009). It is based on quantum tunneling of an electron between the minima of two linear Paul traps, in analogy to the two-cavity IFM discussed in section 1.1.2. As tunneling through a potential barrier depends exponentially on the barrier height and width, the two trap minima have to be generated close to each other.

The proposed setup consists of eight electrodes arranged in a three-dimensional structure with cylindrical symmetry. They serve to create two parallel ring-shaped linear Paul traps. The radius of the ring is on the order of 1 mm and distance between the two minima is on the order of several micron. An electron with a kinetic energy of 100 keV (typical of transmission electron microscopy) is injected into one of the rings and rotates around the trap structure on a circle. As the confining potential of the Paul trap is not strong enough to keep the electron on a circular trajectory at the trap minimum, an additional magnetic field is applied along the axis of symmetry of the setup. The scheme is sketched in Fig. 9.

The idea for performing an interaction-free measurement in this setup is that the two rings represent the reference state $|R\rangle$ and the sample state $|S\rangle$, respectively. The electron is initially inserted into the reference ring, from which it slowly tunnels into the sample ring while rotating around the setup. An opaque object may or may not be present in the sample ring. If it is present, the amplitude in the sample ring periodically encounters the object and a measurement occurs, which stops the coherent build-up of amplitude in the sample ring. This is completely analogous to the two-cavity IFM. The number of round trips $N = T\nu$ before the tunneling from $|R\rangle$ to $|S\rangle$ is complete depends on the tunneling time $T$ and the rotation frequency $\nu$ of the electron around the setup.

We describe the influence of the two linear Paul traps by a time-averaged pseudopo-
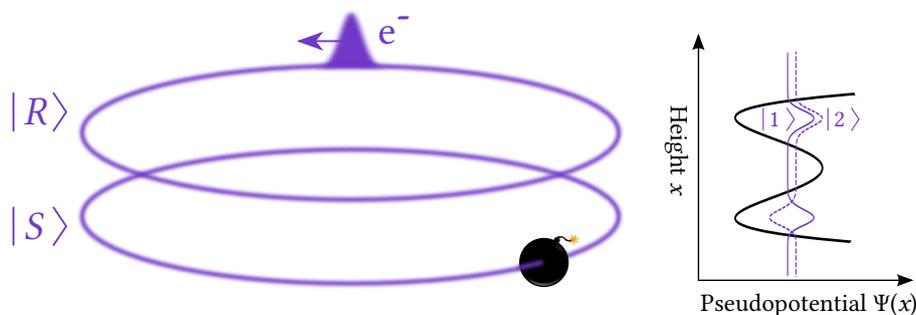


Figure 9: Sketch of the IFM scheme proposed by Putnam and Yanik (2009). An electron is trapped in two coupled ring-shaped guides generated by two linear Paul traps. In a cross section of the two guides, the time-averaged pseudopotential of the Paul traps is a double well. Accordingly, the states where the electron is localized in either of the two rings ($|R\rangle$ and $|S\rangle$) are superpositions of the symmetric and antisymmetric eigenstates of the double well ($|1\rangle$ and $|2\rangle$). The electron starts out in the upper ring $|R\rangle$ and periodically tunnels between the two rings. The presence of an object in the lower ring can be detected as it disturbs this tunneling. The object in this sketch is again represented by the ultra-sensitive bomb from section 1.1.1.

tential[†], as discussed in the last section. In a cross section of the two ring traps, the shape of the pseudopotential is a double well, whose eigenstates $|1\rangle$ and $|2\rangle$ are symmetric and antisymmetric superpositions of the single-well eigenstates. A requirement for a well-defined tunneling time between $|R\rangle$ and $|S\rangle$ is that the electron's initial state $|R\rangle$ is one of the single-well eigenstates, usually the ground state. In terms of the double-well eigenstates, the initial state is then $|R\rangle = (|1\rangle + |2\rangle)/\sqrt{2}$ (see Fig. 9) and the electron oscillates between $|S\rangle$ and $|R\rangle$ from there. The tunneling time $T = 4\pi\hbar/\Delta E$ is half a period of this oscillation and depends on the energy difference $\Delta E$ of $|1\rangle$ and $|2\rangle$. Here, $\hbar$ is the reduced Planck constant. The scheme would work the same way for a superposition of higher eigenstates of the form $(|2n\rangle + |2n - 1\rangle)/\sqrt{2}$ but the ground state has the advantage that it is possible to directly inject electrons into it (Hammer et al., 2014). Note that the state must not involve more than two eigenstates of the double well potential. Otherwise, the different eigenstates would oscillate between the two wells at different frequencies and the amplitude would smear out between them over time.

As the tunneling time increases exponentially with the distance between the two rings, the dual requirement of having two well-separated rings and at the same time allowing quantum tunneling is challenging to realize. The requirement that the distance between the rings should not be too small must be fulfilled for applications in imaging, i.e., to enable raster scanning of a sample through the $|S\rangle$ ring's path. For larger distances, tunneling in a realistic time frame can be achieved by reducing the height of the potential barrier. To investigate the required parameters, we study a one-dimensional double well potential of the form $V(x) = (a(x - x_0)^2 - b)^2$ (which represents the time-averaged pseudopotential) and numerically solve the stationary Schrödinger equation

$$\left(-\frac{\hbar^2}{2m}\frac{\partial^2}{\partial x^2} + V(x)\right)\psi(x) = E\psi(x) \tag{15}$$

using a simple algorithm described by Jelic and Marsiglio (2012). The potential is made up of two wells centered around $x_0$ whose minima are separated by a barrier with a width of $2\sqrt{b/a}$ and a height of $b^2$.

Similar to the parameters proposed by Putnam and Yanik (2009), we assume a distance of 5 μm between the two wells and calculate the shape and energy of the two lowest states for different barrier heights. Two example results for barrier heights of 0.5 μeV and 0.02 μeV are shown in Fig. 10. In the first case, the two eigenenergies are close together, so the tunneling time is $T \approx 187$ μs and the superposition of the first two eigenstates $|R\rangle$ is well localized in the left well. Note, however, that the full width at half maximum (FWHM) of the reference state's probability density $|\psi_R(x)|^2$ is ~1 μm. As the FWHM determines the resolution of imaging when raster-scanning a sample through the $|S\rangle$ ring, this setup would not be sufficient for high-resolution microscopy. The FWHM can be decreased by raising the potential barrier. Unfortunately, the tunneling frequency

---

[†]    An interesting point for future investigation is the question whether the fast oscillation of the Paul trap's potential and the resulting breathing of the wavefunction change the tunneling dynamics. Here, we assume that the pseudopotential is a good approximation and that it can be used as a tunnel barrier, which is also done in the original proposal (Putnam and Yanik, 2009).
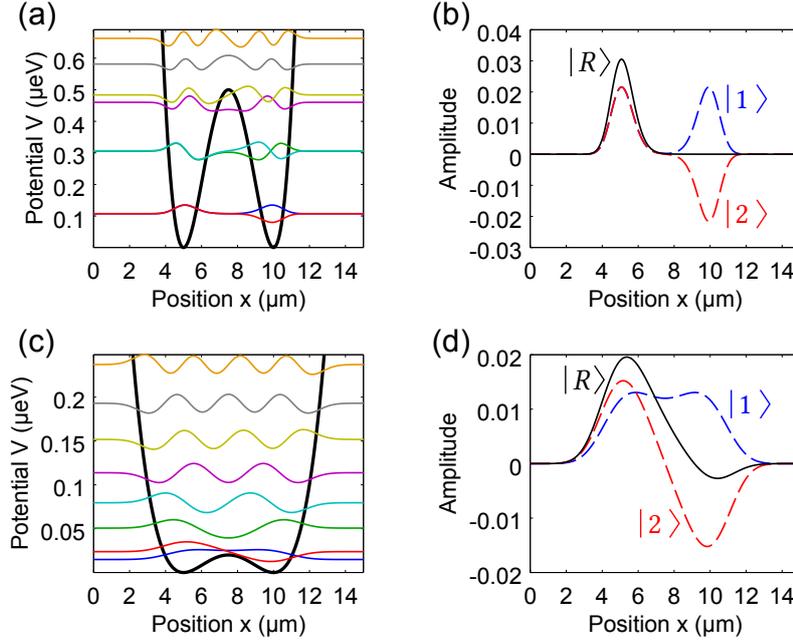
Figure 10: Comparison of a deep and a shallow double well potential. Panels (a) and (c) show the potential $V(x)$ in black with the different energy eigenvalues as colored lines, which additionally indicate the corresponding eigenfunctions. Panels (b) and (d) show the first two eigenfunctions as well as their superposition $|R\rangle = (|1\rangle + |2\rangle)/\sqrt{2}$. In a deep double well (a, b), the difference between the first two eigenenergies is much smaller than the difference to the next higher eigenenergy. The tunneling time is $T \approx 187\,\mu s$ and the superposition of the first two eigenstates $|R\rangle$ is localized in one well. In a shallow well (c, d), the difference between all eigenenergies has the same order of magnitude, so the tunneling is much faster: $T \approx 0.231\,\mu s$. However, the first two eigenstates have a different spatial width and their superposition $|R\rangle$ is *not* localized in one well. Therefore, an interaction-free measurement using the particle's location is not possible in a shallow double well potential.

decreases much faster than the FWHM. For example, for a barrier height of $1\,\mu eV$, the FWHM is still $\sim$830 nm while the tunneling time increases by almost two orders of magnitude to $T \approx 16\,ms$. Achieving a resolution on the nanoscale is not feasible with a distance of $5\,\mu m$ between the rings because the tunneling will be too slow.

While the lack of resolving power presents a problem for imaging, a demonstration experiment of an IFM with electrons would still be possible in the two-ring setup. For this, it may be desirable to decrease the barrier height further in order to achieve a small tunneling time. However, there are also limits to how small the barrier height can be in an IFM, which is shown in Fig. 10 (c, d). Here, the barrier height is so small that the distance $\Delta E$ between the first two eigenenergies is on the same order of magnitude as the energy distance to the next higher eigenenergy, and the tunneling time $T \approx 0.231\,\mu s$ is correspondingly fast. However, in this case, the two states $|1\rangle$ and $|2\rangle$ are no longer simply symmetric and antisymmetric versions of the double well's ground state, but instead have a significantly different spatial shape, similar to the first two eigenstates of a harmonic oscillator. For this reason, their superposition $|R\rangle$ is no longer localized in a single well but has some amplitude in both wells. This makes an interaction-free

Figure 11: Sketch of a modified IFM scheme, similar to the one proposed by Putnam and Yanik (2009) shown in Fig. 9. The difference in the modified scheme is that the two paths of the electron corresponding to the states $|R\rangle$ and $|S\rangle$ are not parallel. For most of the paths, their distance is large enough that tunneling does not occur. The paths only intersect in a small region where they either come close enough for tunneling or may even merge to a single well (as shown in the pseudopotential plot on the right), allowing an exchange of amplitude between them.

measurement impossible because the electron's amplitude cannot start out fully localized in one well and then coherently build up in the second well.

To avoid the discussed problems, we propose a modified scheme where the paths of the electron (i.e., the minima of the two linear Paul traps) in the reference and sample states are not parallel to each other, as shown in Fig. 11. Instead, they are widely separated for most of their length and only intersect in a small region where they are brought closer together. The electron is coupled into the ground state of one of the rings in the separated part. This ground state again corresponds to a superposition of the symmetric and antisymmetric states of the double well potential, but the tunneling frequency is so small that tunneling can be neglected. The electron then travels along the path until it reaches the region of intersection. Here, the paths are either brought close enough that tunneling becomes possible or are even merged to a single potential well. How much amplitude is transferred between $|R\rangle$ and $|S\rangle$ during each passage through the intersecting region depends on the energy difference $\Delta E$ of the lowest two eigenstates in the region and on how much time the electron spends there.

The requirement for this scheme is that an electron initially coupled into a ground state of the reference path $|R\rangle = (|1\rangle + |2\rangle)/2$ remains in the same superposition of eigenstates $|1\rangle$ and $|2\rangle$ while propagating around the path. For this reason, any change of the two paths and the corresponding double well potential must be adiabatic, i.e., slow enough with respect to the motion of the electron that it does not cause an excitation of the electron to higher states. In the region where the paths are close enough together or overlapping, the electron is still in a superposition $(|1\rangle + |2\rangle)/2$ of the potential but the energy difference $\Delta E$ becomes large enough that an oscillation between the initial state and the state $|S\rangle = (|1\rangle - |2\rangle)/2$ becomes possible. When the electron leaves the region of intersection, with the potential again changing slowly enough to ensure adiabaticity, part of the amplitude has been transferred from the first path to the second path.

The intersection region of the two linear Paul traps in the modified scheme represents a beam splitter for electrons. We have discussed such a beam splitter in more detail in

an article (Hammer et al., 2015) that is appended as chapter 4 of this thesis. There we show that the effect of such a Paul-trap-based beam splitter on the electron's state can be regarded as a rotation matrix, so this type of beam splitter can be used for realizing an interaction-free measurement with electrons. We also report results from a first demonstration experiment where a beam of slow electrons with a kinetic energy of 1 eV is split into two beams. While this splitting was achieved with a beam splitter that features neither the coupling of electrons to the ground state nor the adiabatically slow change of the guiding potential, we discuss how the current design can be modified to reach these goals.

If an adiabatic electron beam splitter based on linear Paul traps can be realized experimentally, its applications would go beyond interaction-free measurements with electrons. Such a device would open a new field of on-chip guided interferometry with slow electrons and possibly allow an implementation with electrons of many photon-based experiments from quantum optics. Another possible application of a new type of electron interferometry are precision measurements of electric or magnetic fields.

## 1.3 Summary and outlook

We have introduced interaction-free measurements as a way to reduce the radiation damage incurred by a sample in an electron microscope. A numerical investigation of the results of IFMs in the determination of a sample's transparency has shown that, for this application, IFMs do not always outperform regular microscopy in terms of sample damage. In some cases, however, they may allow one to image a sample with far less damage. The most important example are high-contrast samples that mostly consist of regions that are either very transparent or very opaque. Another example are samples that are highly transparent but have regions with different thickness. Here, IFMs allow a less damaging measurement of the transparency or thickness of the different regions than classical transmission measurements due to the different phase shifts induced by regions of different thickness.

We have further shown that the realization of an IFM with electrons requires a particular type of beam splitter, which can be realized with technology based on linear Paul traps. We have demonstrated that a prototype of such a system can split a single electron beam into two. However, this system does not yet allow a coherent splitting of electrons in the quantum ground state of the guide. Currently, work continues on a redesign of the guide to allow coupling the electron into the transverse ground state (Hammer et al., 2014) and to make the variation of the double well potential along the electron guide smoother by redesigning the splitter with the goal of reaching the adiabatic regime. With a redesigned electron beam splitter or even with the current design, the next step is to demonstrate interference of the output beams in order to study their coherence properties.

A coherent beam splitter represents the first step towards realizing an interaction-free measurement for electrons. More challenges will have to be overcome in order to build such a device. In particular, a cycling scheme has to be devised and the path of the

electrons in both states $|R\rangle$ and $|S\rangle$ must be equal on the length scale of the electron's longitudinal de Broglie wavelength. Even for the slow electrons in our beam splitter, this implies that the path length must be stabilized on the sub-nanometer scale. Additionally, any interaction of the electron with the outside must be minimized to preserve coherence over multiple round trips.

The cycling scheme could be based on circular trajectories as in Fig. 11 or it could be closer to the two-cavity IFM setup and use electron mirrors to turn the linear Paul trap into a resonator (see Fig. 14 on page 41). The necessary electron mirrors can be realized by negative electrostatic voltages on the microwave chip of the Paul trap. The electron can then be coupled into and out of the system by switching the mirror voltages off and on again fast enough.

Much work remains to be done in order to demonstrate an interaction-free measurement with electrons, and it is not yet clear whether IFM-based electron microscopy will be technically feasible in the end. Even if this goal proves too ambitious, however, the development of the necessary technologies, such as new types of electron beam splitters and electron resonators, will allow new ways to manipulate electron matter waves and will have applications beyond interaction-free measurements.

# 2 Optical field enhancement at nanotips

This chapter is about the enhancement of the electric field of light waves that occurs close to the surface of nanotips. We discuss both theoretical considerations and experimental results concerning the strength of this near-field enhancement at tips of varying sizes, shapes, and materials. The theoretical discussion is based on results from extensive numerical simulations to solve Maxwell's equations for a nanotip in a laser focus. The experimental results were obtained by studying photoemission of electrons from nanotips, which occurs when they are illuminated with ultrashort laser pulses. The near-field enhancement is crucial for nanotip photoemission as the emission probability and various features of the emitted electrons depend nonlinearly on the laser's electric field strength at the tip surface .

Using a pulsed laser to trigger the emission of electrons from a nanotip allows a temporal control over the emitted electrons. This technique is promising for applications where time resolution is important, which may also be the case for realizing an interaction-free measurement with electrons. For this reason, the topic of optical field enhancement at nanotips is connected to the proposal of quantum electron microscopy discussed in the last chapter. However, optical near-field enhancement at nanotips has a large variety of applications, and we will discuss it here in a broader context.
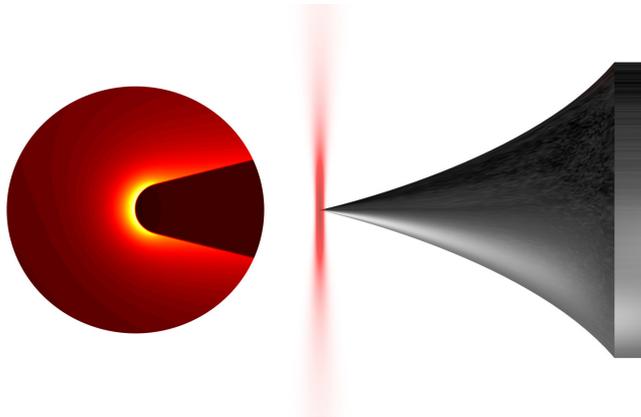


Figure 12: Sketch of an optical near-field at a nanotip. The nanotip is illuminated by a focused laser polarized along the tip's axis of symmetry. This excites a localized near-field mode at the apex of the tip. The spatial extent of the near-field depends on the radius of curvature of the tip. Both are typically on the order of 10 nm. As the electric field strength is enhanced in the near-field, this phenomenon allows the localization of electromagnetic energy on a scale far smaller than the wavelength.

## 2.1  Theory of optical near-field enhancement

Optical near-fields exist close to material surfaces that are interacting with electromagnetic waves (or near the sources of electromagnetic radiation). A well-known example of such a near-field is the evanescent wave that is formed during total internal reflection of light at a glass surface. An important motivation for the study of near-fields and their properties is the localization of electromagnetic radiation to the immediate vicinity of a material surface, a region that can be far smaller than the wavelength of the radiation and Abbe's diffraction limit. This localization is often accompanied by an enhancement of the electric or magnetic field strength of the incoming radiation, which is also relevant for many applications of near-fields. The applications of near-fields are studied in the field of nano-optics (Novotny and Hecht, 2006; Maier, 2007; Sarid and Challener, 2010).

In this chapter, we are interested in near-fields that are excited at the end of nanotips by laser radiation that is polarized in the direction of the tip axis. Such tips typically have a radius of curvature of 5 nm to 100 nm and the enhanced near-field that arises during laser illumination extends over a region that is approximately as large as the radius of curvature, independent of the wavelength of the laser. Thus, nanotips make it possible to localize electromagnetic radiation at optical or infrared frequencies on the nanoscale. The most well-known application of this effect is tip-based scanning near-field optical microscopy (SNOM). Here, a nanotip under laser illumination is raster-scanned in close proximity to a surface. As the enhanced near-field illuminates only a small area of the surface, this technique makes it possible to image a surface with a resolution of ~10 nm by detecting the scattered light from the end of the tip (Wessel, 1985; Inouye and Kawata, 1994; Raschke et al., 2005; Hartschuh, 2008). Closely related is tip-enhanced Raman scattering (TERS), where the efficiency of Raman scattering is increased by the enhanced near-field of a nanotip (Wessel, 1985; Hartschuh, 2008). In other applications, the nanotip is used as a source of either second harmonic photons of the illuminating laser (Bouhelier et al., 2003a; Neacsu et al., 2005b) or as a source of photoemitted electrons (Hommelhoff et al., 2006a,b; Ropers et al., 2007; Barwick et al., 2007).

All the applications of nanotips benefit from a large field enhancement. However, there is no agreement in the literature on how the magnitude of the enhancement depends on the properties (i.e., the shape and the material) of the nanotip (Novotny and Hecht, 2006; Hartschuh, 2008). The most notable disagreement can be found for gold tips, where both theoretical and experimental results vary widely (Martin et al., 2001; Bouhelier et al., 2003a; Neacsu et al., 2005a; Ropers et al., 2007; Behr and Raschke, 2008; Arbouet et al., 2012). For this reason, we study the enhanced near-field at nanotips both experimentally, which will be covered in the next section, and theoretically.

The theory of near-field enhancement at nanotips and other nanoparticles is usually based on Maxwell's equations using local, linear and isotropic materials. While cases exist which need a more complicated theoretical treatment like nonlocal dielectrics (Wiener et al., 2012) or a quantum mechanical smearing of electrons at the material boundary (Zuloaga et al., 2010; Marinica et al., 2012; Ciracì et al., 2012; Teperik et al., 2013), we will follow the standard approach of modeling materials here. We also will not consider magnetic materials.

Materials that are local, linear, and isotropic are defined by a wavelength-dependent dielectric constant $\epsilon(\lambda) = \epsilon_r(\lambda) + i\epsilon_i(\lambda)$, which is the square of the material's complex refractive index $n = n_r + in_i$. Based on their position in the complex $\epsilon$-plane, we can identify several kinds of materials with different characteristic features. Materials with $\epsilon \in \mathbb{R}$ and $\epsilon_r > 0$ are pure dielectrics that are transparent to electromagnetic radiation (because $n_i = 0$). Typical examples are glasses at optical wavelengths or silicon in the infrared. In contrast, materials with $\epsilon_r < 0$ and $0 < \epsilon_i \ll |\epsilon_r|$ are plasmonic metals. They are highly absorptive ($n_i \gg n_r$) and they allow the propagation of surface plasmon polaritons on their surface (Raether, 1988; Novotny and Hecht, 2006). Gold and silver at optical wavelengths are well-known plasmonic metals. Many other materials have an intermediate position on the $\epsilon$-plane, so they are neither transparent to radiation nor plasmonic. See Fig. 47 (c) on page 106 for the dielectric function of some example materials.

To calculate the near-field enhancement at a nanostructure, we must solve Maxwell's equations in three dimensions with a given electromagnetic source (e.g., plane waves, a Gaussian beam or dipole radiation) and a nanostructure defined by its dielectric function $\epsilon(\lambda)$ and its geometric boundary. An enhanced near-field can form at the nanostructure's surface because the electric fields have to fulfill the boundary conditions of Maxwell's equations. In some cases, this problem can be solved analytically. Two important examples are spheres in a plane wave excitation, which can be solved exactly using Mie theory (Mie, 1908; Bohren and Huffman, 2008), and ellipsoids, which can be solved in a quasistatic approximation (discussed in detail in section 8.6.5).

For nanotips, we resort to numerical simulations to calculate the shape and behavior of the near-field. In particular, we employ the finite-difference time-domain (FDTD) method using Lumerical FDTD Solutions, a commercial Maxwell solver. We also cross-check our results with SCUFF-EM, a free Maxwell solver using the boundary element method (BEM). The nanotip is modeled as a cone ending in a rounded tip, with the end at the origin $\mathbf{r} = 0$ of the simulation volume and the tip's axis of symmetry along the $x$ axis. The laser is modeled as a Gaussian beam with a wave vector $\mathbf{k}$ in $z$ direction, a polarization in $x$ direction, and the focus at $z = 0$. A cross section of the resulting electric field at a gold tip is shown in Fig. 13. The enhanced near-field can be clearly seen at the tip apex. It decays on the length scale of the tip's radius of curvature and it is phase-shifted with respect to the laser field.

The main features of the near-field can be expressed by a complex field enhancement factor $\xi = |\xi| \exp(i\phi)$ that includes the magnitude $|\xi|$ of the enhancement and the phase shift $\phi$ of the near-field with respect to the exciting field. The magnitude is defined as the ratio of the maximum of the enhanced near-field $\mathbf{E}_{nf}(\mathbf{r})$ to the amplitude of the exciting laser field $\mathbf{E}_{in}(\mathbf{r})$ in the absence of the nanotip, i.e.,

$$|\xi| = \max_{\{\mathbf{r}\}} \left\{ \frac{|\mathbf{E}_{nf}(\mathbf{r})|}{|\mathbf{E}_{in}(\mathbf{r})|} \right\}. \tag{16}$$

Here, the domain $\{\mathbf{r}\}$ extends over the vicinity of the nanostructure. Typically, the maximum of the near-field enhancement is at the surface.
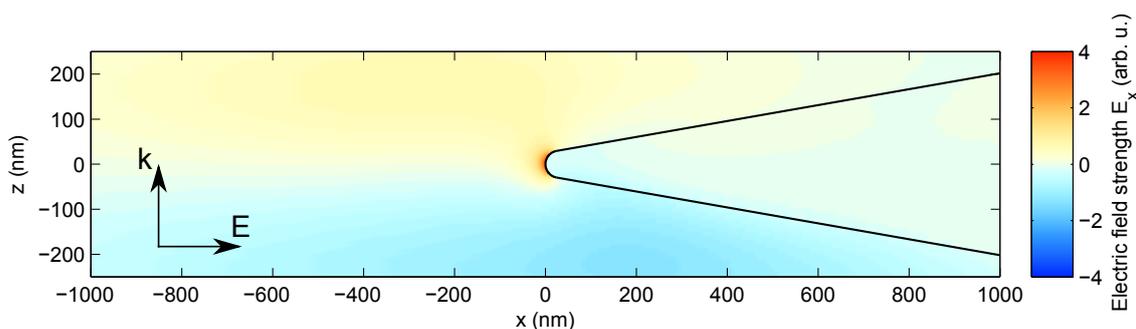
Figure 13: Electric field strength $E_x$ in the vicinity of a nanotip in the focus of a laser. The tip in this example is a gold tip with a radius of curvature of 30 nm and an opening angle of 10°. The laser has a wavelength of 800 nm. The picture shows the electric field strength in $x$ direction on the $y$=0 plane and at the point in time $t_{\mathrm{max}}$ when the strength of the near-field is at its maximum. The tip surface is shown as a black line. The laser's electric field can be seen in the pale blue to orange gradient on the left side of the picture. At $t = t_{\mathrm{max}}$, it is approximately zero at the tip apex because of the phase shift of the near-field with respect to the exciting field. The complex field enhancement factor here is thus $\xi \approx 4 \exp(i\pi/2)$.

We discuss the dependence of the field enhancement factor $\xi$ on the shape and material of the nanotip in an article (Thomas et al., 2015), which is reproduced in chapter 8 of this thesis. The results given there are based on extensive numerical simulations using the FDTD method and cross-checked with the boundary element method (BEM). The main results are:

- Optical field enhancement occurs at nanotips made of any material with $\epsilon \neq 1$ as long as the radius of curvature is significantly smaller than the wavelength. However, the resulting field enhancement factor can vary by orders of magnitude depending on the laser's wavelength and the shape and material of the tip.

- The field enhancement factor depends crucially on both the radius of curvature and the opening angle of the nanotip. It increases for smaller radii and has a peak at relatively large angles. The angle is important for all materials but its effect is much stronger for plasmonic metals, and the position of the peak is different.

- The dependence of the field enhancement factor on the opening angle can be traced back to surface charges excited by the laser along the tip shaft and, for plasmonic metals, to a plasmon resonance effect of the conical geometry.

For more details, please refer to chapter 8.

Our numerical results agree with data on the field enhancement factor obtained from photoemission experiments with tungsten and gold tips. We will now give an introduction to these experiments.

## 2.2 Photoemission of electrons from nanotips

One application of laser-illuminated nanotips is as a source of electrons (Hommelhoff et al., 2006a,b; Ropers et al., 2007; Barwick et al., 2007). The photon energy $E_{\text{photon}} = 2\pi\hbar c/\lambda$ of the employed lasers is usually less than the work function $W$ of the tip material. Electrons then cannot be emitted from the tip via the photoelectric effect (Hertz, 1887; Einstein, 1905). The emission is instead governed by effects that scale nonlinearly with the laser intensity. For this reason, ultrashort laser pulses with a pulse duration on the order of femtoseconds and a high peak intensity of $10^{11}$ to $10^{12}\,\text{W/cm}^2$ (without taking the field enhancement into account) are used to drive photoemission from nanotips. As the ultrashort time scale of the laser pulses carries over to the emitted electrons, laser-illuminated nanotips are promising electrons sources for time-resolved applications in electron microscopy and electron diffraction (Paarmann et al., 2012; Hoffrogge et al., 2014; Gulde et al., 2014; Feist et al., 2015).

The theory of photoemission from nanotips has been discussed in many recent publications (Yalunin et al., 2011; Wachter et al., 2012; Krüger et al., 2012b; Krüger, 2013; Wachter, 2014). Here, we only give a short overview of the aspects of photoemission that are related to the articles reproduced in this thesis and to measuring the field enhancement factor.

Depending on the laser's electric field strength $E$, the wavelength $\lambda$, and the work function $W$ of the tip material, photoemission from metal surfaces is characterized into two different emission regimes (Keldysh, 1965; Bunkin and Fedorov, 1965). The regimes are usually distinguished by the dimensionless Keldysh parameter

$$\gamma = \frac{2\pi c}{\lambda} \frac{\sqrt{2mW}}{eE},$$

(17)

where $e$ and $m$ are the electron charge and mass, $c$ is the speed of light in vacuum, and $E$ is the electric field strength of the laser at the metal surface. For $\gamma \gg 1$, i.e., low field strength and small wavelength, the emission can be treated perturbatively as a multiphoton process. In an article (Thomas et al., 2012) that is included in chapter 5 of this thesis, we discuss a way to generate four-cycle pulses with a commercial erbium fiber laser, and use this laser system to trigger photoemission from a tungsten tip. We measure the emission current as a function of laser power, and we find that it scales nonlinearly with the laser intensity in good agreement with multiphoton emission.

For $\gamma \ll 1$, i.e., high field strength and large wavelength, the electric field strength of the laser field is approximately as strong as (or stronger than) the electric field strength that is binding the electrons inside the metal tip. In this case, a leading-order perturbative approach is no longer justified. Instead, the photoemission is dominated by tunneling of the electrons through the potential barrier modulated by the laser's oscillating electric field.

There is also an intermediate transition regime at $\gamma \approx 1$ where neither the multiphoton nor the tunneling picture fully applies.

While the total emission current scales with the laser's electric field strength at the tip surface, it would be difficult to extract the electric field strength from a current

measurement. The reason is that the current also depends crucially on the total emission area and the variation of the work function in this area. These quantities are difficult to determine in an experiment.

Our measurements of the field enhancement factor instead rely on the electric field's effect on the electron motion *after* the emission from the metal nanotip. While our experiments are in the intermediate regime and the Keldysh parameter is close to 1, the laser intensity is still high enough to observe strong-field effects on the emitted electrons (Bormann et al., 2010; Schenk et al., 2010). An important effect well-known from atomic physics is electron recollision (Corkum, 1993; Lewenstein et al., 1994), where the oscillation of the electron in the laser's electric field after emission causes the electron to recollide with its parent matter (i.e., the metal tip in our case or a gas atom in atomic physics experiments). During the electron recollision, several processes can occur. The most prominent one is high-harmonic generation, where the electron is reabsorbed while emitting a high-energy photon. This process is fundamental to the field of attosecond science as it allows the generation of light pulses with durations far below a femtosecond (Corkum and Krausz, 2007; Krausz and Ivanov, 2009).

For the measurement of the field enhancement factor, we exploit a different process called electron rescattering. Instead of reabsorption, the electron scatters elastically off the tip surface (or off the parent ion in atomic physics) and can gain more kinetic energy in the oscillating electric field than a directly emitted electron (Paulus et al., 1994a,b). This process has recently been observed with electrons emitted from nanotips (Krüger et al., 2011; Herink et al., 2012; Wachter et al., 2012; Piglosiewicz et al., 2014). Its signature can be detected in the kinetic energy spectrum of the emitted electrons: due to the gain in kinetic energy of the rescattered electrons, the overall spectrum features a high-energy plateau of electrons with an almost constant count rate up to an energy $E_{\text{cut-off}}$ where it ends abruptly in a "cut-off". Several example spectra can be seen in Fig. 44 on page 99.

Theoretical and experimental investigations have shown that the cut-off energy scales linearly with the ponderomotive potential $U_{\text{p}} = e^2\lambda^2E^2/(16\pi^2mc^2)$ (i.e., the cycle-averaged kinetic energy of the oscillating electron in the laser field), which is directly related to the electric field strength $E$ close to the surface (Paulus et al., 1994b; Becker et al., 2002; Krüger et al., 2012a; Wachter et al., 2014). Including a correction for the work function, the relation is (Busuladžić et al., 2006)

$$E_{\text{cut-off}} \approx 10.007\,U_{\text{p}} + 0.538\,W\,. \tag{18}$$

By measuring the energy spectrum of the emitted electrons and locating $E_{\text{cut-off}}$ in the spectrum, we can thus obtain the laser's electric field strength at the surface. In contrast to a measurement of the total current, we need not consider the entire emission area here as the cut-off of the energy spectrum depends on the maximum electric field strength at the tip surface. By dividing this field strength by the field strength expected from the laser and focus parameters, we can obtain the absolute value of the field enhancement factor $|\xi|$[†].

---

[†]    Obtaining the phase of the field enhancement factor from photoemission experiments is possible but considerably more difficult (Maisenbacher, 2012).

We use the method based on Eq. 18 to extract the field enhancement factor for tungsten and gold tips of different radii in the 8 nm to 51 nm range, and obtain values in good agreement with numerical simulations. The experimental results are given in two articles (Thomas et al., 2013; Krüger et al., 2014) that are reproduced in chapters 6 and 7 of this thesis. The first article focuses on the results and their relation to Maxwell simulations, showing why the field enhancement factor of gold and tungsten is similar for tips with small opening angles. The second article shows the experimental setup and analysis in more detail, and includes a discussion of rescattering theory and the origins of Eq. 18.

## 2.3 Summary and outlook

We have introduced optical field enhancement at nanotips and discussed how the magnitude of the enhanced near-field depends on key parameters of the setup, in particular on the tip geometry and material. The increase of the field enhancement factor for larger opening angles may guide future development in etching and other tip production techniques, as a larger field enhancement factor would prove beneficial for many applications of laser-illuminated nanotips, including near-field microscopy and photoemission.

We have further shown that the field enhancement factor can be measured with high-intensity laser pulses via electron rescattering, in good agreement with Maxwell simulations. As the experimental results yield the electric field strength within ~1 nm from the tip surface, they allow a measurement of electric fields on a scale that is not accessible to other methods such as near-field microscopy (SNOM). In the future, such measurements can be carried out for other tip geometries and materials to test our numerical results in more experiments. By modifying the setup to resolve the emission angle of the electrons, it may also be possible to obtain a map of the near-field strength on the tip surface.

# 3 Semitransparency in interaction-free measurements

**Originally published in**: Physical Review A 90, 053840 (2014)
**Authors**: Sebastian Thomas, Christoph Kohstall, Pieter Kruit, Peter Hommelhoff

**Abstract**: We discuss the effect of semitransparency in a quantum-Zeno-like interaction-free measurement setup, a quantum-physics based approach that might significantly reduce sample damage in imaging and microscopy. With an emphasis on applications in electron microscopy, we simulate the behavior of probe particles in an interaction-free measurement setup with semitransparent samples, and we show that the transparency of a sample can be measured in such a setup. However, such a measurement is not possible without losing (i.e., absorbing or scattering) probe particles in general, which causes sample damage. We show how the amount of lost particles can be minimized by adjusting the number of round trips through the setup, and we explicitly calculate the amount of lost particles in measurements which either aim at distinguishing two transparencies or at measuring an unknown transparency precisely. We also discuss the effect of the sample causing phase shifts in interaction-free measurements. Comparing the resulting loss of probe particles with a classical measurement of transparency, we find that interaction-free measurements only provide a benefit in two cases: first, if two transparent samples with a high contrast are to be distinguished, interaction-free measurements lose less particles than classical measurements by a factor that increases with the contrast. This implies that interaction-free measurements with zero loss are possible if one of the samples is perfectly transparent. A second case where interaction-free measurements outperform classical measurements is if three conditions are met: the particle source exhibits Poissonian number statistics, the number of lost particles cannot be measured, and the transparency is larger than approximately 1/2. In all other cases, interaction-free measurements lose as many probe particles as classical measurements or more. Aside from imaging of gray levels, another possible application for interaction-free measurements is the detection of arbitrarily small phase shifts in transparent samples. Copyright 2014 American Physical Society.

## 3.1 Introduction

In some applications of imaging and microscopy, the damage that is inflicted on a sample while its image is taken is the main limit on what kind of samples *can* be imaged. Particularly in electron microscopy, the large radiation dose that any sample receives can make the imaging of, e.g., living biological samples impossible (Spence, 2013; Egerton

et al., 2004). Hence, reducing sample damage is crucial for future developments of electron microscopy. Next to other proposals (Okamoto, 2012), a quantum mechanical protocol called "interaction-free measurement" (IFM), previously proven to work with photons (Elitzur and Vaidman, 1993; Kwiat et al., 1995), has been proposed as a means to this end (Putnam and Yanik, 2009). The basic idea of interaction-free measurements is to exploit the wave-like features of quantum particles in order to gain information about an object while reducing the interaction between particle and object to a minimum. This is accomplished by confining the probe particle in a resonator in which it makes multiple round trips. During each round trip, a small part of the wave (the "sample wave") is split off from the original trajectory (the "reference wave") and sent through the sample. After many round trips, the presence of a sample can be inferred from the intensity of the reference wave even though the total intensity in the sample wave has been arbitrarily small. This is explained in detail in section 3.2.

The field of interaction-free measurements started with a discussion on "negative-result" measurements, where the location of an object is inferred from *not* being measured with a detector (Renninger, 1960), which leads to a change in the wave function of the object (Dicke, 1981). Elitzur and Vaidman proposed an IFM scheme employing a Mach-Zehnder interferometer which sometimes detects an absorbing object without any absorption occurring (Elitzur and Vaidman, 1993; Kwiat et al., 1995). In this simple interferometric scheme, only some measurement runs constitute a successful IFM while the probe particle is absorbed in the other runs. The rate of successful IFM runs can be increased arbitrarily close to 1 in more elaborate interferometric setups with multiple round trips through the path containing the sample (Kwiat et al., 1995, 1999).

All applications of interaction-free measurements may come with imperfect absorbers like semitransparent objects. Previous work on semitransparency in IFMs has shown that the rate of successful IFM runs is reduced if a semitransparent object is to be detected instead of a perfect absorber (Jang, 1999; Vaidman, 2003; García-Escartín and Chamorro-Posada, 2005). This can be compensated by increasing the number of round trips in the interferometer (Kwiat, 1998; Azuma, 2006). In this article, we study the effect of semitransparent samples in IFM setups, and we calculate the damage that arises during either an IFM or a conventional measurement in two different situations relevant for imaging: (1) discriminating between two objects which have different transparencies or (2) determining the transparency of an object. We also compare our results to a lower bound for the damage in general quantum measurements of semitransparency, which was derived by Massar, Mitchison, and Pironio for a generalization of interaction-free measurements (Mitchison and Massar, 2001; Massar et al., 2001; Mitchison et al., 2002). Additionally, we discuss the effect of phase shifts in IFMs.

Most of the previous discussion of interaction-free measurements has been focused on the detection of absorbing objects using photons as probe particles. Hence, such measurement schemes have sometimes also been called "absorption-free" measurements (Mitchison and Massar, 2001). Especially if other probe particles like electrons (Putnam and Yanik, 2009) or neutrons (Hafner and Summhammer, 1997) are considered, however, it should be noted that the IFMs are not only absorption-free but also free of any process that prevents the probe particle's wavefunction from continuing undisturbed on its

original path. Scattering out of the path or momentum-changing collisions turn out to have the same effect as absorption. Therefore, we will call all these processes "loss", as in "lost for further interaction with the reference wave". Many of the interaction processes, such as inelastic scattering or electron knock-out processes, cause damage to the sample, which can be prevented using IFM schemes. While the relationship between loss and damage is complicated and depends on the specific setup and sample, we will assume in the following that a higher probability of "loss" means more damage. Interaction-free measurements open up novel applications in cases where sample damage is particularly disruptive. Next to electron microscopy (Putnam and Yanik, 2009), other potential
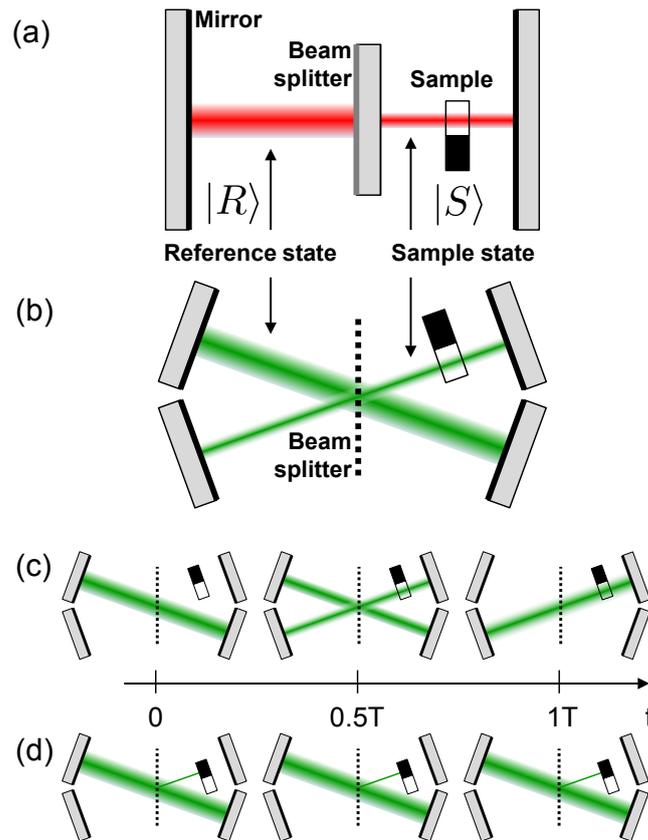


Figure 14: Sketches of quantum-Zeno-like IFM setups. (a) The light mode in the left reference cavity is coupled via a semi-transparent mirror to a mode in the sample cavity on the right, as proposed by Kwiat et al. (1995). Figure (b) shows a possible realization of two coupled cavities for electrons with a diffraction-based beam splitter. (c) With a transparent sample in the sample beam, the probability of finding the electron will coherently oscillate between the reference and sample beam. (d) With a lossy sample in the sample beam, the coherent build-up of probability amplitude in the sample beam is prevented and the electron stays in the reference beam. Depending on whether we measure the probe particle in the sample or in the reference beam, we determine to have a transparent or lossy sample, respectively, in the sample beam. The same concept as in (c) and (d) applies to (a).

applications are the imaging of photo-sensitive materials (Inoue and Björk, 2000) or single-atom detection (Karlsson et al., 1998; Volz et al., 2011).

## 3.2 Interaction-free measurements

There are several different schemes to achieve IFM with a high success rate that have been proposed (Kwiat et al., 1995; Putnam and Yanik, 2009) or realized (Kwiat et al., 1999; Tsegaye et al., 1998) in the literature. Most of them employ techniques based on the quantum Zeno effect, where frequent measurements prevent a quantum system from changing its state (Misra and Sudarshan, 1977). It is this kind of "quantum-Zeno-like" IFM setup that we will discuss in this article. Example schemes are shown schematically in Fig. 14 for either photons or electrons as probe particles.

We can describe the probe particle in a quantum-Zeno-like IFM setup as a three-state system. The first state is the reference state $|R\rangle$, in which the particle starts out. This state is coupled to a second state, the sample state $|S\rangle$. In the examples of Fig. 14, the coupling between the two states is achieved via a beam splitter. The third state of the
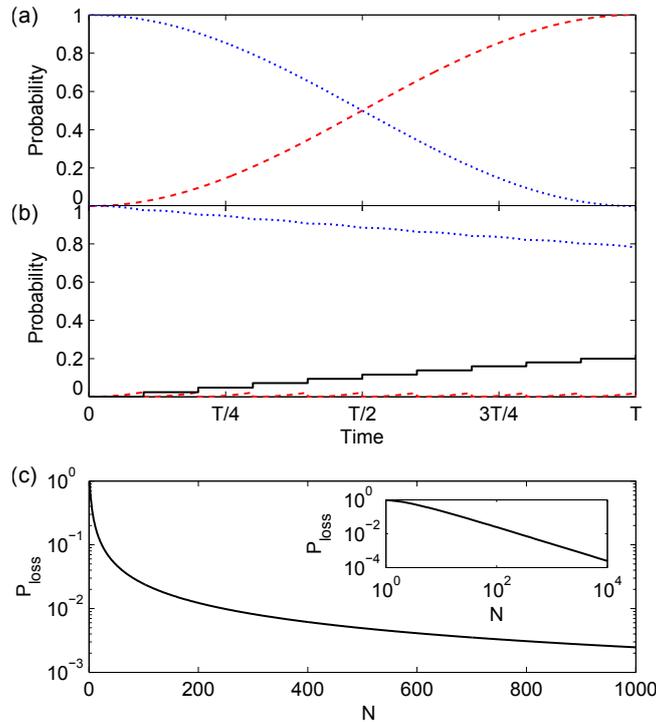


Figure 15: Probabilities $P_R$, $P_S$, and $P_L$ of finding the probe particle in the reference state $|R\rangle$ (dotted blue line), sample state $|S\rangle$ (dashed red line), or loss state $|L\rangle$ (black line). (a) Probabilities versus time for a perfectly transparent sample, as in Fig. 14 (c). At time $T$ the particle is in the sample state. (b) Probabilities versus time for $N = 10$ with an opaque sample, as in Fig. 14 (d). At time $T$, the particle is in the reference state with probability $\sim 0.78$ and lost with probability $\sim 0.22$. (c) Probability $P_L$ at time $T$ as a function of $N$ with an opaque sample. The inset shows the same on a double-logarithmic scale.

system is the loss state $|L\rangle$. It keeps track of the probability that the particle is lost in a sample interaction, for example due to absorption or scattering. Note that $|L\rangle$ may be a continuum of states.

We start out with the particle in the reference state $|R\rangle$. The coupling strength between $|R\rangle$ and $|S\rangle$ is such that, in the absence of a sample, the particle is fully in $|S\rangle$ after $N$ round trips, i.e., $N$ encounters with the beam splitter. This half-finished oscillation from $|R\rangle$ to $|S\rangle$ takes the time $T$, as shown in Fig. 15 (a). (A full Rabi oscillation from $|R\rangle$ over $|S\rangle$ back to $|R\rangle$ would take the time $2T$.) In state $|S\rangle$, the particle may encounter a sample once during each round trip. As in the quantum Zeno effect, an encounter of the particle with an opaque sample constitutes a measurement of the state of the particle with two possible outcomes: either the particle is still in the reference state, and the oscillation restarts from there, or the particle is in the sample state, where it is subsequently lost. The presence of the sample therefore inhibits the coherent evolution from $|R\rangle$ to $|S\rangle$, as shown in Fig. 15 (b) for the example of $N = 10$. To model the probability of losing the particle, we simply transfer the amplitude from $|S\rangle$ to $|L\rangle$ every time the particle encounters an opaque sample.

At time $T$, the observer measures the state of the particle and determines whether it is in $|R\rangle$, $|S\rangle$, or $|L\rangle$. This way, the following information about the sample is obtained: if the particle is still in state $|R\rangle$ or if it is lost in $|L\rangle$, there must be an opaque sample blocking the evolution to $|S\rangle$. If the particle is found in $|S\rangle$ at time $T$, the sample is transparent (or there is no sample). An interaction-free measurement is successful if the presence of the sample is detected without loss via a probe particle in $|R\rangle$. To achieve a high success rate, the probability of finding the particle in $|L\rangle$ needs to be minimized. The loss probability $P_L$ depends on the number of round trips $N$, and is given by (Kwiat et al., 1995)

$$P_L = 1 - \cos^{2N}\left(\frac{\pi}{2N}\right) \xrightarrow{\text{large } N} \frac{\pi^2}{4N}, \tag{19}$$

which converges to 0 for $N \to \infty$, see Fig. 15 (c). Thus, in principle, the existence of a sample can be ascertained without loss. For an intuitive picture of why more sample encounters ultimately lead to less loss in an IFM, consider the following: while doubling $N$ doubles the number of sample encounters, the loss probability during each interaction is reduced by a factor of 4 because the coherent build-up of probability in $|S\rangle$ is approximately quadratic.

Note that the calculations shown in Fig. 15 assume a continuous coupling between $|R\rangle$ and $|S\rangle$, which occurs in some proposals for IFM (Putnam and Yanik, 2009), while other proposals and the scheme in Fig. 14 work with one discrete coupling step in every round trip (Kwiat et al., 1995, 1999). Instead of the continuous oscillation of probabilities shown in Fig. 15 (a), the oscillation proceeds in discrete steps for a discrete coupling. These different couplings lead to the same results in this paper because the particle-sample interaction also occurs in discrete steps.

## 3.3 Semitransparent samples

So far, we have considered only fully opaque samples, which completely block the coherent build-up of the probe particle wave function in the sample state. This "all-or-nothing" IFM scheme is fully loss-free in the limit $N \to \infty$ and thus outperforms any classical detection in terms of sample damage. We now investigate the effect of semitransparent samples in quantum-Zeno-like IFM setups, which are more reminiscent of real-world samples relevant for imaging, e.g., biological samples.

If a particle encounters a semitransparent sample with a transparency $\alpha$, it passes the sample with probability $\alpha$ or it is lost with probability $1 - \alpha$. Lost (i.e., absorbed or scattered) particles are the cause of damage during imaging. Additionally, the sample may cause a phase shift $\phi$ of the particle's wavefunction. One encounter with the semitransparent sample leads to the following modification of the particle's amplitudes $r$, $s$, and $l$ in the three states $|R\rangle$, $|S\rangle$, and $|L\rangle$:

$$
\begin{aligned}
|\psi\rangle &= r\,|R\rangle + s\,|S\rangle + l\,|L\rangle \\
&\to r\,|R\rangle + e^{i\phi}\,\sqrt{\alpha}s\,|S\rangle + \sqrt{|l|^2 + (1-\alpha)|s|^2}\,|L\rangle
\end{aligned}
\tag{20}
$$

Note that this can be thought of as a combination of a unitary transformation between $|S\rangle$ and $|L\rangle$ and a measurement of whether the particle is in $|L\rangle$ (see also the articles by García-Escartín and Chamorro-Posada (2005) and by Mitchison and Massar (2001) for different but equivalent approaches of describing the interaction with a semitransparent
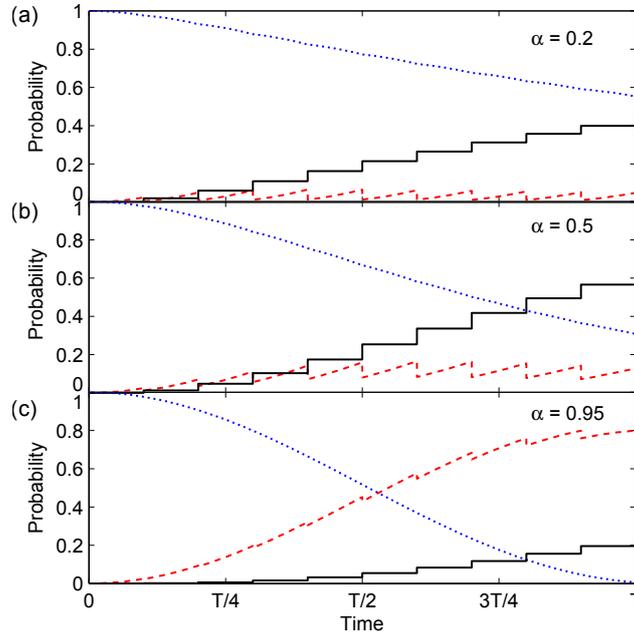


Figure 16: Time evolution of the probe particle state probabilities for different transparencies: $\alpha = 0.2$ (a), $\alpha = 0.5$ (b), $\alpha = 0.95$ (c). Shown are the probabilities $P_R$ (dotted blue line), $P_S$ (dashed red line), and $P_L$ (black line) for $N = 10$.

sample). The loss from $|S\rangle$ to $|L\rangle$ is irreversible and the state $|L\rangle$ merely serves to 'count' the lost amplitude. For $\alpha = 0$ we recover the fully opaque case discussed in the last section. Similarly, setting $\alpha = 1$ and $\phi = 0$ represents the case of an absent object.

We can now simulate the IFM scheme with arbitrary semitransparent samples by starting a particle in the state $|\psi\rangle = |R\rangle$ at $t = 0$, using a time propagator to simulate the coherent evolution from $|R\rangle$ to $|S\rangle$, and periodically interrupting this process $N$ times with a sample encounter according to Eq. 20. In the $|R\rangle = \left(\begin{smallmatrix} 1 \\ 0 \end{smallmatrix}\right)$ and $|S\rangle = \left(\begin{smallmatrix} 0 \\ 1 \end{smallmatrix}\right)$ basis, the propagator for a coherent evolution over a time interval $\Delta t$ is

$$\frac{1}{2} \begin{pmatrix} 1 + e^{-i\pi\Delta t/T} & 1 - e^{-i\pi\Delta t/T} \\ 1 - e^{-i\pi\Delta t/T} & 1 + e^{-i\pi\Delta t/T} \end{pmatrix}. \tag{21}$$

For a time interval of $\Delta t = T/N$, this propagator is equivalent to a beam splitter that completes half an oscillation from $|R\rangle$ to $|S\rangle$ in $N$ steps. This confirms that the continuous and discrete couplings in different IFM setups lead to the same result, as discussed in the last section.

We now simulate the behavior of a particle in a quantum-Zeno-like IFM setup. We will first discuss the case of a semitransparent sample without a phase shift and will include the phase shift in Sec. 3.7. The simulation is then defined by two parameters:

- the number of round trips $N$ within the duration $T$ of half an oscillation

- the transparency $\alpha$ of the sample.

Examples of such simulations for different $\alpha$ are given in Fig. 16. They show the interplay of coherent build-up from $|R\rangle$ to $|S\rangle$ and periodic particle loss due to the presence of the semitransparent sample. For an IFM measurement, the relevant results of a simulation are the three probabilities $P_R$, $P_S$, and $P_L$ at time $T$, when the probe particle state is measured. Fig. 17 displays these probabilities as a function of $\alpha$ for $N = 10, 50$, and 200. $P_R$ starts out close to 1 for $\alpha = 0$ and ends at 0 for $\alpha = 1$, while $P_S$ shows the opposite behavior. The probability of losing the particle is low for $\alpha$ around 0 or 1, but it peaks in between. Both $P_R$ and $P_S$ change swiftly in the region where $P_L$ peaks.

For low and high transparency, the situation is similar to "all-or-nothing" IFM with either a fully transparent or a fully opaque sample: if the transparency is low, the quantum Zeno effect prevents the evolution to the sample state. If the transparency is high, the loss is negligible, so the particle can enter the sample state. For intermediate transparencies, significant parts of the wavefunction can enter the sample state and can be lost. Then there is a high chance of losing the particle. The position of this high-loss region shifts to higher transparencies as the number of passes through the sample increases.

Analyzing the loss peak for different $N$ shows that its height $\max(P_L)$ slowly decreases for larger $N$, converging to a value of $\sim 0.63$, while the position of the peak, $\alpha'$, shifts to high transparencies. The behavior of the probabilities at large $N$ is easier to discern on a logarithmic scale, which is shown in Fig. 18 for $N = 200, 2000$, and 20000. Here, an increase of $N$ simply corresponds to a shift of the probability curves further towards

$\alpha = 1$. This allows us to give an approximate formula for the position of the maximum of the loss peak $\alpha'$ for $N \gg 1$:

$$\alpha' \approx 1 - \frac{4.4}{N}. \tag{22}$$

We now directly see that the "all-or-nothing" IFM process of distinguishing the presence from the absence of an object also works for distinguishing between samples with high transparencies $\alpha_2$ and low transparencies $\alpha_1$ if the contrast is high, i.e., if $(1 - \alpha_1) / (1 - \alpha_2) \gg 1$. In this case, $N$ can be chosen so that $\alpha'$ lies between the two transparencies and the loss probability is low for both $\alpha_1$ and $\alpha_2$. Example transparencies are $\alpha_1 = 0.9$ and $\alpha_2 = 0.9999$ for $N = 2000$ as in Fig. 18 (b). Of course, the loss probability of such a measurement is always higher than in an "all-or-nothing" IFM with the same $N$: $P_L$ is determined by the contrast, which can only be high for $\alpha_2$ close to 1. The loss probability in an IFM as a function of the contrast is plotted in Fig. 19. This plot assumes that all IFMs are performed with the optimum number of round trips $N$, which minimizes the average loss probability at the given transparencies $\alpha_1$ and $\alpha_2$. An approximate formula for the optimum $N$ can be obtained from Eq. 22 and the average
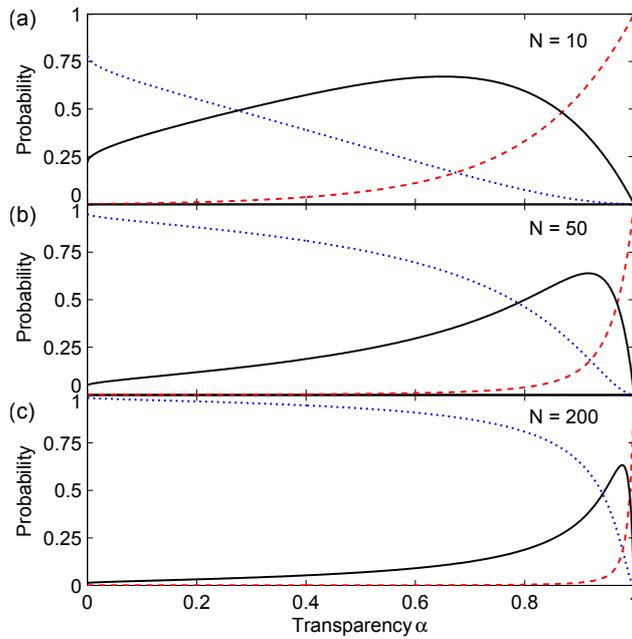


Figure 17: Probabilities for the probe particle to be detected in $|R\rangle$, $|S\rangle$, or $|L\rangle$ at time $T$ as a function of $\alpha$ for $N = 10$ (a), 50 (b), and 200 (c). Shown are $P_R$ (dotted blue lines), $P_S$ (dashed red lines), and $P_L$ (black lines). For low transparencies, the particle is most likely found in the reference state, while the particle is most likely to enter the sample state for high transparencies. In between low and high transparencies, the loss probability has a maximum and the two other probabilities change swiftly.

on the logarithmic scale (i.e., the geometric mean) of $1 - \alpha_1$ and $1 - \alpha_2$:

$$N_{\text{opt}} \approx \frac{4.4}{\sqrt{(1 - \alpha_1)(1 - \alpha_2)}}. \tag{23}$$

If the contrast is large and $\alpha_1 \gg 0$, $N_{\text{opt}}$ represents a good approximation of the exact optimum $N$, which can be found numerically.

If $\alpha_2 = 1$, the contrast is infinite and the loss probability can approach 0 by increasing $N$ and thus bringing $\alpha'$ arbitrarily close to 1. This implies that interaction-free measurements can detect the presence or absence of any transparent object with arbitrarily low loss. That this is possible was already shown by Azuma (2006). There is also a general
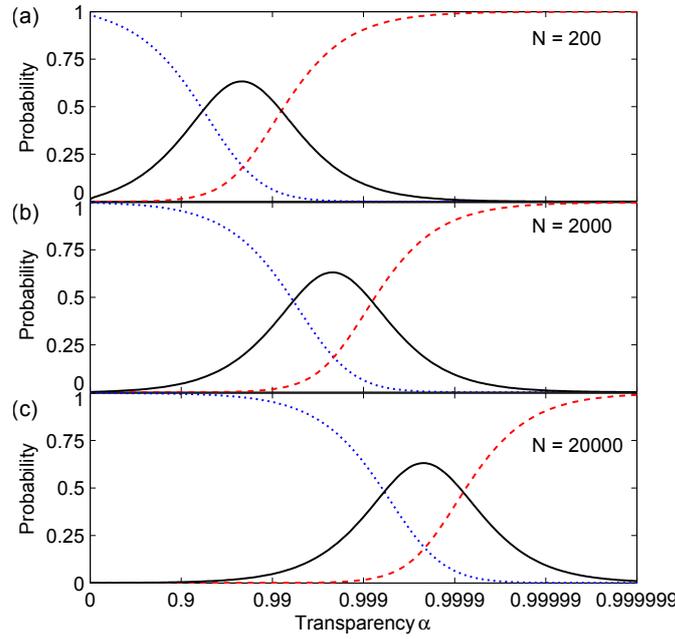


Figure 18: Same as Fig. 17 but for $N = 200$ (a), 2000 (b), and 20000 (c), and on a logarithmic scale. For large $N$, a change of $N$ simply corresponds to a shift of the probability curves along the logarithmic axis.
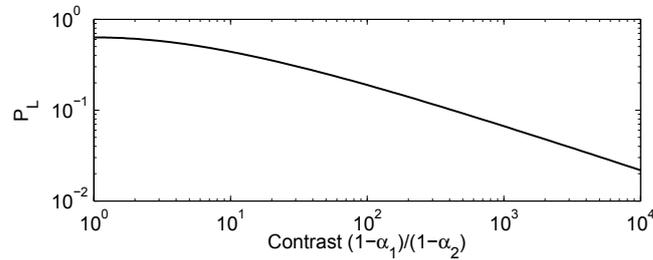


Figure 19: Loss probability as a function of the contrast $(1 - \alpha_1) / (1 - \alpha_2)$ if two transparencies $\alpha_1$ and $\alpha_2$ are to be distinguished in an IFM with $N \gg 1$, assuming that $N$ is always chosen so as to minimize the average loss probability at $\alpha_1$ and $\alpha_2$.

finding on quantum measurements by Mitchison and Massar (2001), which states that it is possible to distinguish an object with any transparency $\alpha_1 < 1$ from a perfectly transparent object $\alpha_2 = 1$ without loss, but it is not possible to distinguish without loss between two semitransparent objects with transparencies $\alpha_{1,2} < 1$. The concrete cases shown in this section will be important for the discussion that follows.

## 3.4 Distinguishing two transparencies

In this section, we discuss the task of distinguishing two a priori given transparencies $\alpha_1$ and $\alpha_2$. We simulate how many particles are lost on average as a function of the measurement error probability. We compare the results of a quantum-Zeno-like IFM scheme to classical measurements and to the minimum number of lost particles in a general quantum measurement (Mitchison et al., 2002).

In a classical measurement, one possibility is to simply count how many particles are transmitted through the sample, i.e., have not been absorbed or scattered out of the beam. In an IFM, one can count how many particles are detected in either the reference state, the sample state, or the loss state. The counts can then be compared to the three probabilities $P_R$, $P_S$, and $P_L$ to infer which of the two given transparencies is more likely.

To reduce the error probability $P_E$ of wrongly identifying the sample, we need to increase the number of probe particles. A measurement is therefore always a trade-off between the number of lost particles, which determines the sample damage, and the error probability.

We evaluate both classical and interaction-free measurements using Monte Carlo simulations, similar to the analysis of classical measurements in the paper by Mitchison et al. (2002). One measurement to distinguish transparencies consists of multiple runs with single probe particles. After each run, the conditional probabilities of the transparency being either $\alpha_1$ or $\alpha_2$ given the current measurement result is evaluated. If either of the probabilities is below a chosen threshold $x$, the measurement is stopped with the more likely $\alpha$ as the result. Otherwise, the measurement continues for another run.

For a classical transmission measurement after $n$ runs with $n'$ detected particles, i.e., $n'$ particles that traversed the sample without being lost, the conditional probability of $\alpha = \alpha_1$ is

$$P(\alpha = \alpha_1) = \frac{\alpha_1^{n'}(1-\alpha_1)^{n-n'}}{\alpha_1^{n'}(1-\alpha_1)^{n-n'} + \alpha_2^{n'}(1-\alpha_2)^{n-n'}} \tag{24}$$

while $n - n'$ particles are lost. For an IFM after $n$ runs with $n_r$ particles detected in the reference state, $n_s$ particles detected in the sample state, and $n_l$ particles lost, the equivalent probability is:

$$P(\alpha = \alpha_1) = \frac{P_R(\alpha_1)^{n_r}P_S(\alpha_1)^{n_s}P_L(\alpha_1)^{n_l}}{P_R(\alpha_1)^{n_r}P_S(\alpha_1)^{n_s}P_L(\alpha_1)^{n_l} + P_R(\alpha_2)^{n_r}P_S(\alpha_2)^{n_s}P_L(\alpha_2)^{n_l}}. \tag{25}$$

We use Monte Carlo simulations to find out the average number of lost particles as well as the average error that arises during the classical and the IFM measurement
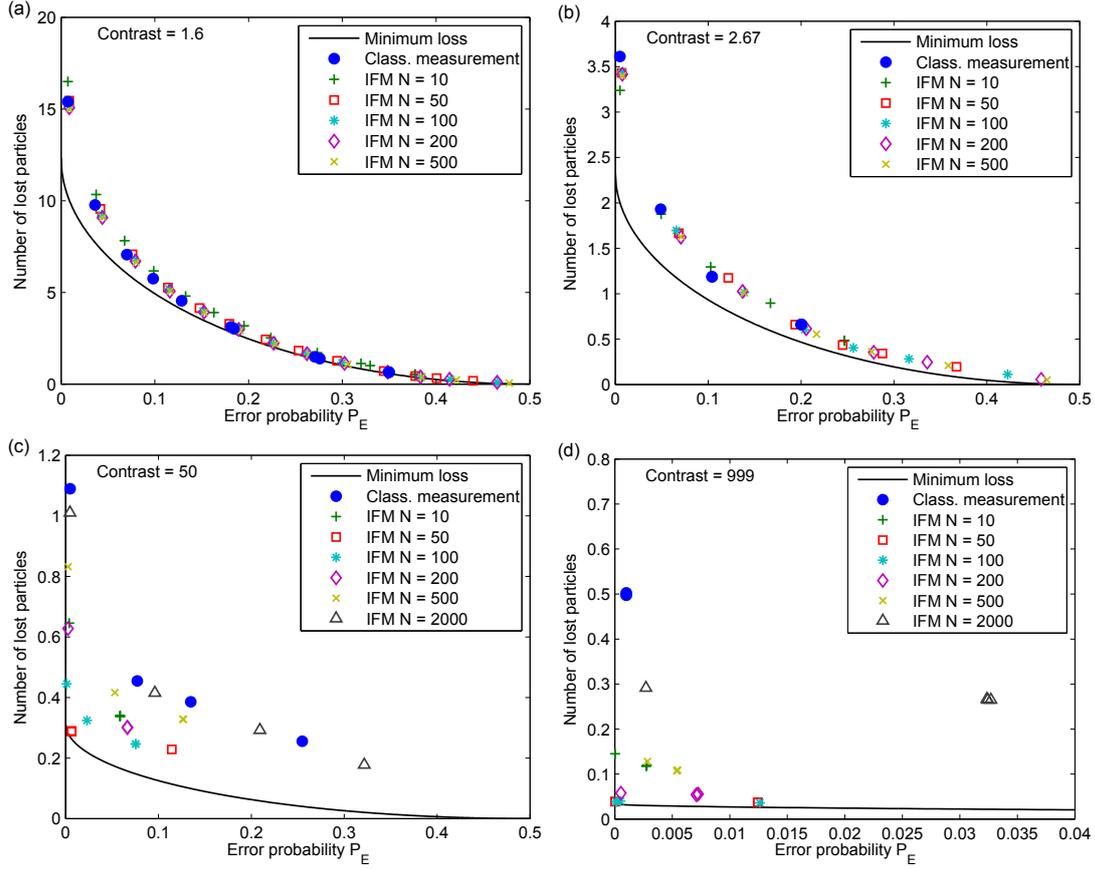
Figure 20: Relationship between the average number of lost particles and the error probability in a measurement to distinguish two transparencies. Shown here are results from simulations of a classical transmission measurement (blue circles), IFM with various parameters (other symbols), and the minimum amount of loss in such a measurement according to Eq. 26 (black line). The task is to distinguish the two transparencies (a) $\alpha_1 = 0.2$ and $\alpha_2 = 0.5$, (b) $\alpha_1 = 0.04$ and $\alpha_2 = 0.64$, as in Fig. 3 of the paper by Mitchison et al. (2002), (c) $\alpha_1 = 0.5$ and $\alpha_2 = 0.99$, (d) $\alpha_1 = 0.001$ and $\alpha_2 = 0.999$. Each data point was obtained by 40000 simulation runs. For example, to distinguish the two transparencies in (c) a classical measurement loses $\sim0.45$ particles on average to reach an error probability of $\sim0.08$, while an IFM with $N = 100$ can reach the same error probability with only $\sim0.25$ lost particles and the minimum amount of loss for this error probability is $\sim0.15$.

schemes. The relationship between error probability and loss is found by varying the error threshold $x$. Results for the number of lost particles versus error probability are shown in Fig. 20. Note that, while the error threshold can be varied continuously, the measurement scheme is ultimately discrete, so different error thresholds may lead to the same result. For this reason, the relationship between lost particles and error probability cannot be given as a continuous function, but only on discrete points. Especially if $\alpha_1$ and $\alpha_2$ have a high contrast, the number of discrete points is quite small as only a few particles are required for distinguishing the transparencies with low error probability.

Fig. 20 (a) and (b) show a measurement of two transparencies with low contrast, while

panels (c) and (d) show a measurement of two transparencies with high contrast. In the low-contrast case, the results for IFM do not depend much on $N$ and are usually similar to a classical transmission measurement. In this case, IFM does not offer a benefit over classical measurements. This is true for any combination of low-contrast transparencies we tried.

IFM outperforms the classical measurement for high contrasts, as shown in Fig. 20 (c) and (d). Here, more particles are lost in a classical measurement than in an IFM, and there is a clear difference between IFMs with different $N$. In (c), the optimum $N$ with the best ratio between lost particles and low error is $N = 50$, while $N = 50$ and $N = 100$ perform approximately equally well in (d), where both achieve a smaller error probability than classical measurements with an order of magnitude less particles lost. At optimum $N$ the maximum of the loss probability is in between $\alpha_1$ and $\alpha_2$ so $P_L$ is small for both, as discussed in the last section. Calculating $N_{\mathrm{opt}}$ numerically, we obtain $N = 54$ for (c) and $N = 73$ for (d), in good agreement with the simulation results.

For $\alpha_2$ closer to 1, the number of lost particles will decrease further while the optimum $N$ will increase. Note that only a single particle is often already sufficient to distinguish the two transparencies with a low error probability in a high-contrast IFM as in Fig. 20 (d). In this case, the average number of lost particles is directly determined by the loss probability given in Fig. 19.

We now compare our results for both classical and IFM to the minimum number of lost particles in a quantum measurement, as derived by Mitchison et al. (2002), which is valid for a more general quantum measurement scheme than the IFM setup discussed here. While the minimum number of lost particles can be reached using a non-constant coupling between $|R\rangle$ and $|S\rangle$ that has to be adapted to the given transparencies $\alpha_1$ and $\alpha_2$, the quantum-Zeno-like IFM setup discussed here is technologically less challenging and has already been realized experimentally using photons as probe particles (Kwiat et al., 1999).

If a sample can have two transparencies $\alpha_1$ or $\alpha_2$ with equal probability and these transparencies are to be distinguished with an error probability of at most $P_E$, then the minimum number of lost particles is

$$n_{\mathrm{min}} = \frac{\sqrt{1-\alpha_1}\sqrt{1-\alpha_2}\left(1 - 2\sqrt{P_E(1-P_E)}\right)}{1 - \sqrt{\alpha_1\alpha_2} - \sqrt{1-\alpha_1}\sqrt{1-\alpha_2}}, \tag{26}$$

following Eq. (1) of the paper by Mitchison et al. (2002). Equation 26 is plotted together with the simulation results in Fig. 20. Using the optimum number of round trips, quantum-Zeno-like IFM can approach the minimum number of lost particles if the contrast of $\alpha_{1,2}$ is high. In the case of low contrast, the minimum number of lost particles is somewhat smaller than what is achieved in either classical or IFM measurements, but leaves room for only a factor of 2 improvement for the error probabilities considered here.

## 3.5 Measuring an unknown transparency

Arguably the most common task in imaging is to measure an unknown transparency $\alpha$. We determine the number of lost particles in an IFM in this case and compare it to a classical measurement.

As in the previous section, running the IFM process $M$ times with a semitransparent sample results in a multinomial distribution of particles that are either detected in $|R\rangle$, detected in $|S\rangle$, or lost in $|L\rangle$. Here, $M$ is the number of times the IFM is repeated, as opposed to $N$, which denotes the number of round trips in a single IFM. The number of particles detected in these states can be used to estimate the probabilities $P_R(\alpha)$, $P_S(\alpha)$, and $P_L(\alpha)$ (see Fig. 17), which yield the transparency $\alpha$.

We assume that we have no prior knowledge about the transparency $\alpha \in [0, 1]$ of a sample. We consider the number of particles detected either in the reference state or in the sample state independently. The number of particles found in one of these states after running the process $M$ times follows a binomial distribution with probability $P(\alpha) = P_R(\alpha)$ or $P_S(\alpha)$, respectively. After estimating the probability $P(\alpha)$ from such a measurement, the uncertainty of the measurement $\Delta P$ (i.e., the confidence interval) can be estimated from the normal approximation of the binomial distribution. For a 95 % confidence level this yields

$$\Delta P \approx (2 \cdot 1.96) \sqrt{\frac{P(\alpha)(1 - P(\alpha))}{M}}, \tag{27}$$

where the factor $2 \cdot 1.96$ is due to the 97.5 percentile point of the normal distribution. To obtain the uncertainty in transparency $\Delta \alpha$ from the uncertainty $\Delta P$, we use the relation $\Delta P = P'(\alpha) \Delta \alpha$, which is valid if the slope $P'(\alpha)$ does not change significantly within the interval $\Delta \alpha$. For any transparency, Eq. 27 can be inverted to find the number of trials necessary for obtaining $\alpha$ with a given uncertainty. Finally, by multiplying this number
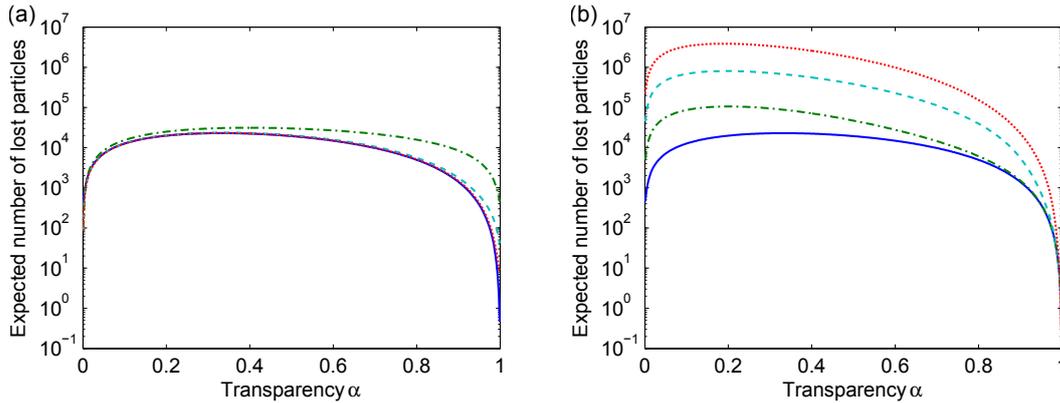


Figure 21: Expected number of lost particles in a measurement of $\alpha$ with uncertainty $\Delta \alpha \leq 0.01$ as a function of transparency using the reference state (a) or the sample state (b) as signal. The curves for a classical measurement (blue line), and IFM with $N = 10$ (dash-dotted green line), $N = 100$ (dashed cyan line), and $N = 500$ (dotted red line).

with the loss probability $P_L(\alpha)$, one obtains the expected number of lost particles $n_{\mathrm{loss}}$ during a measurement of $\alpha$ with a given uncertainty $\Delta\alpha$:

$$n_{\mathrm{loss}} \approx P_L(\alpha)P(\alpha)(1 - P(\alpha)) \left( \frac{3.92}{\Delta\alpha P'(\alpha)} \right)^2. \tag{28}$$

We see that $n_{\mathrm{loss}}$ depends on three factors: the loss probability $P_L(\alpha)$ and the slope and value of the signal $P(\alpha)$. This is true for both IFMs, where we obtain the probabilities from simulations, and classical measurements, where the probabilities are simply $P(\alpha) = \alpha$ and $P_L(\alpha) = 1 - \alpha$.

While the normal approximation allows an estimation of the number of lost particles via a simple analytic formula, it is not valid for $P$ close to 0 or 1, where the estimated uncertainty goes to 0. In the calculations discussed below, we therefore use a different method to find the uncertainty $\Delta P$: the Clopper-Pearson confidence interval (Clopper and Pearson, 1934). This confidence interval is considered conservative, i.e., it tends to overestimate the uncertainty, but it performs significantly better for $\alpha$ close to 0 or 1 than the normal approximation (Brown et al., 2001).

We now compare the number of lost particles in IFM with various $N$ and in a classical transmission measurement. For the comparison, we choose a desired uncertainty $\Delta\alpha$. We convert this to a probability uncertainty $\Delta P$. For any $\alpha$, we then invert the Clopper-Pearson method (with a coverage of 95 %) numerically to find the minimum number of trials $M$ needed to get a confidence interval smaller than $\Delta P$. Finally, we multiply $M$ with $P_L$ to obtain the number of lost particles.

Results for an uncertainty $\Delta\alpha = 0.01$ are shown in Fig. 21. Note that the relative behavior of the curves does not significantly depend on the value of $\Delta\alpha$, while the absolute number of lost particles increases quadratically with $\Delta\alpha^{-1}$.

The results show, first of all, that using the number of particles in the sample state as signal always results in more damage than a classical transmission measurement. This is because the signal slope is very small for small transparencies, while classical measurements have a lower damage probability at high transparencies.

Using the reference state as signal gives a more interesting result: while more particles are lost for low $N$, the number of lost particles is almost exactly the same as for a classical measurement for all $N \gtrsim 50$. This is somewhat unexpected as the signal curves are significantly different for different $N$ (see Figs. 17 and 18). However, we find that the changes of slope, signal, and loss probability compensate each other, so the overall number of lost particles is the same. This phenomenon is also visible in Fig. 20 (a) and (b) in the last section, where classical and interaction-free measurements also perform very similarly.

Note that it would be possible, in principle, to combine information from the reference and sample signal to achieve lower damage. However, as many more particles are required to gain information from the sample signal than from the reference signal, the final result would be similar to the result using only the reference state shown in Fig. 21 (a). Another possibility is using the number of lost particles as signal if it can be measured. Like the reference and sample signals, however, using the loss as signal also does not lead to lower loss than a classical measurement.
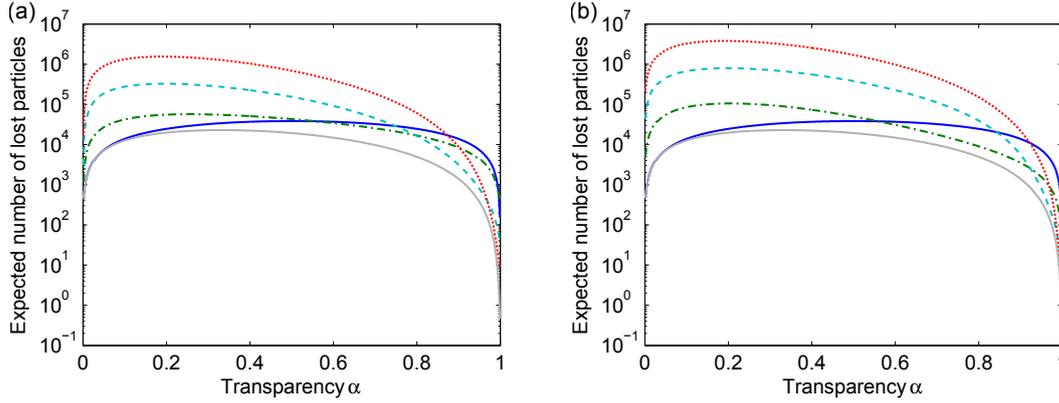
Figure 22: Expected number of lost particles in a measurement of $\alpha$ with uncertainty $\Delta\alpha \leq 0.01$ as a function of transparency using the reference state (a) or the sample state (b) as signal and using Poissonian statistics. The curves shown here are for a classical measurement (blue line), and IFM with $N = 10$ (dash-dotted green line), $N = 100$ (dashed cyan line), and $N = 500$ (dotted red line). For comparison to binomial statistics, the result of a binomial classical measurement is shown as a light gray line (same as the blue solid line in Fig. 21). The binomial measurement outperforms all Poissonian measurements in terms of lost particles.

We conclude that IFM does not offer a benefit over classical measurements for determining an unknown transparency precisely.

## 3.6  Poissonian statistics

So far, we assumed that the particles in the IFM process can be sent in one after another and the total number of particles is known. This led to a detection process governed by binomial or multinomial statistics. Most sources of particles that may be used for imaging or IFM, however, do not produce such number states of particles. Instead, only the average number of particles $\overline{M}$ in any given amount of time is typically known, while the actual number $M$ follows Poissonian statistics. We will now discuss how this affects both classical and IFM measurements of semitransparency.

If we consider a classical measurement with a Poissonian source of particles, we need to distinguish two cases: whether the number of lost particles can be detected or whether it is unknown. For example, lost electrons in electron microscopy are usually scattered by the sample, so the number of lost particles can be measured, while lost photons in light microscopy are often absorbed, so the number of lost particles is unknown. Both the number of detected and the number of lost particles obey a Poisson distribution with average number $\alpha\overline{M}$ and $(1 - \alpha)\overline{M}$, respectively. Similarly, the numbers of detected and lost particles in an IFM scheme also follow Poissonian statistics with average numbers $P_R\overline{M}$, $P_S\overline{M}$, and $P_L\overline{M}$. If lost particles can be measured and the information from all measurements is combined, the error and number of lost particles in Poissonian and

binomial statistics are approximately identical. This is because the number of all particles is counted in this case.

Significant differences only occur if the number of lost particles is not accessible. In this case, the normal approximation of the Poisson distribution yields the expected number of lost particles, similar to the previous section:

$$n_{\text{loss}} \approx P_L(\alpha)P(\alpha) \left( \frac{3.92}{\Delta\alpha P'(\alpha)} \right)^2 . \tag{29}$$

The only difference to the binomial case given in Eq. 28 is the dependence on $P(\alpha)$ here vs. $P(\alpha)(1 - P(\alpha))$ there. This shows that the Poisson distribution behaves similarly to the binomial distribution for small signals $P(\alpha)$ but loses more particles for large signals. As we will see below, this feature of the Poisson distribution leads to a large amount of loss for classical measurements of high transparencies, which allows IFMs to outperform classical measurements there.

We now compare the expected number of lost particles in classical measurements and IFMs for different transparencies. We do not use the normal approximation in the calculation because it is invalid for $P(\alpha)$ close to 0. Instead, we use the $\chi^2$ method to obtain the confidence intervals. Apart from this, the calculation is identical to the Clopper-Pearson calculation in the previous section. The results are shown in Fig. 22, which shows the expected number of lost particles in classical and interaction-free measurements of an unknown transparency $\alpha$. It is the same as Fig. 21 except for Poissonian statistics instead of binomial statistics, assuming that the number of lost particles *cannot* be measured.

First of all, we find that the amount of lost particles using Poissonian statistics is always higher than using binomial statistics. For $\alpha \gtrsim 1/2$, we find that IFMs achieve the same level of uncertainty as classical measurements with fewer lost particles. For very high transparencies $\alpha \gtrsim 0.95$, they can cause over an order of magnitude less loss. For low transparencies $\alpha \lesssim 1/2$ on the other hand, classical measurements show the least amount of loss.

Similar results hold in the comparison of two transparencies. If two transparencies $\alpha_{1,2} \gtrsim 1/2$ are to be distinguished, IFM schemes perform better than classical measurements even if the contrast is not large. For high contrast, the great reduction of loss discussed in section 3.4 also works with Poisson distributions.

We conclude that, in addition to the case of high contrast, interaction-free measurements also outperform classical measurements for a particle source with Poissonian statistics if $\alpha \gtrsim 1/2$ and if the number of lost particles cannot be detected.

## 3.7 Phase shifts

So far, we have discussed semitransparent samples without any phase shift of the probe particle. In this section, we assume a fully transparent sample $\alpha = 1$, which induces a phase shift $\phi$ during every round trip. After $N$ round trips, the particle can be either in the reference state $|R\rangle$ or in the sample state $|S\rangle$.
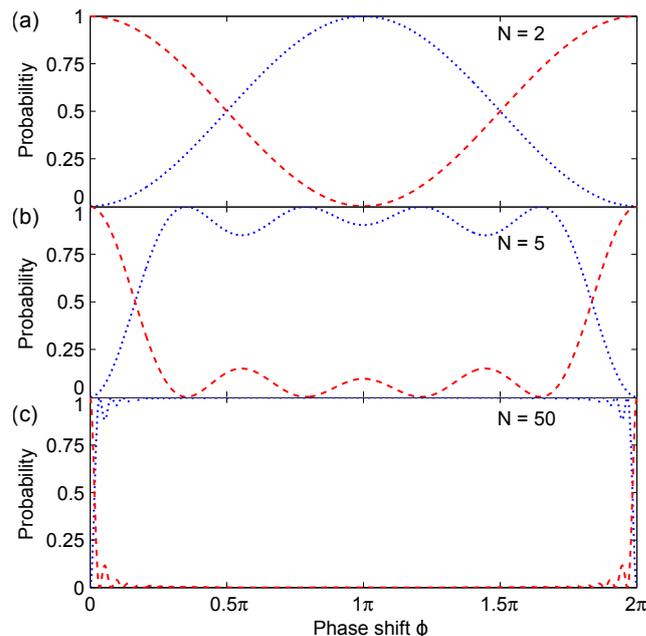
Figure 23: Results for an IFM process of a fully transparent sample as a function of the phase shift $\phi$ induced by the sample for $N = 2$ (a), $N = 5$ (b), and $N = 50$ (c). Shown here are $P_R$ (dotted blue line) and $P_S$ (dashed red line).

Results for the probabilities $P_R$ and $P_S$ at time $T$ for different $N$ are shown in Fig. 23. For $\phi = 0$ or a multiple of $2\pi$, the particle is always found in $|S\rangle$ after $T$. If $N = 2$, we see that the probabilities are simply $P_S = \cos^2(\phi/2)$ and $P_R = \sin^2(\phi/2)$. This configuration is equivalent to a Mach-Zehnder interferometer. If $N$ becomes larger, the probability is transferred from $|S\rangle$ to $|R\rangle$ for smaller phase shifts. For large $N$, almost any phase shift leads to the particle being found in $|R\rangle$ after $T$. A possible application of this behavior may be the detection of small phase shifts.

In an IFM measurement with large $N$, a transparent sample with a phase shift $\phi$ will most likely appear the same as an opaque sample. The phase shift leads to a dephasing of sample state and reference state and thus prevents the coherent transfer of amplitude from $|R\rangle$ to $|S\rangle$. In general, IFM does not allow for the distinction between whether the sample induces a phase shift or whether the sample is opaque. However, if the phase shift is known, it can be compensated with an opposite phase shift. So if two transparencies with a high contrast are to be distinguished and the phase shift induced by the sample with high transparency is known, IFM can still be used by applying an inverse phase shift to the sample state in the IFM setup.

## 3.8 Conclusion

In conclusion, interaction-free measurements outperform classical measurements of transparency in special cases. First, we find that IFMs achieve lower loss than classical

measurements when samples with a high contrast are to be imaged, which is an approximation of the standard "all-or-nothing" IFM and works the same way. Thus, IFMs may significantly reduce the sample damage in imaging of high-contrast samples. Note that the contrast of samples can be artificially enhanced. In transmission electron microscopy for example, staining a sample with metal nanoparticles may be used to achieve a high contrast (Hayat, 2000).

A second regime where interaction-free measurements achieve the same result as classical measurements with fewer lost particles is when the number of particles sent in exhibits a Poisson distribution, the number of lost particles cannot be measured, and the transparency is greater than approximately 1/2. In this case, the advantage of IFMs is not due to an exploitation of the quantum Zeno effect but due to statistical properties of the Poisson distribution.

Finally, we have shown that phase shifts of a sample have to be compensated for in order to measure the transparency of the sample in an IFM. This is because a sample with a non-zero phase shift may appear the same as an opaque sample. Conversely, the sensitivity of IFMs to phase shifts may be exploited to detect small phase shifts in transparent samples.

# Acknowledgments

# 4 Microwave chip-based beam splitter for low-energy guided electrons

**Authors**: Jakob Hammer, Sebastian Thomas, Philipp Weber, Peter Hommelhoff
**Abstract**: We present a novel beam splitter for low-energy electrons using a micro-structured guiding potential created above the surface of a planar microwave chip. Beam splitting arises from smoothly transforming the transverse guiding potential for an electron beam from a single-well harmonic confinement into a double well, thereby generating two separated output beams with 5 mm lateral spacing. Efficient beam splitting is observed for electron kinetic energies up to 3 eV, in excellent agreement with particle tracking simulations. We discuss prospects of this novel beam splitter approach for electron-based quantum matter-wave optics experiments.

## 4.1 Letter

A beam splitter is the quintessential component in many modern physics experiments. The visualization of the quantum mechanical phase hinges on it. Its various realizations have enabled the observation of fundamental physics phenomena such as quantum optics experiments with photons (Mandel and Wolf, 1995), many-body interference experiments with cold atoms in optical lattices (Bloch et al., 2008), neutron interferometry (Rauch and Werner, 2000) and fundamental interference studies with heavy molecules (Juffmann et al., 2012). Prominent among these studies are interference experiments with electrons, which have enabled groundbreaking insight into, for example, the wave-particle duality with massive particles (Davisson and Germer, 1927; Boersch, 1943; Marton et al., 1953; Tonomura et al., 1989) and the Aharanov-Bohm effect (Tonomura et al., 1986).

A plethora of electron interferometry experiments (Hasselbach, 2010) was triggered by the invention of the electrostatic biprism in 1955 (Möllenstedt and Düker, 1955). It is a relatively rugged transverse beam splitting element that also serves as a workhorse in modern commercial electron microscopes employing holographic techniques (Gabor, 1948; Tonomura, 1999). In particular, interference experiments with low-energy electrons have demonstrated reduced radiation damage allowing the nondestructive imaging of biological molecules (Germann et al., 2010).

An entirely new electron optical toolkit arises from the manipulation of slow electrons in free space using a microwave quadrupole guide (Hoffrogge et al., 2011). The generation of the necessary high-frequency electric fields by means of a planar microwave chip

provides ease of scalability and the flexibility to engineer versatile guiding potentials in the near-field of the microwave excitation. This renders surface-electrode structures ideally suited for the implementation of electron beam splitters or resonators with prospects for novel quantum optics experiments with guided electrons. Based on a similar technology, surface-electrode ion traps have been employed to provide finely structured potential landscapes. For example, junctions for trapped ions have been realized (Pearson et al., 2006; Hensinger et al., 2006; Amini et al., 2010; Moehring et al., 2011; Wright et al., 2013; Shu et al., 2014), or double-well potentials with small distances between the potential minima to couple separately trapped ions via the Coulomb force (Brown et al., 2011; Harlander et al., 2011). In this letter we show the concept and the experimental demonstration of a new beam splitter for guided electrons with kinetic energies in the electron-volt range.

Oscillating electric fields allow the generation of a time-averaged restoring force to confine the motion of charged particles in free space (Major et al., 2005). The microwave guide for electrons is based on a two-dimensional, high-frequency quadrupole potential providing transverse confinement, similar to a linear Paul trap (Paul, 1990). The details of this concept are summarized in the Supplemental Material. Stable operation of the guide practically requires oscillation frequencies of the microwave drive in the gigahertz range. The resulting tight transverse confinement is described by a time-averaged, harmonic pseudopotential. Moreover, electrons can be confined in the saddle point of any inhomogeneous high frequency electric potential $\phi(\vec{r}, t) = \phi_{RF}(\vec{r}) \cos(\Omega t)$ with drive frequency $\Omega$ if the potential gradient is nearly constant over the range of the electron's oscillation (Major et al., 2005). We generate such an electric potential by means of a planar microwave chip. As a key feature, this chip-based technology provides the unique possibility to achieve high field gradients in the near-field of a microstructured electrode design allowing for precise control over the motion of the guided electrons.

For the on-chip splitting of the guided electron beam we incorporate a junction in the guiding potential by gradually transforming the driving electric field from a quadrupole to a hexapole symmetry along the chip. Using hexapole electric fields a junction can be realized in the pseudopotential (Wesenberg, 2009). Figure 24 (a) illustrates electric field line plots in the transverse *xz*-plane at three locations along the planar electrode structure. Additionally an isopotential surface of the guiding potential at 0.25 meV is shown, with microwave drive parameters as given below. The electric field line plots and the isopotential surface plot have been obtained by simulating the electric field that is created by the surface electrodes, the design of which is shown in Fig. 24 (b) (Hommelhoff and Hammer, 2014). The microwave signal is applied to the red electrodes, whereas the ground plane is indicated in blue. At a position of $y = 12$ mm along the chip, the electric field in the transverse plane is governed by a strong quadrupole component leading to the creation of a saddle point guiding electrons in the center, as indicated by the red cross. By changing the width of the tapered signal electrode in the center, the electric field above the guiding chip can be transformed along the $y$-direction from a quadrupole to a hexapole symmetry. The hexapole field component gives rise to an additional saddle point that continuously approaches the guiding potential minimum from the chip surface. This is indicated in the field line plot at $y = 15$ mm, where two saddle points
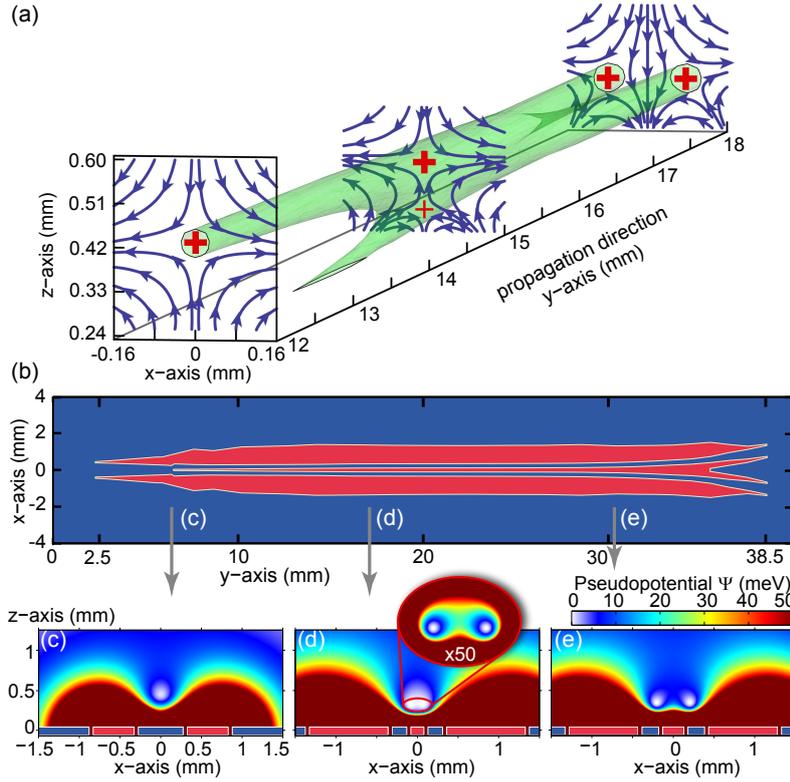
Figure 24: Electrode design of the planar beam splitter chip and pseudopotential simulations. (a) Electric field line plots together with an isopotential surface of the guiding potential at 0.25 meV. (b) Numerically optimized chip electrodes with microwave signal applied to the red electrodes. The remaining blue area is grounded. By means of the tapered central electrode the transition from a quadrupole to a hexapole electric field symmetry is achieved, as shown in (a). (c) Cut through the electrode plane at $y = 6.5$ mm showing the simulated pseudopotential in the transverse plane. The pseudopotential minimum forms at a height of 450 μm above the substrate providing harmonic confinement. (d) At $y = 17$ mm the additional central electrode, with a width of 160 μm, results in the formation of a double-well pseudopotential with a separation of 150 μm between the minima. A fourfold magnified zoom-in is shown in the inset with a 50 times amplified color code. By increasing the width of the center electrode the separation of the double-well minima is gradually increased. (e) At $y = 30$ mm the central electrode is 260 μm wide, leading to a separation of the minima of 400 μm.

form on the vertical $z$-axis. Further along the chip, for increasing $y$, both saddle points merge in the $xz$-plane and subsequently separate in the transverse $x$-direction.

An electric field with a predominant quadrupole component may be generated by five electrodes on a planar chip substrate (Wesenberg, 2008). Figure 24 (c) shows a cut through the electrode structure at $y = 6.5$ mm together with a simulation of the pseudopotential in the $xz$-plane. As a result of the strong quadrupole component, a single guiding potential minimum forms at a height of 450 μm above the chip surface. The simulation is performed with a microwave drive frequency $\Omega = 2\pi \cdot 990$ MHz and a voltage amplitude $V_0 = 16$ V on the signal electrodes. Figure 24 (d) shows a cut through the electrode plane further along the chip at $y = 17$ mm. Here it comprises seven

electrodes with a microwave signal electrode in the center. This leads to the creation of a strong hexapole field component giving rise to a double well in the pseudopotential. By adjusting the width of the central electrode, the separation of the double-well minima can be controlled. The distance between them is 150 µm in Fig. 24 (d) and 400 µm in Fig. 24 (e), which shows the simulated pseudopotential at $y = 30$ mm. The barrier height between the wells is 0.5 meV at $y = 17$ mm and 11.5 meV at $y = 30$ mm.

We have numerically optimized the electrode layout of the microwave chip using the *Surface Pattern* package (Schmied et al., 2009; Schmied, 2010; SurfacePattern, 2015). The hexapole symmetry of the electric field close to the intersection point results in a junction with two incoming and two outgoing channels. By means of a systematic variation of the shape of the chip electrodes, we have reduced distortions in the beam splitter potential that arise from the additional incoming channel and minimized its impact on the trajectories of guided electrons. Details are given in the Supplemental Material.

The microwave signal is delivered to the signal electrodes [drawn in red in Fig. 24 (a)] by a coplanar waveguide structure on the backside of the chip (not shown), which is interconnected to the top side by laser-machined, plated through-holes (see the Supplemental Material for details). The experiments are performed with $\Omega = 2\pi \cdot 990$ MHz and an on-chip microwave power of 4.3 W, which results in $V_0 \approx 16$ V[†].

A home-built thermionic electron gun (Erdman and Zipf, 1982) provides an electron beam with kinetic energies down to 1 eV and beam currents on the order of several ten femtoamperes. As a result of this low electron current electron-electron interaction effects are irrelevant. The beam is collimated using two apertures resulting in a full opening angle of 14 mrad and a spot diameter of about 100 µm at the guide entrance. Behind the microwave chip electrons are detected on a microchannel plate (MCP) electron detector[‡] after traveling 10 mm in free space. Images of the phosphor screen behind the MCP are recorded by a CCD camera[§].

Fig. 25 (a) shows the detector signal recorded for an electron kinetic energy of 1.5 eV and the microwave parameters given above. We observe an electron signal with two symmetrically split up components. The distance between the two main spots is 5 mm, whereas each spot has an average full-width at half-maximum diameter of 0.75 mm. Additionally a faint signal of lost electrons is detected between the two guided components. The guided electrons comprise 80% of the detected signal. Clearly, the injected electron beam is split into two collimated output beams.

In order to fully understand the observed features we perform classical particle tracking simulations. We release electron trajectories from a disk with a diameter of 100 µm and propagate them numerically in the simulated electric field of the beam splitter chip. Fig. 25 (b) shows the resulting simulated electron signal, which is in excellent agreement with the experimentally observed output signal. The color scale illustrates the initial lateral displacement of the electrons along the $x$-axis. Evidently, electrons released

---

[†]   The on-chip driving wavelength $\lambda = 200$ mm is much larger than the longitudinal structure length $L = 38$ mm, allowing us to work in a standing-wave configuration.

[‡]   Photonis, model: APD 2 PS 40/12/10/12 46:1 P20

[§]   The Imaging Source, model: DMK 41AU02
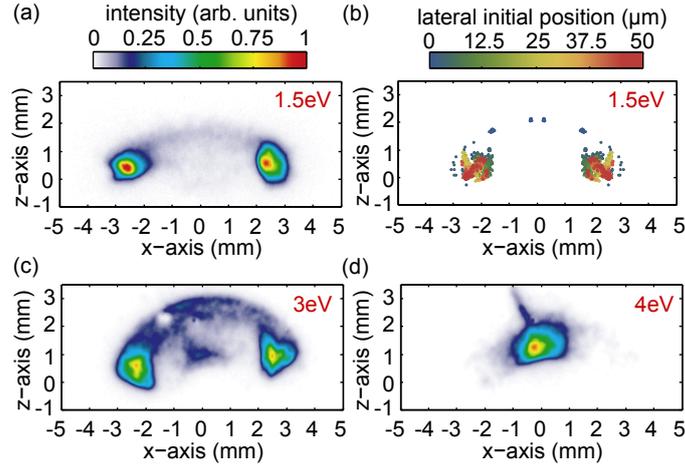
Figure 25: Experimental (a) and simulated (b) detector signal of the split electron beam with $E_{\text{kin}} = 1.5\,\text{eV}$. (a) Clearly two guided beams are visible containing 80% of all detected electrons. A faint signal of lost electrons is detected between the guided electron spots (between $x = -1.5\,\text{mm}$ and $1.5\,\text{mm}$). The color scale depicts the intensity of the raw CCD image. (b) Simulated beam splitter signal based on trajectory simulations. All signatures including the position and size of the output beams and the electron loss are reproduced by the simulation. The color scale corresponds to the initial lateral displacement of the electron trajectories along $x$. See text for details. The dependence of the detected electron signal on the kinetic energy is shown for 3 eV (c) and 4 eV (d). For 4 eV the beam splitting potential is too weak to split up the beam.

closest to the symmetry axis of the beam splitter potential [blue dots in Fig. 25 (b)] are preferentially lost. This can be understood by considering the extreme case of an electron being released at $x = 0\,\text{mm}$. Because of the planar symmetry of the beam splitter potential in the $x$-direction, such a classical trajectory does not encounter any transverse potential gradient and therefore no deflecting force along $x$. As a result, this trajectory cannot follow the pseudopotential minimum paths of the separating double well and is only deflected vertically away from the substrate. For this reason, electrons that propagate closest to the symmetry axis may preferentially become lost from the beam splitter potential. Using quantum mechanical simulations we show in the Supplemental Material that *lossless*, adiabatic splitting of an electron beam can be achieved by means of an optimized beam splitter potential.

Further, we have varied the electron kinetic energy from 1.5 eV to 3 eV. We find that the signal of lost electrons becomes larger with energy as depicted in Fig. 25 (c) as compared to Fig. 25 (a). This is because with increasing forward momentum of the electrons the transverse gradient of the beam splitter potential becomes insufficient to significantly deflect the electrons in the lateral $x$-direction. Accordingly, the electron trajectories cannot follow the separating paths of the potential minimum and are lost from the potential. As a consequence, for energies above 4 eV we observe no splitting anymore and all electrons are detected around $x = 0\,\text{mm}$ in Fig. 25 (d).

The beam diameter of $100\,\mu\text{m}$, attained with the thermionic electron gun, is not matched to the diameter of the quantum mechanical ground state wavefunction (on the order of $100\,\text{nm}$) of the transverse beam splitter potential. As a result, we estimate

that the guided electrons fill up the potential up to energies of 0.75 meV in the current experiment, which is orders of magnitude larger than the quantum ground state energy on the order of 0.1 μeV. Therefore, the experiment is well described by classical particle tracking simulations. However, the direct injection of electrons into low-lying motional quantum states should be possible by matching the incoming electron beam to the ground state wavefunction of the transverse guiding potential (Hammer et al., 2014).

Ultimately, the wave-optical propagation of a guided electron is governed by discretized motional quantum states of the transverse guiding potential. In the following, we illustrate the properties of the microwave beam splitter quantum mechanically and discuss prospects for electron-based quantum optics experiments.

It is instructive to compare the microwave beam splitter for electrons to a typical *amplitude* beam splitter as used in light optics. As detailed above, the beam splitter potential based on a hexapole intersection features two incoming and two outgoing channels. For simplicity we consider a planar symmetry of the beam splitter potential around the intersection point along $y$, as indicated in Fig. 26 (a). We label an incoming electron that occupies the motional ground state of the left (right) arm of the beam splitter with the state $|L\rangle$ ($|R\rangle$). To understand the evolution of these localized input states one needs to consider the transverse energy eigenstates $|1\rangle$ and $|2\rangle$ at different points along the length of the beam splitter [see the insets of Fig. 26 (a)]. While the paths are spatially well separated by a potential barrier these are the symmetric and antisymmetric ground states of a double-well potential, and their energy is (almost) degenerate. The localized input states are a superposition $|L\rangle = (|1\rangle + |2\rangle)/\sqrt{2}$ and $|R\rangle = (|1\rangle - |2\rangle)/\sqrt{2}$ of these eigenstates.

As $|L\rangle$ and $|R\rangle$ are not energy eigenstates, electrons will in principle tunnel between these two states. However, as long as the potential barrier is much larger than the transverse energy of these states, both wells are separated and the tunneling frequency is negligibly low. From a quantum mechanical point of view, the function of the beam splitter is to increase this frequency by bringing the two wells closer together and eventually merging them. In the center part of the splitter, the superposition states $|L\rangle$ and $|R\rangle$ are then no longer spatially separated and, hence, wave amplitude is transferred
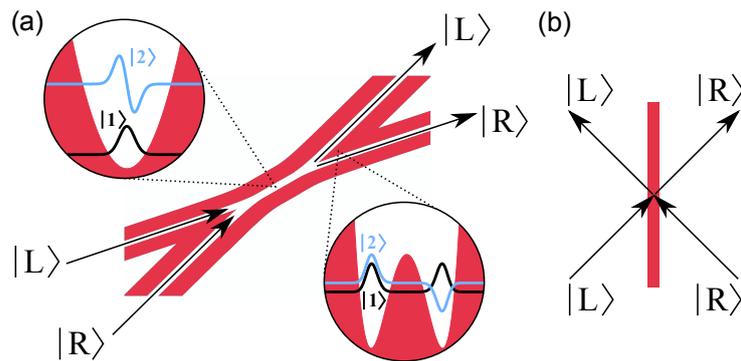


Figure 26: Sketch of an adiabatic microwave beam splitter (a) in comparison to a typical amplitude beam splitter as used in light optics (b).

between $|L\rangle$ and $|R\rangle$. In general an incoming state with amplitudes $l$ in the left and $r$ in the right path is turned to an outgoing state with amplitudes $l'$ and $r'$. If we describe the left path by the state $|L\rangle = \left(\begin{smallmatrix} 1 \\ 0 \end{smallmatrix}\right)$ and the right path by the state $|R\rangle = \left(\begin{smallmatrix} 0 \\ 1 \end{smallmatrix}\right)$, the effect of the beam splitter $B$ can be described as a multiplication of the state with a unitary matrix: $\left(\begin{smallmatrix} l' \\ r' \end{smallmatrix}\right) = B\left(\begin{smallmatrix} l \\ r \end{smallmatrix}\right)$. If we disregard phase shifts, $B$ is essentially a rotation matrix whose angle depends on the oscillation frequency $\omega$ between $|L\rangle$ and $|R\rangle$ and the time the electron spends in the center part of the splitter.

The previous discussion assumes that the electron initially occupies the motional ground state of the transverse guiding potential. As described above, this can be achieved using a diffraction-limited electron gun in order to match the injected electron beam to the ground state wavefunction of the guiding potential. Interestingly, a multi-mode interferometer using higher vibrational states has been investigated in the context of guided atom interferometry (Andersson et al., 2002). Furthermore, the above description requires that an electron initially prepared in the quantum ground state maintains its state while propagating along the beam splitter. The current design lacks this crucial feature of adiabaticity. Using quantum mechanical simulations we have investigated the key prerequisites to achieve adiabatic splitting of the ground state mode. The details of the simulations are described in the Supplemental Material. The amount of transverse vibrational excitations depends critically on the geometric opening angle between the beam splitter paths as well as the energy separation of the transverse eigenstates. As one would expect, a smooth splitting process and, hence, a small opening angle is beneficial. By scaling the guiding potential transversely, we find that the half opening angle of the current design has to be reduced from 40 mrad to 0.1 mrad. In addition, we have to increase the microwave drive frequency to $\Omega = 2\pi \cdot 8\,\text{GHz}$ to obtain beam splitting with 90% of the population remaining in the ground state mode after the splitting. The eightfold higher $\Omega$ effectively increases the curvature of the transverse potential and results in an $\sqrt{8}$-fold larger energy level separation of the single-well potential of $\Delta E \sim 0.24\,\mu\text{eV}$ and, hence, an oscillation frequency $\omega = \Delta E/\hbar \sim 2\pi \cdot 58\,\text{MHz}$. Both, the small beam splitter angle and the higher $\Omega$ require a re-design of the current microwave chip.

As just introduced, beam splitters used in quantum optics experiments [like in Fig. 26 (b)] are usually described by unitary matrices, which reflect the coupling between the amplitudes of two states (Zeilinger, 1981; Schleich, 2005). The microwave beam splitter demonstrated here is a promising new technology because it may become such an *amplitude* beam splitter for electrons. Most current experiments on electron interference rely on the electrostatic biprism, which is a *wavefront* beam splitter. The wavefront beam splitter can be regarded as an electron optical device that generates two virtual sources by a spatial division of the beam. In that case, interference between both output beams relies on the spatial coherence of the electron source (Born and Wolf, 1999). In contrast, using an amplitude splitter the phase between both output beams and their amplitudes are fully determined by the physical properties of the beam splitter device. To this end, the manipulation of electrons using the microwave beam splitter augments the already available, rich electron optical toolkit and may herald new quantum optics

experiments with free electrons. In particular, a novel quantum electron microscopy concept is emerging that employs multiple *amplitude* splittings of a quantum particle's wavefunction for the noninvasive imaging of biological samples (Putnam and Yanik, 2009; Thomas et al., 2014).

# Acknowledgments

## 4.2 Supplemental material

### 4.2.1 Microwave quadrupole guide for electrons

For the guiding of electrons above the surface of a microwave chip we use a two-dimensional, high-frequency electric quadrupole potential $\phi(\vec{r}, t) = \phi_{RF}(\vec{r}) \cos(\Omega t)$, which provides a transverse harmonic pseudopotential to confine electrons along the guide's axis. In order to achieve stable confinement of electrons in the microwave guide, the frequency and the amplitude of the time-dependent electric quadrupole potential have to be matched to the electron's charge-to-mass ratio $Q/M$ and the spatial dimensions of the electrode structure generating the potential. The requirements on the microwave drive parameters can be obtained from the expression of a dimensionless stability parameter $q = \eta(Q/M)(2V_0)/(\Omega^2 R_0^2)$, where stable confinement of an electron requires $0 < q < 0.9$ (Major et al., 2005). Here $V_0$ is the voltage amplitude applied to the electrodes and $R_0$ the height of the saddle point of the quadrupole potential above the chip surface, i.e. the position of the guide's center. Because of the high charge-to-mass ratio of electrons, the stable confinement in the quadrupole guide usually requires drive frequencies in the gigahertz range. Effectively, for small $q$, a time-averaged pseudopotential is generated by the oscillating electric potential, which is defined by $\Psi = Q^2/(4M\Omega^2) |\nabla\phi_{RF}(\vec{r})|^2$. The dynamics of an electron within the pseudopotential are then governed by an oscillatory macromotion with a frequency $\omega = (q/\sqrt{8}) \Omega$ and a potential depth $U = (\eta/u)(q/8)V_0$. The constants $\eta$ and $u$ depend on the geometry of the planar electrode design (Wesenberg, 2008).

### 4.2.2 Numerical optimization of the electrode layout

We have used the *Surface Pattern* package (Schmied et al., 2009; Schmied, 2010; SurfacePattern, 2015) to numerically optimize the shape of the chip electrodes. This package is implemented in Mathematica and is capable of analytically solving the Laplace equation of an arbitrary two-dimensional electrode structure in the gapless plane approximation. The optimization routine uses a Nelder-Mead simplex algorithm, which is a built-in function in Mathematica, to minimize a scalar merit function $M$ by systematic variation of the position of a predetermined number of points, which parametrize the shape of the
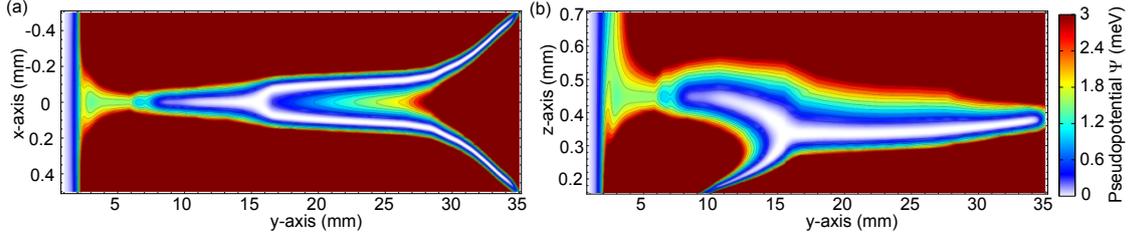
Figure 27: Simulated pseudopotential $\Psi$ of the optimized beam splitter design. (a), Color plot of $\Psi$ in the $xy$-plane (birdseye-view on the chip surface). As the height of the pseudopotential minimum $z_{min}$ varies along the chip electrodes this plot is obtained by calculating $z_{min}$ for every point along $y$ and then plotting $\Psi(x, y, z_{min}(y))$. (b) Color plot of $\Psi$ in the vertical $zy$-plane. Here $x_{min}(y)$ is inserted for every position along $y$. The drive parameters are $\Omega = 2\pi \cdot 1\,\text{GHz}$ and $V_0 = 16\,V$.

chip electrodes. For the electrode optimization we have chosen $M$ to minimize vertical pseudopotential gradients $\partial\Psi/\partial z$ while maintaining a constant trap frequency $\omega_z$ in the vertical direction along the beam splitter path. A planar symmetry with respect to the $x = 0$ plane is requested.

Fig. 1(a) shows the numerically optimized electrode design of the planar microwave chip. We can calculate the electric field created by this electrode structure and, hence, the pseudopotential $\Psi$ (according to the expression given above). The microwave drive parameters in the simulation are $\Omega = 2\pi \cdot 1\,\text{GHz}$ and $V_0 = 16\,V$. In Fig. 27 (a) the pseudopotential is plotted in the $xy$-plane. As the height of the pseudopotential minimum $z_{min}$ varies along the chip electrodes, this plot is obtained by calculating $z_{min}$ for every point along $y$ and then plotting $\Psi(x, y, z_{min}(y))$. Similarly, the pseudopotential in the $zy$-plane is plotted in Fig. 27 (b) by calculating $x_{min}(y)$ and plotting $\Psi(x_{min}(y), y, z)$. Because of fringing electric fields close to the substrate edge, the potential minimum is about 1.5 meV on the first 7 mm along the chip electrodes until quadrupole fields are fully developed leading to a field null along the guide (Hammer et al., 2014). Further along the chip, a junction is generated in the beam splitter potential at about $y = 16$ mm. Here, an additional potential minimum path converges towards the beam splitter path from the substrate surface, as can be seen in Fig. 27 (b).

### 4.2.3 Trajectory simulations

We perform classical particle tracking simulations taking into account the oscillating electric field of the optimized beam splitter chip. We use the Surface Pattern package to calculate the electric field above the planar electrode structure in the gapless plane approximation. The classical particle trajectories are then obtained by numerically integrating the equation of motion for an electron in the oscillating electric field using Mathematica's built-in NDSolve function. The simulations gather 1000 particle trajectories in total that are released at the substrate edge $y = 0$ mm. More specifically, 100 rays are homogeneously distributed on a disk with a diameter of 100 μm and trajectories are released at ten different instants in time with respect to the phase of the microwave
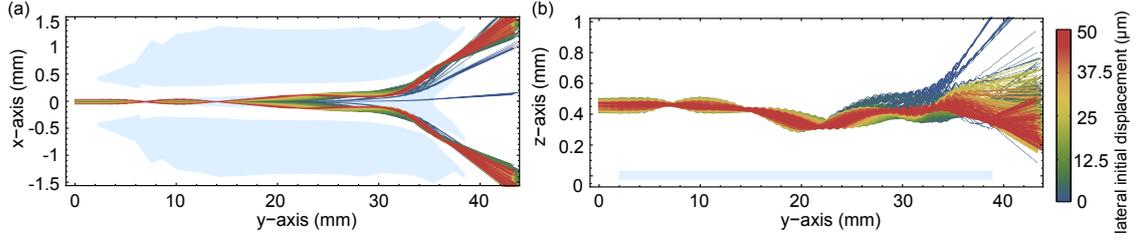
Figure 28: Particle tracking simulations with $E_{kin} = 1.5\,\text{eV}$. (a) Simulated electron trajectories in the $xy$-plane. The electrons perform a secular oscillation on the first 16 mm along the guide. At the beam splitter junction the beam becomes symmetrically divided and two split-up, guided beams are obtained. (b), Electron trajectories in the vertical $zy$-plane. Only trajectories that are released closest to the symmetry axis (blue lines) become lost in the vertical $z$-direction. The trajectories are simulated with $\Omega = 2\pi \cdot 1\,\text{GHz}$ and $V_0 = 16\,\text{V}$.

electric field. This allows us to study if the beam splitting depends on the phase of the microwave drive.

We simulate electron trajectories with microwave drive parameters of $\Omega = 2\pi \cdot 1\,\text{GHz}$ and $V_0 = 16\,\text{V}$. Fig. 28 (a) shows a top view on the simulated electron trajectories in the $xy$-plane. Clearly, the electrons perform oscillations after injection into the guiding potential with a spatial period of 14 mm corresponding to a trap frequency of $\omega = 2\pi \cdot 50\,\text{MHz}$ at an electron kinetic energy of 1.5 eV. In the splitting region from $y = 20\,\text{mm}$ to $y = 30\,\text{mm}$ the beam becomes symmetrically divided in the lateral $x$-direction. The color scale illustrates the initial lateral displacement of the electrons along the $x$-axis. The chip electrodes are indicated in light blue. In Fig. 28 (b) the same trajectories are plotted in the vertical $zy$-plane. As can be seen, the electrons follow the beam splitter path $\gamma(r)$ that bends down towards the substrate when approaching the beam splitter junction at $x \sim 16\,\text{mm}$. Electrons released closest to the symmetry axis of the beam splitter potential [blue lines in Fig. 28 (b)] are preferentially lost from the beam splitter potential in the vertical $z$-direction. This is described in detail in the main text. The simulated beam splitter output signal shown in Fig. 2(b) is obtained from the same trajectory simulations.

To investigate the classical dynamics of guided electrons within the beam splitter potential we study the dependence of the beam splitting process on the initial position of the electron source by comparing particle tracking simulations with experimental measurements. We simulate electron trajectories for a centered and a displaced electron source to study the dependence of the beam splitting signal on misalignment of the electron source. Fig. 29 (a) shows the result of the particle tracking simulations for three different locations of the electron source along the $x$-direction. The simulation as well as the corresponding measurements are performed with $E_{kin} = 1\,\text{eV}$, $\Omega = 2\pi \cdot 1\,\text{GHz}$ and $V_0 = 16\,\text{V}$. For a centered electron beam the trajectories (drawn in red) become symmetrically separated in the region from $y = 20\,\text{mm}$ to 25 mm. Electrons that are released at a positive (negative) $x$-position end up in the output beam at positive (negative) $x$-values. In contrast, for an electron source displaced about 125 µm along the positive or negative $x$-direction all trajectories of the beam (drawn in green and blue) end up in the same output port at negative or positive $x$-values, respectively. The initial lateral displacement
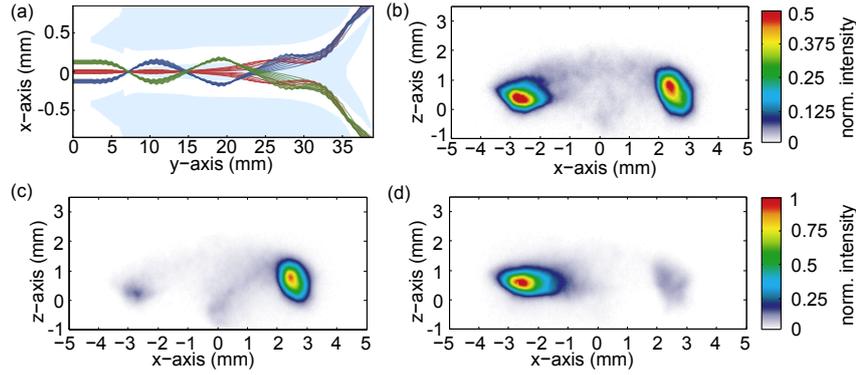
Figure 29: Dependence of beam splitting on the initial position of the electron source with $E_{kin} = 1\,\text{eV}$. (a) Simulated electron trajectories in the $xy$-plane for three different positions of the electron source along the $x$-axis. The underlying signal electrodes are indicated in light blue. (b) For a centered electron gun a symmetric beam splitting signal is measured. The measured beam splitting signals for a displaced electron gun are shown for a negative (c) and a positive (d) displacement along $x$. For a displaced electron gun [(b) and (c)] the measured count rate in one single output beam is twice the count rate in each output beam for a centered electron gun (d).

of the trajectories sets the potential energy of the transverse electron oscillation. For the initially displaced beam the potential energy of the electron oscillation is larger and electrons may cross the potential barrier in the splitting region once more compared to the centered beam.

The same behavior is found experimentally when the electron source is displaced in the $x$-direction. In Fig. 29 (c) the electron source is displaced in the negative $x$-direction, which results in the detection of a single guided spot at positive $x$. By displacing the source in the positive $x$-direction the signal in Fig. 29 (d) is obtained. When the electron gun is centered we obtain a symmetric splitting, as shown in Fig. 29 (b). It is thus possible to modify the ratio of the electron count rate in both output beams by simply displacing the electron source. Furthermore, we find experimentally that the displacement of the electron source does not increase the signal of lost electrons. Consequently, the measured count rate in one single output beam for the displaced source corresponds to the integrated count rate of both output beams for a centered electron gun. This is reflected in the different color scale for Fig. 29 (b) compared to Figs. 29 (c),(d). For the centered beam in Fig. 29 (b) the color scale used spans half the intensity of the color scale used for the displaced beam in Fig. 29 (c) and (d). If we move the electron source even further away along the $x$-direction electron losses start to increase until no beam splitter signal is observed anymore.

## 4.2.4 Microwave design of the beam splitter chip

The electron beam splitter is implemented on a planar microwave chip design that was manufactured by a commercial supplier[†]. The substrate consists of a 0.76 mm thick microwave compatible Rogers RO4350B laminate coated with a 20 µm layer of gold-

---

[†]    Optiprint AG, Auerstrasse 37, CH-9442 Berneck, Switzerland, http://www.optiprint.ch
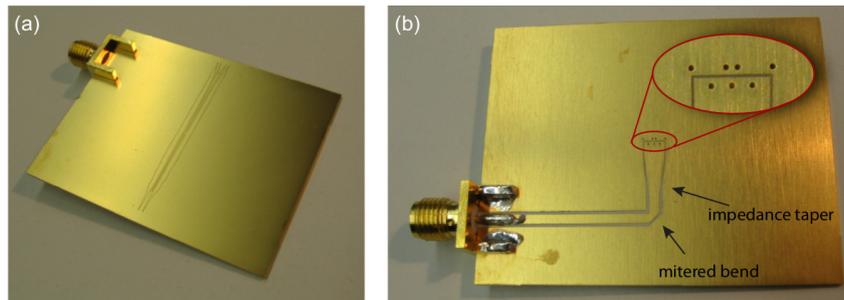
Figure 30: Electron beam splitter microwave substrate. (a), Top side of the microwave substrate comprising the numerically optimized beam splitter electrodes. (b) Back side of the chip showing the microwave feeding line with the mitered bend and impedance taper for improved frequency response. The inset shows a zoom on the plated through holes with a diameter of 200 μm on the backside. They transmit the signal from the feeding line to the beam splitter electrodes.

plated copper. The electrodes are defined by chemical etching of 50 μm wide gaps along the electrode contours into the metal layer. The microwave signal is delivered to the signal electrodes on the top side of the chip [shown in Fig. 30 (a)] by a coplanar waveguide structure on the backside of the chip [shown in Fig. 30 (b)], which is interconnected by laser-machined, plated through-holes with a diameter of 20 μm.

In order to symmetrically feed all electrodes, the feeding coplanar waveguide (cpw) structure on the back side of the chip comprises a 90° mitered bend. By these means the last third of the feeding cpw is aligned parallel to the beam splitter electrodes on the top side and all electrodes are fed symmetrically. Furthermore, a triangular impedance taper was implemented in the cpw layout (Pozar, 2005). This is required as the geometry of the chip electrodes typically results in a characteristic impedance of the electrode structure of $Z_0 = 15\,\Omega$. On the other hand, we use a standard microwave generator with a 50-$\Omega$-matched output as well as 50-$\Omega$ SMA connectors to transmit the microwave signal onto the guiding chip. In order to avoid reflections of the microwave signal at impedance discontinuities, the impedance taper has been implemented in the feeding cpw. Figure 30 (b) shows the implementation of a triangular impedance taper from 50 $\Omega$ down to 25 $\Omega$ (Pozar, 2005). This taper is restricted to a minimal impedance of 25 $\Omega$ because of the limited space on the backside of the chip. A taper down to 15 $\Omega$ would exceed the length of the chip.

### 4.2.5 Optimization of the beam splitter potential

To minimize vibrational excitations from the transverse ground state into higher energetic motional states during the beam splitting process we employ an optimization routine that systematically modifies the shape of the transverse beam splitter potential. The optimization scheme is described in detail by Hänsel et al. (2001a). The simulations take into account the one-dimensional beam splitter potential along the $x$-direction, as this is the dimension where the splitting arises. Furthermore, only the time-averaged pseudopotential is considered.

To find the eigenfunctions of the one-dimensional Schrödinger equation in the trans-
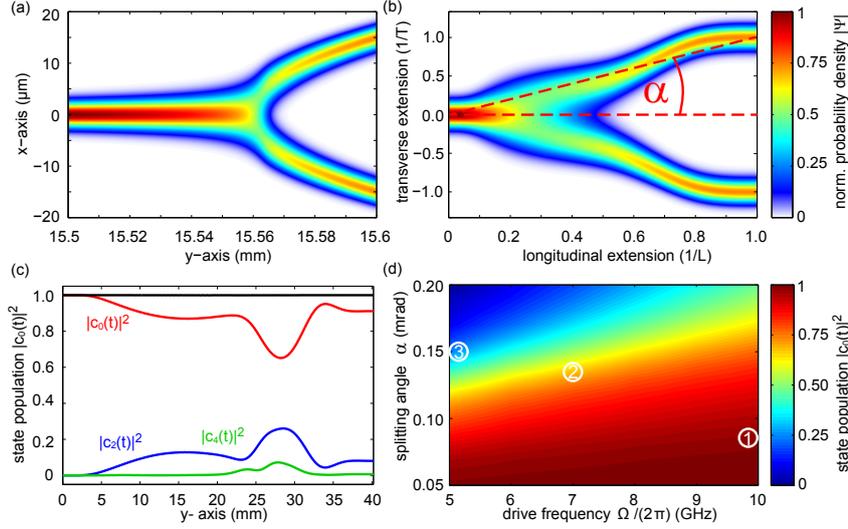
Figure 31: Optimization of the shape of the beam splitter potential. (a) Simulation of the ground state probability density for the beam splitter potential, as experimentally realized in this work, over a length of $100\,\mu m$ where the splitting of the ground state evolves. (b) Ground state probability density for the optimized beam splitter potential, which results from the adiabaticity optimization. (c) Simulated state populations of the three lowest symmetric states for the optimized beam splitter potential. For the optimized potential more than 90% of the population end up in the ground state. Only symmetric states are considered as transitions occur only between states of the same parity. Details on the simulation parameters are given in the text. (d) Simulated ground state population after the splitting process as a function of the drive frequency $\Omega$ and the splitting angle $\alpha$ for $E_{kin} = 1\,eV$, $V_0 = 75\,V$. Circles are discussed in the text.

verse $x$-direction, $\left\{-\frac{\hbar^2}{2m}\frac{\partial^2}{\partial x^2} + V(x)\right\}\psi(x) = E\psi(x)$, we only look for solutions in a region of length $X$ around the center of the guiding potential. $X$ must be significantly larger than the extent of the eigenfunctions of interest. We then expand the Hamiltonian in the basis of standing waves with wavelengths of $2X/n$ up to a finite order $n = 500$. By diagonalizing the resulting matrix using built-in Matlab functions, we obtain a good approximation of the eigenfunctions and eigenenergies of the Hamiltonian for orders $\ll n$. This numerical procedure is described in detail in a paper by Jelic and Marsiglio (2012).

Figure 31 (a) shows the simulated ground state probability density over a length $L = 100\,\mu m$ along the $y$-direction where the splitting of the quantum ground state arises. In the adiabatic limit an electron wave packet, initially prepared in the ground state, continuously adapts its wavefunction to the ground state probability density when propagating along the beam splitter potential. If adiabaticity of the splitting process cannot be assured non-adiabatic propagation of the electron wave packet within the splitting potential manifests itself by conversion of longitudinal momentum into the transverse degree of freedom, thereby exciting the electron wave into a higher energy state of the transverse confining potential.

These transverse vibrational excitations depend critically on the precise shape of the beam splitter potential. To find its optimum shape we follow an optimization

routine that was initially developed to achieve fast and adiabatic splitting of cold atomic clouds in an atom chip magnetic trap (Hänsel et al., 2001b). The optimization routine parametrizes the beam splitter potential along the longitudinal extension, effectively deforming the potential along $y$ by stretching it locally. As a result, a beam splitter potential is obtained that increases the adiabaticity of the wave propagation and reduces vibrational excitations from the ground state into excited states. Fig. 31 (b) shows the simulated quantum ground state probability density for the improved beam splitter potential obtained from the optimization. As expected, a smooth transition into the split-up paths by means of a small splitting angle $\alpha$ is required and obtained from the optimization. Here $\alpha$ is defined as the ratio between the transverse extension $T$, defined as half the separation length at the output, and the length $L$ of the beam splitter.

We study vibrational excitations that arise during the beam splitting process by calculating the state population $|c_i(t)|^2$ for the ten lowest symmetric quantum states by solving the time-dependent Schrödinger equation (see equation (9) in the paper by Hänsel et al. (2001b)). Only symmetric states are considered, as transitions occur only between states of the same parity due to the planar symmetry of the splitting potential. We assume that initially only the ground state is populated. The solid lines in Fig. 31 (c) show the temporal evolution of the state populations (i=0, 2, 4) for $E_{kin}$ = 1 eV along the optimized beam splitter potential. We find that with 90% probability an electron wave packet remains in the ground state after the splitting process, even though during splitting the excited state population may transiently reach values up to 26%. The simulation is performed with $\Omega = 2\pi \cdot 8\,\text{GHz}$[†] (Hoffrogge and Hommelhoff, 2011). This corresponds to an eightfold increased trap frequency $\omega$ with respect to the measurements presented in this paper ($\omega \propto \Omega$ for constant $q$). A constant stability parameter $q = 0.15$ is assured by increasing the voltage amplitude to $V_0 = 75\,\text{V}$ and scaling the beam splitter potential in the transverse dimension by a factor 3.7, which results in a relative reduction of the trap height $R'_0 = R_0/3.7$, which is then on the order of 100 μm. Furthermore, the section of the beam splitter potential that underlies the probability density simulation in Fig. 31 (c) is scaled longitudinally to a length $L$ = 40 mm. The scaling of the beam splitter potential results in a splitting angle $\alpha$ = 0.1 mrad and a smaller beam separation of $\sim$ 8 μm at the end of the beam splitter chip as compared to a separation of 2 mm in the experiments described in the main text. A discussion on the technical realization of these parameters is beyond the scope of this letter.

It is instructive to specify how excitations from the ground state scale with $\Omega$ (and hence $\omega$) and $\alpha$. Figure 31 (d) shows the ground state population probability $|c_0|^2$ after the splitting for varying $\Omega$ and $\alpha$. Clearly, excitations are reduced for small splitting angles $\alpha$ and large $\Omega$. For $\alpha$ = 0.05 mrad and $\Omega = 2\pi \cdot 10\,\text{GHz}$ we find that more than 95% of the ground state population remains in its state during the entire beam splitting process giving rise to a nearly adiabatic trajectory.

---

[†]   Here traveling microwave signals have to be considered, as the on-chip microwave wavelength $\lambda$ becomes smaller than the longitudinal electrode length $L$.

### 4.2.6 Matrix representation of the microwave beam splitter

In order to investigate the quantum dynamics of an electron wave in the microwave beam splitter for electrons and to compare it to a typical 50/50-beam splitter as used in light optics, we have carried out a one-dimensional wave packet simulation in Matlab using the split step method (Fleck et al., 1976; Feit et al., 1982). As described in the main text of the manuscript, we extend the optimized beam splitter potential discussed above to an X-shaped one with two input and two output ports. This could be done by using two splitters in sequence or by placing an electron mirror at the single port of the Y-shaped splitter. In these simulations we numerically solve the time-dependent Schrödinger equation taking into account the optimized beam splitter potential and assuming a free particle with $E_{\text{kin}} = 1\,\text{eV}$ along the $y$-direction.

Figure 32 (a) shows the action of the beam splitter when an electron wave is injected into the ground state of the lower input port, labeled as $|R\rangle$ in the main text. The simulation parameters are $\alpha = 0.08\,\text{mrad}$, $\Omega = 2\pi \cdot 10\,\text{GHz}$ and $V_0 = 75\,\text{V}$. This localized input state corresponds to a superposition $|R\rangle = (|1\rangle - |2\rangle)/\sqrt{2}$ of the energy eigenstates of the beam splitter potential. As a result, the electron wave performs an oscillation in the central region from $y = 30\,\text{mm}$ to $y = 50\,\text{mm}$, where the potential is given by a single well. By tuning the length of the beam splitter in this center part the splitting ratio can be adjusted. Here, the intensity ratio between $|L\rangle$ and $|R\rangle$ in the output of the beam splitter can be 50%. Vibrational excitations into higher energetic states manifest themselves as small distortions of the electron wave in both output arms. In contrast, in Fig. 32 (b), for a balanced input in $|L\rangle$ and $|R\rangle$, interference results in a dark and a bright port at the output of the beam splitter. The small deviation from an ideal dark port, as visible by the almost negligible intensity in $|L\rangle$, results from higher energetic states that become excited during the splitting process. The phase of the wave amplitude in input state $|L\rangle$ is shifted by $\pi/2$ with respect to the wave amplitude in $|R\rangle$ in order to obtain the desired splitting ratio. As described in the main text, the effect of an *amplitude* beam
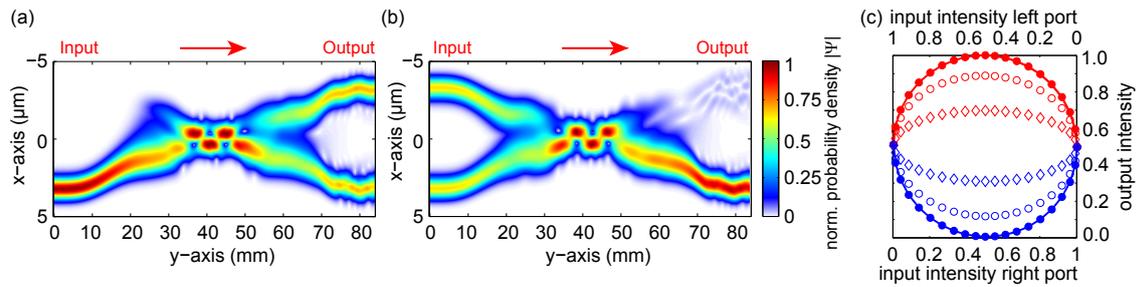


Figure 32: Quantum matter-wave simulations of a 50/50- microwave beam splitter. (a) Injection of the electron wave into the ground state of the input port $|R\rangle$ results in a balanced output with equal intensities in $|R\rangle$ and $|L\rangle$. (b) For a balanced input state interference gives rise to a bright port ($|R\rangle$) and a dark port ($|L\rangle$). (c) Simulated output intensities as a function of the beam splitter input. The red markers correspond to the output intensity $r'^2$ in state $|R\rangle$ and the blue markers to the intensities $l'^2$ in state $|L\rangle$. The marker symbols represent different simulation parameters $\alpha$ and $\Omega$, as described in the text.

splitter can be described as a multiplication of the input states $|L\rangle = \begin{pmatrix} 1 \\ 0 \end{pmatrix}$ and $|R\rangle = \begin{pmatrix} 0 \\ 1 \end{pmatrix}$ with a unitary matrix $\begin{pmatrix} l' \\ r' \end{pmatrix} = B\begin{pmatrix} l \\ r \end{pmatrix}$. Fig. 32 (c) shows the beam splitter output intensities, where blue corresponds to $l'^2$ and red to $r'^2$, as a function of the input intensity ratio. The filled circles correspond to the simulation parameters given above and also used in Fig. 32 (a),(b). Here, vibrational excitations can be almost neglected [see marker ① in Fig. 31 (c)]. The simulated output intensities perfectly match the analytically calculated output intensities, as given by the matrix $B = \begin{pmatrix} \cos(\theta) & -\sin(\theta) \\ \sin(\theta) & \cos(\theta) \end{pmatrix}$ with $\theta = \pi/4$, which fully describes the action of the beam splitter. The solid lines in Fig. 32 (c) correspond to the analytically calculated output intensities obtained from a matrix multiplication with $B$. The open circles in Fig. 32 (c) correspond to different simulation parameters $\alpha = 0.13$ mrad and $\Omega = 2\pi \cdot 7$ GHz. As can be seen, for these simulation parameters the shape of the output intensities turns into an ellipse and not all splitting ratios can be realized any more. This can be explained by vibrational excitations allowing only 72% percent of the population to remain in the ground state [see marker ② in Fig. 31 (c)]. As a result, the excitation of higher energetic states reduces the contrast in the achievable splitting ratios and causes a deviation from the matrix representation described above. This effect becomes even more apparent in the simulation result with $\alpha = 0.15$ mrad and $\Omega = 2\pi \cdot 5$ GHz [see marker ③ in Fig. 31 (c)], which is indicated by the diamonds forming an even more elongated ellipse.

# 5 Generating few-cycle pulses for nanoscale photoemission easily with an erbium-doped fiber laser

**Authors**: Sebastian Thomas, Ronald Holzwarth, Peter Hommelhoff
**Abstract**: We demonstrate a simple setup capable of generating four-cycle pulses at a center wavelength of 1700 nm for nanoscale photoemission. Pulses from an amplified erbium-doped fiber laser are spectrally broadened by propagation through a highly non-linear fiber. Subsequently, we exploit dispersion in two different types of glass to compress the pulses. The pulse length is estimated by measuring an interferometric autocorrelation trace and comparing it to a numerical simulation. We demonstrate highly non-linear photoemission of electrons from a nanometric tungsten tip in a hitherto unexplored pulse parameter range.

## 5.1 Introduction

Femtosecond laser pulses with durations of just a few optical cycles are being used for a large number of applications including pump-probe spectroscopy, non-linear optics, high harmonic generation, and frequency measurements. Accordingly, there is a considerable interest in the generation of few-cycle laser pulses at different wavelengths. In the near-infrared regime, one source of femtosecond laser pulses are erbium-doped fiber lasers, introduced over twenty years ago (Kafka et al., 1989; Tamura et al., 1993). However, they cannot generate few-cycle pulses directly due to the limited gain bandwidth of erbium-doped fibers. Recently, few- and even single-cycle pulses were created based on rather intricate erbium-doped fiber technology by exploiting non-linear effects in custom optical fibers to broaden the pulses' spectrum (Sell et al., 2009; Andrianov et al., 2009; Anashkina et al., 2011) and, in the case of the single-cycle pulse, by an interferometric technique (Krauss et al., 2010).

Theoretical investigations have shown that spectral broadening in a highly non-linear fiber, which can be modeled as the combined effect of dispersion, an instantaneous Kerr response, and a retarded Raman response, leads to a separation of the spectrum into a long- and a short-wavelength part (Sell et al., 2009; Anashkina et al., 2011). Based on this phenomenon, Sell et al. have demonstrated the generation of 8 fs pulses using only the short-wavelength part of the spectrum (Sell et al., 2009), Anashkina et al. have

created 13 fs pulses by compressing a less broad and not completely separated spectrum generated in a short non-linear fiber (Anashkina et al., 2011), and Krauss et al. have succeeded in generating a single-cycle pulse by individually compressing and then recombining both parts of the spectrum (Krauss et al., 2010). All experiments relied on complex setups or optimized, dispersion-shifted fibers.

In this article, we present a similar yet particularly simple scheme to create few-cycle pulses, which uses only the long-wavelength part of spectrally broadened pulses from an erbium-doped fiber laser. Our setup consists entirely of standard commercial components and does not employ a customized non-linear fiber. Using only the long-wavelength part of the spectrum reduces the requirements on experimental components and allows us to compensate the spectral phase by exploiting quadratic dispersion in bulk glass. This enables us to compress the pulses to approximately 23 fs, corresponding to 4.1 optical cycles.

We employ the few-cycle pulses to study photoemission of electrons from sharp metal tips. A nanometric metal tip under laser illumination constitutes a localized electron source with a small emission area that is given by the extent of the enhanced optical near-field induced at the tip apex (Hommelhoff et al., 2006a,b; Ropers et al., 2007). Such experiments have recently reached the strong-field regime (Schenk et al., 2010; Bormann et al., 2010; Krüger et al., 2012a), demonstrating phenomena like electron rescattering (Wachter et al., 2012) and an emission current that depends on the pulses' carrier-envelope phase (Krüger et al., 2011). While most previous experiments in this area have been carried out with Ti:sapphire lasers, going to longer wavelengths changes the dynamics of electron rescattering, modifies the initial emission process via the Keldysh parameter and leads to different material properties of the tip. As a first application of the laser setup, we demonstrate multiphoton photoemission from a tungsten tip triggered by the few-cycle infrared pulses.

Our results demonstrate that photoemission of electrons from sharp metal tips can be investigated with erbium-doped fiber technology. In the future, similar experiments may benefit from passive carrier-envelope phase stability (Krauss et al., 2011; Homann et al., 2012). Spectrally broadened pulses from an erbium-doped fiber laser have previously been used to study second and third harmonic generation as well as plasmon response times at nanoantennas (Hanke et al., 2009, 2012). Very recently, photoemission of electrons from metal tips has been investigated for a wide range of infrared wavelengths using a kilohertz system based on optical parametric amplification and difference frequency generation (Herink et al., 2012).

## 5.2 Experimental setup

An outline of the experimental setup is depicted in Fig. 33 (a). The pulses are generated in a passively mode-locked erbium-doped fiber laser and amplifier (Menlo Systems C-Fiber A). The laser is mode-locked by non-linear polarization evolution. The parameters of the laser system, including the general shape of the spectrum, can be significantly varied by changing the configuration of the wave plates inside the oscillator. Typically, one obtains
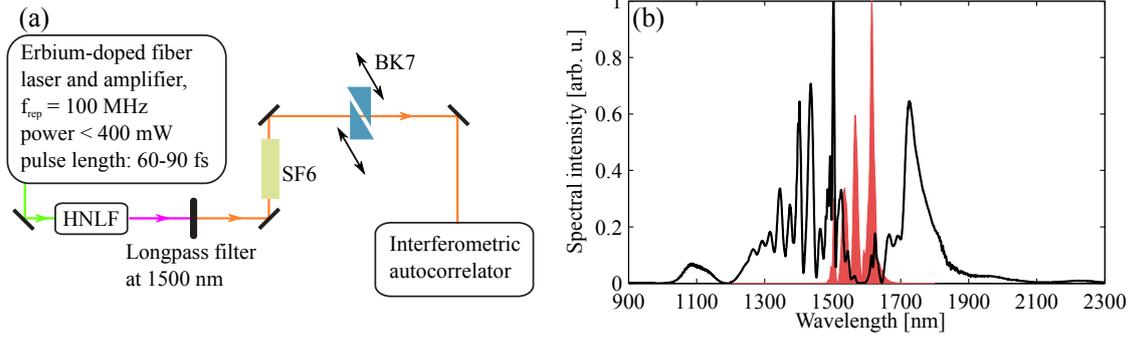
Figure 33: (a) Outline of the experimental setup: pulses are generated in an erbium-doped fiber laser and spectrally broadened in a highly non-linear fiber (HNLF), the short-wavelength part of the spectrum is filtered out, the spectral phase is flattened using dispersion in glass, and the pulse duration is characterized in an autocorrelator. (b) Spectral intensity before (shaded red area) and after spectral broadening (black line) in the HNLF; shown here is a combination of measurements with two spectrum analyzers: Ando AQ6315E and Yokogawa AQ6375.

pulse durations of $\tau = 60$ to $90\,\text{fs}$ (full width at half maximum of the intensity) with an average output power $P$ of up to $400\,\text{mW}$ and a repetition rate of $f_{\text{rep}} = 100\,\text{MHz}$.

The beam is coupled into a highly non-linear fiber (Furukawa Electric OFS HNLF Standard) via an aspheric lens with a focal length of $1.49\,\text{mm}$ (Thorlabs C710TME-C). The fiber is approximately $3.5\,\text{cm}$ long with a typical effective area of $A_{\text{eff}} = 11.7\,\text{μm}^2$, a zero-dispersion wavelength of $\lambda_0 = 1550\,\text{nm}$, and a typical non-linear coefficient of $\gamma = 2\pi n_2/\lambda_0 A_{\text{eff}} = 11.5\,\text{W}^{-1}\text{km}^{-1}$, where $n_2$ is the second-order non-linear refractive index. The results of the spectral broadening due to the propagation through the fiber are shown in Fig. 33 (b). The resulting spectrum may span a range between 1000 and $2300\,\text{nm}$ depending on the parameters of the initial pulses.

After being coupled out of the fiber via another aspheric lens with $11\,\text{mm}$ focal length (ThorLabs A397TM-C), the beam passes an $1500\,\text{nm}$ interferometric longpass filter (Thorlabs FEL1500), which cuts off the short-wavelength part of the spectrum. It should be noted that the short-wavelength part supports pulse durations of less than $10\,\text{fs}$ and may also be used to generate few-cycle pulses (Sell et al., 2009). In order to compensate the spectral phase of the resulting pulses (i.e. of the long-wavelength components of the spectrum), we use quadratic dispersion in different types of glass: a small number of SF6 rods of different lengths (1.2 to $4.8\,\text{cm}$) and a closely-positioned BK7 prism pair, which can be adjusted to fine-tune the amount of glass in the beam (0.6 to $2.2\,\text{cm}$ BK7 path length). The dispersion coefficients $D_n = d^n k/d\omega^n$ of these types of glass in the relevant spectral range from 1400 to $2000\,\text{nm}$ can be obtained from the manufacturer (Schott AG, 2011) and are approximately: $D_2 \in [-200, 800]\,\text{fs}^2/\text{cm}$, $D_3 \in [1500, 4000]\,\text{fs}^3/\text{cm}$, $D_4 \in [-15000, -2000]\,\text{fs}^4/\text{cm}$ for SF6 and $D_2 \in [-1000, -100]\,\text{fs}^2/\text{cm}$, $D_3 \in [1000, 4500]\,\text{fs}^3/\text{cm}$, $D_4 \in [-20000, -3000]\,\text{fs}^4/\text{cm}$ for BK7. SF6 has positive second-order dispersion for wavelengths up to approximately $1900\,\text{nm}$ while BK7 has negative second-order dispersion for wavelengths greater than $1350\,\text{nm}$. Note that a longpass filter blocking the residual components of the driving pulse around $1550\,\text{nm}$ might be advantageous for obtaining short pulses.

We use a Michelson type interferometric autocorrelator with a thin pellicle beam splitter to characterize the pulse duration. A silicon photodiode serves as both second-order non-linear optical element and detector of the two-photon signal.

## 5.3 Results

The results depicted in Fig. 34 show a measurement of typical pulses produced in our setup. During this measurement, the beam passed SF6 rods of a total length of 6 cm and BK7 glass of a total length of 1 cm. The average output power of the fiber laser was 235 mW before broadening in the HNLF and 171 mW after broadening (corresponding to a coupling efficiency of 73 %). Figure 34 (a) depicts the autocorrelation trace we measured after optimizing the amount of glass inside the beam to compensate the spectral phase. The spectrum of the pulses is shown in Fig. 34 (c). It has a center wavelength of 1680 nm. In order to obtain the pulse duration, we compare the autocorrelation trace to simulations of the trace, which are based on the spectrum and assume a higher order spectral phase. Here, we find the best fit between measurement and simulation by assuming a fourth
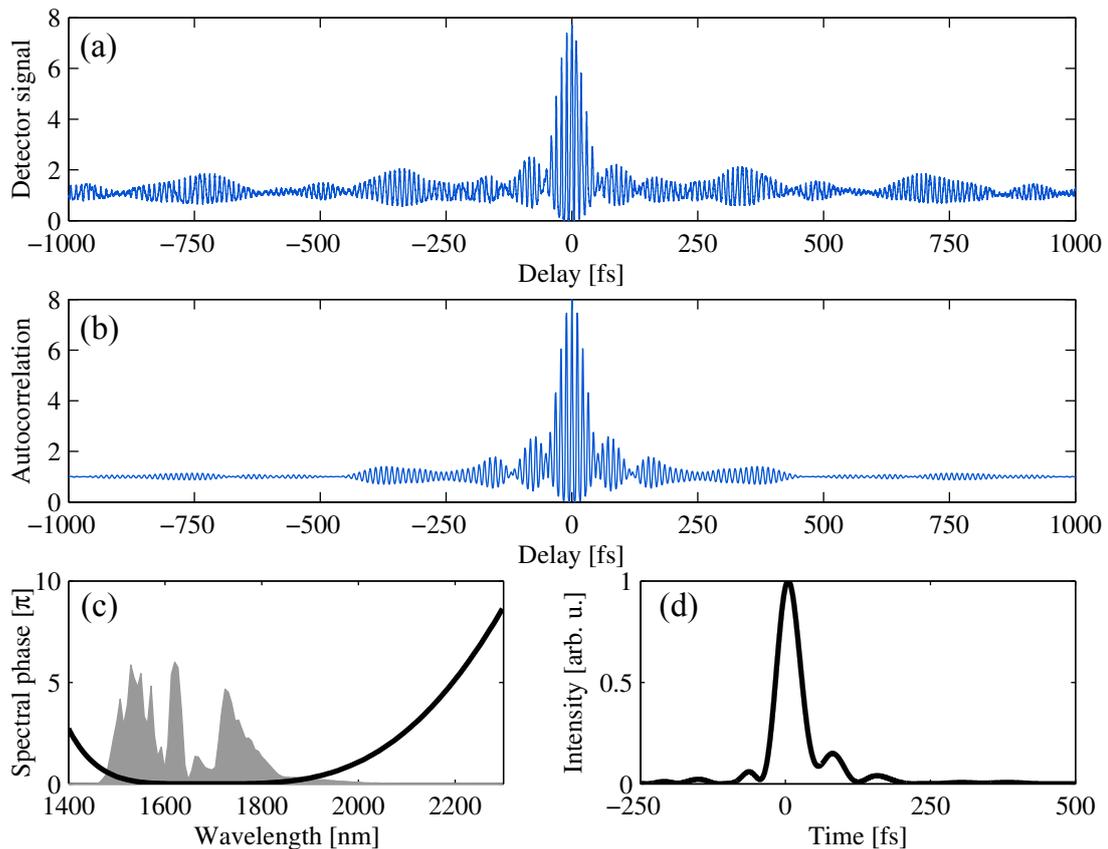


Figure 34: (a) Measured autocorrelation trace; (b) simulated autocorrelation trace; (c) measured spectral intensity (gray area) and the assumed spectral phase (line) used in the simulation; (d) temporal pulse shape corresponding to (c).

order phase. The simulated trace, the assumed spectral phase and the resulting temporal pulse shape are depicted in Fig. 34 (b-d).

The resulting pulse duration is $\tau = (23.1 \pm 1.5)$ fs. We obtained an estimate of the uncertainty by comparing simulated traces with different magnitudes of the spectral phase to the measured trace. The pulse duration is approximately 30 % above the spectrum's Fourier limit of 17.7 fs. Using other types of glass might even help to reduce the pulse duration into the three-cycle regime, closer to the Fourier limit. Note that no double-chirped mirrors or prism compressors are needed to obtain this pulse duration. We hence expect this setup to be easily integrable into a fully fiber-based system, similar to the setup by Anashkina et al. (2011).

While the measured and simulated autocorrelation traces agree very well in the center of the trace (for |delay| < 400 fs) there is only a qualitative agreement for greater delays, where the simulation shows significantly smaller wings. This suggests that our simulation underestimates the amplitude of the satellite pulses. As the autocorrelation signal of these wings remains smaller than 2, the satellites are unlikely to change the pulse duration or to significantly contribute to the highly non-linear photoemission process we will discuss in the next section.

## 5.4 Multiphoton photoemission
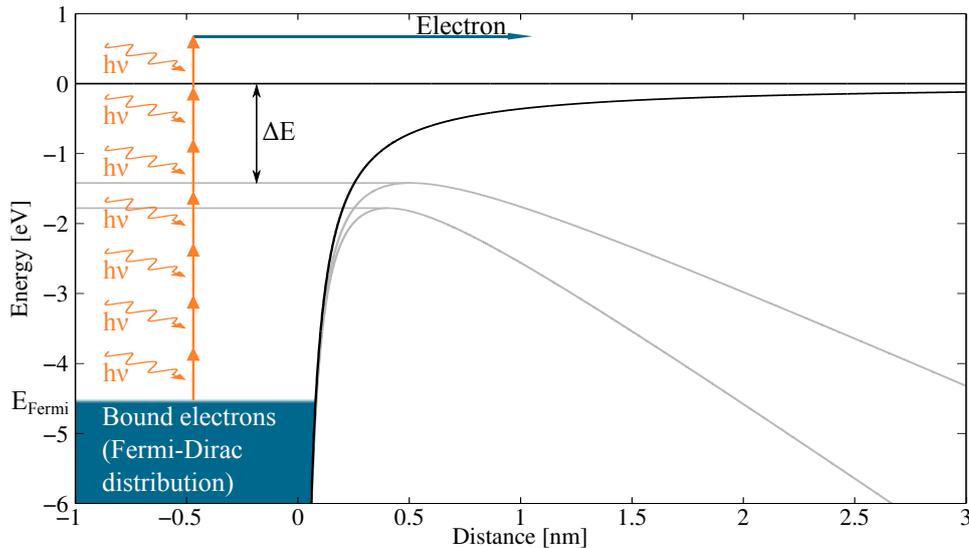


Figure 35: Illustration of multiphoton absorption and the Schottky effect at a tungsten surface: in order to be emitted, an electron's energy must be raised from an energy $E \leq E_{\text{Fermi}}$ to the continuum $E \geq 0$. An additional static voltage at the surface lowers the barrier height, thus reducing the required energy. The barrier is plotted for zero voltage (black line) and for the voltages applied in the experiment, corresponding to fields of 2.2 (lower grey line) and 1.4 GV/m (upper grey line).

As a first application of the laser system, we will present measurements of photoemission of electrons from a sharp tungsten tip. We focus the laser pulses onto the

apex of a sharp tungsten tip using an off-axis parabolic mirror. The waist radius of the beam in the focus is approximately 6 μm ($1/e^2$ of the intensity). The tip is made of (310)-monocrystalline tungsten wire and has a radius of curvature of around 10 nm. Both the tip and the mirror are arranged in an ultra-high vacuum chamber. In addition to the laser field, a static voltage can be applied to the tip. We measure the electron emission current from the tip using a micro-channel plate (MCP) detector. A more detailed description of the setup is given in an article by Schenk et al. (2010).

In this setup, electrons are emitted from the tip surface via the absorption of multiple photons. The photon order of this process depends on the effective barrier height at the surface, which varies with the applied voltage due to the Schottky effect (Gomer, 1961). The effective barrier height is then given by the work function of the material decreased by $\Delta E = (e^3 F / 4\pi\epsilon_0)^{1/2}$. In this equation, $e$ is the electron charge, $\epsilon_0$ is the vacuum permittivity, and $F$ is the static electric field at the surface. Figure 35 shows the potential for three different settings of the static voltage.

To determine the photon order in the experiment, we measure the electron emission current $J$ while varying the average power $P$ of the laser illuminating the tip. For an emission process of photon order $n$, $J$ is proportional to $P^n$. Results of this measurement for two different electric fields $F = 2.2\,\text{GV/m}$ and $1.4\,\text{GV/m}$ at the tip are plotted in Fig. 36. We obtain the photon order by fitting a power law to the measured data.

The fit results suggest that we observe four- and five-photon absorption as the dominant emission process, respectively, which implies that the barrier height lies between 2.2 and 3.0 eV in the first and between 3.0 and 3.7 eV in the second case. Calculating the Schottky effect for the two electric fields and combining the results with the effective barrier height, we find that the work function of the tungsten tip must be between 4.4 and 4.8 eV, which is consistent with previously published values for tungsten (Kawano, 2008).
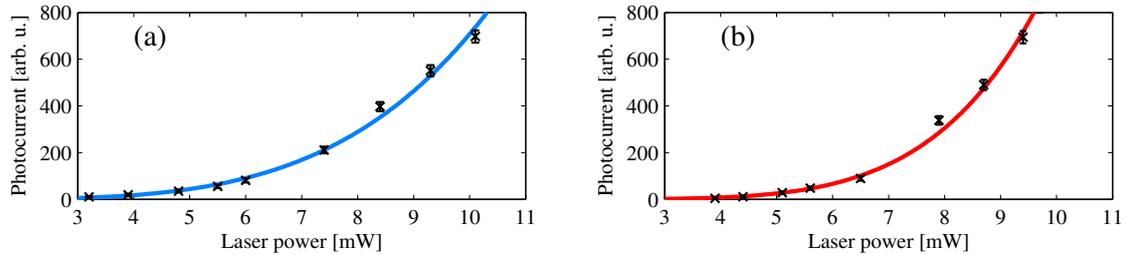


Figure 36: Photocurrent $J$ as function of laser power $P$ for two different static electric fields; (a) $F = 2.2\,\text{GV/m}$, fit result: $J \sim P^{4.0\pm0.3}$; (b) $F = 1.4\,\text{GV/m}$, fit result: $J \sim P^{5.3\pm0.4}$.

## 5.5 Conclusion

We have presented a simple setup capable of generating four-cycle pulses at 1700 nm based on an amplified erbium-doped fiber laser and a commercial highly non-linear fiber. Our results show that exploiting group velocity dispersion in glass is sufficient

to achieve pulse durations down to only four optical cycles. Additionally, we have shown results from photoemission experiments as a first application of our laser system, demonstrating the reliability of the setup.

## Acknowledgments

# 6 Probing of optical near-fields by electron rescattering on the 1 nm scale

**Authors**: Sebastian Thomas[†], Michael Krüger[†], Michael Förster, Markus Schenk, Peter Hommelhoff
**Abstract**: We present a new method of measuring optical near-fields within ~1 nm of a metal surface, based on rescattering of photoemitted electrons. With this method, we precisely measure the field enhancement factor for tungsten and gold nanotips as a function of tip radius. The agreement with Maxwell simulations is very good. Further simulations yield a field enhancement map for all materials, which shows that optical near-fields at nanotips are governed by a geometric effect under most conditions, while plasmon resonances play only a minor role. Last, we consider the implications of our results on quantum mechanical effects near the surface of nanostructures and discuss features of quantum plasmonics.

## 6.1 Letter

The excitation of enhanced optical near-fields at nanostructures allows the localization of electromagnetic energy on the nanoscale (Novotny and Hecht, 2006; Stockman, 2011). At nanotips, this effect has enabled a variety of applications, most prominent amongst them are scanning near-field optical microscopy (SNOM) (Wessel, 1985; Inouye and Kawata, 1994; Kawata et al., 2009; Schnell et al., 2011; Hartschuh, 2008), which has reached a resolving power of 8 nm (Raschke et al., 2005), and tip-enhanced Raman spectroscopy (TERS) (Wessel, 1985; Stöckle et al., 2000). Because of the intrinsic nanometric length scale, measuring and simulating the tips' near-field has proven hard and led to considerably diverging results (see the textbook by Novotny and Hecht (2006) or a review article by Hartschuh (2008) for overviews). Here we demonstrate a nanometric field sensor based on electron rescattering, a phenomenon well known from attosecond science (Corkum and Krausz, 2007). It allows measurement of optical near-fields, integrating over only 1 nm right at the structure surface, close to the length scale where

---

[†]    Both authors contributed equally to this work.

quantum mechanical effects become relevant (Zuloaga et al., 2010; Marinica et al., 2012; Ciracì et al., 2012; Wachter et al., 2012; Teperik et al., 2013). Hence, this method measures near-fields on a scale that is currently inaccessible to other techniques (such as SNOM or plasmonic methods in electron microscopy (García de Abajo, 2010; Koh et al., 2011; Willets, 2012)), and reaches down to the minimum length scale where one can meaningfully speak about a classical field enhancement factor. In the future, the method will allow tomographic reconstruction of the optical near-field and potentially the sensing of fields in more complex geometries such as bow-tie or split-ring antennas.

In general, three effects contribute to the enhancement of optical electric fields at structures that are smaller than the driving wavelength (Martin and Girard, 1997; Martin et al., 2001; Hartschuh, 2008; Zhang et al., 2009). The first effect is geometric in nature, similar to the electrostatic lightning rod effect: the discontinuity of the electric field at the material boundary and the corresponding accumulation of surface charges lead to an enhanced near-field at any sharp protrusion or edge. This effect causes singularities in the electric field at ideal edges of perfect conductors. For real materials at optical frequencies, the electric field is not as strongly enhanced and remains finite (Van Bladel, 1996). The second effect occurs at structures whose size is an odd multiple of half the driving wavelength: optical antenna resonances can be observed there. The third effect concerns only plasmonic materials like gold and silver, where an enhanced electric field can arise due to a localized surface plasmon resonance. Antenna and plasmon resonances depend critically on the shape and material of the structure in question and occur only for specific wavelengths. In contrast, geometric effects are inherently broadband and result in a monotonically increasing field enhancement for increasing sharpness of the structure and for increasing discontinuity in the dielectric constant at the boundary. In spite of their different nature and properties, all three effects can be modeled in the framework of Maxwell's equations with linear optical materials. However, field enhancement calculations remain challenging because they crucially depend on the shape of the illuminated object, while analytic solutions of Maxwell's equations are known only for a few special cases like spheres and infinite cylinders. Accurate field enhancement measurements are equally challenging because of the nanometric length scale and the often unknown exact shape of the structure.

In this letter, we present experimental measurements with a new technique, the results of which we compare to numerical simulations of optical field enhancement at nanometric metal tips. Illuminating such a tip with light polarized parallel to the tip axis leads to the excitation of an enhanced near-field, which is spatially confined in all directions on the length scale of the tip radius (Martin et al., 2001; Novotny and Hecht, 2006; Zhang et al., 2009) (see Fig. 1(a)). The near-field drives a localized source of electrons at the tip apex (Hommelhoff et al., 2006a,b; Ropers et al., 2007). Such photoemission experiments have found applications in a variety of different contexts aside from nanotips (Petek and Ogawa, 1997; Aeschlimann et al., 2007; Dombi et al., 2013). Very recently, it has been observed that part of the electrons can be driven back to the parent tip within a single cycle of the optical field. There, the electrons can scatter elastically and gain more energy in the optical field (Krüger et al., 2011; Yalunin et al., 2011; Herink et al., 2012; Wachter et al., 2012). This process, well known from
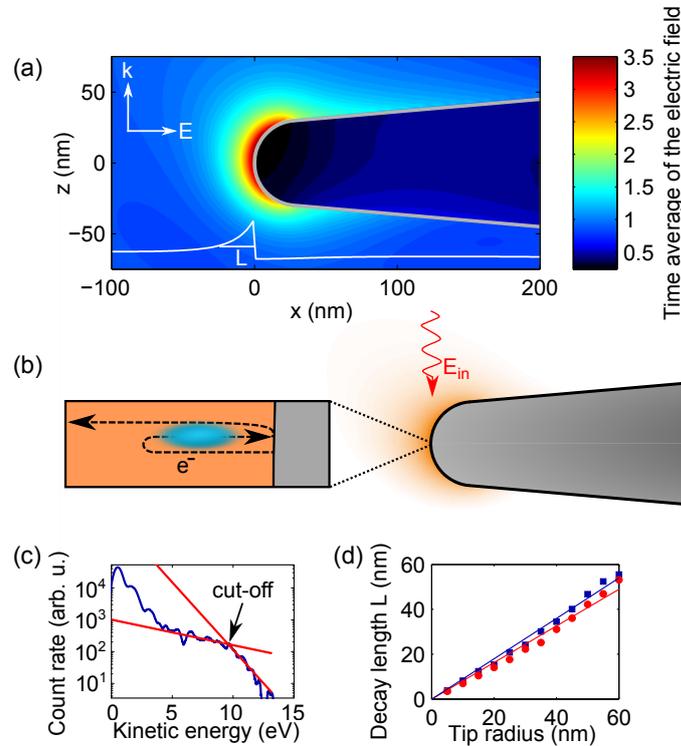
Figure 37: (a) Time-averaged electric field (obtained from the simulation) near the apex of a tungsten tip ($R = 30$ nm, $\lambda = 800$ nm) in a plane spanned by the tip axis and the wave vector **k** of the laser. The tip shape is indicated as a gray line. The white line at the bottom displays the near-field along $z = 0$ with the $1/e$ decay length $L$. The field rises from 1.2 to 3.4 over a distance of 29 nm, where 1 indicates the field strength in the bare laser focus without a tip. Note that the near-field is not symmetric with respect to the tip axis. This asymmetry is more prominent for larger tip radii (Yanagisawa et al., 2010). (b) Illustration of electron rescattering: electrons are emitted in the optical near-field of a metal nanotip. A fraction of the emitted electrons is driven back to the tip surface, where they can scatter elastically. The kinetic energy gained during the rescattering process depends sensitively on the electric field near the tip surface. Thus the strength of the optical near-field is mapped to the kinetic energy of the emitted electrons. (c) Typical energy distribution of electrons emitted in the forward direction. The high-energy plateau ($\sim 5$ to $10$ eV) arises due to rescattering. Its cut-off is related to the local electric field amplitude at the metal. We obtain it from the intersection of two exponential fit functions (red lines). (d) Decay length $L$ as function of tip radius $R$ for tungsten tips (blue squares) and gold tips (red circles), deduced from simulations. The lines show linear fits: $L = (0.90 \pm 0.03)R$ for tungsten and $L = (0.82 \pm 0.04)R$ for gold. As the shape of the near-field mainly depends on the tip geometry, other materials behave very similarly.

atomic physics (Corkum, 1993; Paulus et al., 1994b; Corkum and Krausz, 2007), has been called rescattering and leads to pronounced spectral features that are sensitive to the local electric field. Here we exploit the rescattering effect to probe the near-field in the immediate vicinity of the tip surface, as illustrated in Fig. 37 (b).

Our experiment consists of an almost atomically smooth metal tip with a radius of curvature $R = 8$ to $50\,\mathrm{nm}$. Its apex lies in the focal spot of few-cycle laser pulses derived from a Ti:sapphire oscillator (wavelength $\lambda = 800\,\mathrm{nm}$, repetition rate $f_\mathrm{rep} = 80\,\mathrm{MHz}$, pulse duration $\tau \approx 6\,\mathrm{fs}$). The setup is described in more detail in an article by Schenk et al. (2010). While this laser system reaches intensities of up to $\sim 10^{12}\,\mathrm{W/cm^2}$ in the focus, we do not observe any influence of possible optical non-linearities on the field enhancement factor, and all our results (e.g., the linear dependence of the rescattering cut-off on laser intensity (Wachter et al., 2012)) are consistent with a linear model of the metal's optical response.

Optical field enhancement enables us to observe electron rescattering at moderate pulse energies of less than $1\,\mathrm{nJ}$. We measure the energy distribution of the electrons emitted in the forward direction using a retarding field spectrometer. The recorded spectra yield information about the dynamics of the emitted electrons. A typical spectrum is shown in Fig. 37 (c). At small energies, such spectra display an exponential decrease in count rate, followed by a plateau towards larger energies. The latter is an indication of electron rescattering (Paulus et al., 1994b; Becker et al., 2002; Krüger et al., 2011, 2012a; Wachter et al., 2012). This process has found utmost attention as it is at the core of attosecond science (Corkum and Krausz, 2007).

It has been shown that rescattering is highly sensitive to the peak electric field strength $E$ via the ponderomotive potential $U_\mathrm{p}$ the electron experiences in the light field (Paulus et al., 1994b; Becker et al., 2002; Krüger et al., 2012a): $U_\mathrm{p} = e^2\lambda^2 E^2/(16\pi^2 mc^2)$. Here, $\lambda$ is the laser wavelength, $e$ and $m$ are the electron's charge and mass, and $c$ is the speed of light. The cut-off kinetic energy (see Fig. 37 (c)) after rescattering is given by $T_\mathrm{cutoff} = 10.007\,U_\mathrm{p} + 0.538\,\Phi$, where $\Phi$ denotes the tip's work function (Busuladžić et al., 2006). Measuring $T_\mathrm{cutoff}$ hence yields $U_\mathrm{p}$ (see the supporting information online for details[†]).

Series of spectra for both tungsten and gold tips (Eisele et al., 2011) with various tip radii yield the dependence of the field enhancement factor on tip radius and material. We extract the cut-off position of the rescattering plateau and deduce, via the above expressions, the peak electric field $E$. We stress that $E$, the field acting on the electron, is the *enhanced* field present at the tip's surface. We thus obtain the field enhancement factor $\xi = E/E_\mathrm{in}$, with the laser field $E_\mathrm{in}$ deduced from intensity measurements.

Figure 38 shows the field enhancement factor $\xi$ as a function of the tip radius $R$. For tungsten tips, $\xi$ grows by around a factor of 2 with decreasing $R$, from $2.6 \pm 0.6$ at $(51 \pm 5)\,\mathrm{nm}$ to $5.7 \pm 0.6$ at $(8 \pm 2)\,\mathrm{nm}$. For gold nanotips with radii between $(46 \pm 3)\,\mathrm{nm}$ and $(28 \pm 4)\,\mathrm{nm}$, we obtain field enhancement factors between $\xi = 3.3 \pm 0.6$ and $3.5 \pm 0.6$.

---

[†]  The supporting information contains comments on the rescattering cutoff energy and the measurement of tip radii. This material is available free of charge at http://pubs.acs.org/. The supporting information is not included in this thesis because all the material in there is discussed in more detail in chapter 7.
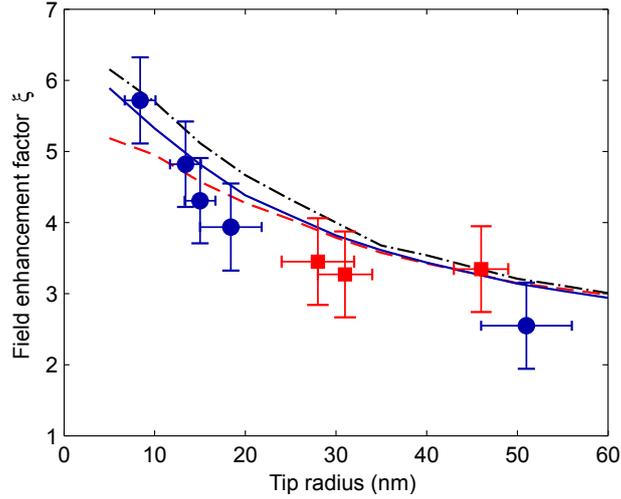
Figure 38: Experimental results for the field enhancement factor of tungsten tips (blue circles) and gold tips (red squares) as a function of the tip radius. The uncertainty in $\xi$ represents an estimated systematic error due to the uncertainty in laser intensity. The lines are simulation results for $\lambda = 800\,\text{nm}$ (W: solid blue line, Au: dashed red line, Ag: dash-dotted black line). The dielectric functions of the metals are taken from experimental data (Lide, 2004) (see Fig. 39 (b)). For technical reasons related to mock surface plasmon reflection, we simulate gold and silver tips with a smaller opening angle than tungsten tips (W: 5°, Au, Ag: 0°). Simulations of tips with different angles show that this should not alter the results by more than 5%.

We have been unable to produce sharper gold tips with a well-controlled surface. Tip radii are determined in situ with the ring counting method in field ion microscopy or, for radii > 20 nm, using a scanning electron microscope (see the supporting information online for details).

We compare our results to fully independent simulations of field enhancement at tungsten, gold, and silver tips. They were performed using Lumerical (7.0.1), a commercial Maxwell solver implementing the finite-difference time-domain (FDTD) algorithm (Taflove and Hagness, 2005). From each simulation, we extract the field enhancement factor by fitting a quadratic decay to the near-field at the moment of greatest enhancement and extrapolating the result to the tip surface. This and other measures are essential to obtain meaningful results, as the finite mesh of the FDTD solver, together with the different length scales involved, makes this problem a tricky one. Further details and simulation results will be published elsewhere. The results for tungsten, gold, and silver are shown in Fig. 38. Experimental and simulation results agree well within the error bars. Note that this agreement is obtained without any free parameters. Both experiment and simulation show that $\xi$ increases smoothly for sharper tips, an indication of field enhancement due to a geometric effect.

Comparing our results to literature values of $\xi$, we find good agreement for tungsten tips (experiment (Neacsu et al., 2005b; Yanagisawa et al., 2010), theory (Yanagisawa et al., 2010; Martin et al., 2001)), while previous results for gold tips are inconsistent (experiment (Neacsu et al., 2005b; Ropers et al., 2007), theory (Martin et al., 2001; Bouhelier et al., 2003a)) with some authors reporting much higher enhancement (Bouhelier

et al., 2003a; Neacsu et al., 2005b; Ropers et al., 2007). A possible explanation for this disagreement is that the near-field at plasmonic materials like gold is exceptionally sensitive to the geometry of the tip (the opening angle in particular (Martin et al., 2001; Zhang et al., 2009)) and its surface condition. This is supported by the large variance in enhancement factors at gold tips reported in the paper by Neacsu et al. (2005b). Note also that far higher field enhancement factors are observed for tips in close vicinity ($\lesssim R$) to surfaces (Yang et al., 2009).

In our experiments with gold tips, we do not observe a large variance of field enhancement factors even though not all the tips had the ideal conical shape assumed in the simulations. A possible reason for this is that, before any measurement, we use field ion microscopy in conjunction with field evaporation to clean the tip surface and to ensure that the tip is almost ideally spherical in the vicinity of the apex. This is likely not the case in many other experiments. Evidently, more research is needed to fully understand the behavior of tips made of plasmonic materials. Such an investigation is beyond the scope of this letter. In the following analysis, we only consider perfectly smooth, conical tips (see Fig. 37 (a)) with small opening angles between 0° and 5°.

It appears, at first glance, surprising that the field enhancement factor of such different materials as tungsten and gold is so similar (see Fig. 38), considering that gold supports the excitation of surface plasmons (Novotny and Hecht, 2006; Stockman, 2011). We therefore analyze the dependence of the field enhancement factor on tip material in a series of simulations where we vary the complex dielectric constant $\epsilon = \epsilon_r + i\epsilon_i$ of the tip. This allows us to give a field enhancement map for all materials with $|\epsilon| \lesssim 40$, shown in Fig. 39. The results demonstrate that field enhancement occurs for any material with $\epsilon \neq 1$, even for pure dielectrics. Furthermore, the enhancement factor increases monotonically with the absolute value of the dielectric constant $|\epsilon|$, confirming that we observe field enhancement due to a geometric effect. We also note a slightly larger enhancement for $\epsilon_r > 0$ than for $\epsilon_r < 0$, which corresponds to an $\epsilon$-dependent phase shift ($< \pi$) of the near-field with respect to the driving field: the field enhancement factor is proportional to the maximum of the total electric field, which is reduced if the driving field and the near-field are out of phase. The $\epsilon$-dependent simulations reveal why the field enhancement factor of tungsten, gold, and silver tips is similar: they have a similar value of $|\epsilon|$ at 800 nm.

In order to obtain higher enhancement factors, materials with larger values of $|\epsilon|$ are required. For example, we find $\xi = 7.6$ for $R = 10$ nm aluminum tips ($\epsilon_{Al} = -64 + 47i$ at $\lambda = 800$ nm, beyond the range of our simulations in Fig. 39). Alternatively, $\xi$ can be increased by using longer wavelengths, because both the tip sharpness relative to the wavelength and the absolute dielectric constant $|\epsilon|$ of many materials increase for longer wavelengths. We expect considerably higher field enhancement at sharp metal tips for mid- and far-infrared or terahertz radiation. An enhancement factor $\xi \approx 25$ has already been reported in SNOM experiments with terahertz radiation (Huber et al., 2008).

In contrast to the increase with $|\epsilon|$, there is one point in Fig. 39 close to $\epsilon = -2$ that shows a significantly higher enhancement than the points surrounding it. This can be interpreted as a localized plasmon resonance, similar to what is known from
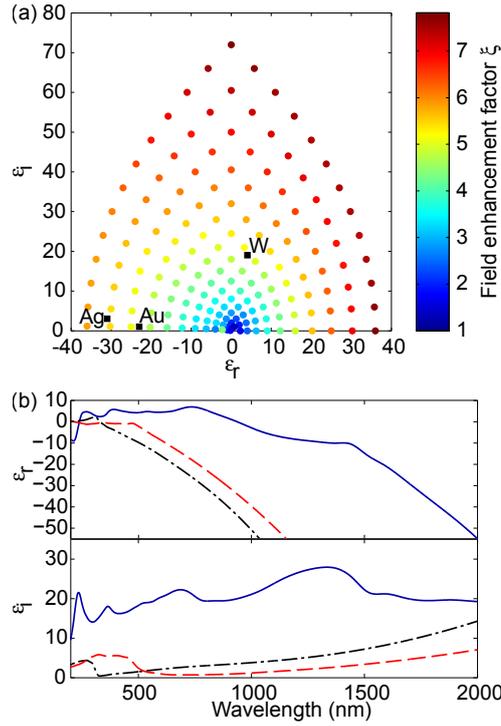
Figure 39: (a) Field enhancement factor as a function of the dielectric constant $\epsilon = \epsilon_r + i\epsilon_i$ obtained from simulations. The simulation parameters are $R = 10\,\text{nm}$, $\lambda = 800\,\text{nm}$, and an opening angle of $0°$. The dielectric constants of tungsten, gold, and silver at 800 nm are shown as black squares. (b) Real part $\epsilon_r$ and imaginary part $\epsilon_i$ of the dielectric constant of tungsten (solid blue line), gold (dashed red line), and silver (dash-dotted black line) as a function of wavelength. The values of the dielectric constant are taken and interpolated from data by Haynes and Lide (2011). Note that the absolute value $|\epsilon|$ of the three materials is similar around 800 nm.

nanospheres (Martin et al., 2001). It can be observed with a wavelength of $\lambda \approx 360\,\text{nm}$ at silver tips (Zhang et al., 2009) or $\lambda \approx 520\,\text{nm}$ at gold tips.

In the analysis of our experimental results, we have neglected the spatial variation of the near-field on the rescattered (field-probing) electrons' path, assuming instead a constant electric field. This is justified as the decay length of the near-field $L$ (see Fig. 37 (d)) is much longer than the maximum extension of the electron's path $M$: For our parameters, both classical (Krüger et al., 2011, 2012a) and quantum mechanical (Wachter et al., 2012; Yalunin et al., 2013) simulations indicate that the electrons' path extends approximately 1 nm from the surface before rescattering. On this scale, the sharpest tips we investigate show a near-field variation of ∼20%. Including this spatial variation into classical calculations of rescattering changes the enhancement factor by 0.4 only, even for the sharpest tip in our experiments. This is less than the measurement uncertainty. For longer wavelengths or higher field strengths, the maximum extension $M$ increases. In this case, the effect may be more significant and can even suppress rescattering completely (Herink et al., 2012).

One intriguing application of our method is the investigation of quantum effects in nanoplasmonics, a new field that has recently been named quantum plasmonics. Self-

consistent quantum mechanical calculations of small nanoparticles (radius of curvature < 2 nm) illuminated by laser pulses show that the excited surface charge density, the root cause of the optical near-field, extends over several ångströms beyond the surface (Zuloaga et al., 2010). This "electron spill-out" reduces the strength of the near-field by up to ~50%. For small nanoparticles, it was shown that these effects are noticeable only at a distance of $Q < 0.5$ nm from the surface, while the near-field retains its classical shape for larger distances. As fully quantum mechanical calculations of larger nanoparticles remain difficult (although large steps are being made in this direction (Teperik et al., 2013)), it is unclear if the length scale of nonclassical behavior $Q$ depends on the size of the nanoparticle. Zuloaga et al. (2010) suspect $Q$ to increase for larger nanoparticles.

While a fully integrated quantum calculation of both field enhancement and electron rescattering is beyond the scope of this letter, we will discuss the effects of quantum plasmonics on rescattering qualitatively. They depend on three length scales: the extent of nonclassical field reduction $Q$, the near-field's decay length $L$, and the rescattered electron's maximum extension $M$. If $Q \approx L$ as in the article by Zuloaga et al. (2010), the maximum of the near-field is significantly reduced, which implies a corresponding reduction of the cut-off energy. Extremely sharp nanostructures ($R \lesssim 3$ nm) will be required to reach this regime if $Q$ does not scale with structure size. As discussed earlier, rescattering may be suppressed in this case, depending on the relation of $M$ and $L$ (Herink et al., 2012).

If $L \gg Q$, only a small fraction of the near-field's extent is reduced in strength so that the maximum of the near-field is almost unchanged. In this case, quantum effects are only noticeable if $M \leq Q$, because the rescattered electron would not be sensitive to the reduced field strength otherwise. The parameters in our experiments are $M \approx 1$ nm (including a non-zero tunneling distance (Busuladžić et al., 2006; Krüger et al., 2012a; Hickstein et al., 2012)) and $L \geq 8$ nm, so quantum effects should only be visible if $Q$ becomes larger than 0.5 nm for larger nanostructures. The agreement between experimental results and classical theory seems to suggest that $M > Q$. Hence, Q does not seem to scale with structure size, as hypothesized by Zuloaga et al. (2010). However, there is still the possibility of quantum plasmonic effects on a larger scale within the error bars of our results. An increase of $Q$ for larger tips might explain the steeper decrease of $\xi$ for larger radii we observe in the experiment as compared to the simulation (see Fig. 38).

In conclusion, we demonstrate a new method of probing optical near-fields within 1 nm distance from the surface of a nanoscale metal tip. The method is based on rescattering of electrons driven by short laser pulses. The length scale on which the near-field is measured reaches down to dimensions that are of utmost interest in the emerging field of quantum plasmonics. Experimental results for the field enhancement factors of tungsten and gold tips agree well with Maxwell simulations. Based on these results, we give a field enhancement map for a wide range of materials. Furthermore, the simulations reveal that geometric effects are the predominant mechanism of optical field enhancement at nanotips in most cases. Exceptions exist close to plasmon resonances. In the future, a tomographic reconstruction of the near-field, likely in three dimensions, will be possible

by measuring the cut-off energy of the rescattered electrons while varying the laser power or wavelength.

## Acknowledgments

# 7 Self-probing of metal nanotips by rescattered electrons reveals the nano-optical near-field

**Authors**: Michael Krüger, Sebastian Thomas, Michael Förster, Peter Hommelhoff
**Abstract**: Self-probing of atoms or molecules by their own electrons is a powerful tool for exploring structural dynamics with high spatial and temporal resolution. Spectra from high-harmonic generation or photoelectron rescattering reveal the quantities of interest, such as the electronic structure of the system under scrutiny. Recently, we have observed the rescattering effect at solids, in particular at metal nanotips. Here we use the self-probing approach in order to investigate an effect inherent to nano-scale systems: Laser light incident on nanotips generates strongly enhanced optical near-fields that crucially depend on their geometry and material. In our experiment, we determine the strength of the near-field of tungsten and gold tips from the high-energy cut-off of rescattered electrons. Detailed experimental results are compared with a numerical solution of the time-dependent Maxwell equations.

## 7.1 Introduction

Strong laser fields enable investigation and control of electron dynamics in a wide range of atomic, molecular and nowadays also solid-state target systems. A fundamental effect employed here is the recollision mechanism (Corkum, 1993), which is based on the notion of a free electron moving in the laser field after photoemission. Driven by the optical field, the electron can return to the parent matter and recollide with it. Upon recollision, several effects have been observed: High-harmonic generation (HHG, (Lewenstein et al., 1994; McPherson et al., 1987; Ferray et al., 1988)) is the most prominent among them and is caused by the recombination of recolliding photoelectrons with the parent matter. The resulting high-energy photons carry information about the properties of the recolliding electron and the structure of the parent matter. HHG has been most successfully exploited for self-probing of molecules by their own electrons, yielding information on their electronic and nuclear structure (see, e.g., the articles by Niikura et al. (2002), Itatani et al. (2004), Baker et al. (2006), Lein (2007), Smirnova et al. (2009), or Blaga et al. (2012)). This approach benefits strongly from the sub-optical-cycle

nature of the recollision mechanism; the time frame of recollision is limited to a tiny fraction of the duration of one optical cycle, hence attosecond time resolution is inherent to self-probing approaches.

As a complement or even as an alternative to HHG, the *rescattering* effect is used for investigations of molecular structure (see, e.g., the articles by Meckel et al. (2008) or Lin et al. (2010)). Rescattering arises due to fully elastic scattering of the recolliding electron with the parent matter and results in high-energy electrons that form a plateau structure in photoelectron spectra (Paulus et al., 1994b; Becker et al., 2002). This effect has been observed not only at atomic and molecular gas targets, but also at dielectric nanospheres (Zherebtsov et al., 2011), metal nanotips (Krüger et al., 2011; Wachter et al., 2012; Herink et al., 2012; Park et al., 2012) and gold nanostructures (Dombi et al., 2013). It was shown that the rescattering effect and the involved electron dynamics at nanotips can be controlled on an attosecond time scale by the waveform of the driving optical field (Krüger et al., 2011), in a similar fashion to atomic gases (Baltuška et al., 2003; Paulus et al., 2003). This implies that self-probing with recolliding electrons is not only possible in the gas phase, but also at nano-scale solid-state targets. We expect that a variety of structural information can be gathered about the solid-state target. Here we use the self-probing approach on nanotips in order to investigate the strength of the optical field in the vicinity of the tips.

The presence of a nanostructure and its optical response modifies the local optical field in time and space. If nanostructures of sizes much smaller than the wavelength of the incident light are used, the induced electron dynamics leads to strongly localized, enhanced optical near-fields (Novotny and Hecht, 2006). This effect allows for the localization of optical fields to sub-wavelength length scales far below the diffraction limit and is exploited in various imaging and spectroscopic techniques. Most prominent among them are apertureless scanning optical near-field microscopy (SNOM, (Heinzelmann and Pohl, 1994; Kawata et al., 2009; Hartschuh, 2008)) and tip-enhanced Raman spectroscopy (TERS, (Wessel, 1985; Stöckle et al., 2000)) that usually use metallic or metal coated nanotips. In this work we expand on our experimental investigation of optical near-fields at metal nanotips presented in (Thomas et al., 2013).

The quantity of interest is the field enhancement factor $\xi$ that is given by the ratio of the enhanced near-field and the incident laser field without the presence of the tip. The systematic investigation of near-fields at metal nanotips and their strength has been mostly limited to numerical simulations (Martin et al., 2001; Yanagisawa et al., 2009) and to experimental measurements using tip-enhanced second-harmonic generation (SHG) (Ropers et al., 2007; Neacsu et al., 2005b; Bouhelier et al., 2003a). Here we use the fact that it is the optical near-field that drives photoemission and rescattering at the apex of the tip (Wachter et al., 2012). The motion of rescattered photoelectrons is governed by the spatial and temporal shape of the near-field and leaves characteristic footprints in photoelectron spectra. In the following, we discuss rescattering and its role as an indicator of the near-field strength in detail.

## 7.2 The rescattering cut-off as a gauge for the optical field

Rescattering manifests itself in photoelectron spectra in a plateau-like structure found at high energies. It is terminated by a soft cut-off at an energy that depends on the intensity of the driving laser field (see inset of Fig. 40 (b) for a typical experimental spectrum). Plateau and cut-off follow from the semi-classical Three-Step Model (TSM) from atomic physics (Corkum, 1993; Paulus et al., 1994b). The TSM splits the rescattering process into three steps: First, an electron is emitted from the surface of the metal nanotip by optically induced tunneling. Second, the electron is considered as classical point-like charged particle and propagates in the laser field obeying Newton's equations of motion. The third step accounts for fully elastic scattering at the surface and the electron propagation up to a distant detector. A numerical evaluation of the TSM yields the maximum kinetic energy a photoelectron can gain when undergoing rescattering. This energy can be identified with the cut-off and is given by $E_{\text{cut-off}} = 10.007\, U_{\text{p}}$, where $U_{\text{p}}$ is the ponderomotive energy. The latter is defined as the mean kinetic energy of a free electron in a continuous-wave (cw) laser field and is given by $U_{\text{p}} = q^2 E_0^2/(4m\omega^2)$. Here $q = -|e|$ is the electron charge, $m$ the electron mass and $E_0$ the amplitude and $\omega$ the (circular) frequency of the laser field. $U_{\text{p}}$ and hence $E_{\text{cut-off}}$ scale linearly with the (cycle-averaged) intensity $I = c\epsilon_0 E_0^2/2$ of the optical field, with $c$ the vacuum speed of light and $\epsilon_0$ the vacuum permittivity. Measuring $E_{\text{cut-off}}$ yields the intensity of the near-field. Three caveats, however, must be taken into consideration. First, the TSM does not account for the displacement of the electron due to the tunneling process. Second, the dipole approximation is not necessarily valid since the near-field varies strongly in the spatial domain close to the nanotip surface. Third, the TSM only accounts for a single active electron and neglects any multi-electron effects.

The first caveat can be addressed with refined theory models. The TSM can be extended to include the displacement of the electron after tunneling in a simple way (Zherebtsov et al., 2011; Krüger et al., 2012a; Hickstein et al., 2012; Lai et al., 2011). We assume that the electron starts on its trajectory with zero initial velocity not at the origin $z_0$ at the surface, but at the geometrical tunnel exit

$$z_{\text{exit}}(t) = -\phi/[|e|E_{\text{L}}(t)] + z_0, \tag{30}$$

which depends on the instantaneous optical field $E_{\text{L}}(t)$ (see Fig. 40 (a)). A modified cut-off energy results, shown in Fig. 40 (b) (wavelength $\lambda = 800\,\text{nm}$, work function $\phi = 5.2\,\text{eV}$): For most intensities of the optical field the cut-off energy is larger than the $10\,U_{\text{p}}$ cut-off law predicts. Although the extended TSM successfully explained experimental results in a range of atomic and solid-state systems (Zherebtsov et al., 2011; Krüger et al., 2012a; Hickstein et al., 2012) it shows serious deficiencies. The unphysical divergence of equation 30 for small instantaneous fields $E_{\text{L}}(t)$ causes irregular behavior of the cut-off at low intensities. For example, in Fig. 40 (b) a hump is visible at around $2 \times 10^{13}\,\text{W cm}^{-2}$.

A model that overcomes this limitation is the Complex Trajectory TSM (CTSM, (Chirilă and Lein, 2006)), closely related to the Photoelectron Model for HHG (Smirnova and Ivanov, 2013). It accounts for the non-classical aspects of tunneling, in particular the motion of the electron "under the barrier", and yields good agreement with numerical
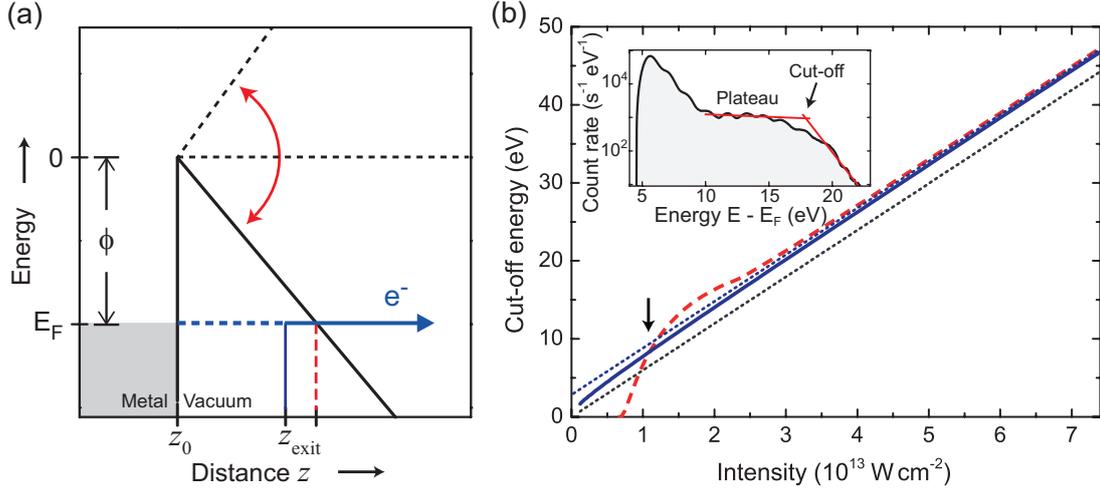
Figure 40: Rescattering cut-off in different theory models. (a) Illustration of the origin of the tunneling displacement at a metal surface. An electron (blue) initially at the Fermi level $E_F$ emerges from the tunnel barrier at the tunnel exit $z_{\text{exit}}$. The Complex Trajectory Three-Step Model predicts a smaller tunnel exit position (solid blue line) than the extended Three-Step Model (dashed red line, see text). (b) Cut-off energy as a function of intensity in different theory models. On display are the $10\,U_p$ law (lower dotted black curve), extended Three-Step Model (dashed red curve), Complex Trajectory Three-Step Model (solid blue curve) and the asymptotic limit (upper dotted black curve, Eq. 31). The arrow indicates the intensity used in the experiment. Inset: Experimental rescattering spectrum. A pronounced plateau and high-energy cut-off is observed. The cut-off position is inferred from the intersection of two exponential decay curves fitted to the spectrum (red curves). The spectrum was recorded with a tungsten tip at a nominal intensity $I_0 = 1.3 \times 10^{11}\,\text{W}\,\text{cm}^{-2}$ using 6-fs laser pulses at 800 nm wavelength.

calculations. The unphysical divergence of $z_{\text{exit}}(t)$ disappears and a smooth behavior of the cut-off as a function of intensity results (see Fig. 40 (b) and (Chirilă and Lein, 2006)). At high intensities the results merge with the extended TSM. The asymptotic limit for high intensities is given by (Busuladžić et al., 2006)

$$E_{\text{cut-off}} \approx 10.007\,U_p + 0.538\,\phi, \tag{31}$$

which is strictly valid only in the tunneling regime of photoemission, at Keldysh parameters $\gamma = \sqrt{\phi/(2U_p)} \ll 1$ (Keldysh, 1965). The cut-off position obtained from all refined models lie within $\pm 12\%$ of this result at a local light intensity of $I = 1 \times 10^{13}\,\text{W}\,\text{cm}^{-2}$ (Keldysh parameter $\gamma \sim 2$). Hence Eq. 31 provides a reasonable approximation even in this regime.

The second caveat follows from the fact that the spatial decay of the near-field in the vicinity of the tip surface has to be taken into consideration (see Fig. 41 (a)). At a local intensity of $10^{13}\,\text{W}\,\text{cm}^{-2}$ and a wavelength of 800 nm, an electron on a rescattering trajectory traverses a region of less than 1 nm distance from the surface (including the tunneling displacement) and averages over the field distribution in this area. Numerical solutions of Maxwell's equations (Thomas et al., 2013) show that the near-field decays to its $1/e$ value within $L \sim 4$ nm from the tip surface for a gold or tungsten tip with a radius of 5 nm. Even for such a tip size, the maximum excursion of the electron trajectory

is much smaller than the near-field decay length $L$. We can therefore assume that the near-field is constant over the electron's path and neglect any spatial variation. With longer driving wavelengths and higher intensities and hence longer electron excursion lengths, however, the decay will inevitably play a role and shift the rescattering cut-off to lower energies than expected from the models (Herink et al., 2012; Yalunin et al., 2013; Park et al., 2013).

The third caveat is due to the fact that employing the single active electron approximation represents a drastic simplification for a complex multi-electron solid-state system. However, calculations using time-dependent density functional theory that explicitly account for electron correlation shows excellent agreement with single active electron models and previous experimental investigations (Wachter et al., 2012; Krüger et al., 2012b). Moreover, in the experiment typically only about 10 electrons per laser pulse are emitted from the nanotip and the interaction time of the pulse with the tip is well below 10 fs. In this parameter range, neither mutual Coulomb repulsion of photoemitted electrons nor electron-electron scattering inside the metal (Petek and Ogawa, 1997) (detected with ~100 fs pulses at tips (Yanagisawa et al., 2011)) does play a significant role by broadening or washing out the electron spectrum. This also means that no secondary effects that amplify rescattering are expected, such as electron trapping by a potential created by a large cloud of other free electrons at the surface (observed at dielectric nanospheres (Zherebtsov et al., 2011)) or surface-plasmon-assisted rescattering (demonstrated with metallic clusters (Fennel et al., 2007)).

## 7.3 Experimental setup for rescattering-based field sensing

The aim of the experiment is to measure the field enhancement factor for metal nanotips of different material and size using the self-probing approach. In our experimental setup, we focus 6-fs laser pulses from a Ti:sapphire laser oscillator (central wavelength 800 nm) on a metal nanotip using an off-axis parabolic mirror (see Fig. 41 (b)). The nanotip is mounted on a 3d nano-positioning stage so that the apex of the conically shaped nanotip can be moved into the region of maximum intensity. The light field is linearly polarized parallel to the tip's symmetry axis so that a strongly enhanced near-field is excited at the apex. Photoelectrons are emitted predominantly in forward direction and are detected by a retarding field electron spectrometer, with a total detection efficiency of about $10^{-2}$. The spectrometer yields an integrated electron spectrum, which is numerically differentiated and smoothed with a Savitzky-Golay algorithm (Schenk et al., 2010). The experiment is carried out in ultrahigh vacuum at a base pressure of $3 \times 10^{-8}$ Pa.

The average laser power is adjusted in such a way that a particular cut-off energy $E_{\text{cut-off}}$ is achieved in rescattering photoelectron spectra. We obtain the field enhancement factor from the enhanced intensity $I$, inferred from $E_{\text{cut-off}}$, and the nominal incident laser intensity $I_0$. This procedure is repeated for tips of different size and material. In our experiment, we chose $E_{\text{cut-off}}$ to be 15 eV with respect to the Fermi energy $E_{\text{F}}$. With an
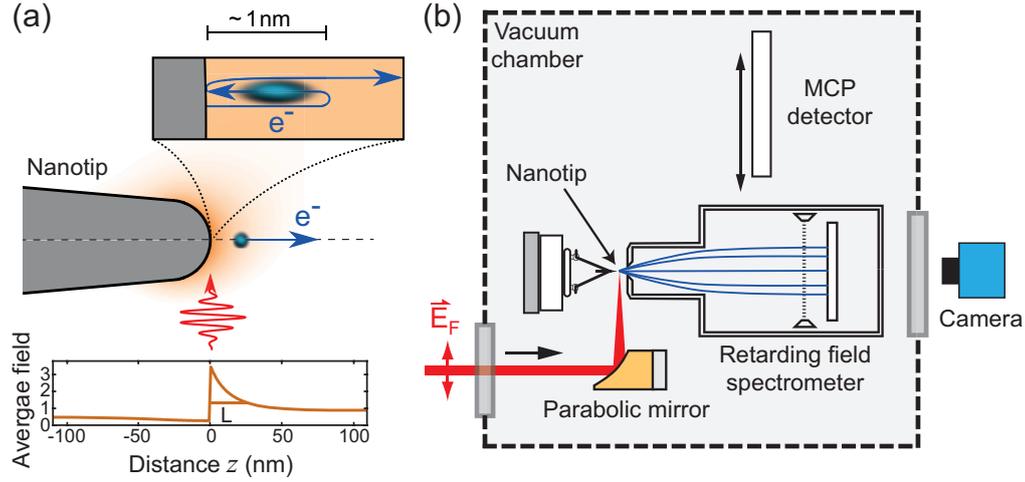
Figure 41: Experimental setup. (a) Illustration of the self-probing approach. Incident laser light (red) excites an optical near-field at the tip apex (orange color plot: time average of the near-field from numerical calculation). Driven by the optical near-field, a photoelectron (blue) undergoes rescattering and averages over a distance of ∼1 nm from the surface. Lower plot: Time-averaged near-field along the tip's symmetry axis $z$, normalized to the strength of the incident field. The field decays to its $1/e$ value within ∼26 nm for the 30 nm tip on display. (b) Sketch of the experimental setup (not to scale). The spectrometer can be exchanged with a micro-channel plate (MCP) detector for field ion microscopy imaging of the tip apex.

effective barrier height $\phi_{\text{eff}}$ of 5.2 eV, this cut-off energy corresponds to an intensity of $I = 1.09 \times 10^{13}$ W cm$^{-2}$ according to Eq. 31. For the determination of $I_0$, the knowledge of the focal spot size $w_0$ is required. We measure $w_0$ both with optical microscopy and with an *in-situ* method based on photoemission from the tip. For the latter, we record the photocurrent as a function of tip position in the focus and reconstruct the local intensity profile from the relationship of current $j$ and intensity $I$ given by the multiphoton power law $j \propto I^n$, with $n$ the minimum number of photons required to overcome the barrier. We estimate the systematic error in $I_0$ to be ±30%.

We investigated tungsten and gold tips of different size. A tip made from single crystal tungsten wire in W(310) orientation was used in the experiment. Different tip sizes were achieved by gradual blunting of the tip by field evaporation (Tsong, 1990) and, in the final step for radii larger than 40 nm, by heating of the tip to a temperature of more than 1000 K. The tip radius $r$ of curvature in each blunting stage was inferred from field ion microscopy (FIM) images with the help of the ring counting method (Tsong, 1990) (see Fig. 42).

This method makes use of the atomic resolution of FIM and gives a reliable estimate of the local radius of curvature of the surface. Atoms terminating atomic layers of the tungsten bcc lattice structure at the surface are visible as bright spots in FIM because they protrude from the rest of the surface. Around the {110} poles, bright ring structures are found. Counting the number of rings $n$ between two crystallographic poles $(h, k, l)$ and $(h', k', l')$ yields the local radius of curvature via the relation $r = ns/(1 - \cos \alpha)$. Here $s$ is the distance of the $(h, k, l)$ planes (here (110), the crystallographic pole in the center
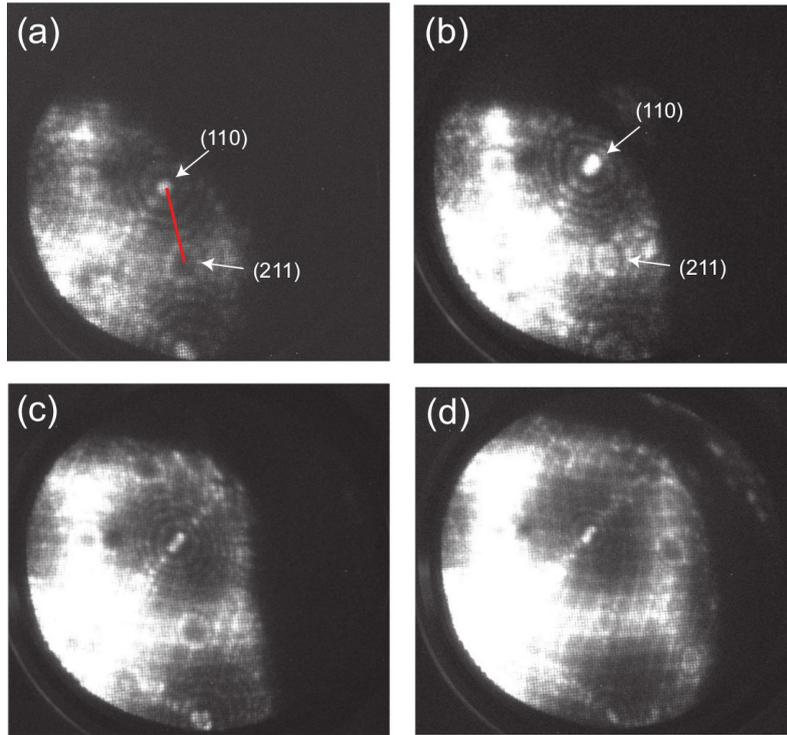
Figure 42: Characterization of a W(310) tip in various blunting stages with field ion microscopy. The tip radius $r$ is inferred from the ring counting method between (110) and (211) poles (red line). (a) $n = 5 \pm 1$ rings, $r = (8.4 \pm 1.7)$ nm. (b) $n = 8 \pm 1$, $r = (13.4 \pm 1.7)$ nm. (c) $n = 9 \pm 1$, $r = (15.0 \pm 1.7)$ nm. (d) $n = 11 \pm 2$, $r = (18.4 \pm 3.4)$ nm.

of the rings). $\alpha$ is the angle between the reference orientation $(h, k, l)$ and a secondary orientation $(h', k', l')$ (here (211)). In our case we find $s = 2.2$ Å and $\alpha = SI30°$. The radius in the final blunting stage could only be determined from a scanning electron microscope (SEM) image (see Fig. 43 (a)). Before each photoemission measurement, the tips were cleaned by field evaporation.

Controlled gradual blunting and *in-situ* FIM characterization of a *gold* nanotip is not possible in our setup. Therefore we used three different polycrystalline gold tips and measured their radii with an SEM after each individual measurement in order to obtain a reliable value for $r$. Figure 43(b)–(d) shows SEM images of the gold tips. The tips vary strongly in their shape. While the tip shown in (b) is similar to the tungsten tip in (a), the tip in (c) has a much larger opening angle with a small protrusion at the end. The gold tip in (d) exhibits an almost spherical protrusion in its apex region with a radius of $r = (28 \pm 4)$ nm.

## 7.4 Results

Rescattering spectra for tungsten with different tip radii ranging from 8 to 51 nm could be recorded (see Fig. 44 (a)). The inset of Fig. 44 (a) displays error bars (standard deviation) for the measurement with 13 nm tip radius, typical for all spectra shown here. The
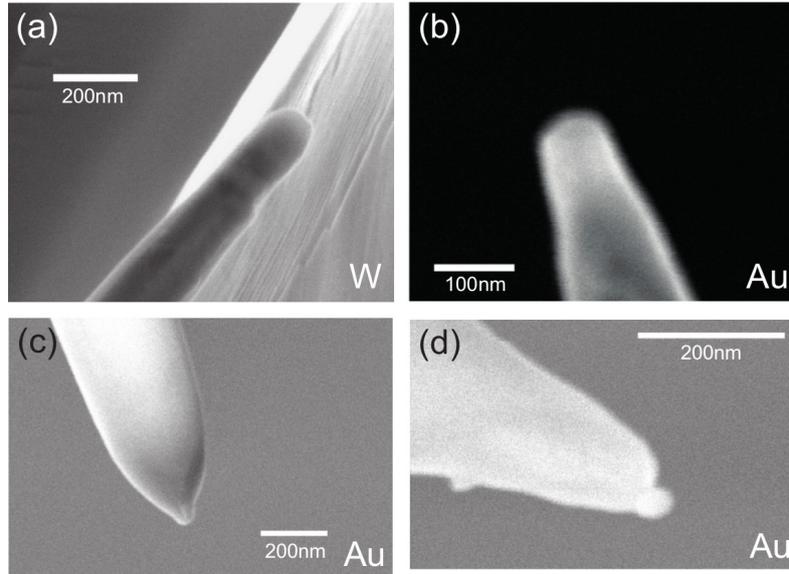
Figure 43: Characterization of tungsten and gold tips with scanning electron microscopy. (a) Image of the tungsten tip in the final blunting state, $r = (51 \pm 5)$ nm. (b)–(d) Images of gold tips with (b) $r = (46 \pm 3)$ nm, (c) $r = (31 \pm 3)$ nm and (d) $r = (28 \pm 4)$ nm.

error was estimated from experimental noise (mostly shot noise of Poisson-distributed electrons) and accounts for data processing. The cut-off positions were determined from the intersection of two exponential decay fits (see inset of Fig. 40 (b)). While the count rate in the direct part at low energies is strongly affected by changing the tip size, the rescattering cut-off remains robust because it essentially depends only on the near-field intensity and not on other properties of the tip. Figure 44 (b) shows photoemission spectra measured with the gold tips. The plateau is not as clear as with tungsten, but the cut-off can definitely be identified.

Figure 45 depicts the extracted field enhancement factors $\xi = \sqrt{I/I_0}$ for tungsten and gold as a function of tip radius $r$. For tungsten, the field enhancement factor increases from $2.6 \pm 0.6$ for $r = (51 \pm 5)$ nm to $5.7 \pm 0.6$ for $r = (8.4 \pm 1.7)$ nm. For gold, $\xi$ ranges from $3.3 \pm 0.6$ for $r = (46 \pm 3)$ nm to $3.5 \pm 0.5$ for $r = (28 \pm 4)$ nm. The uncertainty in $\xi$ is due to the large systematic error in the nominal intensity $I_0$.

In Fig. 45, we also show the results of fully-independent numerical solutions of the time-dependent Maxwell equations for the different tip geometries and materials and incident 5.5-fs laser pulses at 800 nm wavelength. Simulations were carried out using Lumerical FDTD (finite-difference time domain), a commercial Maxwell solver. We simulate the focus of a Gaussian beam within a rectangular box with lengths of several microns. The size of the box is chosen so that the beam intensity is negligible at the simulation boundaries perpendicular to the propagation direction of the laser beam. The tip apex and the laser focus are in the center of the simulation volume. The value of the field enhancement factor is taken from the highest electric field at the tip surface, which we obtain via a fitting procedure of the near-field decay (a typical decay curve is
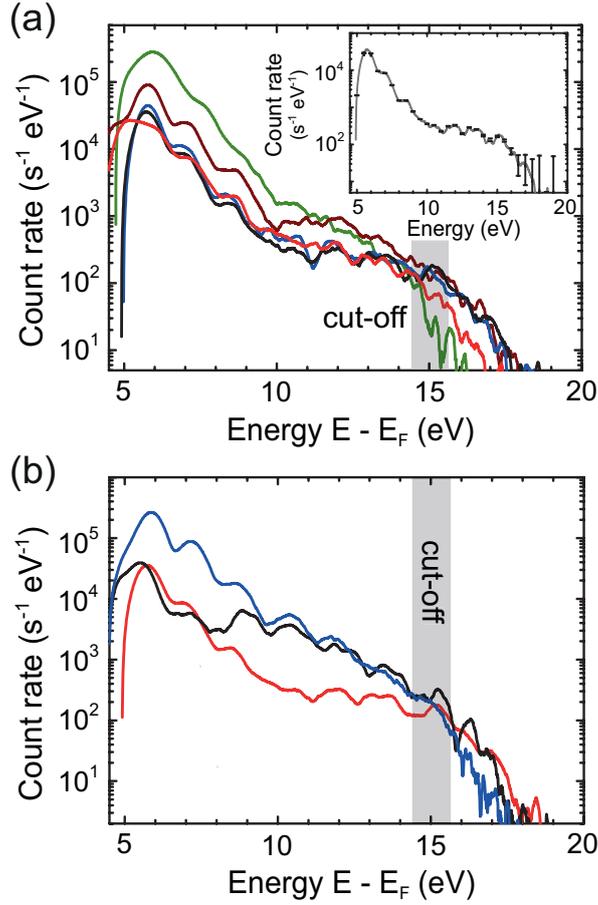
Figure 44: Rescattering spectra for different tip materials and radii. (a) Tungsten tip (red: 8 nm, black: 13 nm, blue: 15 nm, brown: 18 nm, green: 51 nm). Inset: Spectrum of the 13 nm tip with error bars (standard deviation). (b) Gold tips (red: $r = (46 \pm 3)$ nm, black: $r = (31 \pm 3)$ nm, blue: $r = (28 \pm 4)$ nm). A plateau and a pronounced high-energy cut-off are observed, in close analogy to tungsten.

shown in Fig. 41 (a)). This is done in order to avoid numerical artifacts like enhanced field strength due to staircasing.

The experimental values for $\xi$ agree well with the numerical results within the error bars. Both experiment and theory show that $\xi$ increases smoothly for decreasing tip radii. The smaller the nanostructure size relative to the wavelength the stronger the induced near-field becomes. This behavior is compatible with notion that the near-field is mainly a geometric effect; the incident laser field causes surface charge oscillations that result in strong local electric fields due to the geometric boundary conditions imposed by the sharp tip apex.

It is interesting to compare the near-field of nanotips and different nanostructures, e.g. nanospheres. For illuminated nanospheres with a radius $r \ll \lambda$ and an arbitrary dielectric constant $\epsilon$, the field enhancement factor can simply be given by a dipole
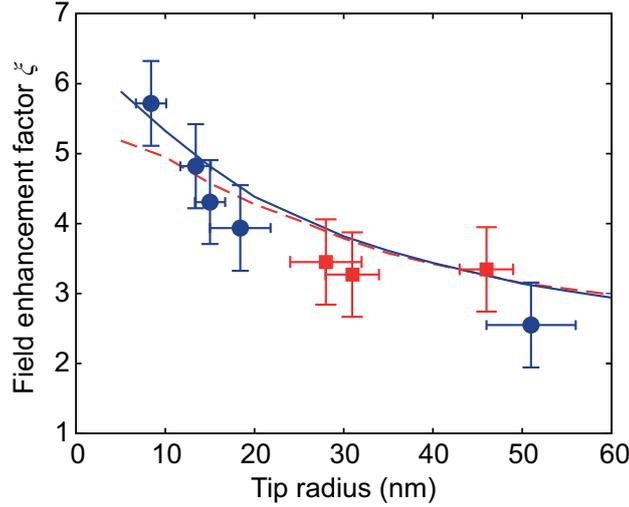
Figure 45: Field enhancement factor of tungsten and gold tips with different radii. Experimental results for the field enhancement factor of tungsten tips (blue dots) and gold tips (red squares) as a function of the tip radius. The uncertainty in $\xi$ represents an estimated systematic error due to the uncertainty in laser intensity. The lines show the results of a numerical calculation for 800 nm light (W: solid blue line, Au: dashed red line).

approximation (Maier, 2007):

$$\xi_{\text{sphere}}(\epsilon) = \left| 1 + 2\frac{\epsilon - 1}{\epsilon + 2} \right|. \tag{32}$$

Note that the enhancement factor $\xi_{\text{sphere}}$ is independent of the sphere's radius in this case. This behavior was investigated numerically for dielectric spheres with increasing radii (see the supplementary material of the paper by Zherebtsov et al. (2011)). The results show that Eq. 32 is valid up to $r \approx \lambda/10$, while higher-order modes are excited at spheres with larger radii, leading to a different shape of the near-field and a higher enhancement factor. The behavior of nanospheres is in stark contrast to our results for nanotips, where the field enhancement factor decreases significantly for larger radii. Evidently, the properties of a nanostructure's near-field depend crucially on its entire geometry and not only on the radius of curvature.

Similar investigations have been performed on dielectric nanospheres by Zherebtsov et al. (2011). For sphere radii of more than ~50 nm they conclude from Maxwell simulations that the near-field enhancement increases with increasing radii – a surprising behavior considering our experimental and theoretical findings with nanotips. Due to field propagation effects the near-field is strongly distorted in the case of large spheres, which leads to an increase rather than a decrease of the maximum near-field strength. In contrast to spheres, these propagation effects are much weaker at nanotips since they exhibit only cylindrical symmetry along the tip pointing direction.

## 7.5 Conclusion

In summary, we have presented a systematic experimental investigation of optical near-fields at metal nanotips using rescattered electrons as a probe. A range of theory models support the notion that the rescattering cut-off found in photoelectron spectra is a robust indicator of the near-field strength. We were able to extract the field enhancement factors of gold and tungsten nanotips with different sizes from the corresponding cut-off energies. The results of our experimental study are in good agreement with a numerical solution of Maxwell's equations and suggest a geometric effect as the mechanism of near-field enhancement for both tip materials.

The method described here can be applied to other nanoscale systems, e.g. to arrays of plasmonic nanostructures on a substrate (Dombi et al., 2013). Furthermore, a full 3d tomographic reconstruction of the spatial structure of optical near-fields is feasible from angularly resolved electron spectra that are recorded for varying laser intensities. The electron excursion length scales linearly with the peak field strength, hence an intensity scan enables a tomographic determination of the spatial decay of the near-field. We also expect that the high time resolution of the self-probing approach can be employed to investigate the temporal waveform of the near-field with attosecond resolution. Numerical calculations suggest that the near-field at nanotips essentially resembles the shape of the incident laser pulse up to a phase shift (Wachter et al., 2012). This phase shift can be determined with the help of carrier-envelope-phase-resolved photoemission measurements.

## Acknowledgements

# 8 Large optical field enhancement for nanotips with large opening angles

**Authors**: Sebastian Thomas[†], Georg Wachter[†], Christoph Lemell, Joachim Burgdörfer, Peter Hommelhoff
**Abstract**: We theoretically investigate the dependence of the enhancement of optical near-fields at nanometric tips on the shape, size, and material of the tip. We confirm the strong dependence of the field enhancement factor on the radius of curvature. In addition, we find a surprisingly strong increase of field enhancement with increasing opening angle of the nanotips. For gold and tungsten nanotips in the experimentally relevant parameter range (radius of curvature $\geq 5\,\text{nm}$ at $800\,\text{nm}$ laser wavelength), we obtain field enhancement factors of up to ~35 for Au and ~12 for W for large opening angles. We confirm this strong dependence on the opening angle for many other materials featuring a wide variety in their dielectric response. For dielectrics, the opening angle dependence is traced back to the electrostatic force of the induced surface charge at the tip shank. For metals, the plasmonic response strongly increases the field enhancement and shifts the maximum field enhancement to smaller opening angles.

## 8.1 Introduction

Optical near-fields arise when a structure illuminated by an electromagnetic wave is smaller than the wavelength of the impinging radiation. At the edges and protrusions of such a nanostructure, the electric field can be significantly enhanced. This nanoscale localization of electric fields has recently found a large number of applications in nano-optics (Novotny and Hecht, 2006; Maier, 2007; Sarid and Challener, 2010). Due to the dynamic lightning rod effect that enables broadband field enhancement (Martin et al., 2001; Goncharenko et al., 2006b; Hartschuh, 2008), nano-sized tips are employed in a variety of applications such as scanning near-field optical microscopy (SNOM), tip-enhanced Raman scattering (TERS), and as sources of second-harmonic generation (SHG) or ultrafast photoemitted electrons (Novotny and Hecht, 2006; Hartschuh, 2008; Kawata et al., 2009; Bouhelier et al., 2003a; Hommelhoff et al., 2006a,b; Ropers et al., 2007; Barwick et al., 2007). The near-field enhancement and localization at the apex of the nanotip play a key role in all these applications. Nonetheless, there is significant disagreement

---

[†]    Both authors contributed equally to this work.
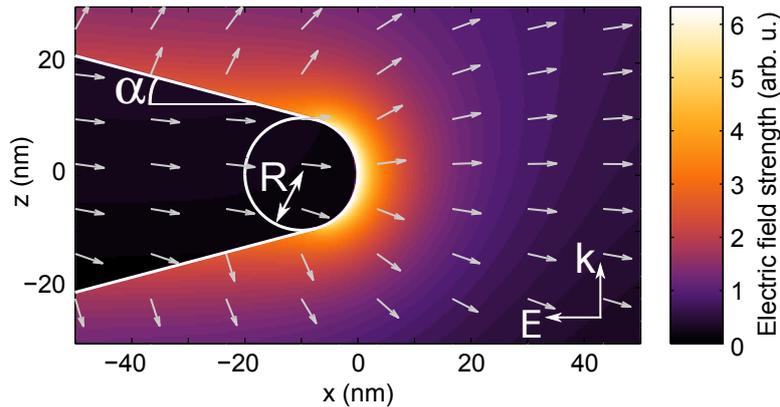
Figure 46: Near-field of a 5 fs, $\lambda = 800$ nm laser pulse for an $R = 10$ nm tungsten tip with an opening angle of $\alpha = 15°$. The laser pulse is propagating in the $z$ direction and is polarized along the $x$ direction. Shown here are the electric field strength (color) and the direction of the field (arrows) at the point in time when the near-field strength is at its maximum.

in the literature about the magnitude of the field enhancement at nanotips (Novotny and Hecht, 2006; Hartschuh, 2008), most notably for gold tips where theoretical and experimental results vary widely (Martin et al., 2001; Bouhelier et al., 2003a; Neacsu et al., 2005a; Ropers et al., 2007; Arbouet et al., 2012; Thomas et al., 2013).

Previous experimental and theoretical investigations have shown that details of the tip geometry near the apex can strongly influence the response (Martin et al., 2001; Neacsu et al., 2005a; Goncharenko et al., 2006a, 2007; Behr and Raschke, 2008; Zhang et al., 2009; Pors et al., 2014; Swanwick et al., 2014). Even though modern nanofabrication techniques such as focused ion beam etching allow manufacturing of nanotips with custom-designed geometries, a systematic study of the relation between the tip design parameters (curvature, opening angle, and material) for realistic illumination conditions is still lacking.

In this article, we investigate optical near-field enhancement at nano-sized tips as a paradigmatic example for a nanostructure. The focus of our study is the behavior of the electromagnetic field at nanotips, and we do not consider thermal effects. We perform fully three-dimensional (3d) numerical simulations employing Maxwell's equations combined with a realistic material-specific optical dielectric function $\epsilon(\omega)$ of nanotips as a pre-laboratory to guide optimization of the techniques that rely on localized field enhancement. We explore the dependence of optical near-field enhancement on the tip geometry for experimentally relevant tungsten and gold tips at 800 nm wavelength and find a strong dependence on both the radius of curvature and the opening angle of the tip. We inquire into the origin of the unexpected field enhancement for larger angles for both materials. We generalize our results to a large class of materials by studying near-field enhancement as a function of the dielectric function of the tip material and find that increased field enhancement for larger angles persists for many materials and laser wavelengths. Technical details of the simulations as well as a comparison of

nanotips to nano-ellipsoids, for which an analytical treatment is possible in the static limit, are given in the Appendix.

## 8.2 Optical field enhancement at nanotips

The contours of the near-field $|\mathbf{E}_{\mathrm{nf}}(\mathbf{r})|$ follow the boundary of the nanostructure and the field strength decreases sharply with distance from the surface on the length scale of the radius of curvature $R$ of the nanostructure (see Fig. 46). For analytics and sensing applications, the most important property of near-fields is the strength of the enhanced near-field $|\mathbf{E}_{\mathrm{nf}}|$ in comparison to the incident field $|\mathbf{E}_{\mathrm{in}}|$ described by the field enhancement factor $\xi$. Its magnitude can be quantified through

$$\xi = \max_{\{\mathbf{r}\}} \left\{ |\mathbf{E}_{\mathrm{nf}}(\mathbf{r})| \,/\, |\mathbf{E}_{\mathrm{in}}(\mathbf{r})| \right\} \;, \tag{33}$$

where the domain $\{\mathbf{r}\}$ extends over the entire region in the proximity of the nanostructure. Typically, the field enhancement is strongest on the surface of the nanostructure.

Additionally, near-fields also feature a phase shift $\phi$ with respect to the exciting field. This can be expressed employing a generalized complex field enhancement factor $\xi = |\xi| \exp(i\phi)$ (Bouhelier et al., 2003b). When the field enhancement factor only weakly depends on the laser wavelength over the spectral width of the pulse, the phase shift $\phi$ is equivalent to a shift of the carrier-envelope phase of few-cycle laser pulses. The latter becomes an important control parameter when the pulse duration is reduced to a few optical cycles as recently demonstrated in strong-field photoemission experiments from nanostructures (Krüger et al., 2011; Piglosiewicz et al., 2014).

To describe optical near-fields at nanotips, we consider a conical nanotip (Fig. 46) with a spherical cap at the apex located in the focus of a Gaussian laser beam. This corresponds closely to the geometry often used in photoemission and second-harmonic generation at nanotips. In SNOM and TERS experiments, the tip is typically close to a surface or another nanostructure, which can also contribute to, and usually increases, the field enhancement. Another interesting setup for applications are tip arrays, where the proximity of neighboring nanotips may influence the field enhancement factor.

We numerically solve Maxwell's equations employing the finite-difference time-domain (FDTD) method, but cross-check our results with the boundary element method (BEM) as discussed in the Appendix. The parameters that characterize our setup are:

- the laser wavelength $\lambda$ and waist radius $w_0$ ($1/e^2$ intensity radius) of the focus,

- the radius of curvature $R$ and opening angle $\alpha$ of the tip (defined as the angle between the tip surface and its axis of symmetry, also called "half-opening angle", Fig. 46),

- and the optical properties of the tip material given by the frequency dependent dielectric function $\epsilon(\omega) = \epsilon_{\mathrm{r}}(\omega) + i\epsilon_{\mathrm{i}}(\omega)$ with $\epsilon_{\mathrm{r(i)}}$ the real (imaginary) part of $\epsilon(\omega(\lambda))$.
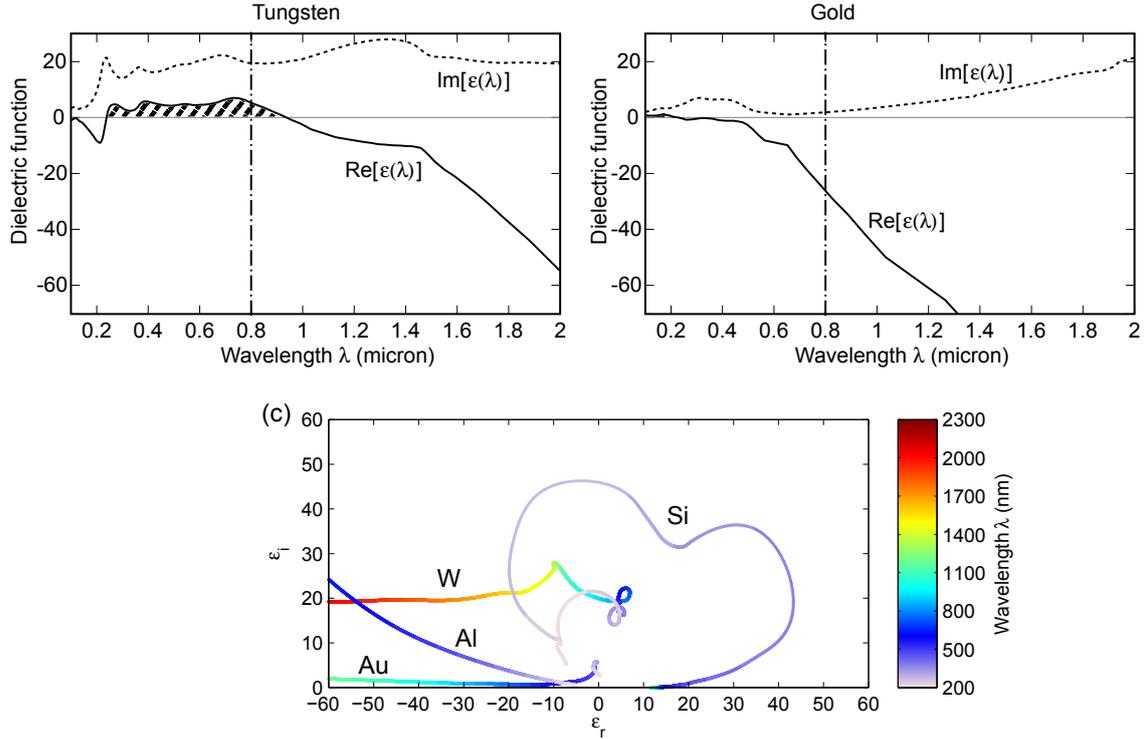
Figure 47: Dielectric function of tungsten (a) and gold (b) between 100 nm and 2000 nm (vertical dash-dotted line: 800 nm). The real part of the dielectric function of gold is smaller than zero over most of the plotted range while tungsten has a positive dielectric function over a large wavelength range (hatched area). (c) shows the "evolution" of the complex dielectric function $\epsilon = \epsilon_r + i\epsilon_i$ of some typical nanotip materials in the $\epsilon_r$-$\epsilon_i$-plane with the wavelength as parameter (color box). Data for $\epsilon(\lambda)$ taken from experimental data samples (Lide, 2004; Palik, 1991).

As the laser beam waist is found not to significantly affect the field enhancement factor, the relevant parameters are reduced to $R$, $\alpha$, $\lambda$, and $\epsilon(\omega)$. Further, we may exploit the scaling invariance of Maxwell's equations (Joannopoulos et al., 2011): an increase of the wavelength $\lambda \rightarrow \lambda' = s\lambda$ is equivalent to a decrease of the tip radius $R \rightarrow R' = R/s$ at the same value of the dielectric constant $\epsilon$. For example, the field enhancement of a tip with $\tilde{R} = 20$ nm at a wavelength of $\tilde{\lambda} = 1600$ nm at dielectric constant $\tilde{\epsilon} = \epsilon(1600\,\text{nm})$ is the same as the field enhancement calculated for a tip of $R = 10$ nm at wavelength $\lambda = 800$ nm with the same dielectric constant $\tilde{\epsilon}$. We have numerically verified this scaling. In principle, this scaling property allows a further reduction of the parameter space. However, the required constancy of $\epsilon$ as a function of $\omega$ (or, equivalently, as a function of $\lambda = 2\pi c/\omega$) imposes strong restrictions on realistic tip materials, and we hence do not exploit this scaling in the following simulations of gold and tungsten. Note that, while the maximum sharpness of the tip in applications is limited by the available fabrication technology, increasing the laser wavelength provides an attractive alternative to realize effectively sharper tips and thus obtain higher field enhancement. (Depending on the application, there may be a trade-off between higher field strengths and other
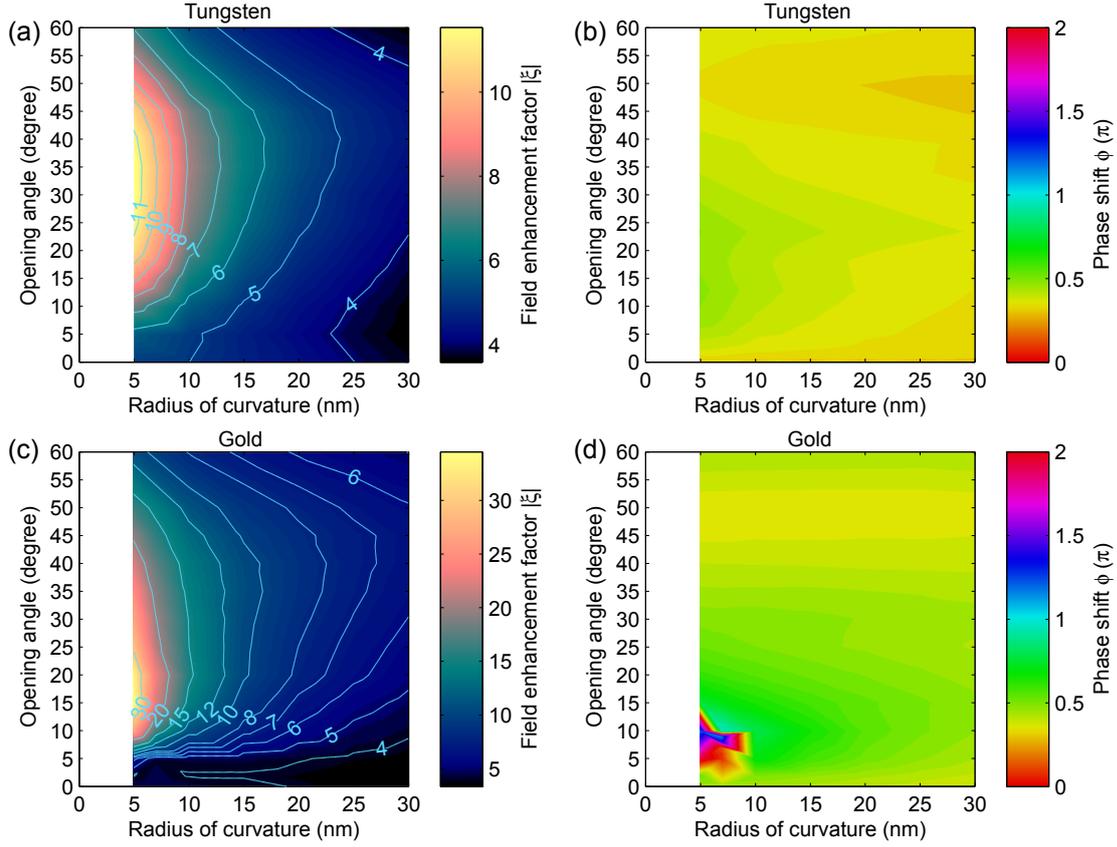
Figure 48: Complex field enhancement factor $\xi = |\xi| \exp(i\phi)$ of tungsten (a,b) and gold tips (c,d) at $\lambda = 800\,\text{nm}$ as a function of the radius of curvature of the tip and of the half-opening angle. Left column: $|\xi|$, right column: $\phi$.

effects of a longer wavelength. In strong-field photoemission of electrons, for example, increasing the wavelength decreases the efficiency (Wachter et al., 2014).)

In the following, we choose a fixed wavelength of $\lambda = 800\,\text{nm}$ for which we have previously found good agreement between experiment and simulation for small opening angles $\alpha \lesssim 5°$ (Thomas et al., 2013) and discuss the effects of the remaining parameters $R$, $\alpha$ and $\epsilon$. One goal is to separate geometry effects from material effects.

First, we investigate the influence of the tip geometry $(R, \alpha)$ on the field enhancement factor for two technologically relevant materials, tungsten and gold. At $\lambda = 800\,\text{nm}$ wavelength, these materials show a markedly different electromagnetic response (Fig. 47): The real part of the dielectric function is positive for tungsten ($\epsilon_\text{W}(800\,\text{nm}) \approx 5 + 19i$) while it is negative for gold ($\epsilon_\text{Au}(800\,\text{nm}) \approx -23 + i$) (Lide, 2004). Tungsten thus behaves in the visible and near-infrared spectral region like a "lossy" dielectric with strong absorption as $\text{Im}(\epsilon)$ is large. On the other hand, the negative dielectric function of gold, typical for metals, indicates plasmonic behavior. Corresponding eigenmodes, the surface plasmon polaritons (SPP), can be sustained at metal-dielectric interfaces. Their

damping characterized by the small imaginary part of $\epsilon$ is weak compared to other nanotip materials.

The calculated field enhancement depends strongly on both the radius and the opening angle of the nanotip (Fig. 48). For both materials, the maximum enhancement is observed for small radii of curvature as expected for the dynamic lightning rod effect that predicts a field enhancement near sharp geometric features. Somewhat unexpectedly, however, we also find a strong dependence of the field enhancement on the tip opening angle for both materials. While the two materials display a similar field enhancement for small opening angles ($\alpha \leq 5°$) in agreement with recent experiments (Thomas et al., 2013), at intermediate opening angles ($10° \lesssim \alpha \lesssim 40°$) the field enhancement is further enhanced. This enhancement is more pronounced for gold tips than for tungsten tips. Gold tips display a distinct maximum enhancement at $\alpha \approx 15°$. For tungsten, the maximum of the field enhancement is much broader and located around $\alpha \approx 40°$. For $R = 5$ nm, the field enhancement factor can reach $|\xi| = 36$ for gold tips near $\alpha = 15°$ and $|\xi| = 12$ for tungsten tips with $\alpha = 35°$. For a larger radius of $R = 30$ nm, the dependence on the opening angle is weaker but still substantial with the maximum located near $\alpha \approx 45°$ for both materials.

The phase shift also depends on both the opening angle and tip radius and is larger for gold tips than for tungsten tips. We observe the largest phase shift at intermediate angles $10° \leq \alpha \leq 30°$ for both materials. We find the absolute value of the field enhancement factor to be robust under variation of the details of the simulation while the phase shift is more sensitive (see the Appendix for details). In the region where the strongest increase of field enhancement is observed for very sharp tips, we were not able in all cases to reliably extract the phase shift from the gold simulations (for $0 < \alpha \leq 10°$ and $R \leq 10$ nm, Fig. 48 (d)). We presume that this is due to a localized surface plasmon mode at the tip apex (see below). See also the article by Anderson et al. (2010) for a discussion of plasmon resonances and their dephasing times at gold tips.

In order to explore the generality of the observed enhancement at large opening angles we varied the underlying tip geometry and considered paraboloid and hyperboloid tips. Paraboloid tips are defined entirely by the radius of curvature with their surface given by $x(y, z) = -(y^2 + z^2)/(2R)$. For gold and tungsten paraboloids with $R = 5$ nm to 30 nm, the field enhancement is similar to conical tips for the same radius of curvature and opening angles around ~10°. For hyperbolic tips, on the other hand, the radius of curvature and the asymptotic opening angle are independent parameters. There, we find that the field enhancement factor for a given radius of curvature depends significantly less on the opening angle than for conical tips. For $R = 10$ nm gold hyperboloids we obtain a field enhancement factor of ~10 independent of the opening angle. This is because, for a constant radius of curvature, the asymptotic opening angle of a hyperbolic tip has only a weak effect on the shape close to the apex and only determines the shape of the shaft far away from the apex (see 8.6.6). This indicates that the field enhancement factor depends crucially on the tip shape in the vicinity of the apex, which provides clues as to its origin.

## 8.3 Model for the opening angle dependence of the field enhancement

We turn now to the modeling of the surprising increase of field enhancement with increasing opening angles. The first key observation is that the main contribution to the field enhancement at the apex is due to the electrostatic force exerted by the surface charge distribution in a small region around the tip apex (see Fig. 49) for all tip radii, opening angles, and tip materials, indicating that retardation effects on the micrometer length scale play only a minor role. This is in agreement with the work of Van Bladel (1996) and Goncharenko et al. (2006b).

Focusing on the mechanism of field enhancement for tungsten and other dielectric materials ($\mathrm{Re}(\epsilon) > 0$), we find that the charge density distribution along the tip shaft is similar for all opening angles (see Fig. 49 (a, c)), extending about $100\,\mathrm{nm} \approx \lambda/8$ along the tip shaft. The effect of this induced surface charge along the tip shank on the enhanced near-field at the apex may be investigated within an electrostatic model. Assuming for simplicity the magnitude of the induced surface charge to be constant along the
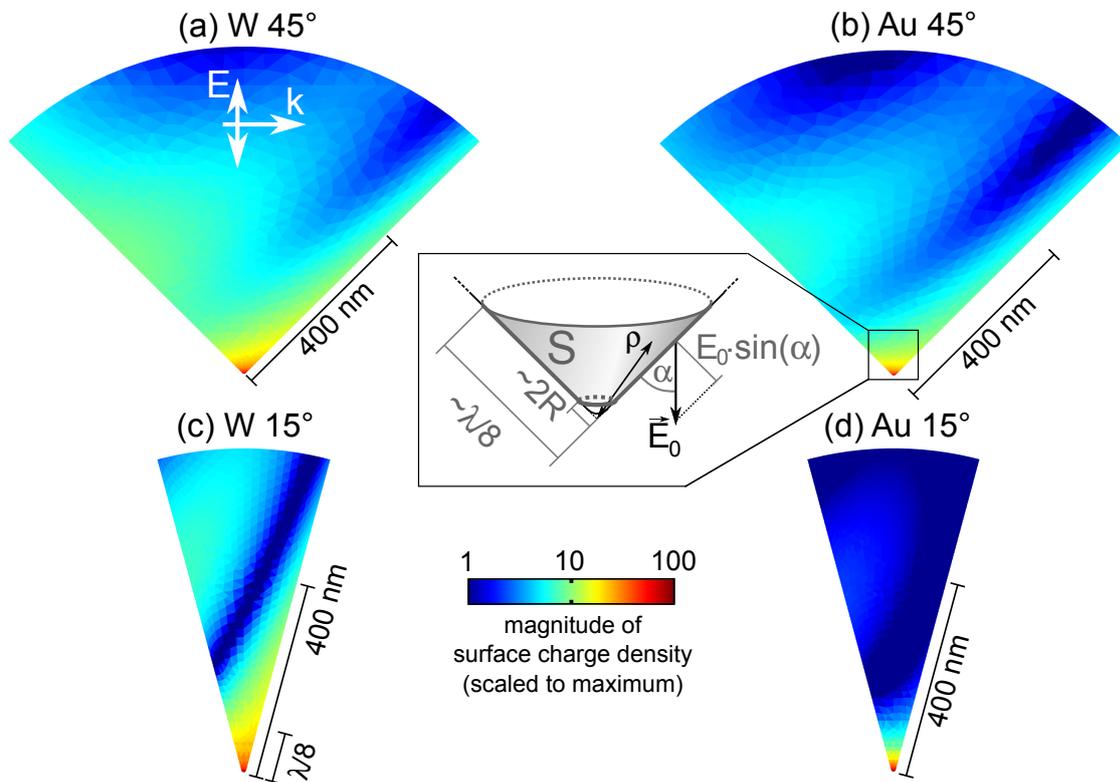


Figure 49: Absolute magnitude of the surface charge density distribution on the nanotip near the apex calculated with the boundary element method. Laser propagation direction from left to right and polarization along tip axis. All tips have a tip radius of $R = 5\,\mathrm{nm}$. Side view. (a) tungsten tip, $\alpha = 45°$; (b) gold tip, $\alpha = 45°$; (c) tungsten tip, $\alpha = 15°$; (d) gold tip, $\alpha = 15°$. Inset (b): Coordinates for electrostatic model (Eq. 34).
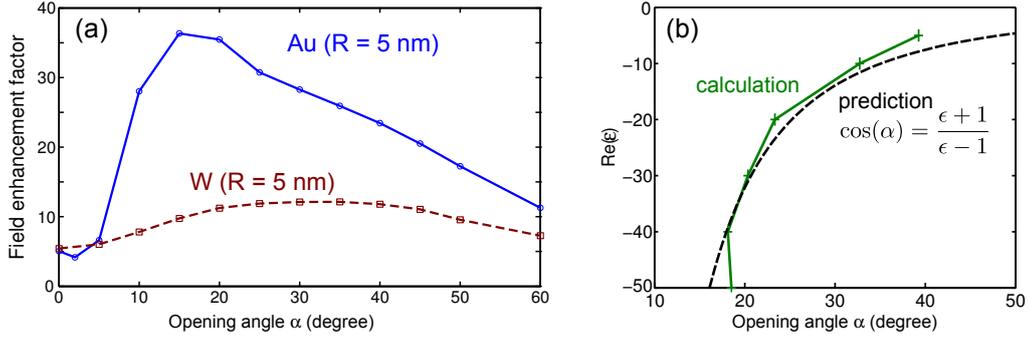
Figure 50: (a) Field enhancement factor as a function of tip opening angle for gold (blue solid line, circles) and tungsten tips (dark red dashed line, squares) with tip radius $R = 5\,\text{nm}$. (b) Maximum field enhancement factor as function of the real part of the dielectric function from FDTD simulations ($\text{Im}(\epsilon) = 5$, $R = 10\,\text{nm}$, green solid line and crosses), resonance angle according to Eq. 38 (dashed line).

tip shank near the apex in a region of size $\sim\lambda/8$ and proportional to the electric field strength perpendicular to the tip surface, the tip angle dependence of the surface charge is $\sigma_0(\alpha) \propto \sin(\alpha)$ (Fig. 49 inset). The contribution of the tip shank towards the field enhancement at the apex is

$$E^{\text{apex}}(\alpha) \approx \int_S d^2S \ \sigma_0(\alpha) \ \frac{1}{\rho^2} \quad . \tag{34}$$

The integral is taken over the surface $S$ of the tip shank from a lower limit near the tip apex ($\rho \gtrsim 2R$) to an upper limit a fraction of the wavelength away from the apex ($\rho \lesssim \lambda/8$), where $\rho$ is the distance from the apex to a point on the tip surface (see Fig. 49 inset). $E^{\text{apex}}(\alpha)$ increases with increasing opening angle because the incident field component perpendicular to the tip surface increases. Eq. 34 yields an angle-dependent component of the field enhancement

$$E^{\text{apex}}(\alpha) \propto \sin^2(\alpha) \cos^2(\alpha) \propto \sin^2(2\alpha) \ . \tag{35}$$

While the details of the angular variation depend on the assumptions for the surface charge distribution and the shape of the surface $S$, Eq. 35 qualitatively describes the observed dependence for dielectrics. This model predicts a slow rise to a maximum field enhancement around 45° in good qualitative agreement to the full calculations for tungsten where we find the maximum around 35°–40° (Fig. 50 (a)). We thus interpret the field enhancement for dielectrics as a geometrical effect that relies on the interplay between magnitude of induced surface charge $\sigma_0(\alpha)$ and the distance of the induced surface charge from the apex.

For plasmonic materials such as gold with $\text{Re}(\epsilon) < 0$, the induced surface charge at large tip opening angles resembles the result for dielectric tips (Fig. 49 (b)), indicating a qualitatively similar mechanism of field enhancement at large angles. However, the maximum field enhancement is attained at a smaller opening angle, and the maximum is

narrower than for dielectric materials (Fig. 50 (a)), pointing to an additional enhancement contribution at small angles *and* small tip radii that is not present for dielectrics. At tip angles near the maximum field enhancement, our simulations show that the charge density distribution along the tip shaft is strongly localized at the apex (Fig. 49 (d)), dominating the more extended pattern of the surface charge found for tungsten tips and larger angles. This suggests that the incident field couples to a surface plasmon mode localized at the tip apex causing the strong enhancement. The importance of surface plasmons for the observed dependence of field enhancement on the tip angle is similar to earlier work on near-field enhancement at the apex of a nanotip (Issa and Guckenberger, 2007) as a result of adiabatic nano-focusing of surface plasmons along the shaft (Babadjanyan et al., 2000; Stockman, 2004). While these observations pertain to a scenario with propagating surface plasmons and not to a localized plasmon resonance at the tip apex (Berweger et al., 2011), their similarity to the present case of the amplification of an external field suggest that surface plasmons may also play a crucial role for the field enhancement.

For a flat interface between a Drude metal with plasmon frequency $\omega_p$ (dielectric function $\epsilon_{\mathrm{Drude}}(\omega) = 1 - \omega_p^2/\omega^2$) and vacuum ($\epsilon_{\mathrm{vac}} = 1$), the resonance condition for the well-known Ritchie surface plasmon (Ritchie, 1957) at frequency $\omega = \omega_p/\sqrt{2}$ is given by

$$\epsilon_{\mathrm{Drude}}(\omega) = 1 - \frac{\omega_p^2}{\omega^2} = -1 \quad . \tag{36}$$

The generalization of Eq. 36 to a cone with semiangle $\alpha$, infinitely sharp tip ($R \to 0$), and dielectric function $\epsilon(\omega)$ reads (Goncharenko et al., 2006b; Vincent, 2009; Vincent et al., 2011)

$$\epsilon(\omega) = \frac{\cos(\alpha) + 1}{\cos(\alpha) - 1} \quad . \tag{37}$$

Eq. 37 provides the link between the resonance frequency $\omega$, the frequency-dependent dielectric function $\epsilon(\omega)$ of the material, and the geometry of the tip described by the opening angle $\alpha$. Eq. 37 can be equivalently written as

$$\cos(\alpha) = \frac{\epsilon(\omega) + 1}{\epsilon(\omega) - 1} \quad . \tag{38}$$

This resonance condition cannot be satisfied for dielectric tips where $\mathrm{Re}(\epsilon) > 0$ for any tip geometry as the right hand side is $> 1$. However, for gold at 800 nm, $\mathrm{Re}(\epsilon) = -23$ and the right-hand side of Eq. 38 predicts a resonance around $\alpha = 23°$ in good agreement to our simulations (Fig. 50 (a)). For materials in the infrared where $\mathrm{Re}(\epsilon) \to -\infty$ (compare Fig. 47), the optimal angle approaches 0°. We confirm that the localized surface plasmon predicted by Eq. 38 is indeed responsible for the field enhancement in our simulations by comparing the resonant angle $\alpha(\epsilon)$ predicted by Eq. 38 with the angle for the maximum field enhancement found in our simulations as a function of the real part of the dielectric function (Fig. 50 (b)). We find overall good agreement between Eq. 38 and our simulations whenever $\mathrm{Re}(\epsilon) < 0$. The results of our simulations are nearly independent of the precise value of $\mathrm{Im}(\epsilon)$ provided it is small, $\mathrm{Im}(\epsilon)/|\epsilon| \ll 1$.

A simple and transparent picture of field enhancement at nanotips thus emerges: For nanotips with large opening angles, the induced surface charge along the tip shank gives rise to a maximum around $\alpha = 45°$ that can be understood from electrostatics. For plasmonic tips with $\text{Re}(\epsilon) < 0$, an additional contribution arises from a localized surface plasmon mode at the tip apex, leading to even higher field enhancement and a sharper maximum at smaller angles.

## 8.4 The dependence on the dielectric function

To extend our results from tungsten and gold to other materials, we performed simulations varying the real and imaginary parts of the dielectric function of the tip material (Fig. 51). We fixed the tip radius at $R = 10\,\text{nm}$ and varied the opening angles between 0° and 30°. The field enhancement factor increases with increasing tip opening angle for any given value of the dielectric function. However, as a function of $\epsilon$, $\xi(\epsilon)$ varies significantly for a given opening angle. For slim tips ($\alpha = 0°$, Fig. 51 (a)), the field enhancement increases with increasing absolute value of the dielectric constant $|\epsilon|$. For $\alpha \geq 10°$, the field enhancement has a sharp maximum at negative real values of the dielectric function, for example at $\epsilon \approx -10 + 0i$ for $\alpha = 30°$ (Fig. 51 (g)). This is interpreted in terms of the plasmon resonance expected around $\text{Re}(\epsilon) = -14$ for $\alpha = 30°$ (Eq. 37). With decreasing tip angle $\alpha \to 0$, Eq. 37 predicts that this resonance moves towards $\text{Re}(\epsilon) \to -\infty$, and we qualitatively observe that the maximum field enhancement and phase shift moves along the $\text{Im}(\epsilon) = 0$ axis towards $\text{Re}(\epsilon) \to -\infty$ with decreasing tip opening angle. Therefore, and at first glance surprisingly, the plasmon resonance does not play a significant role for tips with very small opening angles below 5° and for small absolute values of the dielectric function $|\epsilon|$ found for materials in the optical wavelength range (Fig. 47 (c)). This is the reason why the enhancement factors for plasmonic and dielectric materials closely resemble each other for small opening angles.

The results from Figs. 48 and 51 can be used to roughly estimate the field enhancement factor for other tip materials, radii $R'$ and wavelengths $\lambda'$ than those discussed here. From the value of $\epsilon$ for the material and wavelength in question, the complex $\xi$ for a given opening angle can be obtained from Fig. 51. The so obtained result, however, is only correct for an effective tip sharpness $\kappa = \lambda/R = 800\,\text{nm}/10\,\text{nm}$. The behavior of $\xi$ for a different sharpness $\kappa' = \lambda'/R'$ can be approximated by scaling $\xi$ based on Fig. 48, where the field enhancement factor at $R = 10\,\text{nm}$ should be compared to an effective radius of $800\,\text{nm}/\kappa'$. Depending on how far $\epsilon$ and $\kappa'$ are from the parameters discussed in this article, the resulting $\xi$ can be a good approximation or it may only indicate a trend.

## 8.5 Conclusion

We have explored the material and geometry dependence of optical near-field enhancement at nanostructures with the nanotip geometry taken as the prototypical example.
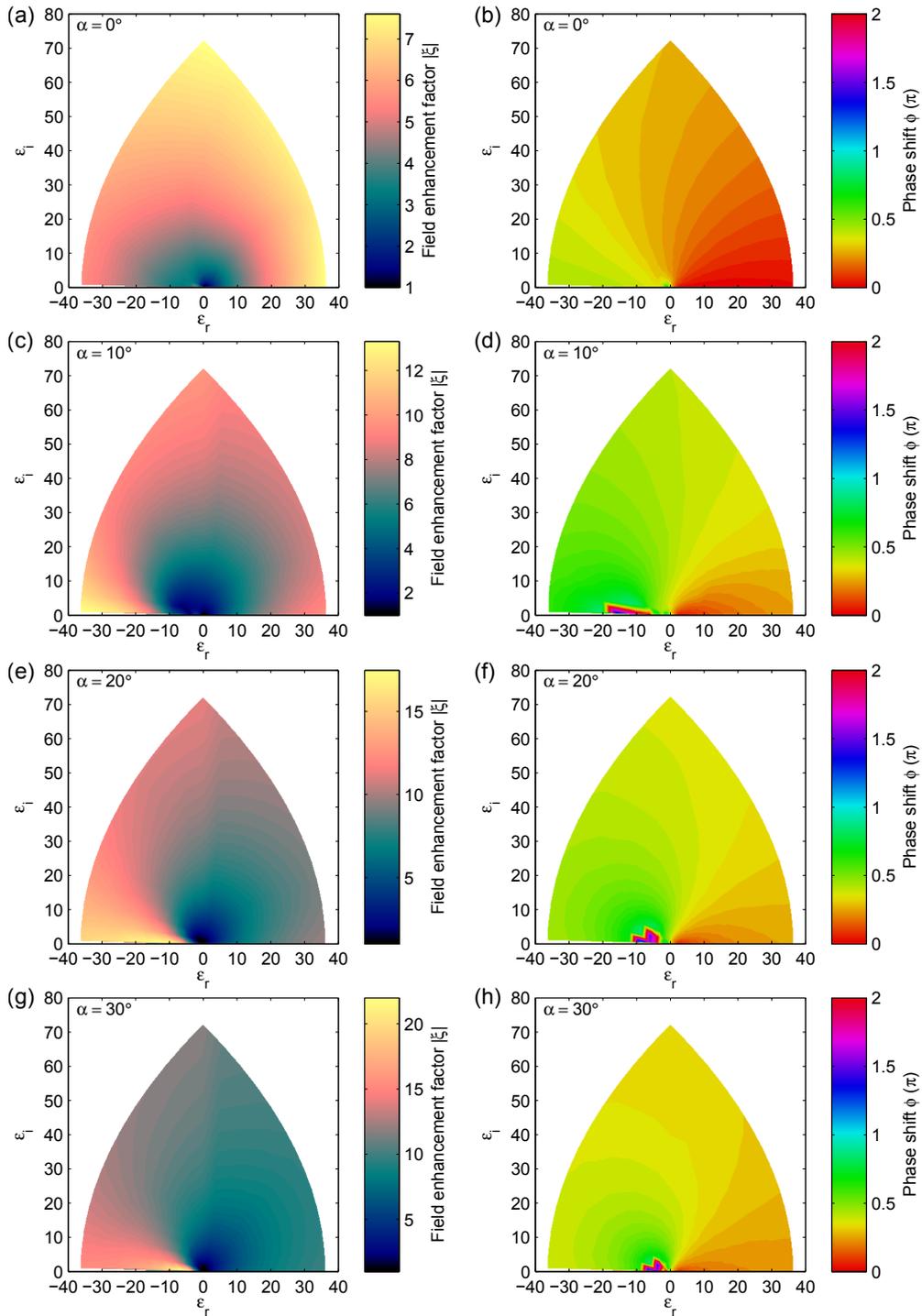
Figure 51: Complex field enhancement factor $\xi = |\xi| \exp(i\phi)$ of $R = 10\,\text{nm}$ tips at $\lambda = 800\,\text{nm}$ as a function of the tip's dielectric constant for opening angles 0° (a,b), 10° (c,d), 20° (e,f), and 30° (g,h) for a selected region in the $\text{Re}(\epsilon)$, $\text{Im}(\epsilon)$ plane covering the range of dielectric functions of many materials at optical wavelengths (see Fig. 47 (c)). Left column: $|\xi|$, right column: $\phi$.

We have discovered that, somewhat counterintuitively, larger field enhancement can be achieved for larger half-opening angles (20° to 40°) of the tip. This enhancement for fixed radius of curvature was found for both tungsten, exemplifying a dielectric response, and gold, a plasmonic material. Two processes contributing to this enhancement could be identified: For large opening angles, the increase of field enhancement can be understood from the electrostatic force of the induced surface charge along the tip shank. This mechanism is effective in both dielectric and plasmonic materials. For the latter, excitation of localized surface plasmons at the apex gives rise to even stronger enhancement at intermediate angles. Varying the real and imaginary part of the dielectric function, we found the same qualitative behavior for a large number of materials, including other practically relevant materials such as aluminum, iridium, palladium, platinum, silicon, and silver. Our results indicate that, compared to currently employed tip shapes, a further field enhancement of magnitude 2 to 4 is achievable by employing tips with larger opening angles. We expect that such tips will provide a substantially increased signal especially for non-linear applications. Note that, while the highest field enhancement factors occur at plasmon resonances, an advantage of off-resonant field enhancement is that it depends less sensitively on the wavelength, which enables working with broadband ultrashort pulses, even in the single-digit femtosecond pulse duration range.

The strong dependence of the enhancement on the tip geometry and not just on the radius of curvature may explain the many different values for the field enhancement factor of gold tips that have been reported in the literature, especially considering that the realistic shape of nanotips is more irregular than the conical tips employed in our simulations. The increase of field enhancement up to an optimal angle of 20°−40° depending on the tip material has escaped earlier studies (Martin et al., 2001) presumably because the dependence on the opening angle was not sampled in sufficiently fine resolution. Our results suggest that higher field enhancement factors $|\xi| > 10$ should be possible even for tungsten tips and other dielectric materials. This is consistent with a recent report of a field enhancement factor of ∼10 for silicon tips with a large opening angle (Swanwick et al., 2014). One reason why we did not observe higher field enhancements in our previous experiments with tungsten (Thomas et al., 2013; Schenk et al., 2010; Wachter et al., 2012) may be related to the etching method we use for tungsten tips, which results in a small opening angle (Klein and Schwitzgebel, 1997).

Our results may have ramifications for scanning near-field optical microscopy, tip-enhanced Raman spectroscopy and other techniques that rely on large field enhancement factors at rugged tips. Modern nanofabrication techniques such as focused ion beam etching could easily lead to the desired tip shape and larger enhancement factors.

## 8.6 Appendix

### 8.6.1 FDTD: simulation setup

Our FDTD simulations of the field enhancement near nanotips were carried out using Lumerical FDTD Solutions, a commercial Maxwell solver. Our simulations encompass a cubic volume $V = X \times Y \times Z$ with the tip apex at the origin $\mathbf{r} = 0$ and the tip shaft along the positive $x$ axis (Fig. 46 is flipped $x \rightarrow -x$ with respect to the coordinates used in our simulation). The exact size of the volume depends on the parameters of a given simulation, as discussed below. As the volume that can be simulated with the FDTD algorithm is necessarily finite, care needs to be taken in the setup of the simulation to avoid unphysical antenna resonances due to the finite length of the simulated tip (see Fig. 52 for an example) (Martin et al., 2001; Zhang et al., 2009). We find that the results do not depend on the length of the tip and the size of the focus if one includes the focal spot inside the simulation volume and ensures that the laser's electric field at the simulation boundaries lateral to the propagation of the beam is negligible. We choose the size of the volume accordingly. Typical values are $X = Y = 8000\,\text{nm}$, $Z = 1000\,\text{nm}$.

The volume is meshed with a rectangular grid of non-constant resolution. At the tip apex, the resolution is considerably higher than in free space at a distance from the tip: the mesh node distance varies from approximately 50 nm in free space to 0.1 nm at the apex of the sharpest tip we simulate.

The laser is modeled as a Gaussian beam with the wave vector parallel to the $z$ axis and the polarization parallel to the $x$ axis and, thus, the tip shaft. The source area (i.e., the area where it enters the simulation) is at the negative $z$ boundary. In our time-domain simulation method, we employ a short laser pulse of duration 5 fs (intensity full width half maximum). Therefore, the laser light has a spectral width $\Delta\lambda$. We have
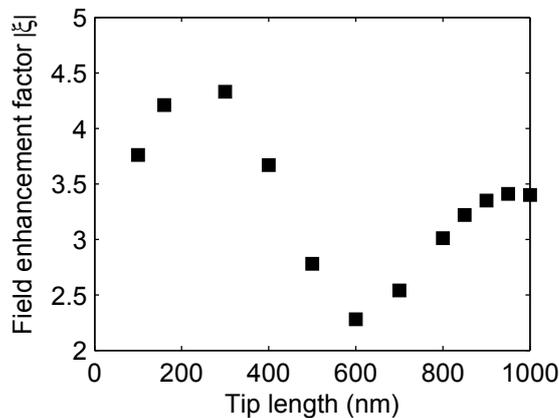


Figure 52: Extracted field enhancement factor as function of tip length for a finite tungsten tip in a plane-wave excitation; the distance between the two peaks is close to the laser wavelength of 800 nm, a clear sign of antenna resonance. The enhancement factor changes by about a factor of 2 for different tip lengths. This shows that simulating a finite tip in a plane-wave excitation cannot give the correct field enhancement factor for a larger nanotip in a laser focus.

verified in several tip geometries that the pulse duration has negligible effects on the field enhancement factor, so our results are also valid for longer pulses and continuous-wave excitations. This would be different for sharp resonances that critically depend on the wavelength. We did not observe such effects for the geometries under investigation.

The nanotip's optical properties are given by a dielectric function $\epsilon = \epsilon_r + i\epsilon_i$, which we obtain from experimental data samples of bulk metal (Haynes and Lide, 2011). As with the pulse duration, the variation of $\epsilon(\lambda)$ for the spectral range of the laser pulse has no effect on field enhancement for the materials we studied in our simulations. This may be different for materials and wavelengths where $\epsilon(\lambda)$ varies rapidly, for example near bulk plasmon resonances.

It is useful to consider the effect of variations $\Delta\epsilon$ from the values of the dielectric constant we assume in our simulations. These could be due to measurement uncertainties in the experimental data samples we use (see the paper by Olmon et al. (2012) for a recent measurement of $\epsilon$ for gold and a comparison to older results). Additionally, a weak dependence of the dielectric constant on the structure size has been found for metal nanostructures smaller than the mean free path of conduction band electrons (Stoller et al., 2006). Another factor that may affect the dielectric constant is the grain size in polycrystalline nanotips (Trollmann and Pucci, 2014). As Fig. 51 shows, small changes of the dielectric constant do not significantly alter the field enhancement factor except when close to a plasmon resonance. For example, a small shift $\epsilon = 5 + 19i \rightarrow 6 + 20i$ on the complex plane only changes the resulting field enhancement by ~2.5% for 20° tungsten tips (Fig. 51 (e)). Larger effects of a small $\Delta\epsilon$ are quite rare and only observed close to resonance: for example, also at $\alpha = 20°$, a shift $\epsilon = -10 + i \rightarrow -9 + 2i$ changes the field enhancement factor by ~20%.

A challenge for FDTD simulations of optical field enhancement are plasmonic tips (i.e., materials with $\epsilon_r \ll -1$ and small $\epsilon_i$, such as gold at 800 nm) as they can cause a variety of numerical artifacts related to the appearance of surface plasmons (Novotny and Hecht, 2006; Raether, 1988), which are excited at the apex and propagate along the tip shaft. Due to the rectangular FDTD mesh grid, the propagation of these plasmons is difficult to simulate (except for $\alpha = 0$) as they can scatter at the discrete steps of the material boundary, causing high loss. In some cases, such discretization errors can lead to unforeseen localized resonances along the tip shaft where electric fields may be 'stuck' long after the laser pulse and surface plasmons are gone. Increasing the mesh resolution along the tip shaft does not prevent the appearance of such numerical artifacts due to the mismatch between the Cartesian grid and the local direction of the tip boundary. However, while these localized resonances hinder simulations of plasmon propagation on the conical shaft for $\alpha \neq 0$ which would be of importance for plasmonic nanofocusing (Stockman, 2004), we found that the field enhancement factor at the apex could still be reliably calculated in almost all cases. Only for sharp gold tips ($R < 10$ nm) with a small but non-zero opening angle near the plasmon resonance (Eq. 38), which exhibit the largest "steps" due to discretization errors discussed above, we observe an effect that prevents a correct simulation of near-field enhancement at the apex. At such tips, surface plasmons are coupled in at the shaft near the apex at the steps caused by discretization errors and propagate along the shaft from there, interfering with the
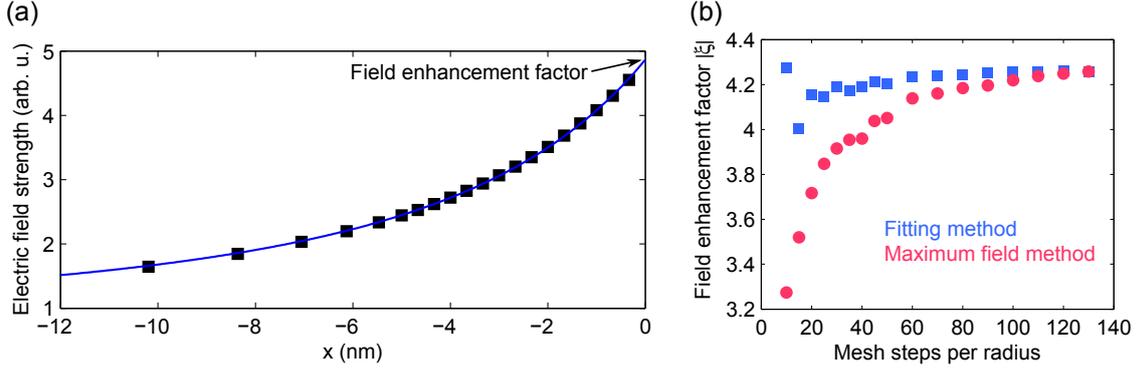
Figure 53: (a) Example of the fitting method. The black dots are on-axis ($y = 0, z = 0$) simulation results of the electric field at the moment of the greatest enhancement. The blue line shows a fit using Eq. 40. (b) Field enhancement factor of a tungsten tip as as function of the mesh resolution near the apex, obtained by different methods: taking the maximum (red circles) and applying a quadratic fit (blue squares). Clearly, the fitting method is computationally less expensive. We typically use 30 or 40 mesh steps per radius for the simulations.

near-field at the apex. This leads to an increased uncertainty for the field enhancement factor, and it can sensitively influence the phase shift.

The simulations were carried out on a desktop computer with an Intel Xeon CPU W3530 at 2.8 GHz and with 18 GB RAM. A single simulation typically took a few hours to complete. (This varied significantly depending on the simulation volume and the mesh resolution.) We exploit the symmetry of the setup with respect to reflection at the $y = 0$ plane to reduce computation time and memory requirements.

## 8.6.2 FDTD: obtaining the field enhancement factor

The magnitude of the field enhancement factor $|\xi|$ is defined as the ratio of the maximally enhanced field strength to the driving field strength. The amplitude of the driving laser pulse in the bare focal plane ($z = 0$) is set to 1 in our simulations. In principle, the field enhancement factor could therefore be obtained by simply taking the maximum of the electric field strengths $\mathbf{E}(\mathbf{r}, t)$ in a simulation:

$$|\tilde{\xi}| = \max_{x,y,z,t} |\mathbf{E}(\mathbf{r}, t)|. \tag{39}$$

However, there are several problems with this approach due to numerical limitations and artifacts. As the electric field strength decreases monotonically with distance from the tip surface, the maximum field strength is always found at a point of the simulation next to the material-vacuum boundary, and depends on the placement of the last grid point with respect to the boundary. Therefore, $|\tilde{\xi}|$ depends on the mesh resolution of the simulation at the boundary of the tip apex. A second problem arises due to stair-casing effects, which may cause an unrealistically high electric field strength at single points of the simulation. This effect is particularly noticeable for plasmonic materials.

To avoid the numerical problems related to simply taking the maximum, we use a more robust and efficient method to obtain $|\xi|$, as illustrated in Fig. 53. Note that the highest field enhancement occurs in the plane of symmetry if the laser polarization is parallel to the tip axis. Additionally, for the tips we investigate ($R \leq 30\,\text{nm}$ and $\lambda = 800\,\text{nm}$), the maximum is at or very close to the tip axis $y = z = 0$. It is therefore sufficient to analyze the on-axis electric fields $\mathbf{E}(x, 0, 0, t)$ in order to obtain the field enhancement factor. The deviation in strength from the actual field maximum is around 6 % for 30 nm radius and less than 1 % for 5 nm radius. If we investigated larger tip radii or, equivalently, smaller wavelengths, the maximum field strength would shift further away from the axis (Yanagisawa et al., 2010) and we would have to take this asymmetry into account.

We obtain the field enhancement factor in the following way. First, we find out the time of the greatest enhancement $t_{\text{max}}$ by locating $\max_t |\mathbf{E}(\mathbf{r}', t)|$ at a point $\mathbf{r}'$ close to the tip apex. Then, we consider the electric field at $t = t_{\text{max}}$ on the $y = z = 0$ line outside the tip ($x < 0$) and fit a quadratic decay

$$f(x) = \frac{a}{(x - x_0)^2} + f_{\text{bg}} \tag{40}$$

to it. We extrapolate the fit function back to the tip surface at $x = 0$, and the value of the fit function at this point yields $|\xi|$. In the fit function, the $1/(x - x_0)^2$ term models the near-field and $f_{\text{bg}} = \cos(\phi)$ is the background field strength of the exciting laser pulse. While the background field amplitude is 1, $f_{\text{bg}}$ also takes the phase shift $\phi$ between near-field and exciting field into account. For the phase shift, see below. $a$ and $x_0$ are the free fit parameters. An example of such a fit is shown in Fig. 53 (a). Note that we only evaluate the fit function and the simulation results on a line that is much smaller than the waist radius $w_0$, so we can assume the background field strength to be constant.

It should be noted that it is not clear from the simulations that the near-field decreases quadratically with distance. In fact, fit functions with powers of 1 to 3 produce an almost equally good fit and yield approximately the same field enhancement factor. If the power itself is allowed to vary in the fit, we obtain non-integer powers between 1 and 3, with different results for different simulations. This is unlike the near-field at nanospheres, for example, which shows a third-order decrease with the singularity exactly at the center of the sphere (Maier, 2007). We have chosen a quadratic fit function because it leads to a position of the singularity $x_0$ close to the center of the sphere at the tip apex. In any case, the choice of fit function changes $\xi$ only insignificantly (by ~1.5 % in the example of Fig. 53 (a)).

A comparison of the enhancement factors obtained by fitting and by simply taking the maximum is shown as a function of the mesh resolution in Fig. 53 (b). The field maximum converges much more slowly than the quadratic fit method, which deviates by less than 5 % from the final value of $\xi$ even for low resolutions, i.e., few mesh steps per radius. They both converge to the same value. This shows that stair-casing effects do not cause unrealistically high field strengths in this series of simulations.

We conclude that the near-field around the tip apex is already modeled correctly at lower resolutions (~40 steps per radius) and that the additional dependence on the mesh resolution comes only from the discretization of the mesh, which we can efficiently

circumvent by extrapolating the near-field to the surface of the tip as described above. As a compromise between precision of the results and computational resource requirements, we used a mesh resolution of $R/40$ as function of tip radius $R$ for all simulations except the ones where we vary the dielectric function of the tip (Fig. 51). There we used a mesh resolution of $R/30$ to speed up the computations.

The phase shift $\phi$ can be obtained by comparing the zero-crossing of the near-field close to the tip with the zero-crossing of the undisturbed pulse at negative $x$. Due to the limited temporal resolution of our simulations and numerical dispersion (Taflove and Hagness, 2005) that shifts the carrier-envelope phase in a mesh-dependent way, this method comes with an unavoidable error, which we estimate to be around $\Delta\phi \approx 0.05\pi$ by comparing simulations of the same nanotip with different mesh resolutions and simulation volumes. With knowledge of both the phase shift and the magnitude of the enhancement, we can completely characterize $\xi = |\xi| \exp(i\phi)$.

In a final step, we apply a correction $\xi \rightarrow \xi/0.95$ to the field enhancement factor. The value of 0.95 is obtained from simulations of the laser pulses without including the nanotip. This correction factor compensates pulse propagation effects in the simulation, which reduce the amplitude of the exciting pulse in the focal plane. We attribute these effects to both numerical dispersion and our use of Gaussian pulses in a regime where the waist radius $w_0$ is of the same order of magnitude as the wavelength $\lambda$.

### 8.6.3 Boundary element method

To rule out systematical errors from the space discretization and time integration in the FDTD simulations, we double-checked the reliability of our simulations by also numerically solving Maxwell's equations with the boundary element method (BEM) as implemented in the public-domain SCUFF-EM package (scuff-EM, 2015; Homer Reid et al., 2013; Homer Reid and Johnson, 2013). Being a frequency-domain method, the boundary element method is free from time integration errors that contribute to the errors in FDTD. Time-domain quantities can be reconstructed by superimposing many frequency components and the convergence of this Fourier synthesis can be checked by increasing the frequency range and resolution. The boundary element method takes advantage of the analytically known solutions of Maxwell's equations in homogeneous media, so that only the surface of the tip is discretized. This can lead to lower memory requirements and improved scaling compared to FDTD, where the three-dimensional simulation volume must be discretized. Importantly, this smooth discretization of the tip surface also allows us to assess the influence of the Cartesian grid that is employed in the FDTD simulations leading to staircasing artifacts.

A typical simulation run proceeds as follows. The tip geometry is defined depending on the geometrical parameters tip radius and opening angle as for the FDTD calculations. First, the surface of the tip is discretized into $N_{\text{panels}}$ triangles employing the public-domain meshing software gmsh (Geuzaine and Remacle, 2009). We use an adaptive mesh to resolve the small-scale features of the near-field around the tip apex with discretization steps of 0.2 nm near the apex. The remainder of the tip is discretized in larger steps of about 1 nm to 20 nm that resolve the geometry of the tip and are much smaller than

the wavelength of surface plasmons that can be excited at the sharp tip apex. The total length of the simulated tip was between 1.7 micron and 6 micron. The inside of the tip is designated the experimental dielectric bulk constant of the material at the working wavelength (Palik, 1991). The incident field is chosen as a focused laser beam as for the FDTD results (Sheppard and Saghafi, 1999). The boundary element method solver SCUFF-EM is then employed to solve for the electromagnetic fields where the numerical cost scales with the size of the BEM matrix, $\sim N_{\mathrm{panels}}^2$. For the calculations presented in this paper, $N_{\mathrm{panels}} \approx 10000$ which corresponds to ~15 GB of RAM. After the BEM matrix equations are solved by standard linear algebra methods, the electric near-field in the region 0.05 nm in front of the tip axis is evaluated and extrapolated to the tip apex. The field enhancement and phase shift are then given by the absolute value and phase of the ratio of the total field perpendicular to the tip surface to the incoming field along the tip axis. The field enhancement is only weakly dependent on the laser wavelength so that the phase shift corresponds to a carrier-envelope phase shift for few-cycle laser pulses when the time-dependent near field is reconstructed by a Fourier transform.

The boundary element method is restricted to piecewise homogeneous material configurations, so that absorbing boundaries like perfectly matched layers that exist for FDTD or finite element methods are precluded. This can lead to problems for materials where the propagation length of surface plasmons on the structure of interest is larger than the size of the structure that can be modeled. For tungsten, which has a large imaginary part of the dielectric function around 800 nm, excitations from the tip apex propagating along the tip shaft decay rapidly (typically within 200 nm (Sarid and Challener, 2010)). However, the situation changes for plasmonic materials like gold where the propagation distance of surface plasmons can be up to several tens of microns, rendering the simulation of the mesoscopic structure up to the length where the plasmons are fully decayed numerically infeasible. We instead use tips of a few micron length also for plasmonic materials and exploit the fact that, for short enough pulses, the incident and reflected electric fields are well separated in time. In frequency space, the reflections of surface plasmons from the back end of the tip contribute to the near-field at the tip apex, leading to unphysical peaks in the electric near-field at frequencies that change for different tip lengths ("antenna resonances"). We filter out the contributions of the reflected surface plasmons by transforming to the time domain and only taking into account the short-time response to a few-cycle laser pulse, as the surface plasmon wave packet that is reflected from the back end of the tip will be delayed by at least 7 fs per micron tip length (speed of light $c \approx 300$ nm/fs). We find that, while the interference pattern stemming from the antenna resonances changes with increasing tip length, the short-time behavior calculated by a Fourier transform of the laser spectrum is well converged if the incident and reflected wave packets are well separated in time, which can be achieved by a tip length substantially below the surface plasmon propagation length. This low-pass filter in the time domain corresponds to filtering out the high-frequency oscillations of the antenna resonances in frequency space, i.e., smearing out the interference fringes over the spectrum of a short incident laser pulse. The BEM
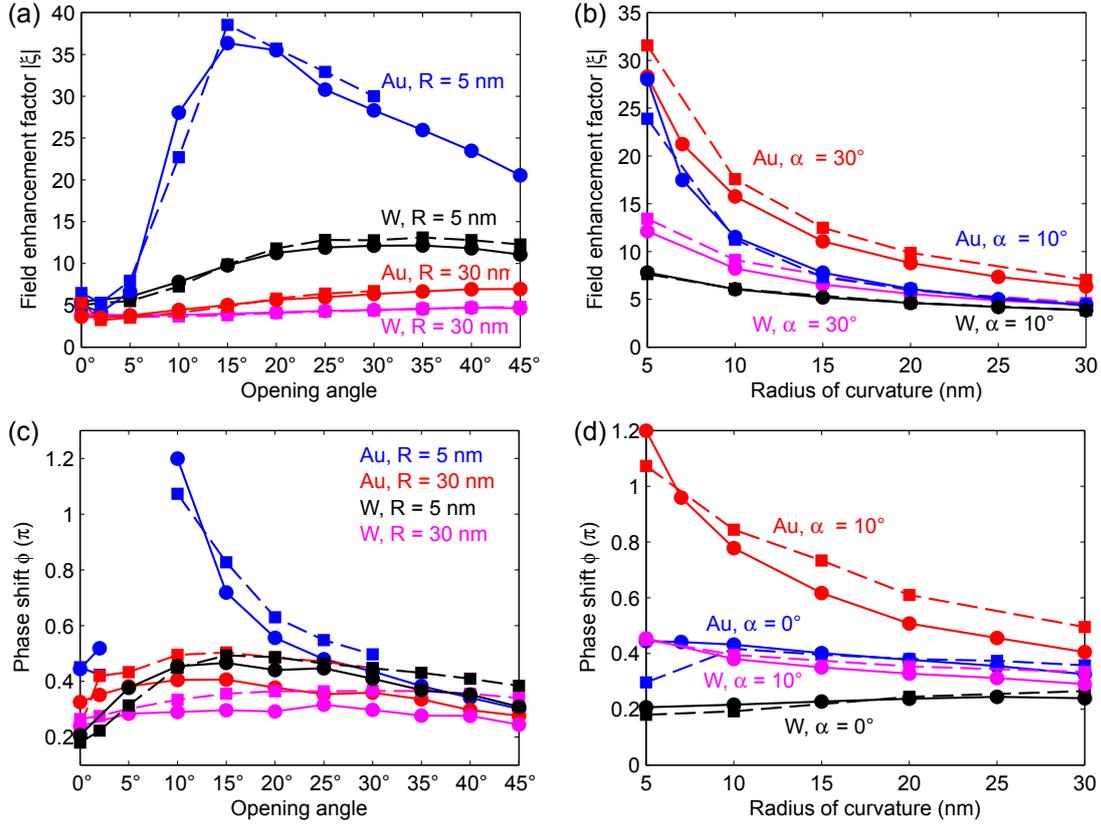
Figure 54: Comparison between FDTD results (circles connected by solid lines) and BEM results (squares connected by dashed lines) for the field enhancement factor $|\xi|$ (a,b) and phase shift $\phi$ (c,d) in different geometries. The missing values for the phase shift of $R = 5$ nm gold tips around $\alpha = 5°$ are due to the numerical problems with this geometry, as discussed in appendix 8.6.1.

calculations for plasmonic materials, where simulations at several wavelengths must be combined, are thus significantly more costly than those for non-plasmonic materials.

## 8.6.4 Comparison between FDTD and BEM results

In Fig. 54, we compare results for the field enhancement factor and phase shift of nanotips obtained from simulations using either the finite-difference time-domain method (FDTD) or the boundary element method (BEM). Shown here are results for different geometries of tungsten and gold tips. In general, we find a good agreement between the two numerical methods. As discussed above, gold tips are more challenging to simulate than tungsten tips for both the FDTD and BEM methods, so it is not surprising that the agreement between the two methods is somewhat better for tungsten than for gold.

The field enhancement factor obtained by the two methods typically agrees within ~10 %, with the exception of a few particular geometries in the vicinity of the plasmon resonance like $(R = 5\,\mathrm{nm}, \alpha = 10°, \mathrm{Au})$ in Fig. 54 (a), where we observe deviations of

around 20 %. For the phase shift, the deviation between the two methods is approximately $0.1\,\pi$.

We conclude that the results presented in this article do not exhibit significant systematic errors due to the choice of simulation method, and that both FDTD and BEM are well suited for the simulation of near-fields at nanotips.

### 8.6.5 Comparison to nano-ellipsoids

To elucidate the relationship between field enhancement and dielectric function, we compare our simulations for nanotips to the near-field of ellipsoids for which an analytic solution is available in the static limit (Martin et al., 2001; Bohren and Huffman, 2008; Sarid and Challener, 2010), see also the article by Neacsu et al. (2005a) and the textbook by Novotny and Hecht (2006). For a rotationally symmetric ellipsoid with two equal axes $b = c$ and a major axis $a$ along the polarization direction, the complex field enhancement factor for a given $\epsilon(\lambda)$ is (in the limit $a, b, c \ll \lambda$)

$$\xi(\lambda) = \frac{\epsilon(\lambda)}{1 + [\epsilon(\lambda) - 1]\,A(r)} \tag{41}$$

with the so-called shape factor $A(r)$ depending on its aspect ratio $r = a/b$,

$$A(r) = \frac{1}{1 - r^2} - \frac{r\,\arcsin\left(\sqrt{1 - r^2}\right)}{(1 - r^2)^{3/2}}. \tag{42}$$

The shape factor varies smoothly from $A(r \to 0) = 1$ for pancake-like oblate ellipsoids via $A(r = 1) = 1/3$ for spheres to $A(r \to \infty) = 0$ for cigar-like prolate ellipsoids. The resulting field enhancement (Eq. 41) assumes its minimum around $\epsilon \to 0$ while its maximum is found at the dipole resonance at the pole of Eq. 41, i.e., for

$$\epsilon = 1 - 1/A(r)\ . \tag{43}$$

Eq. 43 encodes the relationship between dielectric function and geometry in analogy to Eq. 37 with the aspect ratio playing a similar role as the tip opening angle in Eq. 37. For nano-spheres ($A(r = 1) = 1/3$, Fig. 55), we find $\epsilon = -2$, thereby recovering the first Mie plasmon at $\omega = \omega_p/\sqrt{3}$ for a Drude metal ($\epsilon_{\mathrm{Drude}}(\omega) = 1 - \omega_p^2/\omega^2$). Away from the resonance, the field enhancement for a nanosphere asymptotically approaches $\xi(|\epsilon| \to \infty) = 1/A(1) = 3$.

For other aspect ratios, the overall shape of $\xi(\epsilon)$ remains the same while its value $\xi(|\epsilon| \to \infty)$ changes. For any aspect ratio, a resonance is only attainable for materials with a negative dielectric function $\mathrm{Re}(\epsilon) < 0$. The transition from a sphere to a needle-like ellipsoid changing the shape factor from $A = 1/3$ to $A \to 0$ in Eq. 41 magnifies the region of appreciable field enhancement. This is illustrated by comparing Fig. 55 with Fig. 56 (c, d), which shows $\xi(\epsilon)$ for an elongated ellipsoid with aspect ratio 3.5. As the aspect ratio increases, the position of the resonance moves to more negative values of $\mathrm{Re}(\epsilon)$.
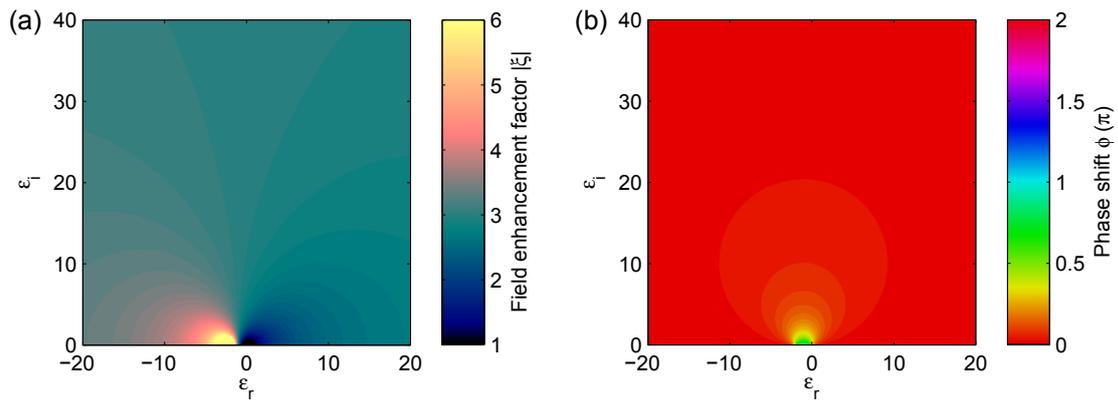
Figure 55: Complex field enhancement factor $\xi = |\xi| \exp(i\phi)$ of nanospheres (aspect ratio $r = 1$, shape factor $A = 1/3$) with radius $R \ll \lambda$ obtained from Eq. 41. (a) $|\xi|$, (b) $\phi$.
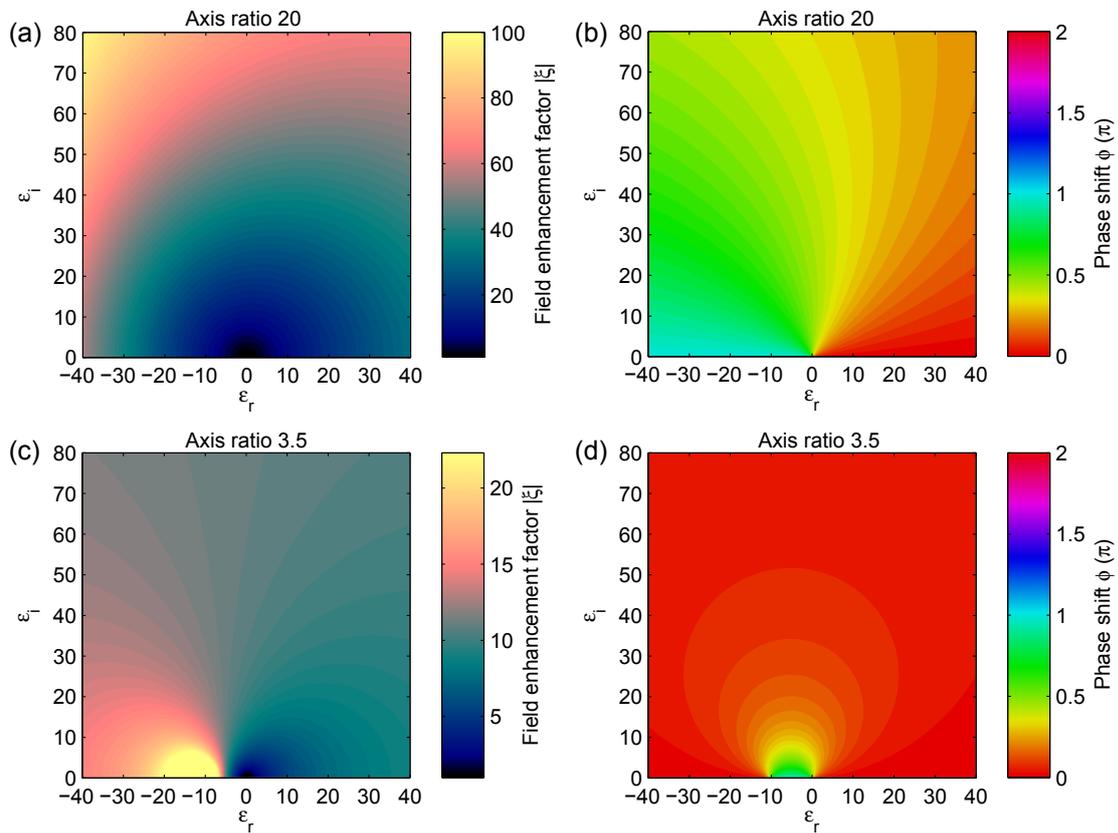


Figure 56: Complex field enhancement factor $\xi = |\xi| \exp(i\phi)$ of ellipsoids with aspect ratios 20 (a,b) and 3.5 (c,d) as a function of the dielectric constant $\epsilon = \epsilon_r + i\epsilon_i$, according to Eq. 41. Left column: $|\xi|$, right column: $\phi$.
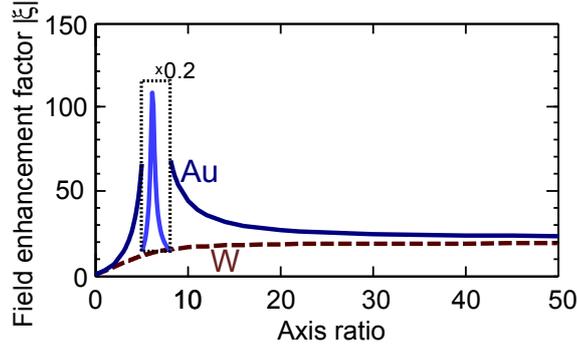
Figure 57: Field enhancement factor $|\xi|$ of tungsten (red dashed) and gold (blue solid) nano-ellipsoids at $\lambda = 800\,\text{nm}$ (Eq. 41). For better visibility, the field enhancement of gold between 5° and 8° is scaled by 0.2 (dotted box).

The field enhancement factor of a needle-like ellipsoid with a large aspect ratio $r = 20$ (Fig. 56 (a, b)) resembles the extreme case $r \to \infty$, where the field enhancement factor is simply $\xi(\epsilon) = \epsilon$. The same result was found for paraboloids in the quasi-static approximation (Chang et al., 2009). The increasing enhancement of the electric field with increasing discontinuity of $|\epsilon|$ at the ellipsoid's boundary can be interpreted as broadband field enhancement due to the lightning rod effect (Thomas et al., 2013). The other extreme case of a pancake-like surface, $r = 0$, yields a vanishing field enhancement $\xi(\epsilon) = 1$.

The near-field at nano-ellipsoids is qualitatively similar to nanotips, with the aspect ratio of the ellipsoid playing a role analogous to the opening angle of the tip. Comparing Fig. 51 and Fig. 56, we find that slim nanotips $\alpha = 0°$ behave similarly to slim ellipsoids with aspect ratio 20 (increasing enhancement factor with $|\epsilon|$, increasing phase shift for larger angles $\arg(\epsilon)$), while broader nanotips with opening angle $\alpha = 30°$ are similar to broader ellipsoids with aspect ratio ~3.5 (broad plasmon resonance in the $\epsilon_r < 0$ region, large phase shift in between 0 and the resonance).

The angle dependence of tungsten and gold tips (Fig. 50 (a)) may be compared to the aspect ratio dependence of tungsten and gold ellipsoids (Fig. 57). The latter show low field enhancement for small aspect ratios and converge to approximately the same enhancement factor of ~20 for high aspect ratios as they share a similar value of $|\epsilon|$ at $\lambda = 800\,\text{nm}$ (see Fig. 47). In between, however, the behavior is different: While the field enhancement factor of tungsten increases monotonically, gold exhibits an additional plasmon resonance at an aspect ratio of around $r = 6$, leading to far higher field enhancement.

### 8.6.6  Comparison of tip geometries

Figure 58 shows a comparison of different tip shapes for the same radius of curvature $R = 20\,\text{nm}$. For any given radius of curvature, there is only one parabolic tip shape, while both conical and hyperbolic tips have the opening angle as an additional free
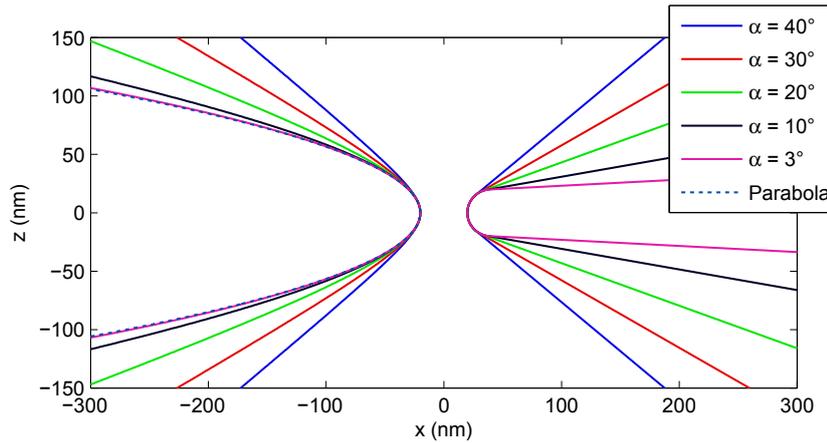
Figure 58: Comparison of parabolic, hyperbolic (left) and conical (right) tip shapes with a radius of 20 nm and different opening angles.

parameter. The main difference between hyperbolic and conical tips is that conical tips are much slimmer close to the apex if the opening angle is small, while the shape of a hyperbolic tip converges to a paraboloid for $\alpha \rightarrow 0°$. This explains the weaker opening angle dependence of hyperbolic tips as compared to conical tips.

# Acknowledgments

# Bibliography

Aeschlimann, M., Bauer, M., Bayer, D., Brixner, T., de Abajo, F. J., Pfeiffer, W., Rohmer, M., Spindler, C., and Steeb, F. (2007). Adaptive subwavelength control of nano-optical fields. *Nature*, 446, 301–304.

Amini, J. M., Uys, H., Wesenberg, J. H., Seidelin, S., Britton, J., Bollinger, J. J., Leibfried, D., Ospelkaus, C., VanDevender, A. P., and Wineland, D. J. (2010). Toward scalable ion traps for quantum information processing. *New J. Phys.*, 12, 033031.

Anashkina, E., Andrianov, A., Muravyev, S., and Kim, A. (2011). All-fiber design of erbium-doped laser system for tunable two-cycle pulse generation. *Opt. Expr.*, 19, 20141–20150.

Anderson, A., Deryckx, K. S., Xu, X. G., Steinmeyer, G., and Raschke, M. B. (2010). Few-femtosecond plasmon dephasing of a single metallic nanostructure from optical response function reconstruction by interferometric frequency resolved optical gating. *Nano Letters*, 10, 2519–2524.

Andersson, E., Calarco, T., Folman, R., Andersson, M., Hessmo, B., and Schmiedmayer, J. (2002). Multimode interferometer for guided matter waves. *Phys. Rev. Lett.*, 88, 100401.

Andrianov, A., Kim, A., Muraviov, S., and Sysoliatin, A. (2009). Wavelength-tunable few-cycle optical pulses directly from an all-fiber er-doped laser setup. *Opt. Lett.*, 34, 3193–3195.

Angert, I., Burmester, C., Dinges, C., Rose, H., and Schröder, R. R. (1996). Elastic and inelastic scattering cross-sections of amorphous layers of carbon and vitrified ice. *Ultramicroscopy*, 63, 181–192.

Arbouet, A., Houdellier, F., Marty, R., and Girard, C. (2012). Interaction of an ultrashort optical pulse with a metallic nanotip: A Green dyadic approach. *Journal of Applied Physics*, 112, 053103.

Azuma, H. (2006). Interaction-free measurement with an imperfect absorber. *Phys. Rev. A*, 74, 054301.

Babadjanyan, A., Margaryan, N., and Nerkararyan, K. V. (2000). Superfocusing of surface polaritons in the conical structure. *Journal of Applied Physics*, 87, 3785–3788.

Baker, S., Robinson, J. S., Haworth, C. A., Teng, H., Smith, R. A., Chirila, C. C., Lein, M., Tisch, J. W. G., and Marangos, J. P. (2006). Probing proton dynamics in molecules on an attosecond time scale. *Science*, 312, 424–427.

Baltuška, A., Udem, T., Uiberacker, M., Hentschel, M., Goulielmakis, E., Gohle, C., Holzwarth, R., Yakovlev, V. S., Scrinzi, A., Hänsch, T. W., and Krausz, F. (2003). Attosecond control of electronic processes by intense light fields. *Nature*, 421, 611–616.

Barwick, B., Corder, C., Strohaber, J., Chandler-Smith, N., Uiterwaal, C., and Batelaan, H. (2007). Laser-induced ultrafast electron emission from a field emission tip. *New J. Phys.*, 9, 142.

Batelaan, H. (2007). Colloquium: Illuminating the Kapitza-Dirac effect with electron matter optics. *Rev. Mod. Phys.*, 79, 929.

Becker, W., Grasbon, F., Kopold, R., Milošević, D., Paulus, G., and Walther, H. (2002). Above-threshold ionization: From classical features to quantum effects. In *Advances in Atomic, Molecular, and Optical Physics*, volume 48, pages 35–98. Academic Press.

Behr, N. and Raschke, M. B. (2008). Optical antenna properties of scanning probe tips: plasmonic light scattering, tip-sample coupling, and near-field enhancement. *The Journal of Physical Chemistry C*, 112, 3766–3773.

Berweger, S., Atkin, J. M., Xu, X. G., Olmon, R. L., and Raschke, M. B. (2011). Femtosecond nanofocusing with full optical waveform control. *Nano Letters*, 11, 4309–4313.

Blaga, C. I., Xu, J., DiChiara, A. D., Sistrunk, E., Zhang, K., Agostini, P., Miller, T. A., and Lin, L. F. D. C. D. (2012). Imaging ultrafast molecular dynamics with laser-induced electron diffraction. *Nature*, 483, 194–197.

Bloch, I., Dalibard, J., and Zwerger, W. (2008). Many-body physics with ultracold gases. *Rev. Mod. Phys.*, 80, 885–964.

Boersch, H. (1943). Fresnelsche Beugung im Elektronenmikroskop. *Physik Z.*, 44, 202.

Bohren, C. F. and Huffman, D. R. (2008). *Absorption and scattering of light by small particles*. John Wiley & Sons.

Bormann, R., Gulde, M., Weismann, A., Yalunin, S. V., and Ropers, C. (2010). Tip-enhanced strong-field photoemission. *Phys. Rev. Lett.*, 105, 147601.

Born, M. and Wolf, E. (1999). *Principles of Optics*. Cambridge University Press, 7 edition.

Bouhelier, A., Beversluis, M., Hartschuh, A., and Novotny, L. (2003a). Near-field second-harmonic generation induced by local field enhancement. *Phys. Rev. Lett.*, 90, 013903.

Bouhelier, A., Beversluis, M. R., and Novotny, L. (2003b). Near-field scattering of longitudinal fields. *Appl. Phys. Lett.*, 82, 4596–4598.

Brown, K. R., Ospelkaus, C., Colombe, Y., Wilson, A. C.and Leibfried, D., and Wineland, D. J. (2011). Coupled quantized mechanical oscillators. *Nature*, 471, 196.

Brown, L. D., Cai, T. T., and DasGupta, A. (2001). Interval estimation for a binomial proportion. *Statistical Science*, 16, 101.

Bunkin, F. V. and Fedorov, M. V. (1965). Cold emission of electrons from the surface of a metal in a strong radiation field. *Sov. Phys. JETP*, 21, 896–899.

Busuladžić, M., Gazibegović-Busuladžić, A., and Milošević, D. B. (2006). High-order above-threshold ionization in a laser field: Influence of the ionization potential on the high-energy cutoff. *Laser Phys.*, 16, 289–293.

Chang, C.-C., Kuo, H.-S., Hwang, I.-S., and Tsong, T. T. (2009). A fully coherent electron beam from a noble-metal covered W(111) single-atom emitter. *Nanotech.*, 20, 115401.

Chiaverini, J., Blakestad, R. B., Britton, J., Jost, J. D., Langer, C., Leibfried, D., Ozeri, R., and Wineland, D. J. (2005). Surface-electrode architecture for ion-trap quantum information processing. *Quant. Inf. Comp.*, 5, 419–439.

Chirilă, C. C. and Lein, M. (2006). High-order above-threshold ionization in stretched molecules. *Phys. Rev. A*, 74, 051401.

Ciracì, C., Hill, R. T., Mock, J. J., Urzhumov, Y., Fernández-Domínguez, A. I., Maier, S. A., Pendry, J. B., Chilkoti, A., and Smith, D. R. (2012). Probing the ultimate limits of plasmonic enhancement. *Science*, 337, 1072–1074.

Clopper, C. and Pearson, E. S. (1934). The use of confidence or fiducial limits illustrated in the case of the binomial. *Biometrika*, pages 404–413.

Corkum, P. B. (1993). Plasma perspective on strong field multiphoton ionization. *Phys. Rev. Lett.*, 71, 1994–1997.

Corkum, P. B. and Krausz, F. (2007). Attosecond science. *Nature Phys.*, 3, 381–387.

Davisson, C. and Germer, L. H. (1927). Diffraction of electrons by a crystal of nickel. *Phys. Rev.*, 30, 705–740.

DeWitt, B. S., Graham, N., Everett, H., and Wheeler, J. A. (1973). *The many-worlds interpretation of quantum mechanics*, volume 3. Princeton University Press Princeton.

Dicke, R. H. (1981). Interaction-free quantum measurements: a paradox? *Am. J. Phys.*, 49, 925–930.

Dombi, P., Hörl, A., Rácz, P., Márton, I., Trügler, A., Krenn, J. R., and Hohenester, U. (2013). Ultrafast strong-field photoemission from plasmonic nanoparticles. *Nano Letters*, 13, 674–678.

Egerton, R., Li, P., and Malac, M. (2004). Radiation damage in the TEM and SEM. *Micron*, 35, 399–409.

Ehberger, D., Hammer, J., Eisele, M., Krüger, M., Noe, J., Högele, A., and Hommelhoff, P. (2015). Highly coherent electron beam from a laser-triggered tungsten needle tip. *Phys. Rev. Lett.*, 114, 227601.

Einstein, A. (1905). Über einen die Erzeugung und Verwandlung des Lichtes betreffenden heuristischen Gesichtspunkt. *Annalen der Physik*, 322, 132–148.

Eisele, M., Krüger, M., Schenk, M., Ziegler, A., and Hommelhoff, P. (2011). Note: Production of sharp gold tips with high surface quality. *Rev. Sci. Instr.*, 82, 026101.

Elitzur, A. C. and Vaidman, L. (1993). Quantum mechanical interaction-free measurements. *Foundations of Physics*, 23, 987–997.

Erdman, P. W. and Zipf, E. C. (1982). Low-voltage, high-current electron gun. *Rev. Sci. Instr.*, 53(2), 225–227.

Facchi, P., Hradil, Z., Krenn, G., Pascazio, S., and Řeháček, J. (2002). Quantum Zeno tomography. *Phys. Rev. A*, 66, 012110.

Feist, A., Echternkamp, K. E., Schauss, J., Yalunin, S. V., Schafer, S., and Ropers, C. (2015). Quantum coherent optical phase modulation in an ultrafast transmission electron microscope. *Nature*, 521, 200–203.

Feit, M., Fleck, J., and Steiger, A. (1982). Solution of the Schrödinger equation by a spectral method. *Journal of Computational Physics*, 47, 412 – 433.

Fennel, T., Döppner, T., Passig, J., Schaal, C., Tiggesbäumker, J., and Meiwes-Broer, K.-H. (2007). Plasmon-enhanced electron acceleration in intense laser metal-cluster interactions. *Phys. Rev. Lett.*, 98, 143401.

Ferray, M., L'Huillier, A., Li, X. F., Lompre, L. A., Mainfray, G., and Manus, C. (1988). Multiple-harmonic conversion of 1064 nm radiation in rare gases. *J. Phys. B: At. Mol. Opt. Phys.*, 21, L31–L35.

Fleck, J.A., J., Morris, J., and Feit, M. (1976). Time-dependent propagation of high energy laser beams through the atmosphere. *Applied Physics*, 10, 129–160.

Freimund, D. L., Aflatooni, K., and Batelaan, H. (2001). Observation of the Kapitza-Dirac effect. *Nature*, 413, 142–143.

Freimund, D. L. and Batelaan, H. (2002). Bragg scattering of free electrons using the Kapitza-Dirac effect. *Phys. Rev. Lett.*, 89, 283602.

Gabor, D. (1948). A new microscopic principle. *Nature*, 161, 777–778.

García de Abajo, F. J. (2010). Optical excitations in electron microscopy. *Rev. Mod. Phys.*, 82, 209–275.

García-Escartín, J. C. and Chamorro-Posada, P. (2005). Quantum interrogation with particles. *arXiv preprint quant-ph/0512019*.

Germann, M., Latychevskaia, T., Escher, C., and Fink, H.-W. (2010). Nondestructive imaging of individual biomolecules. *Phys. Rev. Lett.*, 104, 095501.

Geuzaine, C. and Remacle, J.-F. (2009). Gmsh: A 3-d finite element mesh generator with built-in pre-and post-processing facilities. *International Journal for Numerical Methods in Engineering*, 79, 1309–1331.

Ghosh, P. K. (1995). *Ion traps.* The international series of monographs on physics. Clarendon Press, Oxford.

Gomer, R. (1961). *Field Emission and Field Ionization.* Harvard University Press, Cambridge, Massachusetts.

Goncharenko, A., Chang, H.-C., and Wang, J.-K. (2007). Electric near-field enhancing properties of a finite-size metal conical nano-tip. *Ultramicroscopy*, 107, 151–157.

Goncharenko, A., Dvoynenko, M., Chang, H.-C., and Wang, J.-K. (2006a). Electric field enhancement by a nanometer-scaled conical metal tip in the context of scattering-type near-field optical microscopy. *Appl. Phys. Lett.*, 88, 104101.

Goncharenko, A. V., Wang, J.-K., and Chang, Y.-C. (2006b). Electric near-field enhancement of a sharp semi-infinite conical probe: Material and cone angle dependence. *Phys. Rev. B*, 74, 235442.

Gulde, M., Schweda, S., Storeck, G., Maiti, M., Yu, H. K., Wodtke, A. M., Schäfer, S., and Ropers, C. (2014). Ultrafast low-energy electron diffraction in transmission resolves polymer/graphene superstructure dynamics. *Science*, 345, 200–204.

Hafner, M. and Summhammer, J. (1997). Experiment on interaction-free measurement in neutron interferometry. *Physics Letters A*, 235, 563–568.

Haider, M., Hartel, P., Müller, H., Uhlemann, S., and Zach, J. (2010). Information transfer in a TEM corrected for spherical and chromatic aberration. *Microscopy and Microanalysis*, 16, 393–408.

Haider, M., Uhlemann, S., Schwan, E., Rose, H., Kabius, B., and Urban, K. (1998). Electron microscopy image enhanced. *Nature*, 392, 768–769.

Hammer, J. (2014). *A microwave chip-based beamsplitter for guided low-energy electrons.* PhD thesis, Ludwig-Maximilians-Universität München.

Hammer, J., Hoffrogge, J., Heinrich, S., and Hommelhoff, P. (2014). Phase-resolved electron guiding in optimized chip-based microwave potentials. *Phys. Rev. Applied*, 2, 044015.

Hammer, J., Thomas, S., Weber, P., and Hommelhoff, P. (2015). Microwave chip-based beam splitter for low-energy guided electrons. *Phys. Rev. Lett.*, 114, 254801.

Hanke, T., Cesar, J., Knittel, V., Trügler, A., Hohenester, U., Leitenstorfer, A., and Bratschitsch, R. (2012). Tailoring spatiotemporal light confinement in single plasmonic nanoantennas. *Nano Letters*, 12, 992–996.

Hanke, T., Krauss, G., Träutlein, D., Wild, B., Bratschitsch, R., and Leitenstorfer, A. (2009). Efficient nonlinear light emission of single gold optical antennas driven by few-cycle near-infrared pulses. *Phys. Rev. Lett.*, 103, 257404.

Hänsel, W., Hommelhoff, P., Hänsch, T. W., and Reichel, J. (2001a). Bose-einstein condensation on a microelectronic chip. *Nature*, 413, 498–501.

Hänsel, W., Reichel, J., Hommelhoff, P., and Hänsch, T. W. (2001b). Trapped-atom interferometer in a magnetic microtrap. *Phys. Rev. A*, 64, 063607.

Harlander, M., Lechner, R., Brownnutt, M., Blatt, R., and Hänsel, W. (2011). Trapped-ion antennae for the transmission of quantum information. *Nature*, 471, 200.

Hartschuh, A. (2008). Tip-enhanced near-field optical microscopy. *Angewandte Chemie International Edition*, 47, 8178–8191.

Hasselbach, F. (2010). Progress in electron- and ion-interferometry. *Rep. Progr. Phys.*, 73, 016101.

Hayat, M. A. (2000). *Principles and techniques of electron microscopy: biological applications.* Cambridge University Press.

Haynes, W. and Lide, D. (2011). *CRC Handbook of Chemistry and Physics, 92nd Edition.* CRC Press.

Heinzelmann, H. and Pohl, D. (1994). Scanning near-field optical microscopy. *Appl. Phys. A*, 59, 89–101.

Hensinger, W. K., Olmschenk, S., Stick, D., Hucul, D., Yeo, M., Acton, M., Deslauriers, L., Monroe, C., and Rabchuk, J. (2006). T-junction ion trap array for two-dimensional ion shuttling, storage, and manipulation. *Appl. Phys. Lett.*, 88.

Herink, G., Solli, D. R., Gulde, M., and Ropers, C. (2012). Field-driven photoemission from nanostructures quenches the quiver motion. *Nature*, 483, 190–193.

Hertz, H. (1887). Ueber einen einfluss des ultravioletten lichtes auf die electrische entladung. *Annalen der Physik*, 267, 983–1000.

Hickstein, D. D., Ranitovic, P., Witte, S., Tong, X.-M., Huismans, Y., Arpin, P., Zhou, X., Keister, K. E., Hogle, C. W., Zhang, B., Ding, C., Johnsson, P., Toshima, N., Vrakking, M. J. J., Murnane, M. M., and Kapteyn, H. C. (2012). Direct visualization of laser-driven

electron multiple scattering and tunneling distance in strong-field ionization. *Phys. Rev. Lett.*, 109, 073004.

Hoffrogge, J., Fröhlich, R., Kasevich, M. A., and Hommelhoff, P. (2011). Microwave guiding of electrons on a chip. *Phys. Rev. Lett.*, 106, 193001.

Hoffrogge, J. and Hommelhoff, P. (2011). Planar microwave structures for electron guiding. *New J. Phys.*, 13, 095012.

Hoffrogge, J., Stein, J.-P., Krüger, M., Förster, M., Hammer, J., Ehberger, D., Baum, P., and Hommelhoff, P. (2014). Tip-based source of femtosecond electron pulses at 30 keV. *J. Appl. Phys.*, 115.

Hoffrogge, J. P. (2012). *A surface-electrode quadrupole guide for electrons.* PhD thesis, Ludwig-Maximilians-Universität München.

Homann, C., Bradler, M., Förster, M., Hommelhoff, P., and Riedle, E. (2012). Carrier-envelope phase stable sub-two-cycle pulses tunable around 1.8 µm at 100 khz. *Opt. Lett.*, 37, 1673–1675.

Homer Reid, M. T. and Johnson, S. G. (2013). Efficient computation of power, force, and torque in BEM scattering calculations. *arXiv preprint arXiv:1307.2966*.

Homer Reid, M. T., White, J., and Johnson, S. G. (2013). Fluctuating surface currents: An algorithm for efficient prediction of Casimir interactions among arbitrary materials in arbitrary geometries. *Phys. Rev. A*, 88, 022514.

Hommelhoff, P. and Hammer, J. (2014). Patent pending.

Hommelhoff, P., Kealhofer, C., and Kasevich, M. A. (2006a). Ultrafast electron pulses from a tungsten tip triggered by low-power femtosecond laser pulses. *Phys. Rev. Lett.*, 97, 247402.

Hommelhoff, P., Sortais, Y., Aghajani-Talesh, A., and Kasevich, M. A. (2006b). Field emission tip as a nanometer source of free electron femtosecond pulses. *Phys. Rev. Lett.*, 96, 077401.

Hosten, O., Rakher, M. T., Barreiro, J. T., Peters, N. A., and Kwiat, P. G. (2006). Counter-factual quantum computation through quantum interrogation. *Nature*, 439, 949–952.

Huber, A. J., Keilmann, F., Wittborn, J., Aizpurua, J., and Hillenbrand, R. (2008). Terahertz near-field nanoscopy of mobile carriers in single semiconductor nanodevices. *Nano Letters*, 8, 3766–3770.

Inoue, S. and Björk, G. (2000). Experimental demonstration of exposure-free imaging and contrast amplification. *Journal of Optics B: Quantum and Semiclassical Optics*, 2, 338.

Inouye, Y. and Kawata, S. (1994). Near-field scanning optical microscope with a metallic probe tip. *Opt. Lett.*, 19, 159–161.

Issa, N. A. and Guckenberger, R. (2007). Optical nanofocusing on tapered metallic waveguides. *Plasmonics*, 2, 31–37.

Itano, W. M. (2009). Perspectives on the quantum Zeno paradox. In *Journal of Physics: Conference Series*, volume 196, page 012018.

Itano, W. M., Heinzen, D., Bollinger, J., and Wineland, D. (1990). Quantum Zeno effect. *Phys. Rev. A*, 41, 2295.

Itatani, J., Levesque, J., Zeidler, D., Niikura, H., Pépin, H., Kieffer, J. C., Corkum, P. B., and Villeneuve, D. M. (2004). Tomographic imaging of molecular orbitals. *Nature*, 432, 867–871.

Jang, J.-S. (1999). Optical interaction-free measurement of semitransparent objects. *Phys. Rev. A*, 59, 2322.

Jelic, V. and Marsiglio, F. (2012). The double-well potential in quantum mechanics: a simple, numerically exact formulation. *Eur. J. Phys.*, 33, 1651.

Joannopoulos, J. D., Johnson, S. G., Winn, J. N., and Meade, R. D. (2011). *Photonic Crystals: Molding the Flow of Light.* Princeton University Press.

Juffmann, T., Milic, A., Mullneritsch, M., Asenbaum, P., Tsukernik, A., Tuxen, J., Mayor, M., Cheshnovsky, O., and Arndt, M. (2012). Real-time single-molecule imaging of quantum interference. *Nature Nanotechnology*, 7, 297–300.

Kafka, J. D., Baer, T., and Hall, D. W. (1989). Mode-locked erbium-doped fiber laser with soliton pulse shaping. *Opt. Lett.*, 14, 1269–1271.

Karlsson, A., Björk, G., and Forsberg, E. (1998). "Interaction" (energy exchange) free and quantum nondemolition measurements. *Phys. Rev. Lett.*, 80, 1198–1201.

Kawano, H. (2008). Theoretical evaluation of the effective work functions for positive-ionic and electronic emissions from polycrystalline metal surfaces. *Applied Surface Science*, 254, 7187–7192.

Kawata, S., Inouye, Y., and Verma, P. (2009). Plasmonics for near-field nano-imaging and superlensing. *Nature Photon.*, 3, 388–394.

Keldysh, L. V. (1965). Ionization in the field of a strong electromagnetic wave. *Sov. Phys. JETP*, 20, 1307–1314.

Kent, A. and Wallace, D. (2001). Quantum interrogation and the safer X-ray. *arXiv preprint quant-ph/8112010.*

Klein, M. and Schwitzgebel, G. (1997). An improved lamellae drop-off technique for sharp tip preparation in scanning tunneling microscopy. *Rev. Sci. Instr.*, 68, 3099–3103.

Knoll, M. and Ruska, E. (1932). Das Elektronenmikroskop. *Zeitschrift für Physik*, 78, 318–339.

Koh, A. L., Fernández-Domínguez, A. I., McComb, D. W., Maier, S. A., and Yang, J. K. W. (2011). High-resolution mapping of electron-beam-excited plasmon modes in lithographically defined gold nanostructures. *Nano Letters*, 11, 1323–1330.

Krauss, G., Fehrenbacher, D., Brida, D., Riek, C., Sell, A., Huber, R., and Leitenstorfer, A. (2011). All-passive phase locking of a compact Er:fiber laser system. *Opt. Lett.*, 36, 540–542.

Krauss, G., Lohss, S., Hanke, T., Sell, A., Eggert, S., Huber, R., and Leitenstorfer, A. (2010). Synthesis of a single cycle of light with compact erbium-doped fibre technology. *Nature Photon.*, 4, 33–36.

Krausz, F. and Ivanov, M. (2009). Attosecond physics. *Rev. Mod. Phys.*, 81, 163–234.

Krüger, M., Schenk, M., Förster, M., and Hommelhoff, P. (2012a). Attosecond physics in photoemission from a metal nanotip. *J. Phys. B: At. Mol. Opt. Phys.*, 45, 074006.

Krüger, M., Schenk, M., and Hommelhoff, P. (2011). Attosecond control of electrons emitted from a nanoscale metal tip. *Nature*, 475, 78–81.

Krüger, M., Schenk, M., Hommelhoff, P., Wachter, G., Lemell, C., and Burgdörfer, J. (2012b). Interaction of ultrashort laser pulses with metal nanotips: a model system for strong-field phenomena. *New J. Phys.*, 14, 085019.

Kruit, P., Hobbs, R. G., Kim, C.-S., Yang, Y., Manfrinato, V. R., Hammer, J., Thomas, S., Weber, P., Klopfer, B., Kohstall, C., Juffmann, T., Kasevich, M. A., Hommelhoff, P., and Berggren, K. K. (2015). Designs for a quantum electron microscope. Submitted.

Krüger, M. (2013). *Attosecond Physics in Strong-Field Photoemission from Metal Nanotips*. PhD thesis, Ludwig-Maximilians-Universität München.

Krüger, M., Thomas, S., Förster, M., and Hommelhoff, P. (2014). Self-probing of metal nanotips by rescattered electrons reveals the nano-optical near-field. *J. Phys. B: At. Mol. Opt. Phys.*, 47, 124022.

Kwiat, P. (1998). Experimental and theoretical progress in interaction-free measurements. *Physica Scripta*, 1998, 115.

Kwiat, P., Weinfurter, H., Herzog, T., Zeilinger, A., and Kasevich, M. A. (1995). Interaction-free measurement. *Phys. Rev. Lett.*, 74, 4763–4766.

Kwiat, P. G., White, A., Mitchell, J., Nairz, O., Weihs, G., Weinfurter, H., and Zeilinger, A. (1999). High-efficiency quantum interrogation measurements via the quantum Zeno effect. *Phys. Rev. Lett.*, 83, 4725.

Lai, X. Y., Quan, W., and Liu, X. (2011). Tunneling-induced shift of the cutoff law for high-order above-threshold ionization. *Phys. Rev. A*, 84, 025401.

Leibfried, D., Blatt, R., Monroe, C., and Wineland, D. (2003). Quantum dynamics of single trapped ions. *Rev. Mod. Phys.*, 75, 281–324.

Lein, M. (2007). Molecular imaging using recolliding electrons. *J. Phys. B: At. Mol. Opt. Phys.*, 40, R135–R173.

Lewenstein, M., Balcou, P., Ivanov, M. Y., L'Huiller, A., and Corkum, P. B. (1994). Theory of high-harmonic generation by low-frequency laser fields. *Phys. Rev. A*, 49, 2117–2132.

Lichte, H. and Lehmann, M. (2008). Electron holography: basics and applications. *Rep. Progr. Phys.*, 71, 016102.

Lide, D. (2004). *CRC handbook of chemistry and physics: a ready-reference book of chemical and physical data.* CRC Handbook of Chemistry and Physics, 85th Ed. CRC Press.

Lin, C.-D., Le, A.-T., Chen, Z., Morishita, T., and Lucchese, R. (2010). Strong-field rescattering physics—self-imaging of a molecule by its own electrons. *J. Phys. B: At. Mol. Opt. Phys.*, 43, 122001.

Ma, X.-s., Guo, X., Schuck, C., Fong, K. Y., Jiang, L., and Tang, H. X. (2014). On-chip interaction-free measurements via the quantum Zeno effect. *Phys. Rev. A*, 90, 042109.

Maier, S. (2007). *Plasmonics: Fundamentals And Applications.* Springer.

Maisenbacher, L. (2012). Comparison of the material response in carrier-envelope phase resolved photoemission – metal nanotip vs. atomic gas. Master's thesis, Ludwig-Maximilians-Universität München.

Major, F. G., Gheorghe, V. N., and Werth, G. (2005). *Charged Particle Traps.* Springer, Berlin Heidelberg New York.

Mandel, L. and Wolf, E. (1995). *Optical Coherence and Quantum Optics.* Cambridge University Press.

Marinica, D., Kazansky, A., Nordlander, P., Aizpurua, J., and Borisov, A. G. (2012). Quantum plasmonics: Nonlinear effects in the field enhancement of a plasmonic nanoparticle dimer. *Nano Letters*, 12, 1333–1339.

Martin, O. J. F. and Girard, C. (1997). Controlling and tuning strong optical field gradients at a local probe microscope tip apex. *Applied Physics Letters*, 70, 705–707.

Martin, Y. C., Hamann, H. F., and Wickramasinghe, H. K. (2001). Strength of the electric field in apertureless near-field optical microscopy. *J. Appl. Phys.*, 89, 5774–5778.

Marton, L. (1934). Electron microscopy of biological objects. *Nature*, 133, 527–528.

Marton, L. (1952). Electron interferometer. *Phys. Rev.*, 85, 1057.

Marton, L., Simpson, J. A., and Suddeth, J. A. (1953). Electron beam interferometer. *Phys. Rev.*, 90, 490–491.

Marton, L., Simpson, J. A., and Suddeth, J. A. (1954). An electron interferometer. *Rev. Sci. Instr.*, 25, 1099–1104.

Massar, S., Mitchison, G., and Pironio, S. (2001). Minimal absorption measurements. *Phys. Rev. A*, 64, 062303.

McCusker, K. T., Huang, Y.-P., Kowligy, A. S., and Kumar, P. (2013). Experimental demonstration of interaction-free all-optical switching via the quantum Zeno effect. *Phys. Rev. Lett.*, 110, 240403.

McPherson, A., Gibson, G., Jara, H., Johann, U., Luk, T. S., McIntyre, I. A., Boyer, K., and Rhodes, C. K. (1987). Studies of multiphoton production of vacuum-ultraviolet radiation in the rare gases. *J. Opt. Soc. Am. B*, 4, 595–601.

Meckel, M., Comtois, D., Zeidler, D., Staudte, A., Pavičić, D., Bandulet, H. C., Pépin, H., Kieffer, J. C., Dörner, R., Villeneuve, D. M., and Corkum, P. B. (2008). Laser-induced electron tunneling and diffraction. *Science*, 320, 1478–1482.

Mie, G. (1908). Beiträge zur Optik trüber Medien, speziell kolloidaler Metallösungen. *Annalen der Physik*, 330, 377–445.

Misra, B. and Sudarshan, E. C. G. (1977). The Zeno's paradox in quantum theory. *Journal of Mathematical Physics*, 18, 756.

Missiroli, G., Pozzi, G., and Valdre, U. (1981). Electron interferometry and interference electron microscopy. *Journal of Physics E: Scientific Instruments*, 14, 649.

Mitchison, G. and Jozsa, R. (2001). Counterfactual computation. *Proceedings of the Royal Society of London. Series A: Mathematical, Physical and Engineering Sciences*, 457, 1175–1193.

Mitchison, G. and Massar, S. (2001). Absorption-free discrimination between semitransparent objects. *Phys. Rev. A*, 63, 032105.

Mitchison, G., Massar, S., and Pironio, S. (2002). Minimum number of photons needed to distinguish two transparencies. *Phys. Rev. A*, 65, 22110.

Moehring, D. L., Highstrete, C., Stick, D., Fortier, K. M., Haltli, R., Tigges, C., and Blain, M. G. (2011). Design, fabrication and experimental demonstration of junction surface ion traps. *New J. Phys.*, 13, 075018.

Möllenstedt, G. and Düker, H. (1955). Fresnelscher Interferenzversuch mit einem Biprisma für Elektronenwellen. *Naturwissenschaften*, 42, 41.

Neacsu, C., Steudle, G., and Raschke, M. (2005a). Plasmonic light scattering from nanoscopic metal tips. *Applied Physics B*, 80, 295–300.

Neacsu, C. C., Reider, G. A., and Raschke, M. B. (2005b). Second-harmonic generation from nanoscopic metal tips: symmetry selection rules for single asymmetric nanostructures. *Phys. Rev. B*, 71, 201402.

Nielsen, M. A. and Chuang, I. L. (2010). *Quantum computation and quantum information*. Cambridge University Press.

Niikura, H., Légáre, F., Hasbani, R., Bandrauk, A. D., Ivanov, M. Y., Villeneuve, D. M., and Corkum, P. B. (2002). Sub-laser-cycle electron pulses for probing molecular dynamics. *Nature*, 417, 917–922.

Novotny, L. and Hecht, B. (2006). *Principles of Nano-Optics*. Cambridge University Press.

Okamoto, H. (2012). Possible use of a cooper-pair box for low-dose electron microscopy. *Phys. Rev. A*, 85, 043810.

Olmon, R. L., Slovick, B., Johnson, T. W., Shelton, D., Oh, S.-H., Boreman, G. D., and Raschke, M. B. (2012). Optical dielectric function of gold. *Phys. Rev. B*, 86, 235147.

Paarmann, A., Gulde, M., Müller, M., Schäfer, S., Schweda, S., Maiti, M., Xu, C., Hohage, T., Schenk, F., Ropers, C., et al. (2012). Coherent femtosecond low-energy single-electron pulses for time-resolved diffraction and imaging: A numerical study. *J. Appl. Phys.*, 112, 113109.

Palik, E. (1991). *Handbook of Optical Constants of Solids II*. Academic Press.

Park, D. J., Piglosiewicz, B., Schmidt, S., Kollmann, H., Mascheck, M., Groß, P., and Lienau, C. (2013). Characterizing the optical near-field in the vicinity of a sharp metallic nanoprobe by angle-resolved electron kinetic energy spectroscopy. *Annalen der Physik*, 525, 135–142.

Park, D. J., Piglosiewicz, B., Schmidt, S., Kollmann, H., Mascheck, M., and Lienau, C. (2012). Strong field acceleration and steering of ultrafast electron pulses from a sharp metallic nanotip. *Phys. Rev. Lett.*, 109, 244803.

Paul, H. and Pavičić, M. (1996). Resonance interaction-free measurement. *International Journal of Theoretical Physics*, 35, 2085–2091.

Paul, W. (1990). Electromagnetic traps for charged and neutral particles. *Rev. Mod. Phys.*, 62, 531–540.

Paulus, G. G., Becker, W., Nicklich, W., and Walther, H. (1994a). Rescattering effects in above-threshold ionization - a classical-model. *J. Phys. B: At. Mol. Opt. Phys.*, 27, L703–L708.

Paulus, G. G., Lindner, F., Walther, H., Baltuška, A., Goulielmakis, E., Lezius, M., and Krausz, F. (2003). Measurement of the phase of few-cycle laser pulses. *Phys. Rev. Lett.*, 91, 253004.

Paulus, G. G., Nicklich, W., Xu, H., Lambropoulos, P., and Walther, H. (1994b). Plateau in above threshold ionization spectra. *Phys. Rev. Lett.*, 72, 2851–2854.

Pavičić, M. (1996). Resonance energy-exchange-free detection and "welcher Weg" experiment. *Physics Letters A*, 223, 241–245.

Pearson, C. E., Leibrandt, D. R., Bakr, W. S., Mallard, W. J., Brown, K. R., and Chuang, I. L. (2006). Experimental investigation of planar ion traps. *Phys. Rev. A*, 73, 032307.

Peise, J., Lücke, B., Pezzé, L., Deuretzbacher, F., Ertmer, W., Arlt, J., Smerzi, A., Santos, L., and Klempt, C. (2015). Interaction-free measurements by quantum Zeno stabilization of ultracold atoms. *Nature Communications*, 6, 6811.

Petek, H. and Ogawa, S. (1997). Femtosecond time-resolved two-photon photoemission studies of electron dynamics in metals. *Prog. Surf. Sci.*, 56, 239.

Piglosiewicz, B., Schmidt, S., Park, D. J., Vogelsang, J., Groß, P., Manzoni, C., Farinello, P., Cerullo, G., and Lienau, C. (2014). Carrier-envelope phase effects on the strong-field photoemission of electrons from metallic nanostructures. *Nature Photon.*, 8, 37–42.

Pors, A., Nerkararyan, K. V., and Bozhevolnyi, S. I. (2014). Scaling in light scattering by sharp conical metal tips. *Opt. Lett.*, 39, 3308–3311.

Pötting, S., Lee, E. S., Schmitt, W., Rumyantsev, I., Mohring, B., and Meystre, P. (2000). Quantum coherence and interaction-free measurements. *Phys. Rev. A*, 62, 060101.

Pozar, D. M. (2005). *Microwave Engineering*. John Wiley and Sons, 3 edition.

Putnam, W. P. and Yanik, M. F. (2009). Noninvasive electron microscopy with interaction-free quantum measurements. *Phys. Rev. A*, 80, 040902(R).

QEM (2015). http://www.rle.mit.edu/qem/.

Raether, H. (1988). *Surface Plasmons on Smooth and Rough Surfaces and on Gratings*, volume 111 of *Springer tracts in modern physics*. Springer.

*Bibliography*

Raschke, M. B., Molina, L., Elsaesser, T., Kim, D. H., Knoll, W., and Hinrichs, K. (2005). Apertureless near-field vibrational imaging of block-copolymer nanostructures with ultrahigh spatial resolution. *ChemPhysChem*, 6, 2197–2203.

Rauch, H. and Werner, S. (2000). *Neutron Interferometry*. Oxford University Press.

Reimer, L. and Kohl, H. (2008). *Transmission Electron Microscopy: Physics of Image Formation*. Springer Series in Optical Sciences. Springer.

Renninger, M. (1960). Messungen ohne Störung des Meßobjekts. *Zeitschrift für Physik*, 158, 417–421.

Ritchie, R. (1957). Plasma losses by fast electrons in thin films. *Phys. Rev.*, 106, 874.

Ropers, C., Solli, D. R., Schulz, C. P., Lienau, C., and Elsaesser, T. (2007). Localized multiphoton emission of femtosecond electron pulses from metal nanotips. *Phys. Rev. Lett.*, 98, 043907.

Ruska, E. (1934). Über Fortschritte im Bau und in der Leistung des magnetischen Elektronenmikroskops. *Zeitschrift für Physik*, 87, 580–602.

Salih, H., Li, Z.-H., Al-Amri, M., and Zubairy, M. S. (2013). Protocol for direct counterfactual quantum communication. *Phys. Rev. Lett.*, 110, 170502.

Sarid, D. and Challener, W. (2010). *Modern Introduction to Surface Plasmons: Theory, Mathematica Modeling, and Applications*. Cambridge University Press.

Schenk, M., Krüger, M., and Hommelhoff, P. (2010). Strong-field above-threshold photoemission from sharp metal tips. *Phys. Rev. Lett.*, 105, 257601.

Schleich, W. P. (2005). *Quantum Optics in Phase Space*. Wiley-VCH, Berlin.

Schmied, R. (2010). Electrostatics of gapped and finite surface electrodes. *New J. Phys.*, 12, 023038.

Schmied, R., Wesenberg, J. H., and Leibfried, D. (2009). Optimal surface-electrode trap lattices for quantum simulation with trapped ions. *Phys. Rev. Lett.*, 102, 233002.

Schnell, M., Alonso-Gonzalez, P., Arzubiaga, L., Casanova, F., Hueso, L., Chuvilin, A., and Hillenbrand, R. (2011). Nanofocusing of mid-infrared energy with tapered transmission lines. *Nature Photon.*, 5, 283–287.

Schott AG (2011). *Optical Glass Data Sheets*.

Schowalter, M., Titantah, J., Lamoen, D., and Kruse, P. (2005). Ab initio computation of the mean inner coulomb potential of amorphous carbon structures. *Appl. Phys. Lett.*, 86, 2102.

scuff-EM (2015). http://homerreid.dyndns.org/scuff-em/.

Seidelin, S., Chiaverini, J., Reichle, R., Bollinger, J. J., Leibfried, D., Britton, J., Wesenberg, J. H., Blakestad, R. B., Epstein, R. J., Hume, D. B., Itano, W. M., Jost, J. D., Langer, C., Ozeri, R., Shiga, N., and Wineland, D. J. (2006). Microfabricated surface-electrode ion trap for scalable quantum information processing. *Phys. Rev. Lett.*, 96, 253003.

Sell, A., Krauss, G., Scheu, R., Huber, R., and Leitenstorfer, A. (2009). 8-fs pulses from a compact Er:fiber system: quantitative modeling and experimental implementation. *Opt. Expr.*, 17, 1070–1077.

Sheppard, C. and Saghafi, S. (1999). Electromagnetic Gaussian beams beyond the paraxial approximation. *JOSA A*, 16, 1381–1386.

Shu, G., Vittorini, G., Buikema, A., Nichols, C. S., Volin, C., Stick, D., and Brown, K. R. (2014). Heating rates and ion-motion control in a Y-junction surface-electrode trap. *Phys. Rev. A*, 89, 062308.

Smirnova, O. and Ivanov, M. Y. (2013). Multielectron high harmonic generation: simple man on a complex plane. In Vrakking, M. and Schulz, T., editors, *Attosecond and XUV science: Ultrafast Dynamics and Spectroscopy*, pages 200–256. Wiley-VCH.

Smirnova, O., Mairesse, Y., Patchkovskii, S., Dudovich, N., Villeneuve, D., Corkum, P., and Y., I. M. (2009). High harmonic interferometry of multi-electron dynamics in molecules. *Nature*, 460, 972–977.

Spence, J. (2013). *High-Resolution Electron Microscopy.* Oxford University Press.

Stöckle, R. M., Suh, Y. D., Deckert, V., and Zenobi, R. (2000). Nanoscale chemical analysis by tip-enhanced Raman spectroscopy. *Chem. Phys. Lett.*, 318, 131–136.

Stockman, M. I. (2004). Nanofocusing of optical energy in tapered plasmonic waveguides. *Phys. Rev. Lett.*, 93, 137404.

Stockman, M. I. (2011). Nanoplasmonics: past, present, and glimpse into future. *Opt. Expr.*, 19, 22029–22106.

Stoller, P., Jacobsen, V., and Sandoghdar, V. (2006). Measurement of the complex dielectric constant of a single gold nanoparticle. *Opt. Lett.*, 31, 2474–2476.

SurfacePattern (2015).
http://atom.physik.unibas.ch/people/romanschmied/code/surfacepattern.php.

Swanwick, M. E., Keathley, P. D., Fallahi, A., Krogen, P. R., Laurent, G., Moses, J., Kärtner, F. X., and Velásquez-García, L. F. (2014). Nanostructured ultrafast silicon-tip optical field-emitter arrays. *Nano Letters*, 14, 5035–5043.

Taflove, A. and Hagness, S. (2005). *Computational Electrodynamics: the Finite-Difference Time-Domain Method.* Artech House.

Tamura, K., Ippen, E. P., Haus, H. A., and Nelson, L. E. (1993). 77-fs pulse generation from a stretched-pulse mode-locked all-fiber ring laser. *Opt. Lett.*, 18, 1080–1082.

Teperik, T. V., Nordlander, P., Aizpurua, J., and Borisov, A. G. (2013). Robust subnanometric plasmon ruler by rescaling of the nonlocal optical response. *Phys. Rev. Lett.*, 110, 263901.

Thomas, S., Holzwarth, R., and Hommelhoff, P. (2012). Generating few-cycle pulses for nanoscale photoemission easily with an erbium-doped fiber laser. *Opt. Expr.*, 20, 13663–13668.

Thomas, S., Kohstall, C., Kruit, P., and Hommelhoff, P. (2014). Semitransparency in interaction-free measurements. *Phys. Rev. A*, 90, 053840.

Thomas, S., Krüger, M., Förster, M., Schenk, M., and Hommelhoff, P. (2013). Probing of optical near-fields by electron rescattering on the 1 nm scale. *Nano Letters*, 13, 4790–4794.

Thomas, S., Wachter, G., Lemell, C., Burgdörfer, J., and Hommelhoff, P. (2015). Large optical field enhancement for nanotips with large opening angles. *New J. Phys.*, 17, 063010.

Tonomura, A. (1999). *Electron Holography.* Springer Series in Optical Sciences. Springer, Heidelberg.

Tonomura, A., Endo, J., Matsuda, T., Kawasaki, T., and Ezawa, H. (1989). Demonstration of single-electron buildup of an interference pattern. *Am. J. Phys.*, 57, 117–120.

Tonomura, A., Osakabe, N., Matsuda, T., Kawasaki, T., Endo, J., Yano, S., and Yamada, H. (1986). Evidence for Aharonov-Bohm effect with magnetic field completely shielded from electron wave. *Phys. Rev. Lett.*, 56, 792–795.

Trollmann, J. and Pucci, A. (2014). Infrared dielectric function of gold films in relation to their morphology. *The Journal of Physical Chemistry C*, 118, 15011–15018.

Tsegaye, T., Goobar, E., Karlsson, A., Björk, G., Loh, M. Y., and Lim, K. H. (1998). Efficient interaction-free measurements in a high-finesse interferometer. *Phys. Rev. A*, 57, 3987–3990.

Tsong, T. T. (1990). *Atom-probe field ion microscopy.* Cambridge University Press, Cambridge.

Uhlemann, S., Müller, H., Hartel, P., Zach, J., and Haider, M. (2013). Thermal magnetic field noise limits resolution in transmission electron microscopy. *Phys. Rev. Lett.*, 111, 046101.

Urban, K. W. (2008). Studying atomic structures by aberration-corrected transmission electron microscopy. *Science*, 321, 506–510.

Vaidman, L. (1996). Interaction-free measurements. *arXiv preprint quant-ph/9610033*.

Vaidman, L. (2001). Are interaction-free measurements interaction free? *Optics and Spectroscopy*, 91, 352–357.

Vaidman, L. (2003). The meaning of the interaction-free measurements. *Foundations of Physics*, 33, 491–510.

Van Bladel, J. (1996). *Singular Electromagnetic Fields and Sources*. IEEE Press Series on Electromagnetic Wave Theory. Wiley.

Vincent, R., Juaristi, J., and Apell, P. (2011). Geometry and surface plasmon energy. *arXiv preprint arXiv:1103.2086*.

Vincent, R. P. (2009). *Electronic excitations, energy loss and electron emission in the interaction of charged particles with metallic materials and plasmon modes localized at surface singularities*. PhD thesis, University of the Basque Country.

Volz, J., Gehr, R., Dubois, G., Estève, J., and Reichel, J. (2011). Measurement of the internal state of a single atom without energy exchange. *Nature*, 475, 210–213.

Wachter, G. (2014). *Simulation of condensed matter dynamics in strong femtosecond laser pulses*. PhD thesis, Technischen Universität Wien.

Wachter, G., Lemell, C., and Burgdörfer, J. (2014). Electron rescattering at metal nanotips induced by ultrashort laser pulses. *Journal of Physics: Conference Series*, 488, 012005.

Wachter, G., Lemell, C., Burgdörfer, J., Schenk, M., Krüger, M., and Hommelhoff, P. (2012). Electron rescattering at metal nanotips induced by ultrashort laser pulses. *Phys. Rev. B*, 86, 035402.

Wesenberg, J. H. (2008). Electrostatics of surface-electrode ion traps. *Phys. Rev. A*, 78, 063410.

Wesenberg, J. H. (2009). Ideal intersections for radio-frequency trap networks. *Phys. Rev. A*, 79, 013416.

Wessel, J. (1985). Surface-enhanced optical microscopy. *J. Opt. Soc. Am. B*, 2, 1538–1541.

Whitaker, M. (1998). Interaction-free measurement and the quantum Zeno effect. *Physics Letters A*, 244, 502–506.

White, A. G., Kwiat, P. G., and James, D. F. (1999). "Interaction-free" measurements of quantum objects? In *Mysteries, puzzles, and paradoxes in quantum mechanics*, volume 461, pages 268–271. AIP Publishing.

White, A. G., Mitchell, J. R., Nairz, O., and Kwiat, P. G. (1998). Interaction-free imaging. *Phys. Rev. A*, 58, 605.

Wiener, A., Fernández-Domínguez, A. I., Horsfield, A. P., Pendry, J. B., and Maier, S. A. (2012). Nonlocal effects in the nanofocusing performance of plasmonic tips. *Nano Letters*, 12, 3308–3314.

Willets, K. A. (2012). Probing local electromagnetic field enhancements on the surface of plasmonic nanoparticles. *Progress in Surface Science*, 87, 209 – 220.

Williams, D. and Carter, C. (2009). *Transmission Electron Microscopy: A Textbook for Materials Science.* Springer.

Wright, K., Amini, J. M., Faircloth, D. L., Volin, C., Doret, S. C., Hayden, H., Pai, C.-S., Landgren, D. W., Denison, D., Killian, T., Slusher, R. E., and Harter, A. W. (2013). Reliable transport through a microfabricated X-junction surface-electrode ion trap. *New J. Phys.*, 15, 033004.

Yalunin, S. V., Gulde, M., and Ropers, C. (2011). Strong-field photoemission from surfaces: theoretical approaches. *Phys. Rev. B*, 84, 195426.

Yalunin, S. V., Herink, G., Solli, D. R., Krüger, M., Hommelhoff, P., Diehn, M., Munk, A., and Ropers, C. (2013). Field localization and rescattering in tip-enhanced photoemission. *Annalen der Physik*, 525, L12–L18.

Yanagisawa, H., Hafner, C., Doná, P., Klöckner, M., Leuenberger, D., Greber, T., Hengsberger, M., and Osterwalder, J. (2009). Optical control of field-emission sites by femtosecond laser pulses. *Phys. Rev. Lett.*, 103, 257603.

Yanagisawa, H., Hafner, C., Doná, P., Klöckner, M., Leuenberger, D., Greber, T., Osterwalder, J., and Hengsberger, M. (2010). Laser-induced field emission from a tungsten tip: Optical control of emission sites and the emission process. *Phys. Rev. B*, 81, 115429.

Yanagisawa, H., Hengsberger, M., Leuenberger, D., Klöckner, M., Hafner, C., Greber, T., and Osterwalder, J. (2011). Energy distribution curves of ultrafast laser-induced field emission and their implications for electron dynamics. *Phys. Rev. Lett.*, 107, 087601.

Yang, Z., Aizpurua, J., and Xu, H. (2009). Electromagnetic field enhancement in TERS configurations. *Journal of Raman Spectroscopy*, 40, 1343–1348.

Zeilinger, A. (1981). General properties of lossless beam splitters in interferometry. *Am. J. Phys.*, 49, 882–883.

Zhang, W., Cui, X., and Martin, O. J. F. (2009). Local field enhancement of an infinite conical metal tip illuminated by a focused beam. *Journal of Raman Spectroscopy*, 40, 1338–1342.

Zherebtsov, S., Fennel, T., Plenge, J., Antonsson, E., Znakovskaya, I., Wirth, A., Herrwerth, O., Süßmann, F., Peltz, C., Ahmad, I., Trushin, S., Pervak, V., Karsch, S., Vrakking, M., Langer, B., Graf, C., Stockman, M., Krausz, F., Rühl, E., and Kling, M. F. (2011). Controlled near-field enhanced electron acceleration from dielectric nanospheres with intense few-cycle laser fields. *Nature Phys.*, 7, 656–662.

Zhu, Y. and Dürr, H. (2015). The future of electron microscopy. *Physics Today*, 68, 32–38.

Zuloaga, J., Prodan, E., and Nordlander, P. (2010). Quantum plasmonics: optical properties and tunability of metallic nanorods. *ACS Nano*, 4, 5269–5276.

# Danksagung